Calibration of Airborne L-, X-, and P-band Fully Polarimetric SAR Systems Using Various Corner Reflectors

Abdullah Algafsh
MSc(Eng) UCT

Thesis Presented for the Degree of
DOCTOR OF PHILOSOPHY
in the Department of Electrical Engineering
UNIVERSITY OF CAPE TOWN

November 2017

“A person who never made a mistake never tried anything new”

-Albert Einstein (1879 - 1955)

List of Abbreviations

C	Covariance Matrix
K_L	Lexicographic Format
K_P	Pauli Format
L	Radar Cross Section Loss
Rx	Receive Channel
S	Scattering Matrix
Tx	Transmit Channel
T	Coherency Matrix
β_o	Beta Nought
δ	Crosstalk
γ_o	Gamma Naught
λ	Wavelength
σ_o	Backscattering Coefficient
θ_i	Incident Angle
θ_p	Grid Angle
ε	Error of the Inter-Plate Orthogonality
f	Co-Channel Imbalance
g	Cross-Channel Imbalance
2D	Two Dimensional Spaces
3D	Three Dimensional Spaces
AIRSAR	Airborne Synthetic Aperture Radar

APN	Average Polarimetric Noise
APT	Active Point Target
cm	Centimetre
CP	Compact Polarimetry
CR	Corner Reflector
CRLT	Circular Receive and Linear Transmit
CTLR	Circular Transmit and Linear Receive
DARR	Delft Atmospheric Research Radar
dB	Deci Bel
DCP	Dual Circular Polarimetric
DEM	Digital Elevation Model
DLR	German Aerospace Centre
DN	Digital Number
EM	Electromagnetic
ENVI	Image Analysis Software
ERIM	Environmental Research Institute of Michigan
ERS	European Remote-Sensing
ESA	European Space Agency
FMCW	Frequency Modulated Continuous Wave
GHz	Gigahertz
GNSS	Global Navigation Satellite System
GPS	Global Positioning System
H	Horizontal Polarization
HG	Horizontal Gridded

HH	Horizontal, Horizontal Polarization
HV	Horizontal, Vertical Polarization
Hz	Hertz
IDL	Interactive Data Language
IMU	Inertial Measurement Unit
JPL	Jet Propulsion Laboratory
K	Calibration Constant
KACST	King Abdulaziz City for Science and Technology
Kg	Kilogram
Km	Kilometres
m	Meter
MHz	Megahertz
mm	Millimetre
NASA	National Aeronautics and Space Administration
NESZ	Noise Equivalent Sigma Zero
PCB	Printed Circuit Board
PhD	Doctor of Philosophy
PRF	Pulse Repetition Frequency
RCM	Radarsat Constellation Mission
RCS	Radar Cross Section
RF	Radio Frequency

RFI	Radio Frequency Interference
RISAT	Radar Imaging Satellite
RMS	Root Mean Square
SAR	Synthetic Aperture Radar
SIR	Spaceborne Imaging Radar
SLC	Single Look Complex
SNR	Signal to Noise Ratio
UAVSAR	Uninhabited Aerial Vehicle Synthetic Aperture Radar
UTM	Universal Transverse Mercator
V	Vertical Polarization
VG	Vertical Gridded
VH	Vertical, Horizontal Polarization
VV	Vertical, Vertical Polarization
W	Watt

Abstract

Synthetic aperture radar polarimetry is one of the current developments in the field of remote sensing, due to the ability of delivering more information on the physical properties of the surface. It is known as the science of acquiring, processing and analysing the polarisation state in an electromagnetic field. The increase of information with respect to scalar radar comes at a price, not only for the high cost of building the radar system and processing the data or increasing the complexity of the design, but also for the amount of effort needed to calibrate the data. Synthetic aperture radar polarimetric calibration is an essential pre-processing stage for the correction of distortion interference which is caused by the system inaccuracies as well as atmospheric effects.

Our goal, with this thesis, is to use multiple passive point targets to establish the difference between fully, and compact polarimetric synthetic aperture radar systems on both calibration, and the effects of penetration.

First, we detail the selection, design, manufacture, and deployment of different passive point targets in the field for acquiring X- and P-band synthetic aperture radar data in the Netherlands. We started by presenting the selection and design of multiple passive point targets. These were a combination of classic trihedral and dihedral corner reflectors, as well as gridded trihedral and dihedral corner reflectors. Additionally, we detailed the construction of these corner reflectors. The number of constructed corner reflector totalled sixteen, where six are for X-band and six for P-band, as well as four gridded corner reflectors for X-band. Finally, we present the deployment of the corner reflectors at three different sites with carefully surveyed and oriented positions.

Then, we present the calibration of three different fully polarimetric synthetic aperture radar sensors. The first sensor is the L-band synthetic aperture radar sensor and we acquired data using two square trihedral corner reflectors. The calibration includes an evaluation of two crosstalk methods, which are the Quegan and the Ainsworth methods. The results showed that the crosstalk parameters for the Quegan method are all between -17 dB to -21 dB before calibration, while there is a small improvement in the range of 3 dB after calibration. While the Ainsworth method shows around -20 dB before calibration, and around -40 dB after calibration. Moreover, the phase, channel imbalance, and radiometric calibration were corrected using the two corner reflectors. Furthermore, the other two synthetic aperture radar sensors are X- and P-band synthetic aperture radar sensors, and we acquired polarimetric data using our sixteen corner reflectors. The calibration includes the crosstalk estimation, and correction using the Ainsworth method and the results showed the crosstalk parameters before calibration for X-band are around -23 dB, and they are around -43 dB after calibration, while crosstalk parameters before calibration for P-band are around -10 dB, and they are around -30 dB after calibration. The calibration also includes the phase, channel imbalance, and radiometric calibration, as well as geometric correction and signal noise ration measurement, for both X- and P-band.

Next, we present the performance of gridded trihedral and dihedral corner reflectors using an X-band synthetic aperture radar system. The results showed both gridded trihedral and dihedral reflectors are perfect targets for correcting the amplitude compared to classical corner reflectors; however, it is not possible to use the gridded reflectors to correct the phase as we need a return from two channels to have a zero phase difference between the polarisation channels H - V. Furthermore, we detail the compact polarimetric calibration over three compact polarimetric modes using a square trihedral corner reflector for the X-band dataset. The results showed no change in the $\pi/4$ mode while a 90° phase bias showed in the CTLR mode. Finally, the DCP mode showed a 64.43° phase difference, and it was corrected to have a zero phase, and the channel imbalance was very high at 45.92, the channels were adjusted to have a channel imbalance of 1.

Finally, an experiment to measure the penetration and reduction of P-band signal from a synthetic aperture radar system was performed using two triangular trihedral corner reflectors. Both of them have 1.5 m inner leg dimensions. The first triangular trihedral corner reflector was deployed in a deciduous grove of trees, while the other one was deployed a 10 m distance away on a grass covered field. After system calibration based on the reflector in the clear, the results showed a reduction of 0.6 dB in the HH channel, with 2.28 dB in the VV channel. The larger attenuation at VV is attributable to the vertical structure of the trees. Additionally, we measured the polarimetric degradation of the triangular trihedral corner reflector immersed in vegetation (trees). Further, after calibration, the co-polarisation phase difference is zero degrees for the triangular corner reflector which was outside the trees, and 62.85° for the corner reflector inside the trees.

The designed and fabricated X- and P-band SAR can work operationally with the calibration parameters obtained in this thesis. The data generated through the calibration experiments can be exploted for further applications

Acknowledgements

I wish to express my gratitude to all the following people and organisations who contributed in some way to the work described in this thesis and for assistance and support during my research in the University of Cape Town over the past four years.

Thanks to my parents for allowing me to realise my own potential. All the support they have provided me over the years was the greatest gift anyone has ever given me. Through highs and low they were always encouraging and supportive of my endeavours, and for this I cannot even begin to express my gratitude.

My wife Hessah Alhuwairini and my beautiful five year old daughter Hla who have been with me since I started in 2013, and they share all the beautiful moments with me in Cape Town. They were a very supportive, and it would not happened without them. Also, my new four month old boy Mohammed who has just joined us.

My supervisor, Professor Michael Inggs, for his support, patience, and encouragement throughout my graduate studies. It is not often that one finds an advisor and colleague that always finds the time to listen to the little problems and roadblocks that unavoidably crop up in the course of performing research. His technical and editorial advice was essential in the completion of this dissertation and he has taught me innumerable lessons, and given insights on the workings of academic research in general. My co-supervisor Dr Amit Mishra who provided valuable input, especially in the context of academic procedure.

The Radar Remote Sensing Group at the University of Cape Town, past and

present for the stimulating discussions, motivation, inspiration and company during my studies. Notably those who first got me interested in synthetic aperture radar and for all the fun we have had in the last four years.

The technical and administrative staff from the faculty of engineering and built environment especially from the Electrical Engineering department of the University of Cape Town, in particular Nicole and Carol for providing solutions to the numerous administrative related issues I encountered.

I am grateful for the funding sources that allowed me to pursue my graduate school studies from King Abdulaziz City for Science and Technology (KACST) in Riyadh, Saudi Arabia. Also, for my managers in KACST, past and present who supported me during my studies, and got me interested in Synthetic Aperture Radar.

DroneSAR in South Africa for providing all the support during the design and construction of the corner reflectors, as well as managing the radar project.

The small workshop in Cape Town that helped me in building the gridded corner reflectors which took more effort than expected to build.

Adriano Meta from Metasensing for all the support he provided during the research, and the wonderful camping to collect the data. Additionally, Alex who spent many days of deploying the corner reflectors in extremely cold weather at Teuge airport, as well as the insulation of the system on the airplane.

My deepest thanks go to the members of my family. My two brothers Abdulaziz and Saleh from who supported me during my study abroad and for taking care of everything back home. My brother, Ibrahim who is recovering from cancer and hope he gets well soon.

Finally, I would like to dedicate this work to my older brother Mohammed who I lost as a result of a car accident. I hope that this work makes you proud.

Contents

List of Figures

List of Tables

Chapter 1

Introduction

Early research in radar polarimetry appeared in the 1940's, focusing on characterising aircraft targets by using polarised radar echoes. During the 1940's, Sinclair played a significant role in the field of radar polarimetry, with his introduction of the concept of the scattering matrix [1]. He showed that a radar target acts as a polarisation transformer, by representing the properties of a coherent radar target in the scattering matrix [2]. Six years later, Kennaugh proposed the optimal target polarisation concept for reciprocal, and target in monostatic cases. Kennaugh's idea was used as the basis for related studies for the following twenty years [1].

A PhD thesis by Huynen in the 1970's started the new age of radar polarimetry; this researcher used Kennaugh's concept of optimal target polarisation to develop a way of targeting radar phenomena [1] [3]. The advancements of radar polarimetry shifted to a higher gear in 1985, when JPL proposed a fully polarimetric L-band airborne SAR system known as AIRSAR. Later, AIRSAR became the primary imaging polarimeter for twenty years, with two more frequencies, which are the P- and C-bands. JPL researchers, especially Van Zyl who introduced the polarisation signature to characterise the scattering mechanisms, made significant contributions to the developments of SAR polarimetry techniques, between the 1980's and the 1990's. Ten years later, a decline in the volume of polarimetric radar research from JPL caused the cessation of AIRSAR's operations, due

to the changes that had occurred in remote sensing initiatives. The decline was picked up by European researchers, with the support of ESA; they were able to develop different SAR sensors, as well as achieving alternative experiments with improvements in spatial resolution and well calibrated polarimetric data [2].

Polarimetric calibration is an important pre-processing step for the correction of distortion, caused by system inaccuracies and atmospheric effects [4]. In earlier years, polarimetric calibration was not a priority for researchers, however with improvements in technology, polarimetric calibration is becoming the norm [5] [6]. Scientists in the field of SAR polarimetry reached a stage where they needed calibrated SAR data to compare data from alternate SAR sensors and carry out multi-temporal studies over large areas, as well as extracting geophysical parameters from backscatter. Also, different backscatter phenomena types could be well understood, if polarimetric SAR data is calibrated [7].

Nowadays, polarimetric calibration remains an active research area, due to the implementation of new and different SAR sensors by various organisations worldwide. Some of these sensors are fully polarimetric and some are planned to be compact polarimetric SAR sensors. For example, the C-band RCM, a compact sensor transmitting a circular left or right, and receiving both vertical and horizontal polarisation, is planned to be launched in 2018. The calibration of fully and compact polarimetric data will help to better target classification and will improve the accuracy of the data.

To date, existing literature has shown limited work in the polarimetric calibration of the fully and compact polarimetric modes. Several issues still have to be investigated to establish the difference between a fully calibrated compact polarimetric and a fully polarimetric SAR system. The primary concern is the crosstalk correction, as well as system channel amplitude and phase corrections. This thesis presents the use of multiple trihedral and dihedral corner reflectors to establish the difference between fully calibrated compact polarimetry and fully polarimetric data, as well as penetration measurements of low frequency SAR systems. Additional details on the design, testing, and deployment of the corner reflectors for X- and P-band are also presented.

1.1 Synthetic Aperture Radar Polarimetry

The SAR system is typically mounted on a flying platform, like an aircraft or a satellite, which enables it to produce images of large swaths of terrain. While the platform is in flight, the radar transmits pulses at a specific frequency (known as the PRF), and it receives raw data in the form of backscattering signals that are sampled and stored in a matrix. In order to generate information from this raw data, it must be compressed and processed to produce a 2D radar image, known as single look complex (SLC) images [8].

SAR polarimetry is known as the science of acquiring, processing and analysing the polarisation state of an electromagnetic field [9]. In SAR polarimetry, information about the geographical feature of interest is embedded within the polarisation of the electromagnetic wave. The system creates polarised waves using antennas that transmit and receive EM waves with particular polarisation. Fig. 1.1 address the three different polarisation complexity levels from the radar system which are: single, dual, and quad polarisation. Single polarised SAR transmits either horizontal H, or vertical V polarisation and receives only one polarisation. Additionally, dual polarised SAR transmits either horizontal H or vertical V polarisation, and receives both H and V. Eventually, quad polarised SAR transmits both horizontal H and vertical V polarisation, and receives from the four polarimetric channels (HH, HV, VH, VV). All four polarisation channels are used for quad polarimetric SAR, meaning that it provides more information than dual-polarised SAR data.

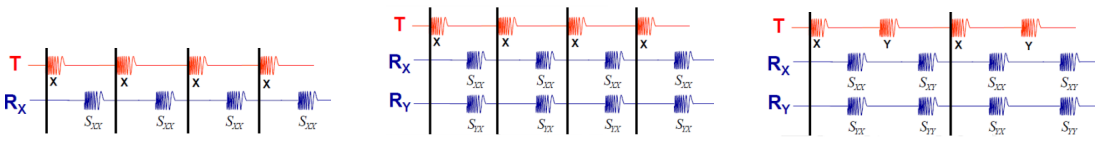

Figure 1.1: *Three different polarisation complexity levels from the radar system where; (a) Single polarisation, (b) Dual polarisation, and (c) Quad polarisation. [10]*

1.1.1 Compact Polarimetry

In the past years, new SAR modes have emerged that are different from the transmit horizontal H or vertical V in dual polarisation systems known as compact polarimetry (CP). Fig. 1.2 shows the classification of classical SAR modes in contrast to the three compact modes. The classical modes adopted only the horizontal and vertical polarisation for both transmit and receive which led to four polarimetric modes which are: single (HH or VV), dual (HH, HV or VV, VH), and quad (HH, HV, VH, VV) [11].

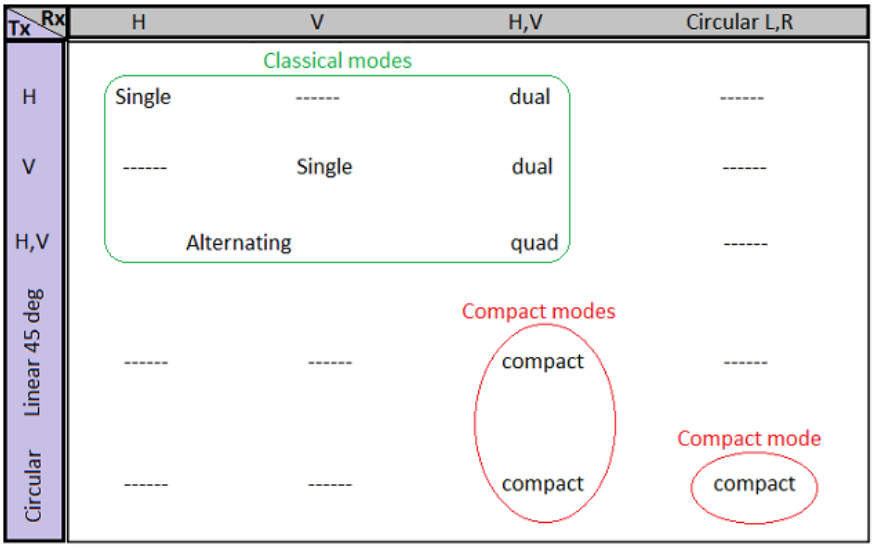

Figure 1.2: *Classical and compact polarimetric modes. [11]*

Compact polarimetry has the ability of reducing the complexity, cost, mass, and data rate of a SAR system while attempting to obtain many capabilities of quad polarisation systems [12]. The first compact polarimetric mode is the $\pi/4$ mode and was introduced by Souyris et al. in 2005 [13]. Fig. 1.3(a), shows the idea of the first compact mode where we transmit only one polarisation which is oriented at 45° with respect to the horizontal, and receive the return in both horizontal and vertical polarisation. The second compact mode is the circular receive and linear transmit (CRLT) mode, also known as the hybrid mode [14]. The CRLT was proposed by Raney in 2007 and is shown in Fig. 1.3(b), which

transmits on circular polarisation, and receives on both linear horizontal, and vertical polarisation. The last compact mode called the dual-circular polarimetric (DCP) mode which was proposed by Stacy and Preiss in 2006 [15]. As shown in Fig. 1.3(c), the idea is to transmit a circular polarisation either right or left, and receive both left and right polarisation.

In all the previous compact polarimetric modes, there would be only one transmit/receive cycle required compared to two in a full polarisation system. This results in reducing the pulse repetition frequency, as well as the data rate by factor of two, for giving swath width [16].

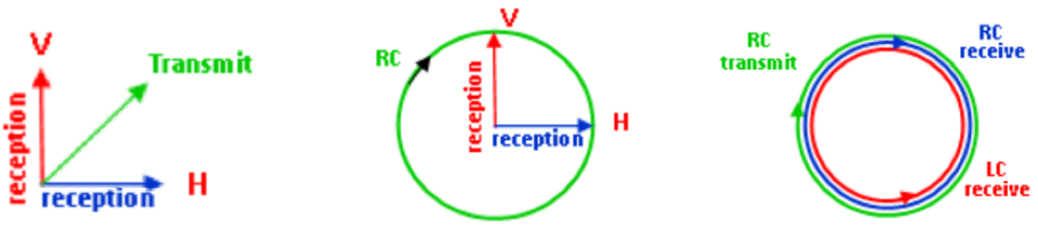

(a) *(b)* *(c)*

Figure 1.3: *Compact polarimetric modes: a) $\pi/4$ mode and b) CRLT mode and c) DCP mode. [17]*

The scattering vectors $\vec{K_{CP}}$ for the three different compact modes $\pi/4$, dual circular polarimetric (DCP), and right circular transmit and linear receive mode (CTLR) are represented in Table 1.1 [12] [17].

Table 1.1: *The scattering vectors $\vec{K_{CP}}$ for the three different compact modes $\pi/4$, (DCP), and (CTLR). [12]*

Compact Mode	Scattering Vectors $\vec{K_{CP}}$
$\pi/4$	$[S_{hh}+S_{hv} \quad S_{vv}+S_{hv}]^T/\sqrt{2}$
DCP	$[S_{RR} \quad S_{RL}]^T] = [S_{hh}-S_{vv}+i2S_{hv} \quad i(S_{hh}+S_{vv})]^T/2$
CTLR	$[S_{hh}-iS_{hv} \quad -iS_{vv}+S_{hv}]^T/\sqrt{2}$

1.1.2 Scattering, Covariance, and Coherency Matrix

A horizontal or vertical polarised wave that is incident to a particular geographical feature of interest can create a radar signal with a backscattered portion that has contributions from both the horizontal and the vertical polarisation. Due to the fact that the horizontal and vertical polarisation provide enough information to describe the electromagnetic wave, the backscattering properties make it possible to describe the earth feature using scattering matrix given by [18]:

$$S = \begin{bmatrix} S_{HH} & S_{HV} \\ S_{VH} & S_{VV} \end{bmatrix} \tag{1.1}$$

In this situation, the 2×2 scattering matrix $[S]$ is comprised of four complex elements. The diagonal elements represent the co-polarised channels, while the off-diagonal elements represent the cross-polarised channels. Using the scattering matrix, it is possible to compute the strength, polarisation, and polarisation signature of a scattered wave at every imaged pixel, regardless of the polarisation of the incident wave. To obtain the complex elements of the scattering matrix, it is necessary to calculate the magnitude and phase of the four polarimetric channels: HH, HV, VH, and VV [18].

It is possible to use the scattering matrix to describe the backscattering properties for either coherent or pure targets. However, for distributed scatterers that are dominated by partially polarised waves, the scattering matrix is not sufficient for obtaining information. In addition, it is necessary to take the second derivative of the scattering matrix to yield the covariance and coherency matrices [18]. For this, the vectorised form of the scattering matrix must be used, in both the lexicographic basis, and the Pauli basis. The lexicographic format, in which the reciprocity condition is assumed, is given by:

$$K_L = \begin{bmatrix} S_{HH} \\ \sqrt{(2)}S_{HV} \\ S_{VV} \end{bmatrix} \tag{1.2}$$

The covariance matrix is derived by multiplying the lexicographic vector in

Eq. 1.2 with its complex conjugate transpose $C = K.K^*$ to form the covariance matrix:

$$C = \begin{bmatrix} S_{HH}.S_{HH}^* & \sqrt{(2)}S_{HH}.S_{HV}^* & S_{HH}.S_{VV}^* \\ \sqrt{(2)}S_{HV}.S_{HH}^* & 2S_{HV}.S_{HV}^* & \sqrt{(2)}S_{HV}.S_{VV}^* \\ S_{VV}.S_{HH}^* & \sqrt{(2)}S_{VV}.S_{HV}^* & S_{VV}.S_{VV}^* \end{bmatrix} \tag{1.3}$$

Also, the Pauli format with assuming reciprocity is written as follows:

$$K_P = \frac{1}{\sqrt{(2)}} \begin{bmatrix} S_{HH} + S_{VV} \\ S_{HH} - S_{VV} \\ 2S_{HV} \end{bmatrix} \tag{1.4}$$

The coherency matrix is derived by multiplying the Pauli vector in Eq. 1.4 with its complex conjugate transpose $T = K_P.K_P^*$ to form the coherency matrix.

$$T = \frac{1}{2} \begin{bmatrix} <| S_{HH} + S_{VV} |^2> & < (S_{HH} + S_{VV})(S_{HH} - S_{VV})^* > & 2 < (S_{HH} + S_{VV})S_{HV}^*) > \\ < (S_{HH} - S_{VV})(S_{HH} + S_{VV})^* > & <| S_{HH} - S_{VV} |^2> & 2 < (S_{HH} - S_{VV})S_{HV}^*) > \\ 2 < S_{HV}(S_{HH} + S_{VV})^* > & 2 < S_{HV}(S_{HH} - S_{VV})^* > & 4 <| S_{HV} |^2> \end{bmatrix} \tag{1.5}$$

1.1.3 Point Targets

Point targets are generally categorised into two major groups which are passive and active point targets [19]. Both passive and active point targets permit adequate RCS for a better target to clutter separation [20]. The active point target consists of a transmit and receive antenna with an RF amplifier in between. The APT works by detecting the signal, and then using the RF amplifier to amplify the signal to transmit it again with a time delay as shown in Fig. 1.4 [21] [22].

The APT is a powerful tool for calibrating both airborne and spaceborne SAR systems because of its small physical size and its ability to calibrate radars that operate in any polarisation configuration [23]. Additionally, the APT can provide very high RCS comparing to passive point targets but it is exorbitantly expensive to build, and the characteristics of the scattering are more sensitive to the change

of environmental temperature than passive point targets [24]. For example, the calibration experiment of ERS-1 [1] SAR using APT in Japan had a RCS of over 60 dBm^2 which is difficult to obtain by using passive point targets because it requires a reflector with an inner leg dimension up to 5 m with a higher frequency [25].

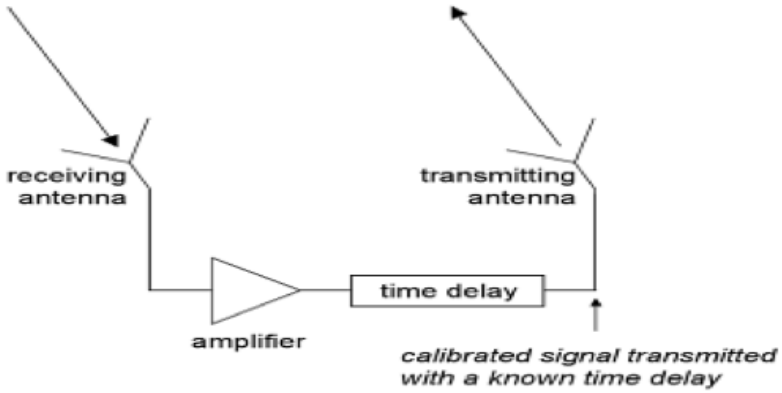

Figure 1.4: *Active point target also known as active radar calibrator. [22]*

The second major group of point targets is passive point targets, such as trihedral and dihedral corner reflectors. They are well known in polarimetric calibration and have long been used as radar reflectors and calibration targets because they are inexpensive to build, and provide a good backscattering response for a wide range of incident angles [26] [27]. The trihedral corner reflector consists of three electrically conductive surfaces, and the surfaces have different shapes; triangular, square, and circular as shown in Figs. 1.5(b) - 1.5(c) - 1.5(d), while the dihedral corner reflector consists of only two surfaces that are on orthogonal planes as shown in Fig. 1.5(a) [28].

[1] ERS-1 is the first purely civilian Earth observation C-band SAR satellite which was launched in July 1991 by European Space Agency (ESA) and is no longer in operation

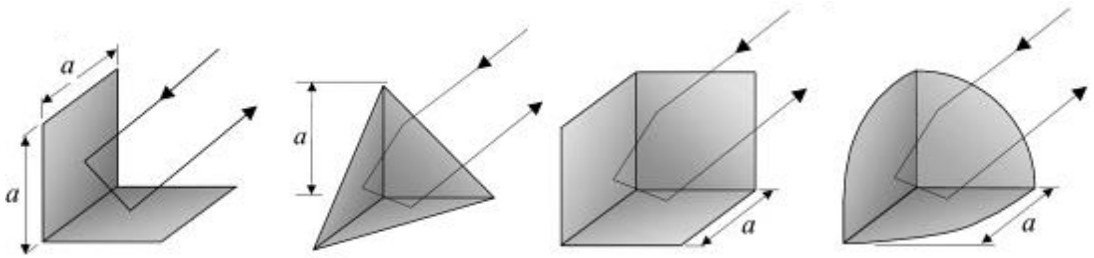

Figure 1.5: *Passive point targets where; (a) Dihedral corner reflector, (b) Triangular trihedral, (c) Square trihedral, and (d) Circular trihedral. [22]*

Each shape of the corner reflector has different backscatter properties [20]. Table 1.2 shows the theoretical maximum RCS for the common corner reflectors where both the inner leg dimension, and the frequency control the maximum RCS. Also, the beam widths show the range of angles over which their responses stay above half that at bore sight(less than 3 dB down on maximum [2]) [22].

Table 1.2: *Properties of passive point targets. [22]*

Corner Reflector	Maximum RCS	3 dB beam-width
Dihedral	$\sigma = \frac{8\pi a^2 b^2}{\lambda^2}$	$\pm 15°$
Triangular Trihedral	$\sigma = \frac{4\pi a^4}{3\lambda^2}$	40° cone angle about bore sight
Square Trihedral	$\sigma = \frac{12\pi a^4}{\lambda^2}$	23° cone angle about bore sight
Circular Trihedral	$\sigma = \frac{15.6a^4}{\lambda^2}$	32° cone angle about bore sight

1.1.4 Polarisation Signature

A polarisation signature is known as a graphic way of representing scattering characteristics in 3D. The polarisation signature is frequently used for SAR polarimetric calibration to correct any distortion in the image especially with return from corner reflectors. The graphic of polarisation signature shows the difference

[2] The 3 dB down means that the angle a way from bore sight at which the response is -3 dB compared with the maximum [22]

in scattering intensity and normalised scattering cross-section, as well as offering a wealth of information about the many properties of a surface.

Four independent variables describe the polarisation signature which are; the ellipticity and orientation of the incident wave, and the ellipticity and orientation of the backscattered wave. However, due to the complexity of interpretation, two variables will be used at a time namely, the ellipticity and orientation of the incident wave to represent the polarisation signature [29]. The polarisation signature is either co-polarised or cross-polarised polarisation. The co-polarised signature represents the return from the two linear co-polarised channels (HH and VV) while the cross-polarised signature represents the return from the linear cross-polarised channels (HV and VH).

Figs. 1.6 and 1.7 show the theoretical polarisation signature for the trihedral and dihedral corner reflectors. The variables on the X-axis represent the ellipticity angle of ±45° while the variables on the Y-axis represent the orientation angle between 0° and 180°. The maximum is for the co-polarised signature when the ellipticity angle is zero for linear polarisation, while the minimum is accurate when the ellipticity angle is ±45° for circular polarisation [30].

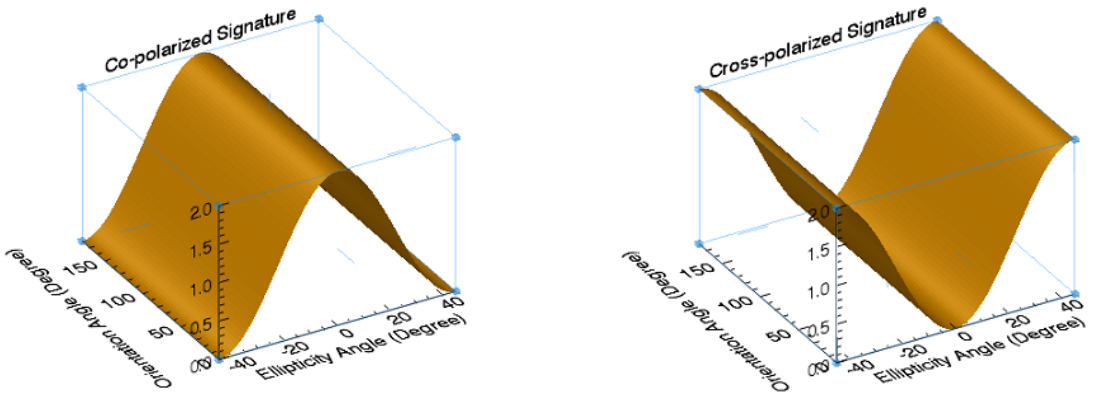

(a) *(b)*

Figure 1.6: *Theoretical polarisation signature of trihedral corner reflector where; (a) Co-polarisation signature, and (b) Cross-polarisation signature.*

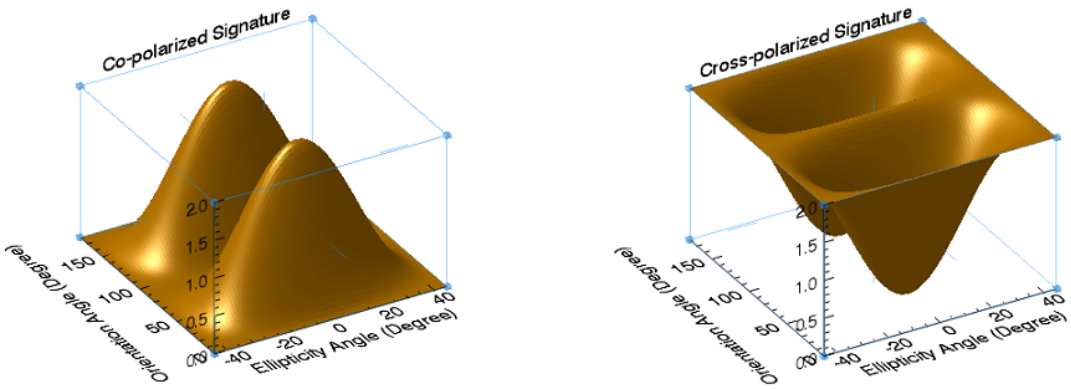

(a) *(b)*

Figure 1.7: *Theoretical polarisation signature of dihedral corner reflector where; (a) Co-polarisation signature, and (b) Cross-polarisation signature.*

Furthermore, the dihedral corner reflector can be rotated by 45° around the radar line of sight, and it results in zero for the linear horizontal co-polarised response, and a maximum for the linear horizontal cross-polarised response. This mean the dihedral corner reflector can be used to have a cross-polarisation response to calibrate the cross-polarisation return.

1.1.5 Motivations

There are many SAR sensors under development by different organisations in the world. Many of these are quad polarimetric systems, and others are planned to be compact polarimetric systems. While it must be conceded that compact polarimetric data currently is not yet mature enough to replace fully polarimetric data for the calibration issues to have accurate data. Compact polarimetric data needs to be well calibrated to achieve better target classification for a researcher. The motivation behind using a number of varying passive point targets to establish the difference between fully calibrated quad and compact polarimetric systems is presented in the following benefits for consideration.

Currently the most pertinent motivation for using passive point targets to calibrate both fully and compact polarimetric data is that they are inexpensive to

build, easy to manufacture, and deploy in the field to cover the swath image for calibration. The passive point targets require no power to operate and their maintenance is low compared to active radar calibrators such as a transponder.

The main benefit of using CP sensors is because they are able to reduce complexity, cost, mass, and data rate of an SAR system while attempting to obtain many capabilities of full polarisation systems. The CP sensors require only half of the transmitted power, and half of the PRF compared to a fully polarimetric SAR system. This results in a better performance of the swath coverage area and revisit-time, also making the compact polarimetric sensors a suitable choice for Earth-observing purposes.

A further benefit is the opportunity of having a low frequency SAR system such as P-band due to its numerous applications. Using a P-band SAR system allows penetration of low to moderate vegetation, as well as the estimation of soil texture from a time series of measurements during a drying out period following precipitation.

1.1.6 Limitations

One of the biggest challenges in the field of SAR, is the cost of collecting data. The flying cost in Europe is very expensive, and the availability of pilots needs to be scheduled days before flying. These limitations are due to the large size of the Yagi antenna for P-band which requires a large airplane with high wings such as the Cessna 208B for installation. On the other hand, flying with only X-band would reduce the cost of flying as it can be installed on a smaller airplane.

Another challenging point was the deployment of corner reflectors. The near, and far side, were inside the airports and close to the runway. The airport authorities gave us very limited time to deploy the reflectors, and move them before sunset, and we were not allowed to leave them overnight. Some of the reflectors could not be deployed, such as the dihedral corner reflectors inside the airport, however in the midfield, we were able to deploy all the reflectors as it was outside the airport. The midfield is an open field which is used for parachuting activities.

Also, most of the open areas around the airport are private houses and the people did not allow us to deploy our reflectors around their dwellings.

The fundamental and unavoidable limitation of SAR is the huge amount of data rate. For example, after processing X-band raw data to SLC images processed with 0.5 m spacing in horizontal and vertical, we had about 100 GHz of data for only one track of X-band. Processing L-, X-, and P-band data required a number of external hard drives and processing took a long time due to the huge amount of data received.

1.2 Research Hypothesis

The research hypothesis for this thesis is therefore:

It is possible to use multiple trihedral and dihedral corner reflectors to establish the difference between a fully calibrated compact polarimetric system and a fully polarimetric SAR system.

The research questions associated with this hypothesis are as follows:

- What are the requirements for passive point targets based on number, type of corner reflectors, and assumptions to be made on fully and compact polarimetric calibration?
- What is the optimum design of gridded trihedral and dihedral corner reflectors? and do the gridded trihedral and dihedral corner reflectors provide results similar to classical trihedral and dihedral corner reflectors?
- Is it possible to correct the phase and channel imbalance by using external reflectors for the three compact polarimetric modes?
- What is the difference between a fully calibrated compact polarimetric system and a fully polarimetric SAR system?
- What is the signal reduction and penetration of P-band through trees on fully and compact polarimetry?

- What is the polarimetric degradation of triangular trihedral corner reflector immersed in vegetation (Trees)?

1.3 Statement of Originality

The candidate believes that the following parts of this work constitute original contributions to the field of SAR polarimetry:

- The simulation measurements on the effect of perforating the corner reflector on maximum radar cross section.
- The presentation of the optimum design and performance measurements of gridded dihedral and trihedral corner reflectors using X-band to have only horizontal or vertical reflection from the reflector.
- The presentation of measurements of signal penetration of low radar frequency on trees using two triangular trihedral corner reflectors for quad and compact polarimetry.
- The presentation of polarimetric degradation of triangular trihedral corner reflector immersed in vegetation(Trees).

1.4 Publications

The research detailed in this thesis has contributed to the following publications:

A Algafsh, M Inggs, A Mishra, *Investigation of calibration aspects of fully and compact polarimetric SAR systems*, Microwave Conference (APMC), 2016 Asia-Pacific IEEE, pp. 1-5. [31]

A Algafsh, M Inggs, A Mishra, *The effect of perforating the corner reflector on maximum radar cross section*, Microwave Symposium (MMS), 2016 16th Mediterranean IEEE, pp. 1-4. [32]

A Algafsh, M Inggs, A Mishra, *Measurements of Signal Penetration for P-band SAR System Through Trees Using Two Trihedral Corner Reflectors*, Geoscience and Remote Sensing Symposium (IGARSS), 2017 IEEE International, (Accepted)

A Algafsh, M Inggs, A Mishra, *Crosstalk Estimation and Correction Using Quegan and Ainsworth Methods*, Radio and Antenna Days of the Indian Ocean (RADIO), 2017 IEEE, (Accepted)

A Algafsh, M Inggs, A Mishra, *Signal Penetration of Low SAR Frequency Over Three Compact Polarimetric Modes*, Radio and Antenna Days of the Indian Ocean (RADIO), 2017 IEEE, (Accepted)

A Algafsh, M Inggs, A Mishra, *Calibration of Compact Polarimetric SAR Sensor Using Gridded and Classical Corner Reflectors*, Geoscience and Remote Sensing, IEEE Transactions on, (Accepted)

A Algafsh, M Inggs, A Mishra, *Calibration of Fully Polarimetric X- and P-band SAR Sensors Using Multiple Corner Reflectors*, Geoscience and Remote Sensing, IEEE Transactions on, (Submitted)

1.5 Tools

Various software tools were used in the research such as IDL 4.8, ENVI 4.8, PolSARpro 4.2.0, and Matlab.

- FEKO is a computational electromagnetic software product developed by Altair Engineering, and used during the simulation of the corner reflectors.

- IDL is a programming language used for data analysis. It is popular in particular areas of science, such as astronomy, atmospheric physics and medical imaging.

- ENVI is image analysis software, which is used by geographic information system professionals, scientists, and image analysts to extract meaningful information from imagery.

- PolSARpro is an ESA open source toolbox, and used for polarimetric SAR data processing and education. The software is able to handle dual polarisation, as well as quad polarisation data from a wide range of SAR space and airborne missions.

1.6 Thesis Outline

This introductory chapter is followed by a literature review in Chapter 2 to provide comprehensive insight to both the background, and current development of synthetic aperture radar polarimetric calibration. More detailed summaries of each chapter are presented below.

1.6.1 Literature Review

The literature review in Chapter 2 covers relevant and/or significant research efforts that have been published relating to the field of SAR polarimetric calibration. The content in this chapter is organised into three parts which are; passive point targets, fully polarimetric calibration and, compact polarimetric calibration.

The first part introduces the relevant research for passive point targets in Section 2.1 which can be used in the calibration of SAR polarimetric data. Firstly, we introduce the review on classical trihedral and dihedral corner reflectors in Section 2.1.1, as well as rotating the dihedral corner reflector by 45° to generate cross-polarisation return. Then, we present the relevant research on gridded corner reflectors in Section 2.1.2 to obtain a specific polarisation return from the target.

The second part introduces the relevant research for fully polarimetric calibration in Section 2.2. Firstly, Section 2.2.1 details a number of crosstalk methods which have been developed since the early 1990's to estimate and correct the crosstalk parameters, as well as a comparison between the crosstalk methods in Section 2.2.1.5. Secondly, we present the polarimetric phase and amplitude calibration in Section 2.2.2. The section includes two techniques that have been used for the phase correction, which have a calibration tone that is built into the radar system in Section 2.2.2.1, while the other technique does not have a calibration tone in the system in Section 2.2.2.2. Finally, we detail the radiometric calibration in Section 2.2.3 relating to the pixel's values of the backscattering coefficient of ground targets.

The third part introduces the relevant research of limited work that has been published on the compact polarimetric calibration in Section 2.3. This part includes all the relevant research on the three compact polarimetric modes $\pi/4$, DCP, and CTLR.

1.6.2 Passive Point Targets

Chapter 3 details the selection, design, construction, and deployment of different passive point targets which were used for the calibration of the XP-SAR airborne system.

The chapter begins in Section 3.1 by introducing the X-, and P-band main radar parameters in which we designed the passive point targets based on them. Then, we present the selection of the passive point targets which was based on the five characteristics that influence the success of external calibration target in Section 3.2. Initially we selected trihedral corner reflectors to generate co-polarisation components, as well as dihedral corner reflectors, rotated by 45°, to generate cross-polarisation components. Additionally, the shape of the trihedral was chosen to be square for X-band, while it is triangular for P-band, as it is more structurally rigid.

Secondly, in Section 3.3 we detail the design of the passive point targets which

includes the plate material and the size of corner reflectors to be 40 dB higher than the noise sigma equivalent zero curves of the X- and P-SAR systems.

Furthermore, the design section in 3.3.3 includes a simulation analysis of the effect of perforating the corner reflector on maximum RCS. We used four different hole sizes and three varying hole centre spacings to analyse the effect. The hole sizes which were used are one-tenth, one-sixth, one-quarter, and one-third of the radar wavelength for X-band (30 cm) with 10 mm, 12 mm, and 15 mm varying hole centre spacings. The results showed that a hole size of one-tenth of the wavelength, reduced the maximum RCS by less than 1 dBm^2 from the theoretical RCS, and the spacing between the two holes did not have much effect, while one-sixth of the wavelength reduced the maximum RCS by about 1 dBm^2, and the reduction between the spacing is very small at about 0.10 dBm^2. Finally, a hole size with one-quarter of the wavelength reduced the maximum RCS by more than 2 dBm^2, and the reduction between the spacing increased, while one-third of the wavelength had a reduction of about 4 dBm^2.

Moreover, the design section introduces the optimum design of gridded corner reflectors in 3.3.4. The section starts by analysing the effect of the grids width and the gap between the grids on the reduction of RCS section when the incident wave is parallel or perpendicular to the grids, as well as the discrimination between the channels. The second part of the section describes the design of gridded trihedral and gridded dihedral corner reflectors using square 50 cm surfaces. The analyses for the effect of wire widths and the gap between the wires showed that a gap of one tenth of the wavelength, at 0.5 mm, is the optimum choice, especially for the smaller size of reflector to have a better discrimination between the channels with only a 0.4 dBm^2 reduction on the maximum RCS.

Secondly, we present the construction of these passive point targets in Section 3.4. The total constructed classical corner reflectors are twelve reflectors with two sizes (0.5 m inner leg dimension for X-band, and 1.5 m inner leg dimensions for P-band). We constructed three square trihedral and three dihedral corner reflectors for X-band, while three triangular trihedral, and three dihedral corner reflectors for P-band using 1.2 mm aluminium plate were used. Additionally,

the section includes the construction of two gridded trihedral, and two gridded dihedral corner reflectors using a 3 mm aluminium plate, with a 570 mm inner leg dimension.

Finally, Section 3.5 presents the deployment of the corner reflectors at three different sites, with carefully surveyed and oriented positions, using GNSS for the test flights. The planned test sites are three areas, where two of them (near field and far field), being inside Teuge Airport, the Netherlands, while the third one (mid field) is an open field outside the airport which is used for parachuting activities. The three sites are flat and a distance away from clutter.

1.6.3 Fully Polarimetric Calibration

Chapter 4 presents, in two parts, the calibration of three different fully polarimetric SAR sensors; L-, X-, and P-band, using multiple passive point targets. Additionally, the chapter includes the installation of the three SAR systems on a Cessna 208B Grand Caravan.

The first part begins in Section 4.2 by illustrating the insulation of the L-band system onto the Cessna 208B Grand Caravan, and the deployment of the two square trihedral corner reflectors which we borrowed from Metasensing to acquire the data in October 2015. Then, we detail the calibration of the L-band SAR sensor using two square trihedral corner reflectors, which were deployed inside Teuge airport in the Netherlands.

The calibration of L-band starts by evaluating two crosstalk methods in Section 4.2.3.1 which are the Quegan and the Ainsworth methods. The result for Quegan showed that the crosstalk parameters are all between -17 dB and -21 dB before calibration, while a little improvement in the range of about 3 dB after calibration, while the Ainsworth method showed the crosstalk parameters before calibration of around -20 dB, while it is around -40 dB after calibration.

Then, we used the two square trihedral corners for the estimation and correction of the co-phase difference, the co-channel imbalance, as well as the radiometric

calibration while the cross-channels were corrected by averaging the return over the image. It was shown that the co-phase difference for the first reflector is zero degrees and 6° for the second reflector, as well as a co-channel imbalance of 1 for both reflectors. Finally, the radiometric calibration was corrected using the integral method to obtain the backscattering coefficient of the two reflectors, and the result showed a reduction of about 2.8 dB.

The second part of the chapter begins in Section 4.2 by illustrating the insulation of the X- and P-band systems to acquire the data in November 2016 on a Cessna 208 Grand Caravan, and then we detail the calibration of X- and P-band SAR sensors using six corner reflectors (three trihedral, and three dihedral rotated 45°) for X-band, and two trihedral corner reflectors for P-band which were deployed in and outside Teuge airport, the Netherlands.

The X-band data set was fully calibrated in Section 4.3.2 where we started by using the Ainsworth method for crosstalk estimation and correction. The crosstalk for all the parameters before calibration was around -23 dB, and they were around -43 dB after calibration.

Following that, we used six corner reflectors (three square trihedral for the co-channels and three dihedral corner reflectors rotated by 45° for the cross-channels) for the phase, the channel imbalance, the radiometric calibration, and the geometric correction. The result for the co-channel showed a phase difference for the three square reflectors RMS of 62.74° before correction, while the RMS for the three square reflectors was 0.75° after correction. Also, the co-channel imbalance had an RMS of 1.44 before correction and 1 after correction.

Furthermore, the result for the cross-channels showed a phase difference for the three dihedral reflectors RMS of 109.2° before correction, while the RMS for the three dihedral reflectors was 1.5° after correction. Additionally, the cross-channel imbalance had an RMS of 1.1 before correction and 1.02 after correction. Polarisation signatures were plotted for all the corner reflectors before and after calibration, as shown in Fig. 1.8; the co-polarisation signature for the square trihedral corner reflector in the midfield before and after calibration.

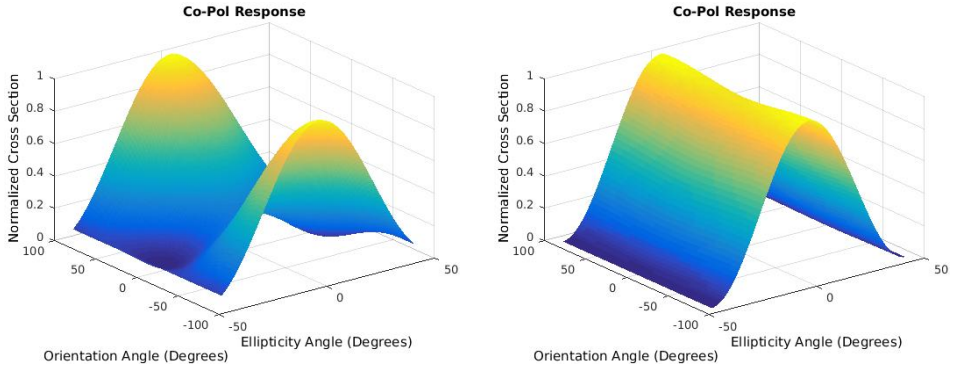

(a) *(b)*

Figure 1.8: *Co-polarisation signature for square trihedral corner reflector in the mid field where; (a) Before and (b) After calibration.*

The radiometric calibration result showed a very small reduction in overall backscattering coefficient for the three square trihedral corner reflectors, and the three dihedral corner reflectors of about 0.5 dB.

Finally, the surveyed positions of the X-band corner reflectors were used for geometric correction, and the results showed an RMS of 1.48 m in Northing and an RMS of 4.73 m in Easting before correction, and an RMS of 0.943 m in Northing, and an RMS of 0.769 m in Easting after correction.

The P-band dataset was fully calibrated in Section 4.3.5 which starts by using the Ainsworth method for crosstalk estimation and correction. The crosstalk for all the parameters before calibration were around -10 dB, and they were around -30 dB after calibration.

Following that, we used two triangular trihedral corner reflectors in the mid- and far-fields for the correction of the Phase, the channel imbalance, the radiometric calibration, and the geometric correction. The dihedral reflectors for the P-band were not deployed due to the limited time of deployment, as well as restrictions from the airport authorities due to the size of the test apparatus. Additionally, the trihedral reflector in the near field was out of the swath after processing, and we ended up having the two trihedral corner reflectors in the mid- and far-fields.

The result for the co-channel showed a phase difference for the two triangular reflectors RMS of 158.9° before correction, while the RMS for the three square reflectors was 0.7° after correction. Moreover, the co-channel imbalance had an RMS of 1.67 before correction and 1.02 after correction. Furthermore, the radiometric calibration result showed a reduction in overall the backscattering coefficient for the two triangular trihedral corner reflectors of about 1 dB.

Eventually, the surveyed positions of the P-band corner reflectors were used for geometric correction, and the results showed an RMS of 2.536 m in Northing, and an RMS of 4.019 m in Easting before correction, and an RMS of 1.85 m in Northing and an RMS of 0.34 m in Easting after correction.

1.6.4 Compact Polarimetric Calibration

Chapter 5 illustrates the performance of two gridded trihedral and two gridded dihedral corner reflectors in the first topic. The first gridded trihedral and dihedral corner reflectors use horizontal wires to obtain a reflection on the horizontal channel, while the second gridded trihedral and dihedral corner reflectors have vertical wires to obtain a reflection on the vertical channel. The second topic of this chapter, contained in Chapter 5 discusses an investigation into the calibration of the three compact polarimetric modes; $\pi/4$, DCP, and CTLR using classical square trihedral corner reflectors on X-band datasets which we simulated on 30 November 2016.

Firstly, in Section 5.2 we detail the performance of both gridded trihedral and dihedral corner reflectors which were deployed in the midfield next to the classical square trihedral corner reflector. It is shown that both the gridded trihedral and the gridded dihedral corner reflectors are perfect targets for correcting the amplitude, and the results are similar to the classical square trihedral corner reflector in terms of amplitude, however, it is not possible to use the gridded corner reflectors as a calibration target, due to the fact that if we need to correct the phase, a return from two channels is required to ensure a zero phase difference between the polarisation channels H - V.

The integral method was used to measure the backscattering coefficient for the gridded corner reflectors. The reduction in RCS for the gridded trihedral corner reflector was 5 dB in simulation, and 2 dB in actual measurements. Furthermore, the backscattering coefficient for the two gridded dihedral corner reflectors, where we have the reflection, is 31.8 dB giving a reduction in the RCS of 0.6 dB in measurements, while it was 2 dB in simulation. The difference between the simulation and construction is due to the increase of cutting by 7 cm while cutting the aluminium plates, which resulted in an increase in the total RCS.

The second topic of this chapter, contained in Section 5.3 presents the compact polarimetric calibration over three compact polarimetric modes using the square trihedral corner reflector in the midfield. We estimated the phase and channel imbalance for each mode using the square trihedral corner reflector. It is shown that in the calibration of the $\pi/4$ mode in Section 5.3.1, no change in phase between the two compact polarimetric channels, and additionally, there is no change in the channel imbalance.

Then, we present the CRLT mode in Section 5.3.2, and the result showed a very small change in the channel imbalance of 0.004, and the phase difference between the two compact polarimetric channels was 90° before correction. We corrected the phase by rotating the HH channel by 90° to have a zero phase difference between the two compact polarimetric channels, as well as adjusting the channel to have a channel imbalance of 1.

Finally, Section 5.3.3 presents the calibration of the DCP mode and the result showed a 64.43° phase difference, and it was corrected to have a zero phase difference between the two compact polarimetric channels. Furthermore, the channel imbalance was very high, at 45.92 between the two channels, and we adjusted the two compact polarimetric channels to have a channel imbalance of 1.

1.6.5 Vegetation Penetration for Quad and Compact Polarimetry

The penetration topic of this research, contained in Chapter 6 discusses penetration and reduction of P-band signal from both fully and compact polarimetric SAR systems using two triangular trihedral corner reflectors, which were deployed in the field around Teuge airport in the Netherlands. Also, the chapter includes a consideration in polarimetric degradation of the triangular trihedral corner reflector immersed in vegetation (trees) of both fully, and compact polarimetric data.

The chapter begins in Section 6.2 by giving an overview of the relevant and/or significant research efforts that have been published relating to the penetration of SAR in different applications. Then, the deployment of the two triangular trihedral corner reflectors, where one of them is deployed in a deciduous grove of trees, while the other one is deployed 10 m away, on a grass covered field, is presented in Section 6.3. The section also includes the SAR acquisition of the data.

Following on in Section 6.4 detailed measurements of P-band signal for fully polarimetric datasets are given by using the two triangular trihedral corner reflectors. After the system calibration based on the corner reflector was in the clear, the result showed a reduction of 0.6 dB in the HH channel, with a 2.28 dB reduction in the VV channel. The larger attenuation at VV is attributable to the vertical structure of the trees. Along with the above, we measured the polarimetric degradation of the triangular trihedral corner reflector immersed in vegetation (trees), and the result showed a shift in phase of 62.85°.

Co- and cross-polarisation signatures were presented to show the difference between the two triangular trihedral corner reflectors among the trees and in the clear. Fig. 1.9 shows the co-polarisation signature for the two triangular trihedral corner reflectors where; (a) In the clear, and (b) Between the trees.

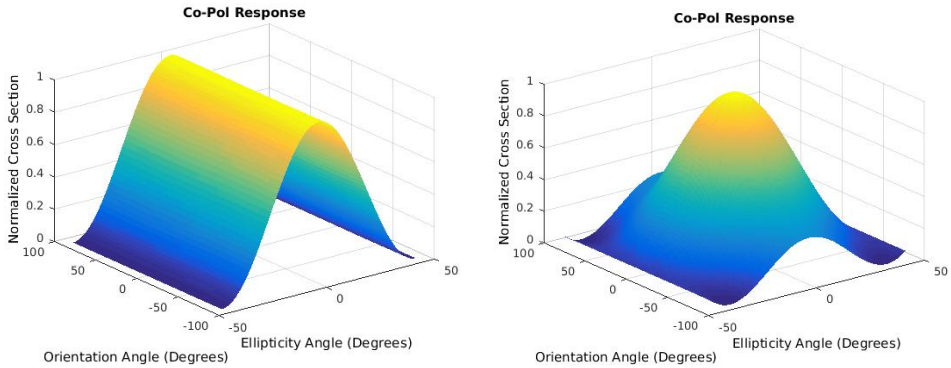

(a) *(b)*

Figure 1.9: *Co-polarisation signature for two triangular trihedral corner reflectors where; (a) In the clear, and (b) Between the trees.*

At the end of the section, we investigate the penetration of P-band signal and polarimetric degradation for the three compact polarimetric modes; $\pi/4$, DCP, and CTLR using the two triangular trihedral corner reflectors. After deriving these modes, the triangular trihedral corner reflector outside the trees was used as a reference target to calibrate the phase difference between H - V channels to be zero for each mode, and then the channel imbalance to be 1 for the three compact polarimetric modes in Section 6.5.

Section 6.5.1 presents the penetration and polarimetric degradation on the $\pi/4$ mode. The result, after calibration, showed a reduction of 0.6 dB in the H channel while it was 2.28 dB in the V channel, which is similar to the fully polarimetric data. The only change was a 1.5 dB reduction in amplitude for both linear horizontal, and vertical channels from fully polarimetric data due to the division of both channels by square root of 2.

Then, Section 6.5.2 presents the penetration and polarimetric degradation on the dual-circular polarimetry (DCP) mode. The result after calibration showed a zero phase difference for the corner reflector outside the trees, while a 64.66° phase difference showed for the corner reflector immersed in the trees. Moreover, the channel imbalance was 1 for the corner reflector outside the trees, while a 0.023 channel imbalance showed for the corner reflector immersed in the trees.

The reduction of signal was -30.4 dB in the horizontal channel, and it was 2.36 dB in the vertical channel.

Finally, Section 6.5.3 presents the penetration and polarimetric degradation on the circular receive and linear transmit (CRLT) modes. The result showed similar results to the $\pi/4$ mode in terms of signal reduction, however, the phase difference between the horizontal and vertical polarisation was -90° for the corner reflector in the clear, while it was -27.15° for the corner reflector immersed in the trees before calibration. After calibrating the data, based on using the corner reflector outside the trees as a reference point target, the phase difference for the corner reflector on the clear became zero, while the polarimetric degradation for the corner reflector immersed in the trees was 64.66°.

1.6.6 Summary

This chapter provides a brief introduction to synthetic aperture radar polarimetry. We presented various types of passive point targets and the use of polarisation signatures, as well as the motivation, and limitations of the research. This leads to the formulation of the main hypothesis, and the five questions associated with the hypothesis. Lastly, we conclude with a thesis outline which contains a detailed description of each chapter in the thesis. In the following chapter, we cover relevant and/or significant research efforts that have been published relating to the field of the SAR fully, also compact polarimetric calibration, using passive point targets.

Chapter 2

Literature Review

The concept of polarimetric calibration is dated back to the 1990's, and it is very important to understand the above-mentioned concept for the correction of distortion interference which is caused by system inaccuracies. Van Zyl, Quegan, Sarabandi, Ulaby, and Freeman have led the developments into polarimetric calibration using passive point targets, and became popular figures in the calibration of SAR polarimetric data. What follows is presented in three sections, and is relevant, and/or significant research efforts that have been published related to the field of SAR polarimetric calibration.

The first section introduces the relevant research for passive point targets which can be used in the calibration of SAR polarimetric data. The review includes both trihedral and dihedral corner reflectors, as well as the gridded trihedral corner reflector with two different grid angles. Furthermore, the section provides various ways of polarisation selection by rotating the dihedral reflector by 45° to reflect a specific polarisation channel. The second section introduces the relevant research for fully polarimetric data. The section starts by presenting several crosstalk methods that have been developed since the 1990's. The second part in section two introduces various ways of correcting the phase, and amplitude by using corner reflectors as well as radiometric correction. Finally, the relevant research for limited work that has been published on compact polarimetric calibration is presented in the third section for the three compact modes.

2.1 Passive Point Targets

Passive point targets, such as trihedral and dihedral corner reflectors, are commonly used for SAR calibration because of their large RCS, and a wide RCS pattern. Additionally, corner reflectors are inexpensive to manufacture, and easily deployed in the field without requiring power to operate. Two types of corner reflectors will be focused on, namely trihedral, and dihedral corner reflectors. Furthermore, the review includes a different selection of polarisation; by rotating the dihedral corner reflector to reflect a specific polarisation channel.

2.1.1 Trihedral and Dihedral Corner Reflectors

In 1984, Ulaby et al. presented an active reflector for a radar calibrator to calibrate both co- and cross-polarised returns from the radar [21]. There was no passive reflector at that time to calibrate cross-polarised returns, which led Hirosawa et al. in 1988 carrying out an experiment using a dihedral corner reflector as a passive reflector to calibrate a cross-polarised channel [33]. The experiment was directed by the National Space Development Agency of Japan and by using the aircraft of the Canada Centre for Remote Sensing. Four reflectors of the same size were deployed in the field, and the results were satisfactory, with uncertainty estimated to be +1.1/ -1.2 dB surrounding the reflectors. The main goal of the experiment was to test the feasibility of only one set of dihedral corner reflectors, and the author recommended arranging a number of arrays (sets of dihedral reflectors) with an extended range of RCS.

During the 1990's Van Zyl from the Jet Propulsion Laboratory conducted joint research with Kahny at the IHE high precision laboratory measuring how the construction of corner reflector affected the calibration of polarimetric SAR [34]. The goal of the research was to determine the scattering behaviour of a triangular trihedral corner reflector. He used the reflectors to prove the accuracy of polarimetric SAR calibration. Results showed that the edges of the corner reflector, when it is mechanically constructed, influences the scattering parameters. Additionally, the magnitude of the RCS, which vary in a range of ± 1.5 dB with

respect to optical solution, has to be considered in theoretical calculations, to avoid a 3 dB error in calibration results. Finally, he pointed out that the shape of the walls of the reflector should be less than 0.5% as it causes a decrease in RCS for practical reflectors.

In 1994, Unal et al. calibrated the Delft Atmospheric Research Radar (DARR) by using a rotatable dihedral corner reflector [35]. They showed that by rotating the dihedral corner reflector around the line of sight, which is the line between the radar and the target, the scattering matrix changed. They used only one dihedral corner reflector measuring 1.5 $\times$ 1.06 m^2, which provided a 38.9 dBm^2 RCS. Several scattering matrices with different rotation angles and two range resolutions were used to achieve the polarimetric calibration. The results were successful with an improved scattering matrix elements accuracy of 0.5 dB for the power, and 5° for the phase.

In 1994, Sarabandi et al. published results of a cross-calibration experiment using JPL SAR, and the University of Michigan truck-mounted polarimetric scatterometer [36]. They used a trihedral corner reflector to calibrate the SAR while the University of Michigan truck-mounted polarimetric scatterometer was calibrated using a metallic sphere. The data was collected off five different surfaces within the same area to evaluate the accuracy of the calibration process. Three of the surfaces were bare surfaces with varying roughness, and the other two were covered with varying tall grasses specific to each one. The results showed that the calibration, by using a point target, is unreliable and the error in the SAR data is caused by the interactions with the ground, and the uncertainties, in the shape of the trihedral. The author suggested using a large number of trihedral corner reflectors to remove the ground contribution by averaging.

Sarabandi et al. published further work in 1995 on the polarimetric calibration of SIR-C by using both a point, and distributed target [19]. They used two methods for calibration which are by using a point target, or by using a distributed target to calibrate the SIR-C, and compare the results with a calibrated image from the JPL. Eight trihedral corner reflectors were manufactured at JPL and used as a point target for calibration. The result showed a maximum discrep-

ancy in backscattering coefficients of 2 dB between the two calibration methods, as well as a 10° maximum discrepancy between the coherent phase differences. Furthermore, they noted that the point targets were deployed over a surface with a radar backscatter so as to not be zero, the RCS for the reflectors had to be much larger than the direct backscatter of the terrain. Furthermore, both the target coherent interaction and the terrain had to be as small as possible.

In 1996, Sarabandi et al. published a paper on the optimum corner reflectors for calibration of imaging radars [26]. They introduced five characteristics that influence the success of external calibration procedure, which are: large radar cross section, wide radar cross section pattern, the insensitivity of the radar cross section to the surrounding area, stability of the radar cross section, and finally the size of the reflector to be small. The paper also introduced a general class of corner reflector, known as a self-illuminating corner reflector. The reflector has high aperture efficiency and it was constructed and measured at X-band. The results showed that the self-illuminating corner reflector has two major improvements which are: The uncertainty of the RCS due to the interaction from the ground with reflector is very small compared to a triangular corner reflector. The second improvement is the size of the panel area is two thirds that of the triangular one specific for RCS.

In 2001, Ugsang et al. analysed some of the aspects of using five small trihedral corner reflectors to make them identifiable in the SAR image [37]. The small reflectors were designed with a 1 m width using aluminium plates, and they were deployed using differential GPS to measure the geographic locations. The results indicate that the exact location for the reflectors cannot be identified in the image if the difference between the return from the corner reflectors, and background targets, is below 12 dB. The site where the corner reflectors are deployed has to be free from multipath contributions, and a distance from power lines, including housing structures. Additionally, the use of GPS for geometric correction of SAR data was acceptable with less than half a pixel of RMS error.

In 2001, Satake el al. from the Tokai University in Japan developed corner reflectors to reflect a specific polarisation [38]. They developed a 45° rotated dihedral

corner reflector to have only cross-polarisation reflection of (HV and VH), and a 22.5° rotated dihedral corner reflector to have all the possible polarimetric reflection (HH, HV, VH, and VV). Furthermore, they placed a thin wire in the direction of selected polarisation for the dihedral reflector to reflect a horizontal (HH) or vertical (VV) polarisation. The reflectors showed a suitable result for phase calibration between polarimetric channels but they had some error in the reflected power due to the reflectors misalignment and structure.

In 2001, Wakabayashi et al. published results of a calibration experiment using four rectangular trihedral corner, and four dihedral corner reflectors with three different rotation angles [39]. The dihedral corner reflectors were rotated at 0°, 22.5°, and 45°, and the incidence angle was set to 53° for each reflector. The corner reflectors were used to compare crosstalk, gain balance, and polarisation signature at each reflector, with the results showing an improvement of 6 dB in crosstalk, as well as 3 dB in gain balance. The polarisation signatures for each reflector were corrected to have an ideal response.

After the German SAR satellite TerraSAR-X was successfully launched in 2007, Doring et al., from the German Aerospace Centre (DLR), presented a paper on Wave Propagation in Communication, Microwave Systems and Navigation [40]. The paper describes the calibration of satellite TerraSAR-X before it was ready for scientific and commercial use, to have highly accurate data. They used passive and active radar calibrators, and ground receivers to achieve the calibration process. The passive calibrators are two triangular trihedral corner reflectors with different inner leg dimension having different RCS. They chose trihedral corner reflectors because they are relatively insensitive to misalignments. Also, the author describes four factors that control the uncertainty of the RCS which are: misalignment from cardinal direction, error of the inter-plate orthogonality, deviation of the plate curvature, and surface irregularities. They were able to meet inter-plate orthogonality of less than 0.2°, plate curvature of less than 0.75 mm, and plate surface irregularities of less than 0.5 mm.

In 2009, Lihai et al. published research discussing the characteristics of point target for synthetic aperture radar imaging [41]. The dihedral corner reflector

has a very narrow beam-width in the elevation plane while the trihedral corner reflector is insensitive to misalignments. The results were obtained from a Ku-band SAR system with different dihedral corner and triangular trihedral corner reflectors, deployed on a uniform surface, using a GPS and a compass. The reason for deploying the reflectors on a uniform surface was to have a very low ground reflection. Results showed that the bore-sight of the SAR sensor should be pointed directly along the bore-sight line of the corner reflectors as any error in angle, will lead to the loss of echo.

In 2010, Li et al. from Shanghai University published an analysis of RCS characteristics for dihedral corner reflectors by changing different parameters such as the width, length, and intersection angle [42]. The result showed that the length of the dihedral corner reflectors had a smaller effect on RCS compared to the effects which were caused by the width and intersection angle.

In 2012, Chapin et al. from NASA JPL designed and deployed a 4.8 m triangular trihedral corner reflector with a total weight of 238 Kg for L- and P-band to be used for radiometric calibration of SAR data [43]. Each face in the corner reflector consists of 12 identical modular triangles to be assembled in the field. The use of varying modular design of the corner reflector allows them to have different sizes and shapes. For example, they can use 4 modular triangles to have a 2.4 m by 2.4 m dihedral corner reflector, or by using 3 modular triangles to have a 2.4 m trihedral corner reflector.

In 2013, Garthwaite et al. from Geoscience Australia published a paper describing the design of radar corner reflectors for calibrating SAR sensors using X-, and, C-band [44]. They chose to design a triangular trihedral corner reflector due to the simplicity of manufacture, long term structural rigidity, large and stable RCS, and a 3 dB beam-width of about 40° which is independent of both wavelength and plate size. The idea was to design one size of triangular trihedral corner reflector to be used for both X- and C-band. The RCS was estimated to be between 38-46 dBm^2 for X-band, and 47-54 dBm^2 for C-band, which led to a triangle size of about 1.1 m - 1.7 m for X-band, and 2.5 m - 3.7 m for C-band. The size ranges for both bands were not overlapping, and the problem was solved

by choosing a site to deploy the reflectors with signal clutter lower than the average. Four reflectors were designed and manufactured with leg dimensions of 1.0 m, 1.5 m, 2.0 m, and 2.5 m from 6 mm thick aluminium.

Further, the paper described three tolerances to be met during manufacturing of the corner reflectors. The first tolerance to be considered is the inter-plate orthogonally, as the RCS of the reflector decreases if the angle departs from 90°. The second tolerance for consideration is the deformation of the plate from a perfectly flat plane along it is whole length. Finally, the third tolerance to be considered is the involvement of any small scale deviation from perfect flatness such as ripples. Furthermore, some of the trihedral reflectors were perforated mesh to allow for quick drainage from heavy rain, as well as cleansing of dust, and the reduction of the effect of wind. The mesh perforation may cause a reduction in the RCS, and in order to not have an effect on the RCS, the hole diameter must be less than one sixth of the radar wavelength. However, the physical punching of aluminium sheet to make the mesh, shows major stresses to the sheet that cause deviations from flatness.

Qin et al. published further work in 2013 describing the design of corner reflectors [45]. They introduced holed plates to the design of corner reflectors to allow resistance to all weather conditions. The holes would reduce the wind forces, and rain effect. Additionally, the weight of the reflectors would be lower than regular reflectors. They were able to reduce the weight of the reflectors to 35% with a hole dimension of less than $\lambda/8$.

In 2014, Zhou et al. improved the trihedral corner reflector for high precision SAR calibration and validation [46]. The purpose of the improved trihedral reflector was to reduce the interaction between the reflector and the ground, as well as, to reduce the edge diffraction by minimizing the panel length for the external edge. The smaller edge length would reduce the effect of edge diffraction for reflectors of low frequency such as P-band, where the size of the reflectors is not larger than a wavelength. Furthermore, the author points out that the unexpected ground interaction would increase the RCS up to 1.34 dB at bore-sight and the solution is to cut the tip reflection area to have pentagonal-panel geometry.

Robertson published an experimental result in 1947, on the effect of the inter-plate orthogonality on the RCS when the angle varies from 90° [47]. The measurements were done using trihedral corner reflectors, and the results showed that the RCS is more affected if the angle between the plates is less than 90°. The RCS was reduced by about 2 dB with a 91° angle between the plates, while the reduction was about 5 dB with an 89° angle between the plates. Moreover, the result showed a proportional relationship between the wavelength and the reduction of the RCS.

In 1995, Zink et al., from the German Aerospace Centre (DLR), represent the loss of the RCS due to the inter-plate orthogonality when the angle varies from 90° as follows [48]::

$$L_{dB} = 60\ log_{10}\frac{(\pi/2)^2\ \cos(a_\lambda \sin(2\varepsilon))}{(\pi/2)^2\ -(\pi a_\lambda \sin(2\varepsilon))^2} \tag{2.1}$$

Where: $a_\lambda = (1/2\lambda)\sqrt{(A_{eff}/0.87)}$, λ is the wavelength of the selected frequency, A_{eff} is the effective area of the passive point target, and ε represents the error of the inter-plate orthogonality.

In 2016, Zhang et al. published a paper discussing the imaging characteristics of corner reflector under multi-azimuth angles via simulations [49]. The simulation was carried for the azimuth angle between zero and 180° and the incidence angle between 30° and 90°. The results showed that the corner reflector imaging characteristics are affected by some of the azimuth angles, and the best azimuth angle is 90°, while they remain steady with the incidence angle. The best incidence angle was between 60° and 70°.

2.1.2 Gridded Trihedral Corner Reflector

In 1992, Sheen et al., from the environmental research institute of Michigan (ERIM), introduced a new polarimetric SAR calibration reflector known as a gridded trihedral corner reflector [50]. The idea behind the grid was to change the incident wave's polarisation which resulted in the calibration target having

a return from the cross-polarisation channels. The gridded trihedral reflector is a normal triangular trihedral corner reflector, but the grid is added to one of the conducting faces to have only reflection from the cross-polarisation channels (HV, VH). The actual response of the gridded trihedral was examined in SAR imagery by the environmental research institute of Michigan (ERIM). They deployed four gridded trihedral reflectors in the field to calibrate the P-3 [1] SAR system.

Figs. 2.1(a) and 2.1(b), show two gridded triangular trihedral corner reflectors with different grid angles to change the incident wave, and result in a calibration target with a return from the cross-polarisation channels. A comparison between the theoretical response, and the measured response for the gridded trihedral was made using the polarisation signature. The measurements were done for each band and results showed the response for both X-, and, C-band matched the theory better than L-band [51]. Additionally, they mentioned that the gridded trihedral reflector is a preferred device for airborne SAR calibration as navigation errors would cause changes from the intended observation geometry, and the changes would not result in the reflector's scattering properties changing drastically. The trihedral corner reflectors were manufactured using aluminium plate with 0.25 inch thickness and 107 cm long perpendicular edges. Furthermore, the grid was made by etching parallel lines on a printed circuit board. The lines of the grid were 0.5 mm wide, and spaced by 4 mm, which represent one-eightieth of the free space of the X-band wavelength. They concluded that the gridded trihedral corner reflector was stable, inexpensive, and easy to deploy in the field with the only disadvantage being that the gridded trihedral corner reflectors needed to be calibrated before using them as calibration targets [52].

In 2009, Lavalle et al. started the work on gridded trihedral corner reflectors in their research of a possible approach for calibrating dual polarimetric C-band SAR data [53]. They estimated the system distortion parameters, which were one transmit crosstalk, two receive crosstalk, and receiving channel imbalance, using two approaches. The first approach used trihedral and oriented dihedral reflectors as well as distributed target with azimuthal symmetry. The second

[1] P-3 is a fully polarimetric L-, C-, and X-band SAR system which was developed by ERIM to be mounted in aircraft and carried out calibration activities in Kay West, Florida

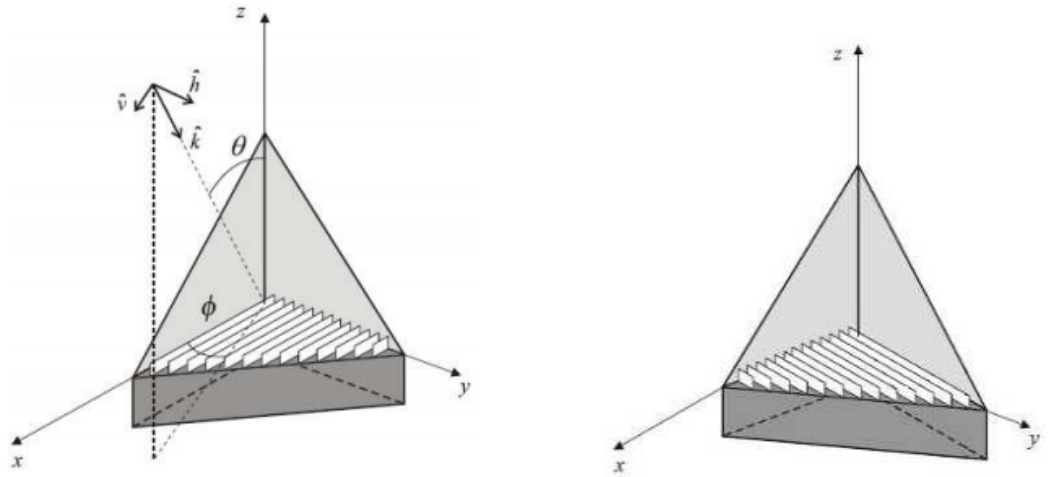

(a) *(b)*

Figure 2.1: *Two forms of gridded trihedral corner reflectors to have a cross-polarisation return from the HV and VH channels. (a) Trihedral Corner Reflector with 0° grid angle. (b) Trihedral Corner Reflector with 90° grid angle. [11]*

approach used trihedral and two gridded trihedral reflectors with two different grid angles, with no need of the reciprocity assumption between transmit and receive. They concluded that gridded trihedral reflectors are the preferred choice for dual polarimetric calibration as they have low polarimetric noise which was lower than -30 dB for both gridded reflectors.

Lavalle's PhD, submitted in 2010, provided an in-depth theoretical explanation of the use of gridded trihedral reflectors in the calibration of dual polarimetric sensors [11]. The ideal response of the gridded trihedral reflector can be written in terms of both the incident angle θ_i and the angle θ_p that the parallel grid forms with the vertically polarised component of the incident wave as follows:

$$S_{GT} = \frac{A_{GT} e^{j\phi_{GT}}}{\cos^2\theta_i + \sin^2\theta_i \sin^2\theta_p} \begin{bmatrix} \sin^2\theta_p & -\sin\theta_p \cos\theta_p \cos\theta_i \\ -\sin\theta_p \cos\theta_p \cos\theta_i & \cos^2\theta_i \cos^2\theta_p \end{bmatrix} \quad (2.2)$$

Where S_{GT} is the scattering of the gridded trihedral corner reflector and A is the absolute calibration factor.

In 2011, Quegan et al., used two gridded trihedral corner reflectors with other mixed radar calibrators for the calibration of lower frequency P-band space-borne circular transmit and linear receive (CTLR) [54]. It was noted that the calibration with four devices provided more accurate estimates of the radar system parameters than the other strategy, which involved only three devices. Additionally, the use of gridded trihedral corner reflectors provides significant advantages over the normal rectangular trihedral and dihedral reflectors. The primary advantage is that the lower average polarimetric noise (APN), is very low compared to trihedral and dihedral corner reflectors. The second advantage is the insensitivity to pointing accuracy. However, there is a negative to using gridded trihedral reflectors, such as the required accurate construction of the grid, as well as the microwave absorber layer being likely to be affected by rain. In contrast, using trihedral and dihedral corner reflectors instead of gridded trihedral leads to small construction effects, but the dihedral narrow beam-width causes difficulties in the orientation of the reflector, which also leads to high polarimetric noise due to pointing error.

2.2 Fully Polarimetric Calibration

A large volume of research has been published, and many experiments were done over the past thirty years on the calibration of fully polarimetric SAR data. The importance of full polarimetric calibration is to ensure accurate extraction of geophysical parameters, and obtain better target classifications [55] [6].

2.2.1 Polarimetric Crosstalk Calibration Methods

Scores of crosstalk calibration methods have been developed since the early 1990's for estimating and correcting the crosstalk parameters of accurate calibration. The first method was developed by Van Zyl in 1990 and modified by several authors assuming co- and cross-polarised responses of natural targets with azimuthal symmetry are uncorrelated and reciprocity assumed [56] [57].. Klein

improved Van Zyl's method in 1992 with two different transmission and reception distortions [58] [59]. Furthermore, a direct (non-iterative) method, and more general than Van Zyl's method, was developed by Quegan in 1994 by using the minimum least square principle, and small crosstalk [60] [61]. Finally, Ainsworth presented a posteriori method in 2006 using the obtained polarimetric SAR data without invoking reflection symmetry [62] [55]. Today, the two polarimetric crosstalk calibration methods by Van Zyl, and Quegan are the standards for crosstalk calibration of polarimetric SAR data [63]. The following presents the various crosstalk methods that have been published relating to the crosstalk of fully polarimetric, as well as different experiments to compare the crosstalk methods.

2.2.1.1 Van Zyl Method

In 1990 Van Zyl from JPL proposed a crosstalk method to estimate and correct the crosstalk parameters [56]. He assumed that the co- and cross-polarised responses of natural targets with azimuthal symmetry are uncorrelated, as well as using the reciprocity assumption for transmit and receive on the radar system [58]. Van Zyl used a system model in the following form to show the transmitting and receiving effects on symmetrised scattering matrix:

$$\Big[Z\Big] = A\mathrm{e}^{i\phi}\Big[R\Big]\Big[S\Big]\Big[T\Big] \tag{2.3}$$

where; $\Big[R\Big]$ and $\Big[T\Big]$ are the receiving and transmitting system. Additionally, $\Big[S\Big]$ is the desired scattering matrix, A is the overall absolute amplitude factor, and ϕ is the overall absolute phase. Therefore, by ignoring the background noise, the measured symmetrised scattering matrix $\Big[Z\Big]$ is written as follows:

$$\begin{bmatrix} Z_{hh} & Z_{hv} \\ Z_{vh} & Z_{vv} \end{bmatrix} = A\mathrm{e}^{i\phi}\begin{bmatrix} 1 & \delta_2 \\ \delta_1 & f \end{bmatrix}\begin{bmatrix} S_{hh} & S_{hv} \\ S_{vh} & S_{vv} \end{bmatrix}\begin{bmatrix} 1 & \delta_1 \\ \delta_2 & f \end{bmatrix} \tag{2.4}$$

where the crosstalk, when vertically polarized electric fields are transmitting

or receiving represented by δ_1 while the crosstalk when horizontally polarized electric fields are transmitting or receiving represented by δ_2. Also, f is one-way channel imbalance in amplitude and phase. The crosstalk can be separated from both channel imbalance and radiometric calibration by rewriting the matrix $\left[T\right]$ as follows:

$$\begin{bmatrix} 1 & \delta_2 \\ \delta_1 & f \end{bmatrix} = \begin{bmatrix} 1 & 0 \\ 0 & f \end{bmatrix} \begin{bmatrix} 1 & \delta_1 \\ \delta_2/f & 1 \end{bmatrix} or \left[T\right] = \left[T_c\right] \left[T_x\right] \tag{2.5}$$

The same expression is written for the receiving system where both $\left[R_c\right] \left[T_x\right]$ are independent of the system crosstalk. Therefore:

$$\left[Z\right] = \left[R_x\right] \left[R_c\right] \left[S\right] \left[T_c\right] \left[T_x\right] or \left[Z\right] = \left[R_x\right] \left[W\right] \left[T_x\right] \tag{2.6}$$

where $\left[W\right]$ has the last two steps of calibration which are amplitude imbalance and absolute calibration, and the intermediate scattering matrix is written as follows:

$$\begin{bmatrix} W_{hh} & W_{hv} \\ W_{vh} & W_{vv} \end{bmatrix} = A\mathrm{e}^{i\phi} \left[R_c\right] \left[S\right] \left[T_c\right] \tag{2.7}$$

The two matrices $\left[R_x\right]$ and $\left[T_x\right]$ have the elements δ_1 and δ_2/f and they can be estimated without external devices by using the following two assumptions; The first assumption is the parameters δ_1 and δ_2 have to be small compared to 1, and the system is being isolated. The second assumption is the scattering matrix for co-polarised and cross-polarized components to be uncorrelated $\langle {W^*}_{hh} {W^*}_{hv} \rangle = 0$ and $\langle {W^*}_{vv} W_{hv} \rangle = 0$. Finally, $\langle W_{hv} {W^*}_{hv} \rangle$ was estimated using $\delta_1 = \delta_2/f = 0$ with an initial value from matrix 2.8 and then the crosstalk parameters were calculated with a first guess from matrix 2.6 until we reach a stable estimate,

and the crosstalk calibration is obtained from the following equation:

$$\Big[W\Big] = \Big[R_x\Big]^{-1}\Big[Z\Big]\Big[T_x\Big]^{-1} \tag{2.8}$$

2.2.1.2 Klein Method

In 1992 Klein, from JPL, improved Van Zyl's method by not assuming the radar system to be reciprocal on transmit and receive [64] [60] [59]. The following system model was used by Klein to represent the received signals by excluding the system noise:

$$\begin{bmatrix} O_{hh} & O_{hv} \\ O_{vh} & O_{vv} \end{bmatrix} = \begin{bmatrix} R_{hh} & R_{hv} \\ R_{vh} & R_{vv} \end{bmatrix}\begin{bmatrix} S_{hh} & S_{hv} \\ S_{vh} & S_{vv} \end{bmatrix}\begin{bmatrix} T_{hh} & T_{hv} \\ T_{vh} & T_{vv} \end{bmatrix} \tag{2.9}$$

where: $\Big[O\Big]$ is the observed scattering matrix, and: $\Big[S\Big]$ is the ideal scattering matrix for the target. The O_{ij} represents the complex scattering matrix amplitude for the polarisation of; i receiving and j transmitting. Furthermore, the quantity T_{ij} is related to the transmission in channel j if channel i is excited while the quantity; R_{ij} is the response in channel i to a stimulus j. The crosstalk estimated by Klein was as follows [60]:

$$\check{T}_{hv} = \frac{T_{hv}}{T_{vv}} \qquad \check{T}_{vh} = \frac{T_{vh}}{t_{vv}} \qquad \check{R}_{hv} = \frac{R_{hv}}{R_{vv}} \qquad \check{R}_{vh} = \frac{R_{vh}}{R_{hh}} \tag{2.10}$$

2.2.1.3 Quegan Method

In 1994 Quegan proposed a direct (non-iterative) method to estimate and correct the crosstalk parameters using the minimum least square principle, as well as assuming the crosstalk terms to be small [60] [61]. Moreover, the crosstalk parameters were to be obtained from areas with low correlation between both co- and cross-polarisation [58]. The model used by Quegan to represent the radar

system is as follows:

$$\begin{bmatrix} o_{hh} & o_{hv} \\ o_{vh} & o_{vv} \end{bmatrix} = \begin{bmatrix} r_{hh} & r_{hv} \\ r_{vh} & r_{vv} \end{bmatrix} \begin{bmatrix} s_{hh} & s_{hv} \\ s_{vh} & s_{vv} \end{bmatrix} \begin{bmatrix} t_{hh} & t_{hv} \\ t_{vh} & t_{vv} \end{bmatrix} \tag{2.11}$$

Quegan Used the assumption for the reciprocity of the scattering matrix, and small off-diagonal terms for both R and T matrices to address Eq. 2.11 as follows [65]:

$$\begin{bmatrix} o_{hh} \\ o_{hv} \\ o_{vh} \\ o_{vv} \end{bmatrix} = Y \begin{bmatrix} a & v + aw & vw \\ au & a & v \\ az & 1 & w \\ auz & u + az & 1 \end{bmatrix} \begin{bmatrix} K^2 & 0 & 0 \\ 0 & K & 0 \\ 0 & 0 & 1 \end{bmatrix} \begin{bmatrix} s_{hh} \\ s_{hv} \\ s_{vv} \end{bmatrix} \tag{2.12}$$

where; Y $= r_{vv}/t_{vv}$ represents the overall system gain in the VV channel, K$=r_{hh}/r_{vv}$ represents the receive channel imbalance, and a$=(r_{vv}t_{hh})/(r_{hh}t_{vv})$ represents the ratio of the receive and transmit channel imbalance. The crosstalk terms are estimated by Quegan as follows [65]:

$$z = \frac{t_{hv}}{t_{hh}} \qquad v = \frac{t_{vh}}{t_{vv}} \qquad w = \frac{r_{hv}}{t_{vv}} \qquad u = \frac{r_{vh}}{r_{hh}} \tag{2.13}$$

Finally, the crosstalk terms for both Klein and Quegan are related as follows [60]:

$$z = \check{T}_{vh} \qquad v = \check{T}_{hv} \qquad w = \check{R}_{hv} \qquad u = \check{R}_{vh} \tag{2.14}$$

2.2.1.4 Ainsworth Method

In 2006 Ainsworth proposed a posteriori method to calibrate the crosstalk between channels, as well as imbalances in the channel gains, by using the obtained polarimetric SAR data without invoking reflection symmetry [66] [62] [55] [63]. The method did not involve a known distributed target for polarimetric SAR data, and couldn't promise orientation angle preservation [55]. Changing the

scattering matrix to a vector format and writing the Quegan's model as follows [58]:

$$\begin{bmatrix} o_{hh} \\ o_{hv} \\ o_{vh} \\ o_{vv} \end{bmatrix} = \begin{bmatrix} ka & va^{-1} & wa & vwk^{-1}a^{-1} \\ kza & a^{-1} & wza & wk^{-1}a^{-1} \\ uka & uva^{-1} & a & vk^{-1}a^{-1} \\ uzka & ua^{-1} & za & k^{-1}a^{-1} \end{bmatrix} \cdot \begin{bmatrix} s_{hh} \\ s_{hv} \\ s_{vh} \\ s_{vv} \end{bmatrix} = \Big[M\Big] \cdot \begin{bmatrix} s_{hh} \\ s_{hv} \\ s_{vh} \\ s_{vv} \end{bmatrix} \tag{2.15}$$

where; both k and a are the channel imbalance, and described as: k=$\frac{r_{hh}}{r_{vv}}$ and a=$(r_{vv}t_{hh})/(r_{hh}t_{vv})$. Finally, the crosstalk parameters are presented as follows [58]:

$$z = \frac{t_{hv}}{t_{hh}} \qquad v = \frac{t_{vh}}{t_{vv}} \qquad w = \frac{r_{hv}}{t_{vv}} \qquad u = \frac{r_{vh}}{r_{hh}} \tag{2.16}$$

2.2.1.5 Comparison of Crosstalk Methods

In 1994, Skriver et al. applied Klein's and Quegan's methods to the Danish polarimetric airborne SAR (EMISAR)[2]. The results showed that Quegan's method provided more robust estimates for the crosstalk parameters than Klein's method, with results similar to corner reflectors [60]. Moreover, the results agreed with further data that was presented by Skriver et al. for the AIRSAR data [67].

A comparison of polarimetric techniques was made in 2010 by Wuping et al. to compare, and analyse, the methods of Quegan and Ainsworth for crosstalk calibration of fully polarimetric data with low, and high crosstalk [68]. They acquired data from the test site near Sanya City, Hainan Province of China done by the East China Research Institute of Electronic Engineering. The results showed that the method by Ainsworth performs well for fully polarimetric data with low crosstalk, while the method by Quegan is applicable for full polarimetric data with high crosstalk.

[2] EMISAR is C-band SAR system for the Technical University of Denmark operated on Gulfstream G3 aircraft of the Royal Danish Air Force

In 2011 Chen et al. published an experimental result for the calibration of airborne polarimetric SAR with different crosstalk calibration techniques [58]. They compared two crosstalk methods, which were Quegan's method and Ainsworth's method, and the results showed that Ainsworth's method gave a better performance of polarimetric SAR calibration than Quegan's method as there were fewer assumptions for the calibration method [58]. Quegan's method assumed system symmetry, reciprocity, and a distributed target with azimuth symmetry, while Ainsworth's method only assumed reciprocity which means the two cross channel HV and VH are identical. Ainsworth's method had a wider application scope and showed much more accurate results for complex surface futures than Quegan's method.

In 2013, Zhang et al. improved the polarimetric calibration based on the methods of Quegan and Ainsworth for crosstalk calibration [55] [63] [69]. They did a large number of experiments on crosstalk calibration and they discovered that Quegan's method was able to estimate the crosstalk parameters stably, but inaccurately, while the Ainsworth's method was able to estimate the crosstalk parameters accurately but unstably. They improved the crosstalk estimation based on the methods of Quegan and Ainsworth to estimate the parameters stably and accurately. The idea was to initialize the parameters of the crosstalk with the estimation of Quegan's method, and then to calculate the correction values for the four estimations, and then finally update the parameters of the crosstalk with the Newton iteration method. The improved method was applied to SAR data from the Chinese airborne X-band, and the results showed that the estimations of the crosstalk parameters were stable and accurate, even if the crosstalk is high.

In 2015, Fore et al. from the JPL published an experimental result for the calibration of UAVSAR [70]. They evaluated the methods of Quegan and Ainsworth for crosstalk calibration, and the results showed that Quegan's method gives crosstalk estimates that depend on target type, while Ainsworth's method gives more stable crosstalk estimates. Also, the methods of Quegan and Ainsworth can estimate leakage of the co-polarisation to the cross-polarisation, and, being in the order of -30 dB.

2.2.2 Polarimetric Phase and Amplitude Calibration

The correction of the existing co-polarised channel imbalances for both phase and amplitude is an important step in obtaining accurate polarimetric SAR data [30]. There are two techniques that have been used for the phase correction. The first technique is presented in Fig. 2.2(a), and requires a calibration tone that is built into the radar system, while the other technique presented in Fig. 2.2(b), does not require a calibration tone built into the system, and the calibration can be performed relying on external passive point targets. The two techniques' details are presented in the following two sections:

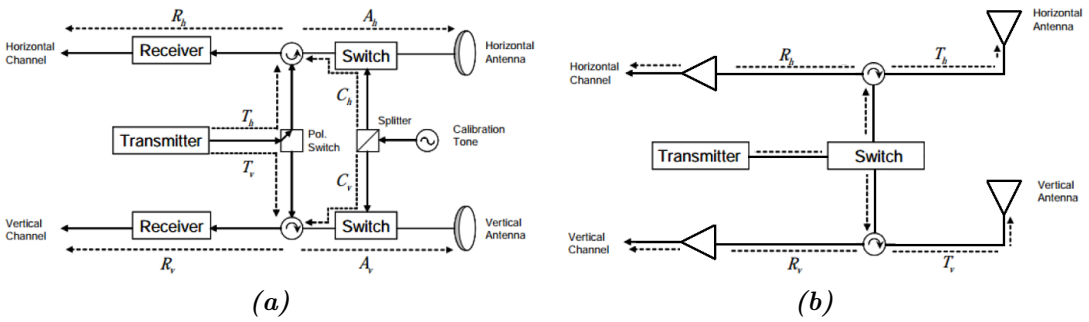

Figure 2.2: *Polarimetric phase calibration where; (a) The system model of NASA/DC-8 with calibration tone built into the radar system [71]. (b) Without calibration tone built into the radar system [72].*

2.2.2.1 Calibration Tone Built Into The Radar System

The first technique was presented by Van Zyl et al. in 1992 to calibrate the relative phase of radar polarimetry by using the phase information of the receiver calibration tone, as well as the knowledge of the antenna path differences among channels, without needing any assumptions on the scattering behaviour of the scene [73] [74] [72]. Additionally, the polarisation signatures of passive point targets, such as trihedral corner reflectors, were used to verify the technique of phase calibration. The phase calibration procedure was described by using the system model of NASA/DC-8, as shown in Fig. 2.2(a), which includes a

calibration tone to achieve the phase calibration. The receive matrix is written from the scattering matrix as follows:

$$R = \begin{bmatrix} S_{hh} \exp j(\phi_{Th} + 2\phi_{Ah} + \phi_{Rh}) & S_{hv} \exp j(\phi_{Tv} + \phi_{Ah} + \phi_{Av} + \phi_{Rh}) \\ S_{vh} \exp j(\phi_{Tv} + \phi_{Ah} + \phi_{Av} + \phi_{Rv}) & S_{vv} \exp j(\phi_{Tv} + 2\phi_{Av} + \phi_{Rv}) \end{bmatrix} \tag{2.17}$$

Where terms such as ϕ_{Th} represent the phase of the signal, because in Fig. 2.2(a), the dotted line is labelled T_h. For example, if we consider the term R_{hh}, the signal goes to the circulator coming from the transmitter through the path T_h, then along the path A_h from the circulator to the horizontal antenna, before it is radiated. Then, when the signal is received, it goes through the path A_h again, from the horizontal antenna to the circulator, and then finally through R_h, between the circulator and the horizontal channel [30]. Eq. 2.17 can be rearranged in terms of relative phase paths, with the overall absolute phase extracted, and written as follows:

$$R = \exp j(\phi_{Tv} + 2\phi_{Av} + \phi_{Rv}) \begin{bmatrix} S_{hh} \exp j(\phi_T + 2\phi_A + \phi_R) & S_{hv} \exp j(\phi_A + \phi_R) \\ S_{vh} \exp j(\phi_T + \phi_A) & S_{vv} \end{bmatrix} \tag{2.18}$$

Where; $\phi_T = \phi_{Th} - \phi_{Tv}$, $\phi_A = \phi_{Ah} - \phi_{Av}$, and $\phi_R = \phi_{Rh} - \phi_{Rv}$. These three are the unknown phase to calibrate. ϕ_A, represents the difference in the antenna path phase, and it involves cables or wave-guides to maintain the stability over time, and can be measured in the aircraft during assembly of the radar system. Furthermore, the calibration tone is used to obtain the receiver path difference, ϕ_R, during data collection, and can be written as follows:

$$\phi_R = \phi_{caltone} - \phi_C \tag{2.19}$$

Where; $\phi_{caltone}$ represents the phase difference from the phase information of the calibration tone in the horizontal and vertical channels [74] [30]. Also, ϕ_C can be

minimised by careful design, and it should remain stable over long periods due to the path length differences through cables that are involved in it. Finally, the last unknown, ϕ_T, can be recovered by making use of the reciprocity assumption and the phase of the complex product can be written as follows:

$$R_{hv}{}^{*} R_{vh} = S_{hv} S_{vh}{}^{*} \exp j(\phi_R - \phi_T) \tag{2.20}$$

Due to the system noise, the phase of the complex product will vary slightly from pixel to pixel, and to have a much better estimate for ϕ_R - ϕ_T we have to average the phase of the complex product over the image. The ϕ_T can be recovered as follows:

$$\phi_T = \phi_R - arg\langle R_{hv} R_{vh}^{*} \rangle \tag{2.21}$$

2.2.2.2 Without Calibration Tone Built Into The Radar System

The second technique was presented by Zebker et al. in 1990 to calibrate the relative phase of radar polarimetry without a calibration tone built into the radar system as shown in Fig. 2.2(b), and relying on external passive point targets such as trihedral corner reflectors [75] [76] [71]. The receive matrix is written from the scattering matrix as follows:

$$R = \begin{bmatrix} S_{hh} \exp j(\phi_{Th} + \phi_{Rh}) & S_{hv} \exp j(\phi_{Tv} + \phi_{Rh}) \\ S_{vh} \exp j(\phi_{Th} + \phi_{Rv}) & S_{vv} \exp j(\phi_{Tv} + \phi_{Rv}) \end{bmatrix} \tag{2.22}$$

Where the phase factors correspond to the paths which are shown in Fig. 2.2(b), and for simplicity, the phase in VV is factored out as follows:

$$R = \exp j(\phi_{Tv} + \phi_{Rv}) \begin{bmatrix} S_{hh} \exp j(\phi_T + \phi_R) & S_{hv} \exp j\phi_R \\ S_{vh} \exp j\phi_T & S_{vv} \end{bmatrix} \tag{2.23}$$

Where; $\phi_T = \phi_{T,h} - \phi_{T,v}$, and, $\phi_R = \phi_{R,h} - \phi_{R,v}$. By using the reciprocity assump-

tion, the difference, ϕ_T - ϕ_R, can be solved by having the phase of the complex product $R_{hv}{R_{vh}}^* = S_{hv}{S_{vh}}^* \exp j(\phi_T - \phi_R)$ to be averaged over the image. Finally, knowing the dominant scattering mechanism for an area in the image, the remaining factors for phase calibration can be determined, and the two relations (ϕ_T + ϕ_R) and (ϕ_T - ϕ_R) are obtained for the each phase ϕ_T and ϕ_R , which relates matrix R to the following matrix S:

$$S = \begin{bmatrix} R_{hh} \exp -j(\phi_T + \phi_R) & R_{hv} \exp -j\phi_R \\ R_{vh} \exp -j\phi_T & R_{vv} \end{bmatrix} \tag{2.24}$$

2.2.3 Radiometric Calibration

The radiometric calibration of synthetic aperture radar is the final step in the calibration process, and it is important work for relating the pixel's value to the backscattering coefficient of ground targets [77]. According to Van Zyl [30], even if we have the knowledge of antenna gain patterns, and the system parameters, the radiometric calibration is best achieved by using external calibration targets, such as trihedral corner reflectors or transponders [6] [78] [79] [80]. Sometimes, naturally distributed targets, like a patch of rainforest, could be used for the radiometric calibration [81].

A great volume of papers were published on the radiometric calibration of SAR systems, as well as numerous methods used to relate the pixel's value to the backscattering coefficient. In [82] Kasischke detailed the philosophy behind the radiometric calibration, and he presented the necessary equations of radiometric calibration, as well as the effect of these terms on calibration., Frulla et al. also presented radiometric calibration procedures for the ERSSAR, and some of these procedures are; the spreading loss effect, and the non-uniform antenna pattern correction [83]. Moreover, further radiometric calibration work was done for the two Chinese airborne SAR using different trihedral corner reflectors, and the results showed that the radiometric calibration accuracy for both systems is better than 2 dB [84]. The following details the previous studies which were exposed, and experiments that were made on the radiometric calibration of airborne SAR

systems using external calibration targets, as well as a number of methods which were used to relate the pixel's value to the backscattering coefficient.

Two main methods exist for deriving the perceived point target RCS from SAR image, known as the peak, and, integral methods [85] [86]. In 1990, Gray et al. published a paper showing that the peak response of the point target depends strongly on the processor focus and resolution, while the integral response from a passive point target is weakly dependent on these parameters [87] [88]. The derivation of the peak method is based on the reflected power from the corner reflector, and computed from the maximum amplitude data within the target response, following which it is then multiplied by the slant range resolution, and the azimuth resolution.

On the other hand, the derivation of the integral method is based on the reflected power from the corner reflector, and computed by summing up the power of all pixels in an area that may include the power from the corner reflector, and then subtracting it from the background clutter by summing all the pixels around the corner reflector, and then multiplying the results by the pixel spacing in both range and azimuth [89].

In 1992, Woode proposed an integral method based on interpolated value, which is similar to the previous integral method, with a difference being the method used to compute the integrated energy [90] [91]. The integrated energy is calculated based on summing the pixels over a square region around the peak location, and is corrected by an estimation of the clutter in a border around the peak location, which leads to the general calibration factor of the integration method on interpolated values.

In 1992, Ulander et al. published a paper on the accuracy of using point targets for SAR calibration [92]. He analysed the peak, and integral methods for radiometric calibration by using a reference point target. The results showed that both methods are unbiased, however, the peak method is sensitive to system focus, and requires knowledge of the equivalent rectangle system. Also, an exact expression for the RMS errors were derived for both methods, and the results from the peak method is smaller than, or equal to that from the integral method

for a well-focused system. Finally, he recommended the integral method for robust radiometric calibration, or when non-linear phase errors are present, as the method does not require knowledge of the impulse response.

In 1994, Holecz et al. presented a method focusing on the second step which is called rigorous determination of both backscattering coefficient (σ_o) and (γ_o) [93]. The purpose of the paper was to show the importance of computing an accurate estimate of RCS per unit area, as well as the need of geometric calibration, and how that is a fundamental step in radiometric calibration. The advantage of the method is the ability of determining the backscattering coefficient (σ_o) in any cartographic reference system, and the original SAR image geometry. Furthermore, a model was developed by Kasischke et al. to estimate a relative error bound which is associated with backscattering coefficient (σ_o) for radiometric calibration [94]. The idea was to estimate the expected error for different channels, and then compare it with actual RMS errors which were obtained during the initial calibration. The results showed that the actual errors were in the order 0.7 dB, and lower.

In 2008, Dostovalov et al. improved the radiometric calibration accuracy using super resolution methods by processing L-band airborne SAR data with a group of corner reflectors [95]. The goal was to separate the corner reflector's main response, and eliminate the effect of multipath interference, then finally the improvement of radiometric calibration accuracy. The results showed that the magnitude degradation for the response from the corner reflector at HH channel can be explained by the presence of one more point, such as an object shifted 160° relative to the phase of main object. Moreover, the amplitude of the corner reflector which was analysed must be increased by 20% (1.6 dB) to make the amplitude of all the corner reflectors get within the group close to their theoretical RCS.

In 2012 Wang et al. published an experimental result for using multiple trihedral corner reflectors to calibrate high resolution images, including antenna pattern correction, and radiometric calibration [88]. Three images were acquired with variable off-nadir angles. The result showed that the calibration with multiple

images together, to acquire the large antenna pattern, is feasible and the images accomplish a uniform relative calibration even if the images have different imaging geometry, and radiometric characteristics. Additionally, the estimated RCS for the different corner reflectors meets the actual RCS, and the estimated error from the calibrated image for the corner reflectors is less than 1.0 dB.

In 2014, Zongmin et al. from the Chinese academy of science published an analysis of X-band airborne SAR radiometric calibration using two point targets with a side length of 0.3706 m, and 0.4159 m [96]. They used the peak, and the integral methods to compute the calibration constant. The results from the two methods were feasible, and the calculation of the backscattering coefficient matched with the theory for the corner reflectors.

In 2014, El-Darymli et al. presented an investigation of different ways of radiometric calibration in SAR images [97]. The investigation accommodated for the case of point target, the backscattering coefficient (σ_o), and other forms, such as radar brightness (β_o), and (γ_o), as well as their relevance to the backscattering coefficient (σ_o). The results showed that the radar brightness, (β_o), gave the most accurate results compared to backscattering coefficient, (σ_o), and (γ_o) as it is independent of the sea level.

A further work on the radiometric calibration was presented for the Indian RISAT-1 [98] [99] [100]. They discussed two methods for antenna pattern estimation, which are; the statistical method, by using images data statistics, and the calibrated antenna pattern method. The results showed that it is preferable to use the calibrated antenna pattern method because if the extraction is done correctly, it works on extreme heterogeneous terrains.

2.3 Compact Polarimetric Calibration

Very limited work has been published in the past ten years on compact polarimetric calibration. Compact polarimetric calibration is still an active research area due to the implementation of new different compact SAR sensors around

the world [101]. Table 2.1 summarises all the current and future compact polarimetric sensors around the world.

Table 2.1: *Current and future compact polarimetric sensors*

Sensor	*Band*	*Polarisation*	*Country*	*Launch Date*
RISAT-1	C	RH , RV	India	April 2012
PALSAR-2	L	RH , RV	Japan	May 2014
SAOCOM 1/2	L	RH , RV or LH , LV	Argentina	Oct 2017
RCM 1/2/3	C	RH , RV	Canada	Dec 2018
XL-SAR	L	Three modes	Saudi	Dec 2019

2.3.1 Calibration of $\pi/4$ mode

In 2005, Souyris et al. proposed the first compact mode, ($\pi/4$ mode), and he gave a brief description on the calibration of $\pi/4$ mode with the necessity of covering several issues in order to complete the calibration of this mode [13]. The measured target vector for the $\pi/4$ can be written as follows:

$$\vec{K}_{\pi/4} = \begin{bmatrix} 1 & \delta_2 \\ \delta_1 & f \end{bmatrix} \cdot \begin{bmatrix} h & x \\ x & v \end{bmatrix} \cdot \begin{bmatrix} 1+\delta \\ 1-\delta \end{bmatrix} \tag{2.25}$$

where; f is one-way complex co-polarised channel imbalance, and δ represents the complex transmitted crosstalk, and δ_1 and δ_2 represent the received crosstalk. By assuming reciprocity between both transmission, and reception, we will have the following relation between the previous crosstalk terms:

$$\delta_1 = \delta \quad and \quad \delta_2 = 1 - f - \delta \tag{2.26}$$

Also, Souyris points out that by assuming an azimuthally symmetric, the number of unknowns will be reduced by three. Finally, by deploying a corner reflector, we can get a relation that links both f and δ ,and reduces the number of unknowns by two. Without investigating in more detail, Souyris concluded that the radar returns from an azimuthally symmetric natural target, and at least one trihedral

corner reflector, are enough to achieve the calibration process for the $\pi/4$ compact mode.

2.3.2 Calibration of Hybrid Mode

In 2008, Freeman et al. introduced a new system model for the calibration of Hybrid mode [102], in which the scattering vectors are measured as follows:

$$\begin{bmatrix} M_{RH} \\ M_{RV} \end{bmatrix} = A(R,\theta)e^{j\phi}.\frac{1}{\sqrt{2}}\begin{bmatrix} 1 & \delta_2 \\ \delta_1 & f \end{bmatrix}\begin{bmatrix} \cos\Omega & \sin\Omega \\ -\sin\Omega & \cos\Omega \end{bmatrix}\begin{bmatrix} S_{HH} & S_{HV} \\ S_{VH} & S_{VV} \end{bmatrix} \begin{bmatrix} e^{-j\Omega} + \delta_c e^{j\Omega} \\ -j(e^{-j\Omega} - \delta_c e^{j\Omega}) \end{bmatrix} + \begin{bmatrix} N_1 \\ N_2 \end{bmatrix} \tag{2.27}$$

where; S_{HH}, S_{HV}, S_{VH}, and S_{VV} represents the components of the scattering matrix, while M_{RH} and M_{RV} represents the measured scattering vectors. Additionally, f is the channel imbalance, and δ_1 and δ_2 are the received crosstalk. The model takes Faraday's rotation into account, and the model was used as the basis of a novel algorithm for the calibration of Hybrid mode using both active and passive reflectors.

In 2010, Freeman et al. published further work on the potentials of a compact polarimetric SAR system, and suggested a procedure of calibrating the Hybrid mode using three corner reflectors [103]. They thought that more external targets were needed to calibrate the system, even if there were fewer unknowns in compact polarimetry, compared to full polarimetry, where we consider the reciprocity, and only one trihedral is needed to calibrate the system.

In 2011, Quegan et al. used the system model for the calibration of Hybrid mode by Freeman on his further work on the calibration of satellite CTLR compact polarimetric low frequency SAR using mixed radar calibrators [54]. He suggested a calibration method using the Amazonian forest, and corner reflectors. They used a gridded trihedral reflector which gave significant advantages over trihedral

and dihedral, because of their much lower APN, and insensitivity to accurate pointing. However, the previous two methods by Freeman and Quegan assumed the compact mode was transmitting a perfect circular polarisation.

In 2014, Touzi et al. published a paper on the requirements on the calibration of hybrid-compact SAR [101]. They explained how important it is to correct for the compact transmitted waves non-circularity, and the actual technology does not permit the generation of a perfect compact polarimetry. They stated that they are working on the correction of non-circularity transmitted polarisation.

In 2015, Hong et al. published a paper on crosstalk correction [104]. They introduced a method on the correction of transmit talk in reconstruction of Quad polarisation from compact polarimetry data. The paper also mentioned that it is impossible to correct the crosstalk on transmit in measured scattering vectors, even if the transmit crosstalk is already estimated and known. They proposed a calibration algorithm to correct transmit crosstalk by reconstructing Quad polarisation covariance, or coherence matrix from compact polarimetry measurements. The algorithm is achievable for any transmit crosstalk amplitude which is no larger than -15 dB.

2.4 Summary

In this chapter, initially, we presented the relevant and/or significant research efforts that have been published related to the field of SAR polarimetric calibration. We addressed the relevant research for passive point targets. Then, we illustrated the fully polarimetric calibration, which included the crosstalk, phase, channel imbalance, as well as radiometric estimation and correction. Lastly, we presented a limited research effort on the compact polarimetric calibration. The following chapter presents the selection, design, manufacture, and deployment of twelve classical trihedral and dihedral corner reflectors for X- and P-band, as well as four gridded corner reflectors for X-band.

Chapter 3

Passive Point Targets

This chapter details the selection, design, construction, and deployment of different passive point targets, which were used for the calibration activities of the Saudi XP-SAR airborne. In the following, we first present the selection and design of multiple passive point targets. These were a combination of classic trihedral, and dihedral corner reflectors for X- and P-band, as well as gridded trihedral, and gridded dihedral corner reflectors for only X-band.

Secondly, in Section 3.4 we present the construction of these corner reflectors in South Africa, and the shipment to the Netherlands for the test flights. The total constructed corner reflectors are sixteen corner reflectors of two sizes (0.5 m inner leg dimension for X-band, and 1.5 m inner leg dimensions for P-band).

Finally, in Section 3.5 we present the deployment of the corner reflectors at three different sites with carefully surveyed and oriented positions for the test flights. The planned test sites are in three areas, where two of them (near and far field) are inside Teuge Airport, the Netherlands, while the third one (mid field), is an open field outside the airport which is used for parachuting activates. The three sites are flat and a distance away from clutter.

3.1 Introduction

The airborne XP-SAR sensor is a dual frequency X- and P-band SAR project between King Abdulaziz City for Science and Technology (KACST), and droneSAR. The (KACST) (Riyadh, Saudi Arabia) commissioned droneSAR (Pty) Ltd (Simonstown, South Africa) to supply a dual band, (X- and P-Band), fully polarimetric imaging radar, together with a means to calibrate the system completely. MetaSensing (Noordwijk, Netherlands) was selected as the sensor supplier.

Table 3.1 shows the main parameters of the XP-SAR sensors. The system is a fully polarimetric SAR system whereby it transmits both horizontal and vertical, and receives both horizontal and vertical polarisation. The system is equipped with two integrated navigation systems which consist of the GNSS and inertial unit system which can be also interfaced with other navigation systems available on board the aircraft. An important element of the entire design of the radar system has been the careful choice of no-export-restricted RF and navigation subsystems, still guaranteeing appropriate performance of the system. The system reaches bandwidths of 500 MHz at X-band, and 200 MHz at P-band. Both frequency bands are transmitted simultaneously. Two receiving channels per band operate at the same time, while the two transmitters can switch, on a pulse to pulse basis, in order to implement polarimetric, and interferometric mode. Depending on the operating mode, real time filtering and compression of the raw radar data can be commanded in order to reduce data rate, and enlarge the data storage capabilities to more than six hours. Once the storage is full, the solid state disks can be removed, and replaced with empty ones.

3.2 Passive Point Target Selection

The selection of passive point targets was based on the five characteristics that influence the success of external calibration target, which are: large RCS, wide RCS pattern, stability of the RCS, the insensitivity of the RCS to the surrounding area, and the size for the reflector to be small. Trihedral and dihedral corner

Table 3.1: *X- and P-band radar parameters. [105]*

Parameters	X-band	P-band
Frequency	9.6 GHz	400 MHz
Bandwidth	500 MHz	200 MHz
Slant Range Resolution	up 0.3 m	up 0.75 m
Azimuth Resolution	up to 20 cm	up to 20 cm
Transmitted Power	10 W (average)	50 W (peak)
Polarimetry	Quad Polarisation	Quad Polarisation
Interferometry	Single pass	Repeat pass
Slant range coverage	4 to 8 Km	4 to 8 Km

reflectors were selected because of their large RCS, and wide RCS pattern [26]. Both trihedral and dihedral corner reflectors will not generate cross-polarisation components ($HV = VH = 0$), and the horizontal and vertical backscattering cross sections are identical ($HH = VV$), however, the co-polarised components are not in phase for the dihedral corner reflector, and it is in phase for the trihedral corner reflector [30]. The rotation of the dihedral corner reflector by 45° generates cross-polarisation components, and results in zero co-polarisation return ($HH = VV = 0$), which solves the problem of not having a cross-polarisation return from both the trihedral and the dihedral corner reflectors.

Furthermore, the gridded trihedral, and gridded dihedral corner reflectors are selected to be used as a passive point target, to have only horizontal or vertical returns from the reflector depending on the incident wave. The grid will change the incident wave's polarisation, and results in an even horizontal, or vertical return. The gridded dihedral and gridded trihedral corner reflectors with zero grid angles, will generate only vertical reflections, while the gridded trihedral corner reflector with a 90° grid angle, will generate only a horizontal reflection.

The trihedral corner reflector consists of three electrically conductive surfaces, and the surface can be triangular, square, or circular as shown in Figs. 1.5(b)-1.5(c), and 1.5(d). The circular surfaces generate higher RCS than the triangular, and the square surface for the same size of inner leg dimension which made it

very bright in the image. The circular surface is the less attractive choice due to the complicated process of cutting the surfaces, as well as the higher cost of manufacture. The triangular surface is the most common design, but it generates lower RCS for the same size of inner leg dimension than square and circular.

Fig. 3.1 shows the theoretical relation between RCS and inner leg dimension of triangular, and square trihedral corner reflectors for X- and P-band. The triangular surface is a suitable choice, especially for higher radar frequencies such as X-band, because it is more structurally rigid than the square plate, and the size of the triangle will be small with higher RCS values, which causes less material to be used. But for lower frequencies such as P-band, the square surface is a much better choice than a triangular surface because a triangular reflector will be very large, and the weight of the reflector becomes very high which could cause errors, and results in a reduction in the RCS. For example, NASA-JPL designed a triangular trihedral corner reflector for P-band to be used for radiometric calibration of SAR data [43]. The inner leg dimension was 4.8 m and the weight was 238 Kg which made it very difficult to deploy in the field, especially in our case where we would deploy more reflectors to cover the swath image.

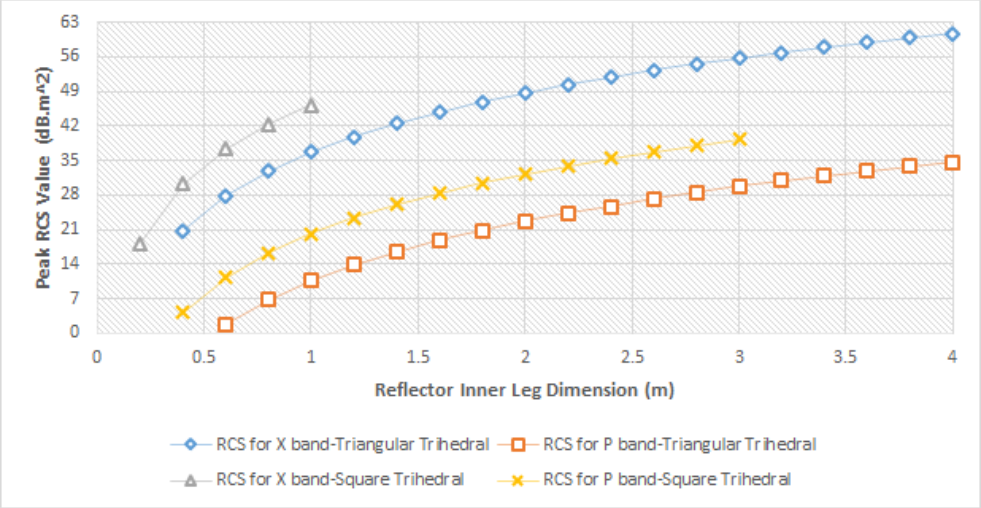

Figure 3.1: *Theoretical RCS relation with Inner leg dimension of the triangular and square trihedral corner reflectors for X- and P-band.*

The numbers of corner reflectors to be selected are based on the idea of having a different polarisation return from the polarimetric channels, and cover the swath image (near, mid, and far field). A total of ten trihedral corner reflectors, and six dihedral corner reflectors were selected to be used for the two X- and P-band. Six of the trihedral corner reflectors are classic trihedral reflectors, where three of them are square surfaced for X-band, and three of them are triangular surfaced for P-band. The other four corner reflectors are gridded trihedral, and gridded dihedral corner reflectors with different grid angles. We will use two gridded square trihedral reflectors, with 0°, and 90° grid angles, as well as two gridded dihedral corner reflectors with 0° , and 90° grid angles. Additionally, the dihedral corner reflectors will be rotated 45° to obtain a cross-polarisation reflection.

3.3 Passive Point Targets Design

The design of the corner reflector starts by detailing the type of plate material to be used, based on a number of factors, such as; weight, price, and conductivity. Also, the section includes that the optimum size of the corner reflector be bright, as well as investigates the effect of perforating the corner reflectors on maximum RCS, using four different hole sizes, and three varying hole centre spacings. Finally, a number of tolerances were introduced to be met during the manufacturing of the corner reflectors in order to reduce the effect of errors on maximum RCS.

3.3.1 Plate Material

Numbers of different electrical conductive materials such as steel, aluminium, copper, and brass could be used to construct corner reflectors. But, one of the most important factors to consider before choosing the material of the plate is the weight, especially for longer wavelengths such as L- and P-band, where the size of the corner reflector becomes larger. Aluminium is the optimum choice of material to construct all the different types of corner reflectors that we will

design. The choice of aluminium is due to its density, which will reduce the weight of the reflectors even if it costs more than other materials such as steel.

The steel has a higher density, in the range between 7.75 - 8.05 g/cm^3, while the density of aluminium is between 2.6 - 2.9 g/cm^3. For example, if we design a square trihedral corner reflector 500 mm by 500 mm × 750 mm and a 2 mm width using aluminium plates, the total weight of the reflector is 5.6 Kg. However, if we use steel to design the square reflector, the total weight will increase to 16 Kg. Weight is a very important factor to consider, especially when designing corner reflectors for lower frequencies such as P-band, where we will have bigger sized reflectors.

3.3.2 Size of Coroner Reflectors

The size of the corner reflectors was chosen to be 40 dB higher than the noise sigma equivalent zero curves in Fig. 3.2 for both X- and P-band. A ground range was selected from the curves of 4 Km, with higher and lower values of the noise equivalent sigma zero, to calculate the inner leg dimensions of the different types of corner reflectors. For the X-band, the noise equivalent sigma zero ranges from -9 dB to -36 dB, while it ranges from -23 dB to -32 dB for the P-band. The sizes of the triangular and square trihedral, as well as the dihedral corner reflectors were calculated, based on the equations of the theoretical maximum RCS in Table 1.2, to give a 40 dB signal to noise ratio at the output of the radar. Knowing the wavelengths for X- and P-band from the radar parameters in Table 3.1, and having the maximum RCS to be 40 dB (10,000*X), where X is the value of noise sigma equivalent zero curves for X- and P-band SAR system in Fig. 3.2.

Table 3.2 summarises the calculation of the sizes of the inner leg dimensions at each ground range for all the corner reflectors. The results of X-band square trihedral corner reflectors showed that at higher noise equivalent sigma zero of -9 dB, was 0.41 m inner leg dimension, and we chose the size for X-band trihedral to be a little higher to be 0.5 m to ensure the corner reflector would be bright

enough in the image. Also, the X-band dihedral corner reflector results were close to the trihedral, and the size at 40 dB higher than the noise equivalent sigma zero, was 0.46 m, and we chose the size to be 0.5 m. By using a 0.5 m inner leg dimensions for both trihedral and dihedral corner reflectors of X-band, the maximum RCS is 34.18 dBm^2 for the square trihedral, while it is 32.42 dBm^2 for the dihedral corner reflector.

On the other hand, the size for the P-band triangular trihedral corner reflector, in Table 3.2 at -23 dB noise equivalent sigma zero is 1.6 m, and 0.96 m at -32 dB. We chose the size of the inner leg dimension to be 1.5 m due to its rigidity, and the maximum RCS becomes 15.76 dBm^2. Finally, the dihedral corner reflector for P-band is between 0.55 m for -32 dB noise equivalent sigma zero, and 0.92 m for the lowest noise equivalent sigma zero which is -23 dB. We chose the size of the inner leg dimension to be 1.5 m and the maximum RCS became 23.54 dBm^2.

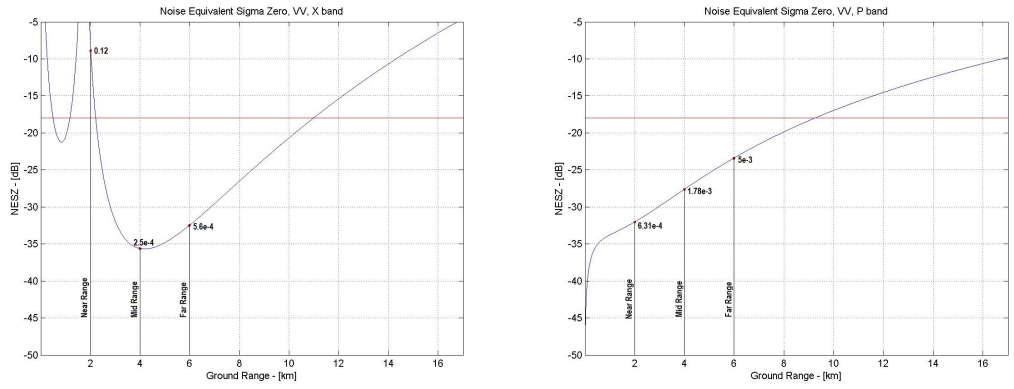

(a) ***(b)***

Figure 3.2: *Noise sigma equivalent zero curves as a function of ground range for X- and P-band at VV when flying at 3 Km altitude with a look angle of 60 degrees where; (a) X-band and (b) P-band. [105]*

Table 3.2: *Inner leg dimensions for X- and P-band trihedral and dihedral corner reflectors based on selecting three points of NESZ over the ground range*

Parameters	Trihedral Corner Reflector		Dihedral Corner Reflector	
	X-Band	P-Band	X-Band	P-Band
Near Field	0.41 m	0.96 m	0.46 m	0.55 m
Mid Field	0.09 m	1.24 m	0.10 m	0.71 m
Far Field	0.11 m	1.60 m	0.21 m	0.92 m

3.3.3 Perforating the Corner Reflectors

Perforating the reflector is an advantage in designing the corner reflectors to reduce the effect of wind, and allow quick drainage from heavy rain, as well as cleansing from dust. In this section we used four different hole sizes, and three varying hole centre spacings, to analyse the effect of perforating the corner reflector on maximum RCS. The hole sizes which were used were; one-tenth, one-sixth, one-quarter, and one-third of the X-band wavelength, with 10 mm, 12 mm, and 15 mm varying hole centre spacings. The first hole size, which is one-tenth, was not tested as there was no reduction between 12 mm and 15 mm, and companies need to have very special machinery to perforate the panel with such small holes. Moreover, a hole size of one-third of the radar wavelength with a 10 mm hole centre spacing, is not possible to be tested as there will be no spacing with it. Finally, the results and discussion section is presented in the end to compare the results for the best choice of hole size, and spacing for perforation of the corner reflector. We have chosen 50 cm by 50 cm square trihedral corner reflector in our analysis with a radar frequency of 10 GHz, using FEKO software.

3.3.3.1 One-tenth of the wavelength

The first square trihedral corner reflector was perforated with a hole size of 3 mm which is one-tenth of the radar wavelength of X-band (10 GHz), and has two varying hole centre spacings; 12 mm, and 15 mm. Fig. 3.3 shows the maximum

RCS for the two different spacings; 12 mm, and 15 mm which is about 33.3 dBm^2 for the two varying hole centre spacings.

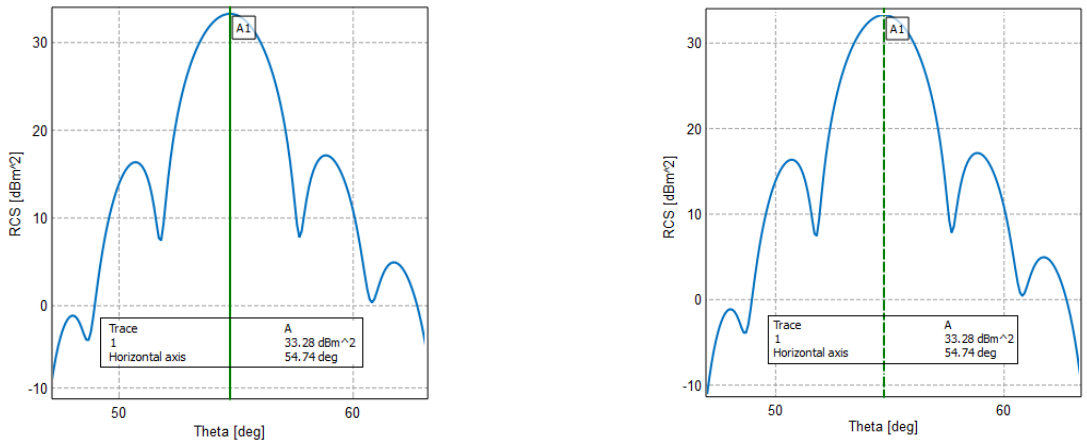

Figure 3.3: *Hole sizes of 3 mm. (a) 12 mm hole centre spacing and (b) 15 mm hole centre spacing.*

3.3.3.2 One-sixth of the wavelength

The second square trihedral corner reflector was perforated with a 5 mm hole size, representing one-sixth of the radar wavelength. Fig. 3.4 shows three varying hole centre spacings; 10 mm, 12 mm, and 15 mm. The maximum RCS for the 10 mm, 12 mm, and 15 mm spacing are; 33.09 dBm^2, 33.18 dBm^2, and 33.23 dBm^2. The RCS decreases when the hole centre spacings increase but it is a very small amount of reduction for the RCS, which is; 0.09 dBm^2 from 12 mm to 10 mm, and 0.05 dBm^2 from 15 mm to 12 mm. The less spacing between the holes, the more open area, which results in weight reduction, and which reduces the effect of wind, as well as cleansing from dust.

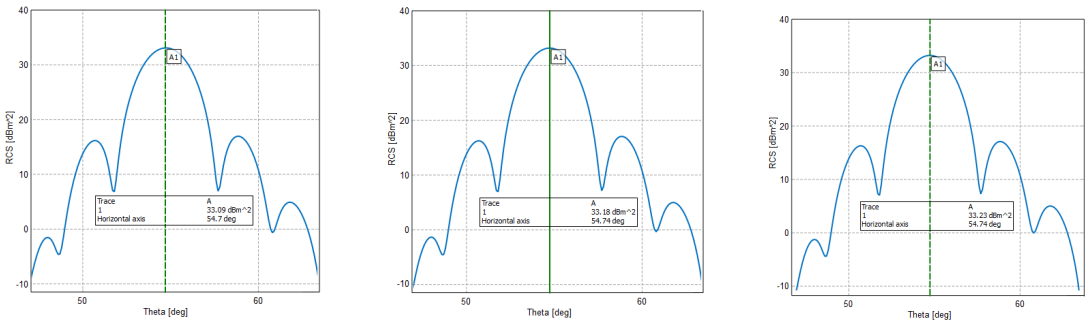

(a) *(b)* *(c)*

Figure 3.4: *Hole sizes of 5 mm. (a) 10 mm spacing, (b) 12 mm spacing, and (c) 15 mm spacing.*

3.3.3.3 One-fourth of the wavelength

The third reflector was perforated with a 7.5 mm hole size which is one-fourth of the radar wavelength. Fig. 3.5 shows three varying hole centre spacings; 10 mm, 12 mm, and 15 mm. The maximum RCS for the 10 mm, 12 mm, and 15 mm spacing are; 30.7 dBm^2, 32.2 dBm^2, and 32.7 dBm^2. The RCS reduction increases in smaller hole centre spacings. The reduction of RCS from 15 mm to 12 mm spacing is 0.5 dBm^2, while it is 1.5 dBm^2 from 12 mm to 10 mm spacing.

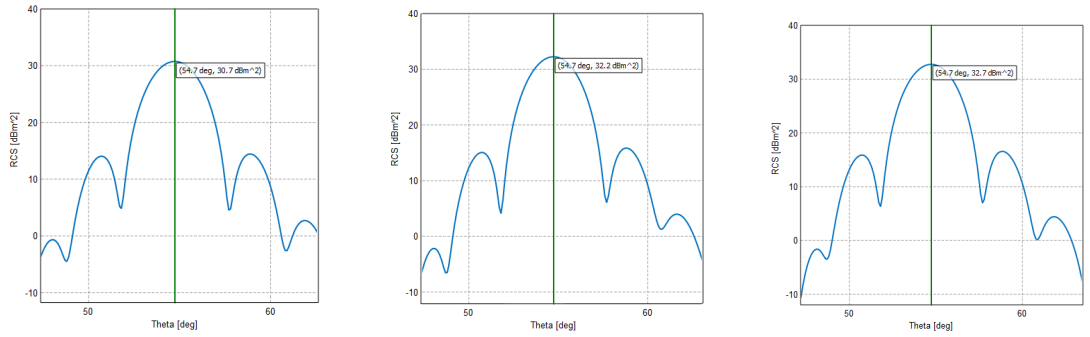

(a) *(b)* *(c)*

Figure 3.5: *Hole sizes of 7.5 mm. a) 10 mm spacing and b) 12 mm spacing and c) 15 mm spacing.*

3.3.3.4 One-third of the wavelength

The fourth corner reflector was perforated with a 10 mm hole size representing one-third of the radar wavelength. Only two varying hole spacings of 12 mm, and 15 mm were analysed as shown in Fig. 3.6 as it would not be possible for the 10 mm hole centre spacings to be analysed with a 10 mm hole size. The maximum radar cross section for the 12 mm and 15 mm spacings are 26.8 dBm^2 and 29.5 dBm^2. The reduction of RCS from 12 mm to 15 mm spacing is 2.7 dBm^2.

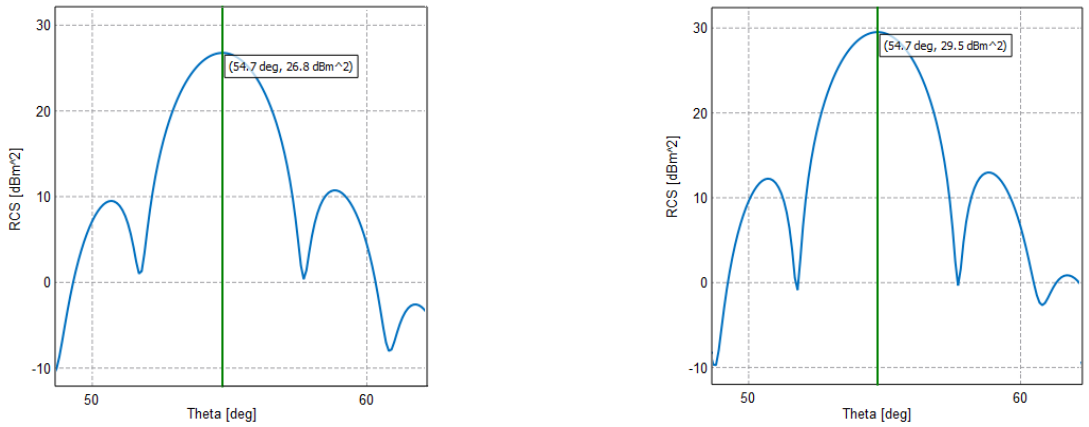

Figure 3.6: *Hole sizes of 10 mm. (a) 12 mm spacing and (b) 15 mm spacing.*

3.3.3.5 Results and Discussions

Table 3.3 summarises the results of the four different hole sizes, as well as the three varying hole centre spacings. The reduction in radar cross section for the first square trihedral reflector is less than 1 dB, and it did not affect the radar cross section for the two hole centre spacings; 12 mm, and 15 mm. The 10 mm spacing was not done as it requires a huge memory for the simulation, and the results should be similar to the two hole centre spacings 12 mm and 15 mm. Also, most manufacturing companies do not have the ability to perforate the panel with very small hole sizes and small spacings, and if they do it would be very expensive.

The second square trihedral corner reflector which was perforated by one-sixth of the wavelength (5 mm), has a reduction of about 1 dBm^2, and the effect of spacing between the three varying hole centre spacings is about a 0.10 dBm^2 reduction on maximum radar cross section. The third square trihedral corner reflector which was perforated by one-fourth of the wavelength (7.5 mm), showed three different amounts of reduction among the three hole sizes, and between the three varying hole centre spacings. The 15 mm and 12 mm spacings had a reduction of 1.48 dBm^2 and 1.98 dBm^2, while the 10 mm was reduced by 3.48 dBm^2. Additionally, the reduction between the 15 mm spacing and the 12 mm spacing was 0.5 dBm^2, while the reduction between the 12 mm spacing and the 10 mm spacing was 1.5 dBm^2. Finally, the forth square trihedral corner reflector which was perforated by one-third of the wavelength (10 mm) had the worst effect on maximum radar cross section, and the reduction of maximum radar cross section between the two spacings was 2.7 dBm^2. The 15 mm spacing reduced the radar cross section by 4.68 dBm^2, while the 12 mm spacing reduced the radar cross section by 7.38 dBm^2.

The first two corner reflectors which are one-tenth of the wavelength, and one-sixth of the wavelength, are the optimum choice for perforating the corner reflector due to the low reduction on maximum radar cross section. The last two corner reflectors, which are one-fourth of the wavelength and one-third of the wavelength, are not the preferred choice as the amount of reduction is very high. In our case, we are going to perforate our corner reflectors with one-sixth of the wavelength of X-band, and the hole centre spacing is 12 mm. The reason behind the choice is because the reduction will be 1 dBm^2, and we will have more open area to allow quick drainage from heavy rain, cleansing from dust, and reduction in the effect of wind, as well as, reducing the weight of the corner reflectors.

The reflectors are going to be deployed in Riyadh, Saudi Arabia where the weather is dusty and windy most of the time, and a 5 mm hole size with 12 mm centre spacings will help to reduce the effect of strange weather. Also, the plate, which will be perforated, should be thick enough to maintain its flatness, and it should not effect the maximum radar cross section. The perforating of the corner reflectors was not done due to the high cost of perforating each panel

and it might be done once the corner reflectors arrived to Saudi Arabia.

Table 3.3: *The effect of perforating the corner reflector on maximum radar cross section with four different hole sizes and three varying hole centre spacings*

Hole Size	10 mm	12 mm	15 mm
$\lambda/10$	-	33.3 dBm^2	33.3 dBm^2
$\lambda/6$	33.09 dBm^2	33.18 dBm^2	33.23 dBm^2
$\lambda/4$	30.7 dBm^2	32.2 dBm^2	32.7 dBm^2
$\lambda/3$	-	26.8 dBm^2	29.5 dBm^2

3.3.4 Gridded Corner Reflectors

Transpolarising surfaces of trihedral reflectors could even have non-cross-polarisation applications, such as a polarisation selective where it reflects only horizontal, or vertical by choosing the azimuth angle of incidence [106]. Dual polarimetric data has two channels to be measured, while the full polarimetric data has four channels. A gridded corner reflector could be used as a polarisation selective in the dual polarimetric calibration to produce only horizontal, or vertical reflection. Different algorithms [53] [11] [54] were developed in the past years and they require a calibration target without a cross-polarisation response, and a reflection from only one of the co-polarisation channels.

In this Section, we introduce the optimum design of gridded corner reflectors for calibration of dual polarimetric SAR sensors, to have a reflection from only the horizontal or vertical channels. The section starts by analysing the effect of the grids width, and, the gap between the grids on the reduction of maximum radar cross section, when the incident wave is parallel or perpendicular to the grids, as well as the discrimination between the channels. The second part describes the design of gridded trihedral, and gridded dihedral corner reflectors based on the analysis in the first part, using a square with 50 cm surfaces.

Furthermore, the construction of the gridded trihedral and dihedral corner reflectors is detailed in Section 3.4.3, using 3 mm aluminium sheets and stainless

steel welding rods of 1.2 mm in diameter. The simplest and cheapest design of transpolarising the surfaces for a corner reflector is by using a PCB as a dielectric substrate, as it is relatively inexpensive, and has low losses. But even though these PCB's have low losses, such as Rogers RO4003C, they cannot be a perfect absorber, and they are better used for generating a cross-polarisation reflection such as in [106] [107] [108]. We used a flexible foam sheet broadband microwave absorber, ECCOSORB AN-73 (εr = 1.03, tan δ= 0.00186), which was designed to reflect less than -17 dB of normal incident energy above specified frequencies, and relative to a metal plate. The design of the gridded corner reflector includes an analysis of the effect in spacing, and wire width when the plan wave is parallel, or perpendicular to the wires. Then we designed the dihedral, and trihedral models using FEKO software to generate the simulation results.

3.3.4.1 Effect of Spacing and Grid width

The effect of the wire width, and the gap between the wires was analysed using 30 cm flat plates, and operated at around 10 GHz (X-band), giving a maximum theoretical RCS of 20.5 dBm^2. Four different gaps between the wires were used in the analysis, they were; 1.5 mm, 3 mm, 5 mm, and 7.5 mm, representing one twentieth, one tenth, one sixth and one quarter of the wavelength. Also, three different wires were used for each gap, which were; 0.5 mm, 1 mm, and 1.5 mm. The analysis was carried out for incident waves parallel, or perpendicular to the wires using FEKO software, which is based on methods of moments for simulation as follows:

3.3.4.1.1 one-twentieth of the wavelength The first gap is 1.5 mm representing one-twentieth of the X-band wavelength with three different sizes of wires. Fig. 3.7 shows the maximum response from the flat plate when the incident wave is parallel to the wire. The reduction in RCS is only 0.1 dBm^2, and it did not change over the three wires. Also, Fig. 3.8 shows the response when the incident wave is perpendicular to the wire, where the discrimination between the parallel and perpendicular is much better when the size of wire is decreased.

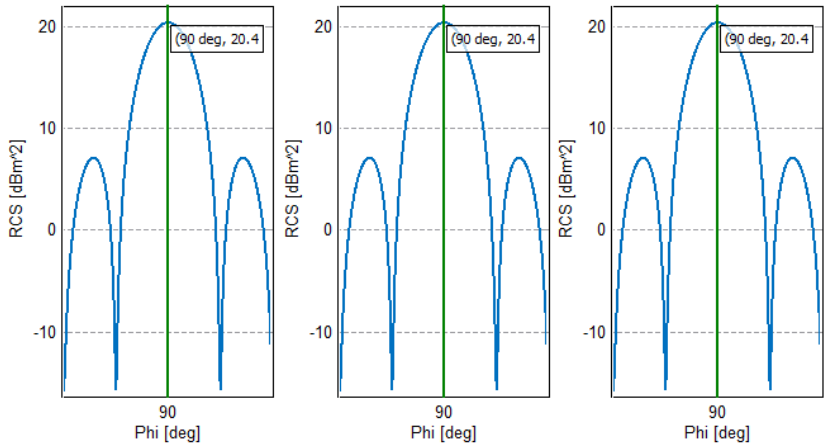

Figure 3.7: *Incident wave parallel to grids with a gap of one-twenty of the wavelength using three grid widths; 0.5 mm, 1 mm, and 1.5 mm.*

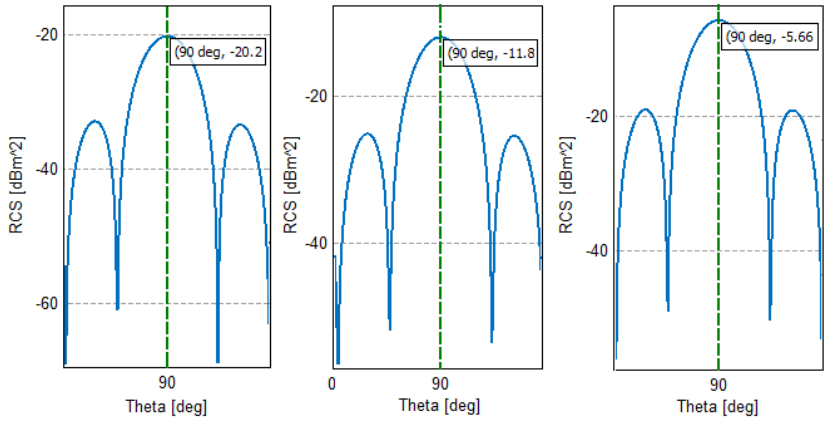

Figure 3.8: *Incident wave perpendicular to grids with a gap of one-twenty of the wavelength using three grid widths; 0.5 mm, 1 mm, and 1.5 mm.*

3.3.4.1.2 One-tenth of the wavelength The second gap of 3 mm represented one-tenth of the wavelength, with three different sizes of wire. Fig. 3.9 details a reduction in RCS of 0.1 dBm^2 between the three wires when the wave is parallel to the wire, and the reduction decreases when the size of the wire increases. Also, Fig. 3.10 shows the response when the incident wave is perpendicular to the wire, where the discrimination between the parallel and perpendicular is much better when the size of wire is decreased.

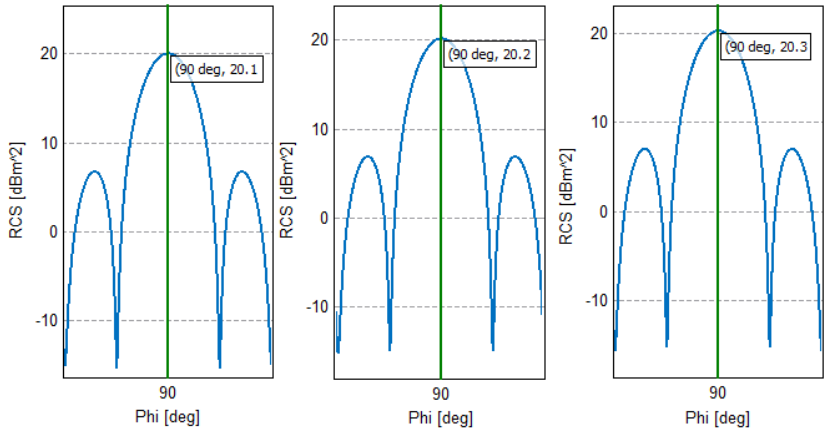

Figure 3.9: *Incident wave parallel to grids with a gap of one-tenth of the wavelength using three grid widths; 0.5 mm, 1 mm, and 1.5 mm.*

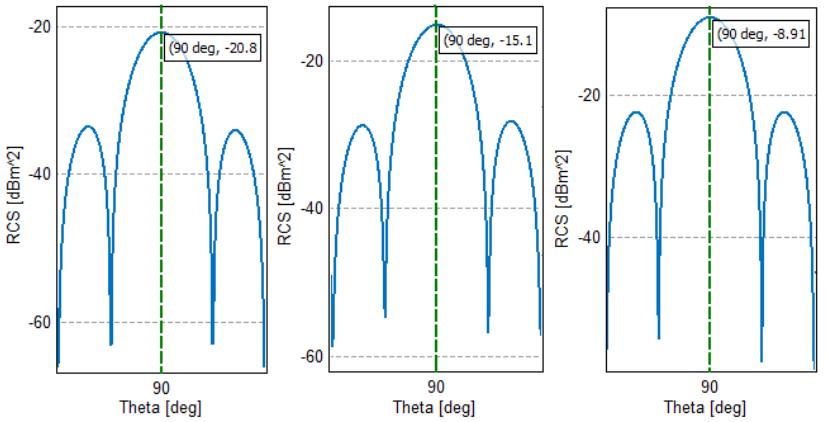

Figure 3.10: *Incident wave perpendicular to grids with a gap of one-tenth of the wavelength using three grid widths; 0.5 mm, 1 mm, and 1.5 mm.*

3.3.4.1.3 One-sixth of the wavelength The third gap between the wires was 5 mm which is one-sixth of the wavelength of X-band, with three different sizes of wire. Fig. 3.11 shows the maximum response when the incident wave is parallel to the wire. The reduction in RCS is more than 1 dBm^2, and is it increases over the three wires; 0.5 mm, 1 mm, and 1.5 mm. Additionally, the results in Fig. 3.12 which tabulates the response for the wave perpendicular to the wire showing a decrease in the reduction over the three wires, which results

in better discrimination between the parallel, and perpendicular waves to the wires.

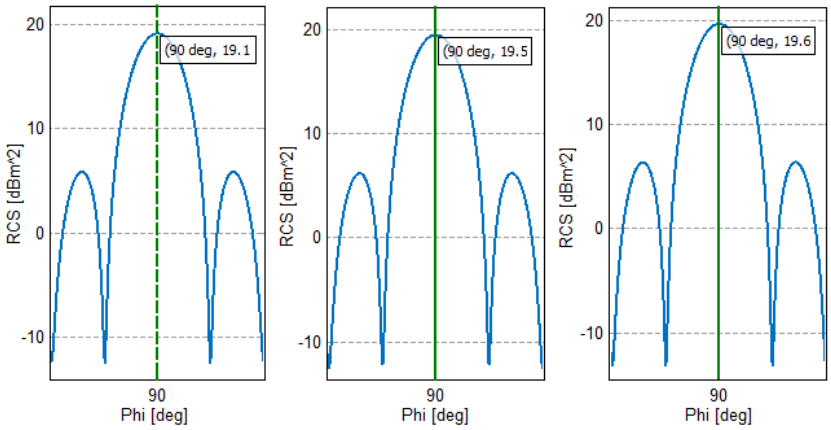

Figure 3.11: *Incident wave parallel to grids with a gap of one-sixth of the wavelength using three grid widths; 0.5 mm, 1 mm, and 1.5 mm.*

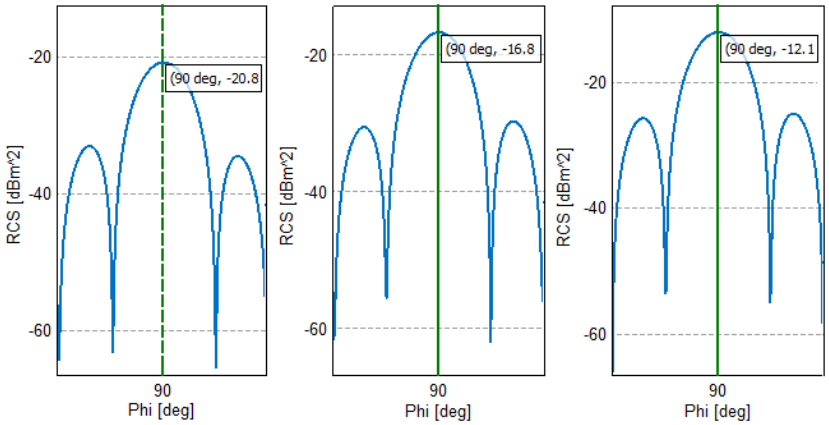

Figure 3.12: *Incident wave perpendicular to grids with a gap of one-sixth of the wavelength using three grid widths; 0.5 mm, 1 mm, and 1.5 mm.*

3.3.4.1.4 One-quarter of the wavelength The last gap between the wires was 7.5 mm representing one-quarter of the wavelength with three sizes of wire. Fig. 3.13 shows a large reduction of RCS from the theoretical when the wave is parallel to the wires of about 2 dBm^2, and about 0.5 dBm^2 between the three different wires. This reduction in RCS makes it the worst choice for designing a

gridded reflector. Also, Fig. 3.14 shows a lower discrimination for the response when the incident wave is perpendicular to the three wires. A small difference shows between the 0.5 mm and 1 mm wires, which is 0.4 dBm^2 while it increases between 1 mm, and 1.5 mm to 3 dBm^2.

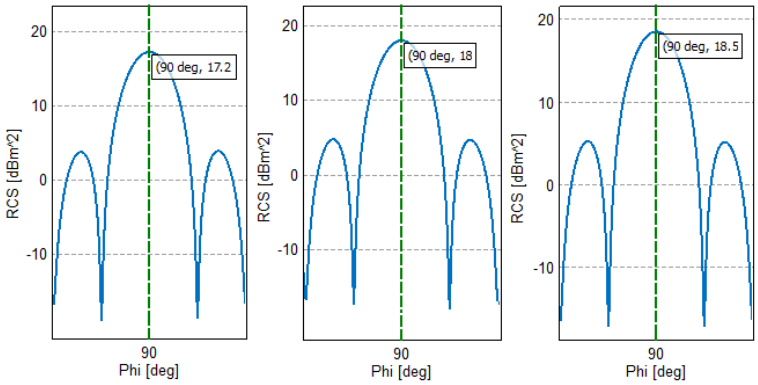

Figure 3.13: *Incident wave parallel to grids with a gap of one-quarter of the wavelength of the wavelength using three grid widths; 0.5 mm, 1 mm, and 1.5 mm.*

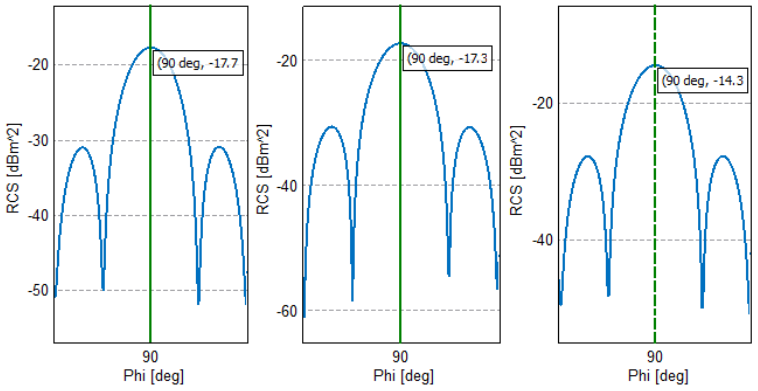

Figure 3.14: *Incident wave perpendicular to grids with a gap of one-fourth of the wavelength using three grid widths; 0.5 mm, 1 mm, and 1.5 mm.*

Table 3.4 summarises the analysed results of the effect of spacing, and grid width, on maximum radar cross section with four different gap sizes, and three different sizes of wire. The results show that the 3 mm gap, and 0.5 mm wire has the best discrimination, but the construction is difficult as 0.5 mm is very thin, and the gap is small.

3.3.4.2 Gridded Dihedral Corner Reflectors

Two gridded dihedral corner reflectors were designed to operate around 10 GHz (X-band). The first dihedral was designed using vertical stainless steel welding rods on both surfaces to have reflection from the vertical channel, while the second dihedral corner reflector was designed using horizontal stainless steel welding rods to have a reflection from the horizontal channel. The diameter of the welding rods was 1.2 mm and the length was 50 cm. A gap of 5 mm, which represented one-sixth of the wavelength, was selected to have a better discrimination between the perpendicular and parallel plane waves. The maximum theoretical RCS for the dihedral corner reflector with 50 cm inner leg dimension was 32.4 dBm^2.

Figs. 3.15 and 3.16 show the reduction of RCS when the plane wave is parallel to the rods, which is about 2 dBm^2, and about 55 dB lower than that of the plane wave when it is perpendicular to the rods.

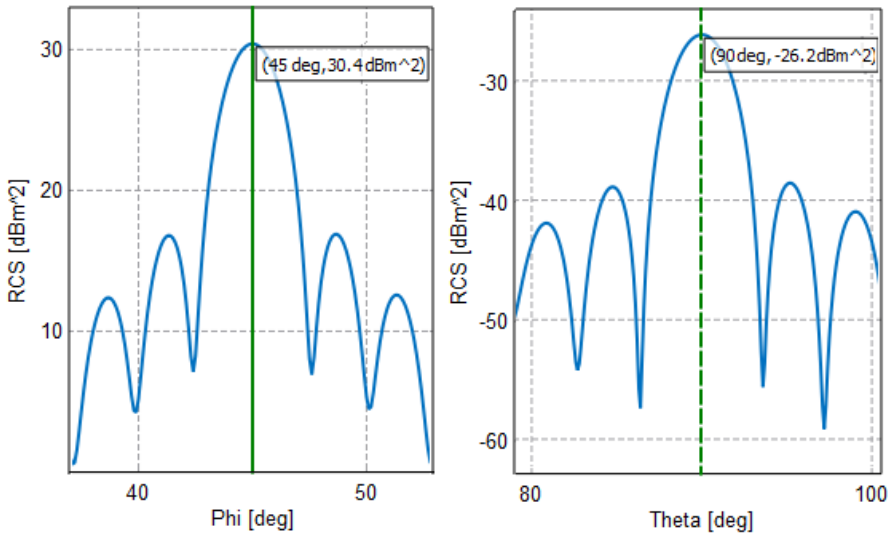

Figure 3.15: *Gridded dihedral corner reflector with horizontal plane wave where left is parallel and right is perpendicular to the stainless steel welding rods.*

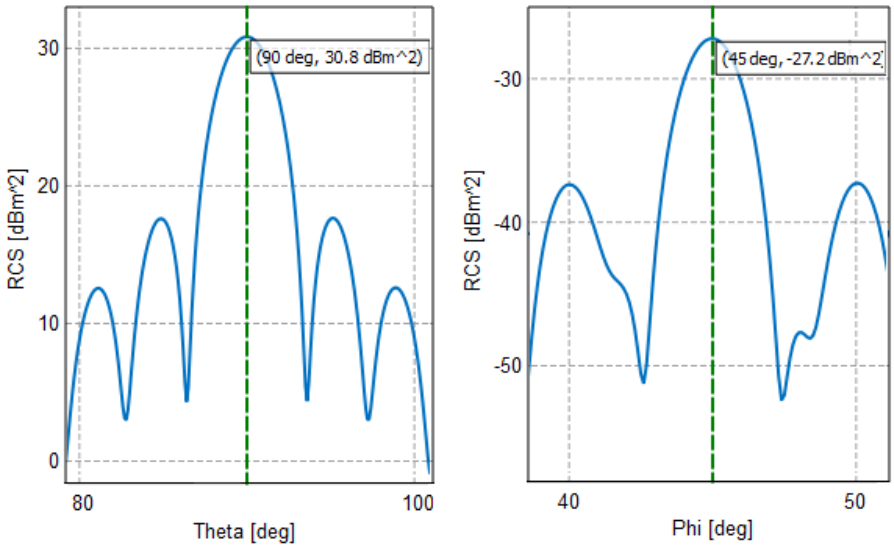

Figure 3.16: *Gridded dihedral corner reflector with vertical plane wave where left is parallel and right is perpendicular to the stainless steel welding rods.*

3.3.4.3 Gridded Trihedral Corner Reflectors

Two square trihedral corner reflectors were designed, with stainless steel welding rods replaced on all three surfaces of the reflector, to reflect only the horizontal or the vertical channel, and operate around 10 GHz (X-band). A gap of 3 mm between the rods was used, which represented one tenth of the wavelength, the diameter of the welding rods was 1.2 mm. The maximum theoretical RCS for a square trihedral corner reflector with a 50 cm inner leg dimension is 34.2 dBm^2. Figs. 3.17 and 3.18 show the reduction of RCS when the plane wave is parallel to the rods, which is about 5 dBm^2, and about 60 dB lower than that for the plane wave when it is perpendicular to the rods. The reduction of RCS can be improved by using a smaller gap, such as 1.5 mm, but it will be difficult to build the reflector and it would require a large number of rods.

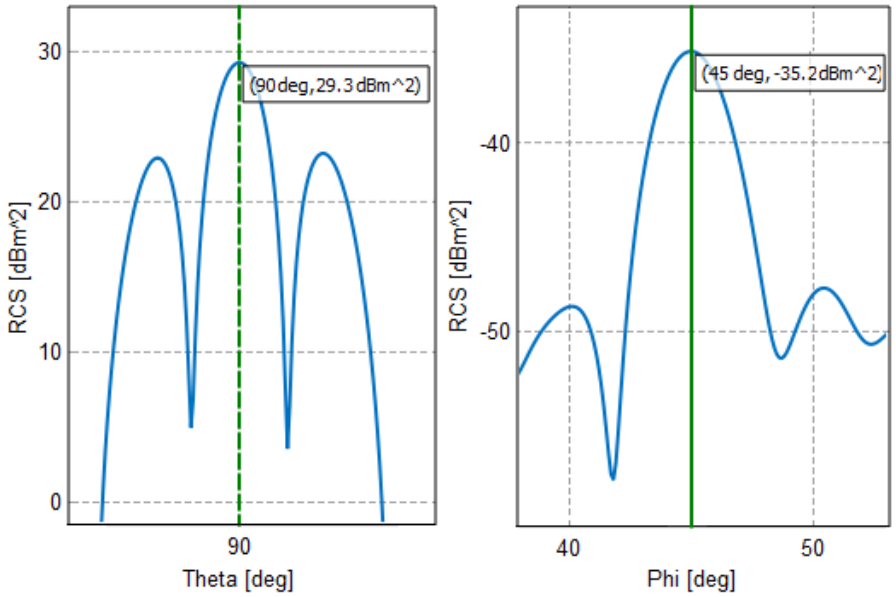

Figure 3.17: *Gridded trihedral corner reflector with horizontal plane wave where left is parallel and right is perpendicular to the stainless steel welding rods.*

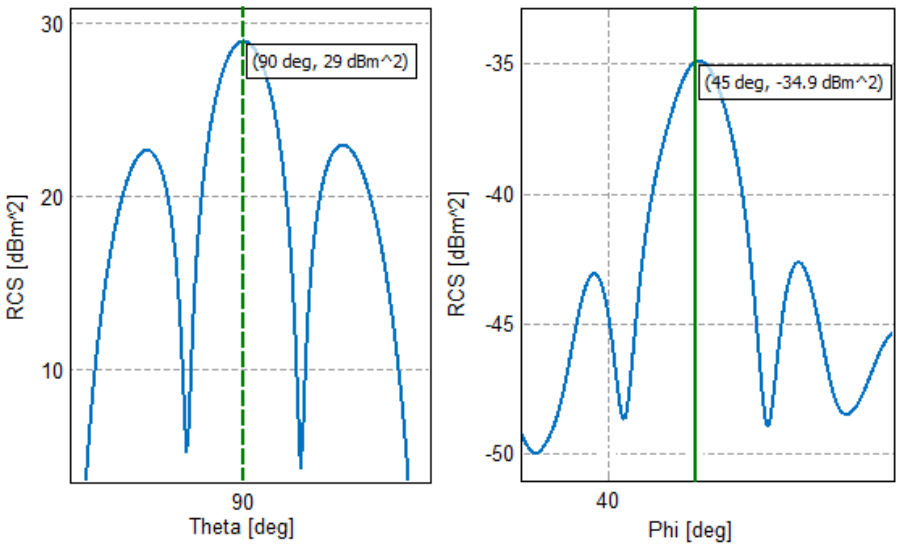

Figure 3.18: *Gridded trihedral corner reflector with vertical plane wave where left is parallel and right is perpendicular to the stainless steel welding rods.*

3.3.5 Manufacturing Tolerances

Manufacturing the corner reflectors require a number of tolerances to be met in order to reduce the effect of errors on the maximum RCS of the corner reflectors [44]. The first tolerance to consider is the inter-plate orthogonally because the radar cross section of the reflector decreases if the angle departs from 90°. We have to pay more attention to the inter-plate orthogonality of P-band corner reflectors, because the reduction of the RCS will be greater when the radar wavelength is longer. An excellent choice to maintain 90° inter-plate orthogonality is the use of plastic gussets to assure the orthogonality of the plates.

The second tolerance for consideration is the deformation of the plate from a perfectly flat plane along its entire length. Finally, the third tolerance to consider is the involvement of any small scale deviation from perfect flatness such as ripples. Furthermore, some of the trihedral reflectors were perforated mesh to allow for quick drainage from heavy rain, as well as cleansing from dust, and reduction in the effect of wind. The mesh perforation may cause a reduction in the RCS, and in order to not have an effect on the RCS, the hole diameter must be less than one-sixth of the radar wavelength. However, the physical punching of aluminium sheets to make the mesh shows major stresses to the sheets that cause deviations from flatness.

3.4 Passive Point Targets Construction

The twelve classical trihedral and dihedral corner reflectors were manufactured by Titanium Company in Johannesburg, South Africa, to be shipped to the Netherlands to acquire data for this thesis, and then to be shipped again to Saudi Arabia for KACST, as per the agreement between droneSAR and KACST.

Furthermore, the four gridded corner reflectors had a very limited budget and were manufactured at the University of Cape Town, South Africa, following which they were shipped to Johannesburg to join the twelve reflectors. The following sections detail the construction of these corner reflectors.

3.4.1 Construction of X-band Corner Reflectors

Three trihedral and three dihedral reflectors were manufactured for X-band with an inner leg dimension of 500 mm. The thickness of the aluminium plate is a very important factor in our construction of the corner reflectors, as the higher the thickness, the higher the cost of manufacturing, as well as higher costs of shipping. Aluminium plate with a thickness of 1.2 mm was chosen to construct the trihedral and dihedral corner reflectors.

Twelve 500 mm by 500 mm panels were manufactured, where nine of them were for the square trihedral reflectors, and six of them for the dihedral corner reflectors. Small 90° plastic gussets were used to ensure the orthogonality of the plates, as shown in Fig. 3.19. The reason behind choosing the plastic gussets was to avoid unwanted backscatter from the corner reflectors. Furthermore, six tripods were manufactured with the ability of rotating 360° in azimuth and 65° in elevation. Each reflector was mounted on top of a tripod that is adjustable in azimuth and elevation.

Figure 3.19: *Three X-band dihedral corner reflectors mounted on their tripods.*

3.4.2 Construction of P-band Corner Reflectors

Three trihedral, and three dihedral corner reflectors were manufactured for P-band with a 1.5 m inner leg dimension. Two important factors were considered during the manufacturing of the corner reflectors with longer inner leg dimensions which were; inter-plate orthogonally because the RCS of the reflector decreases if the angle departs from 90°, and the deformation of the plate from a perfectly flat plane along its entire length.

In the beginning, we manufactured one square trihedral corner reflector with an inner leg dimension of 1.5 m, as shown in Fig. 3.20(a). We used 9 panels of 500 mm by 500 mm for each surface, and they were bolted together to form a 1.5 m by 1.5 m square surface. The square trihedral corner reflector was not rigid enough, and the plate was not perfectly flat along its entire length which would cause a reduction in RCS.

We decided to manufacture the trihedral corner reflectors using triangular surfaces even if the maximum RCS is lower, but the reflector would be more rigid, and the inter-plate orthogonally would be at exactly 90°. We manufactured three triangular trihedral corner reflectors with a 1.5 m inner leg dimension, as shown in Fig. 3.21, using aluminium plate with a thickness of 1.2 mm. Each surface consisted of three 500 mm by 500 mm square panels, and three triangular panels which were bolted together to form a triangular surface with a 1.5 m inner leg dimension.

Furthermore, three dihedral corner reflectors were manufactured with a 1.5 m inner leg dimension, using aluminium plate with a thickness of 1.2 mm. Two plastic gussets were used as shown in Fig. 3.20(b), to assure the inter-plate orthogonality. Additionally, two adjustable legs were manufactured for each dihedral corner reflector to support the surfaces from any wind movement. Finally, six tripods were manufactured with the ability to rotate 360° in azimuth and 65° in elevation. Each reflector was mounted on top of a tripod that is adjustable in azimuth and elevation.

(a) ***(b)***

Figure 3.20: *P-band corner reflectors. (a) Square trihedral with 1.5 m inner leg dimension before cutting it to be triangular trihedral and (b) Dihedral corner reflector with 1.5 m inner leg dimension supported by two plastic gussets to maintain 90° inter-plate orthogonality.*

Figure 3.21: *Three triangular trihedral corner reflectors with 1.5 m inner leg dimension for P-band.*

3.4.3 Construction of Gridded Corner Reflectors

The dihedral, and trihedral corner reflectors were manufactured using 3 mm aluminium plate with a 570 mm inner leg dimension. The microwave absorbers were mounted on each surface of the aluminium plate for both the trihedral, and dihedral reflectors to obtain low reflectivity. For correct operation, the white (front) face of the microwave absorber is directed towards the signal to be attenuated. Stainless steel welding rods of 1.2 mm in diameter were used for the grids. The reasons behind using 1.2 mm rods was because the welding rods only have two available sizes; namely 1.2 mm, and 1.6 mm, additionally they are solid and easy to construct. A thinner diameter of wire can be used to obtain a much better discrimination between the channels, however the construction would be complicated as the gap between the wires needs to be very small.

Fig. 3.22 shows the two dihedral corner reflectors with vertical, and horizontal reflection. 570 mm by 10 mm aluminium edges were welded onto the plates to be used for connection with the stainless steel welding rods. Due to the small hole sizes, and the gap between them, we could not make the small holes on the aluminium edges. We used 500 mm by 17 mm strips from a printed circuit board and we made 1.25 mm holes, which is the required gap for each reflector to have been accurately constructed.

Figure 3.22: *Two gridded dihedral corner reflectors where left is vertical wires and right is horizontal wires.*

Finally, the trihedral, and dihedral corner reflectors were mounted onto an aluminium triangular base which has three long screws, one in each corner of the triangular base, to allow for adjustment of the level, as shown in Fig. 3.23. Both trihedral and dihedral reflectors can rotate up to 90° in range and up to 60° in azimuth.

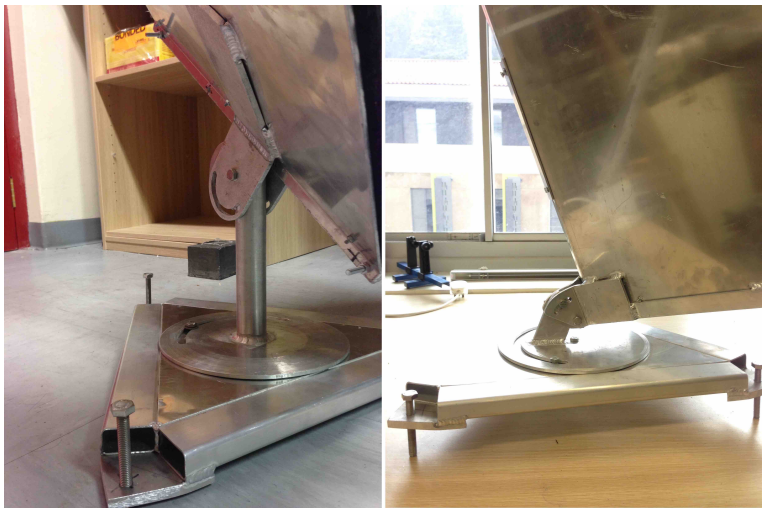

Figure 3.23: *Two triangle bases where left is for dihedral and right for trihedral corner reflector.*

3.5 Passive Point Targets Deployment

Sixteen corner reflectors for X- and P-band were deployed at three different sites inside, and outside the Teuge airport, the Netherlands, to cover the entire swath of the image. As shown in Fig. 3.24, the near, and far field, are inside the airport, and the airport authority were very strict and they only allowed us a couple of hours to deploy the reflectors, and remove them after flying. Furthermore, a pick-up truck as shown in Fig. 3.25, was used to move our corner reflectors from the hanger to the deployment sites, as we were not allowed to drive our own cars, or walk inside the airfield without their permission. Finally, the third site (mid field), was an open field and used for parachuting activities. We had easy access and it was safe to leave the reflectors for a couple of days for acquisitions.

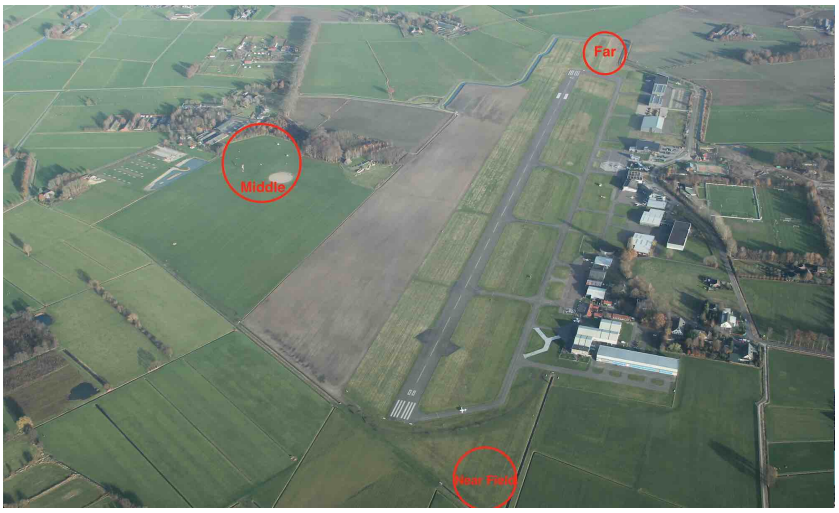

Figure 3.24: *Three sites, in red circles, where the corner reflectors were deployed in and around the airport.*

(a) ***(b)***

Figure 3.25: *A pick-up truck for Teuge airport authorities which they used to move our corner reflectors to the three sites for deployment.*

A detailed map of deployment for the corner reflectors is shown in Fig. 3.26 for the three sites. There were four reflectors in the near field and four reflectors in the far field, while there were eight reflectors deployed in the mid field due to the easy access to the field, and no restrictions from airport authorities. Moreover, the map shows a distance between the reflectors in both azimuth and ground range to avoid any overlap on the image for the reflectors.

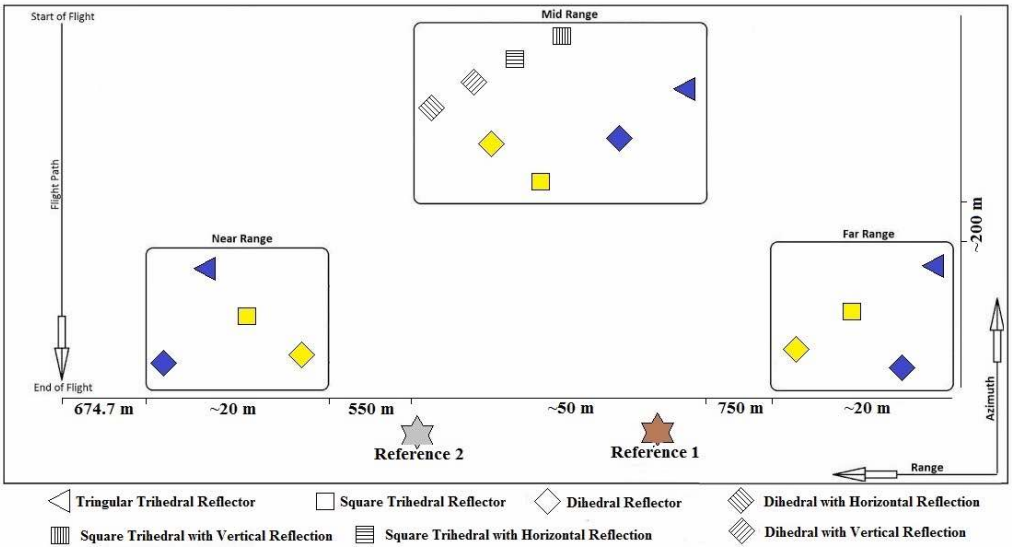

Figure 3.26: *A map of deployment for the corner reflectors in the three sites and in the bottom two reference points for the azimuth rotation of the corner reflectors.*

Fig. 3.27 shows the three different incidence angles for each site at a 750 m flying altitude. The total distance from the near to the far field is 1425.3 m, and from the near field to the flight path is 674.7 m. The three incidence angles were calculated based on the right-angled triangle-geometry, and they were used for the elevation angles rotation as well as the radiometric calibration.

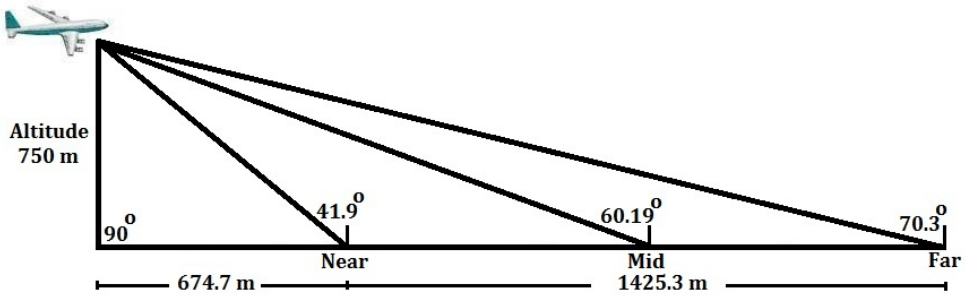

Figure 3.27: *Three incidence angles for each site (near, mid, far field) flying at 750 m altitude perpendicular to the runway.*

The deployment strategy for the corner reflector consisted of five major steps.

We first surveyed the position of the corner reflectors using global navigation satellite systems (GNSS). The second step was to position the reflectors exactly at the points which were surveyed. The third step was levelling the tripods using digital angle level levelling. The fourth step was the azimuth angle rotation to the reference point using a digital degree wheel, and finally, the digital angle level levelling used again for the elevation angle rotation for each corner reflector.

3.5.1 Corner Reflectors Site Positions

Two global navigation satellite systems were used to survey the positions for the corner reflectors in the three sites. The first GNSS, as shown in Fig. 3.28(a),Atlas H10 which is the Hemisphere GNSS correction service, offering the most innovative correction service in the industry. Atlas H10 provides positioning accuracies down to 8 cm at 95% (4 cm RMS), as well as convergence times of 10 to 40 minutes. During the campaign, we surveyed the positions of the X- and P-band corner reflectors on 22, 23, and 24 November 2016 using Atlas H10, and then due to technical problems on the X-band radar, we had to deploy the X-band corner reflectors again, and fly on 30 November 2016. We had to survey the positions of the X-band corner reflectors using Metasensing GNSS which is from Hampshire and is shown in Fig. 3.28(b). The reason behind using their GNSS was because the cable of the Atlas H10 GNSS was broken during the previous positioning, so we had to borrow their GNSS to survey the positions for the corner reflectors of X-band, which was done on 30 November 2016.

Table 3.5 shows the surveyed positions of the X-band trihedral, and dihedral corner reflectors as well during acquisitions on 30 November 2016, while Table 3.6 shows the surveyed positions of the P-band corner reflectors during acquisitions on 23 November 2016. The position of the P-band corner reflector in the mid-field is the same as for the acquisition on 24 November 2016, as we kept the reflector for the following day since it was outside the airport and the area was safe.

(a)

(b)

Figure 3.28: *Two global navigation satellite systems which we used to survey the position of the corner reflectors. (a) Our atlas H10 GNSS system and (b) Metasensing GNSS which is from Hampshire.*

Table 3.5: *Position of the X-band corner reflectors on 30 November 2016*

Parameters	Trihedral Corner Reflector		Dihedral Corner Reflector	
	Easting [m]	Northing [m]	Easting [m]	Northing [m]
Near Field	297962.67	5791998.46	297978.03	5791986.41
Mid Field	298583.84	5792578.52	298605.47	5792591.66
Far Field	299432.14	5792121.82	299399.13	5792105.84

Table 3.6: *Position of the P-band corner reflectors on 24 November 2016*

Parameters	Trihedral Corner Reflector		Dihedral Corner Reflector	
	Easting [m]	Northing [m]	Easting [m]	Northing [m]
Near Field	297962.67	5791998.46	297978.03	5791986.41
Mid Field	298583.84	5792578.52	298605.47	5792591.66
Far Field	299432.14	5792121.82	299399.13	5792105.84

After surveying the positions for each corner reflector, we installed the tripods on the surveyed positions. The tripod had a hole in the top middle, as shown in Fig. 3.29(a), to use it, a rope with a weight is attached to one end of the rope to locate the corner reflector exactly at the surveyed position. At the bottom of each leg of the tripods, there is a hole to insert a peg to fixing each leg to the ground. Finally, we used digital levelling as shown in Fig. 3.29(b), to level the tripod to be flat, by adjusting the length of each leg of the tripod.

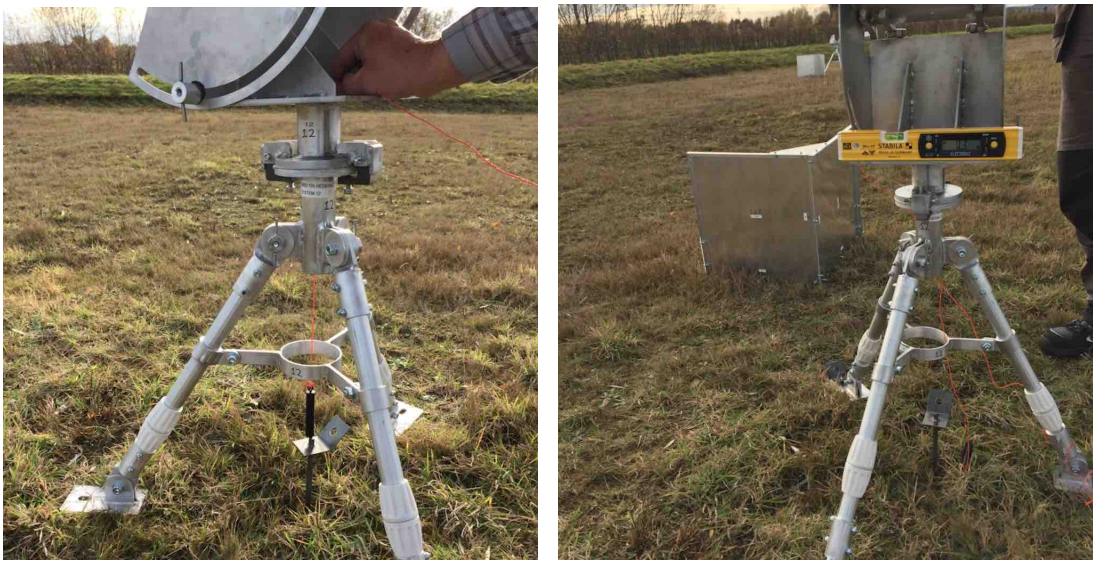

(a) *(b)*

Figure 3.29: *Installation of the tripods on the surveyed positions. (a) Using a rope with a weight is attached to one end of a rope to locate the reflector exactly at the survey position and (b) Using a digital levelling to Level the tripods to be flat using the three legs*

3.5.2 Azimuth Angles Rotation for Trihedral and Dihedral Reflectors

The azimuth angles strategy is based on selecting a reference point for pointing the corner reflectors toward the reference point, and then by knowing the angle from the reference point to the flight path, we can rotate each reflector from the

reference point to the flight path. We selected two reference points because we could not find a reference point that could be seen from all three sites. As shown in Fig. 3.30(a), the first reference point which is the aerial over the control tower of the airport, which was used for the azimuth rotation of the corner reflectors in the far site. The second reference point in Fig. 3.30(b), is the edge of the Gray building and it was used for the azimuth rotation of the corner reflectors in the near and middle sites. We used Google Earth to obtain the location of these reference points, and calculate the azimuth rotation from the reference points to the flight path.

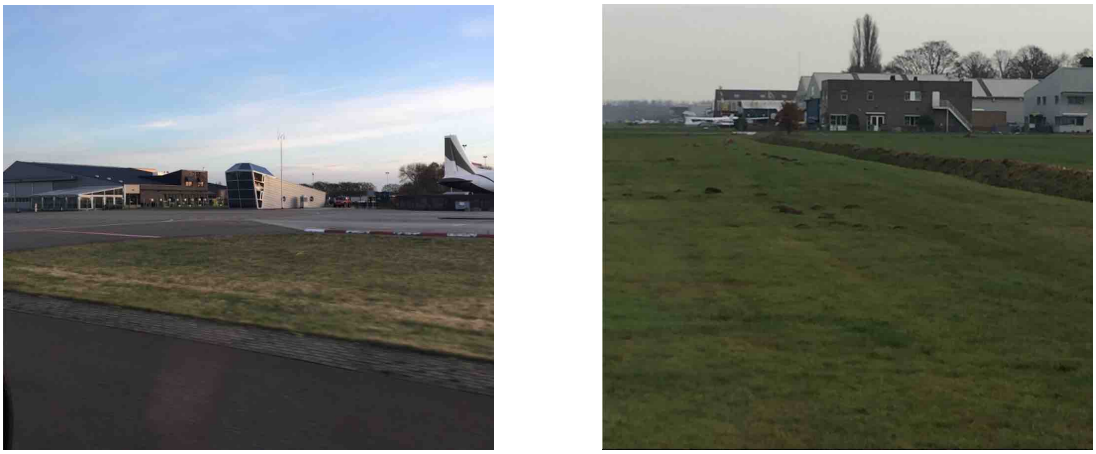

(a) ***(b)***

Figure 3.30: *Two reference points for the azimuth rotation of the corner reflectors. (a) First reference point which is the aerial over the control tower and it was used for the far site, and (b) Second reference point which is the edge of the Gray building and it was used for the near and middle sites.*

The azimuth rotation for the corner reflectors in the far field was by 9.4° from the aerial over the control tower in a clockwise direction. Additionally, the azimuth rotation for the corner reflectors in the mid field was by 55° from the edge of the Gray building, again, in a clockwise direction. Finally, the near site had different azimuth angles due to the azimuth distance between them; where it was 177° from the edge of the Gray building, clockwise for the P-band dihedral, and 172° for the P-band trihedral. The azimuth angle for the X-band corner reflectors was

174°. The azimuth rotation started by pointing the corner reflector toward the reference point, using a gun-sight as shown in Fig. 3.31(a). The gun-sight is made by Simmons and it was mounted on the centre of the top plate of the tripod. After we pointed the middle centre of the corner reflector toward the reference point, we used a digital degree wheel as shown in Fig. 3.31(b), for the azimuth rotation to ensure accurate angle rotation. The digital degree wheel is made by Prisma Electronics with an accuracy of 0.1°. It is a digital reading device, and is used for the measurement of the diagram phase of 2-stroke engines, and for the tuning up of the camshaft in the 4-stroke engines to within a tenth of a degree of precision. The device can read the absolute position of the crankshaft 100 times per second in order to not miss a hundredth of a degree of measurement.

(a) *(b)*

Figure 3.31: *Azimuth rotation for the corner reflectors. (a) A gun-sight used to point the corner reflectors toward the reference point, and (b) Digital degree wheel used during the azimuth rotation of the corner reflectors.*

3.5.3 Azimuth Angles Rotation for Gridded Reflectors

The bases of the gridded corner reflectors are different from the previous trihedral and dihedral reflectors due to the higher cost of tripods. Moreover, the gridded corner reflectors do not have a crankshaft connected to the digital degree wheel

as we manufactured the gridded corner reflectors with a very limited budget. Following the levelling of the base as shown in Fig. 3.32(a), to be flat, we used a gun-sight to point the reflectors toward the second reference point, which was the edge of the Gray building, and by using a digital compass for the azimuth rotation as shown in Fig. 3.32(b). The gridded corner reflectors were rotated by 58° from the edge of the Gray building in a clockwise direction.

(a) *(b)*

Figure 3.32: *Deployment of gridded corner reflectors in the mid field. (a) Levelling the base to be flat on the ground, and (b) Using the gun-sight to point it toward the second reference point for azimuth rotation.*

3.5.4 Elevation Angles Rotation

The corner reflectors were rotated in elevation for each site based on the incidence angle in Fig. 3.27. A digital levelling measurement was used for the rotation of the corner reflectors angles in elevations. Table 3.7 summarises the results for the elevation angles rotation in three different fields. Due to the low-flying altitude, the trihedral corner reflectors were rotated downward to obtain the maximum response from the reflectors. Further, Fig. 3.33 shows the corner

reflectors after deployment in the mid field, where Fig. 3.33; (a) are the dihedral corner reflectors for X- and P-band rotated by 45°, while Fig. 3.33(b) is the triangular trihedral corner reflector for P-band. The deployment of the rotated dihedral corner reflector for P-band was very complicated, because the reflector was heavy, and it took four hours to deploy it. Additionally, the elevation angle for the P-band dihedral was adjusted at the base of the tripod so when we installed the two plates, we thought the reflector moved downward by some angle due to the weight of the plates.

(a) ***(b)***

Figure 3.33: *Corner reflectors after deployment in the mid field. (a) Dihedral for X- and P-band rotated by 45°, and (b) Triangular trihedral for P-band.*

The elevation angle rotation for the gridded dihedral, and gridded trihedral corner reflectors is similar to the trihedral and dihedral reflectors in the mid-field. Fig. 3.34 shows the elevation angle rotation for the gridded dihedral, and gridded trihedral corner reflectors, where in Fig. 3.34(a) using a rope to support the reflector, and Fig. 3.34(b) a front look at the gridded dihedral reflector.

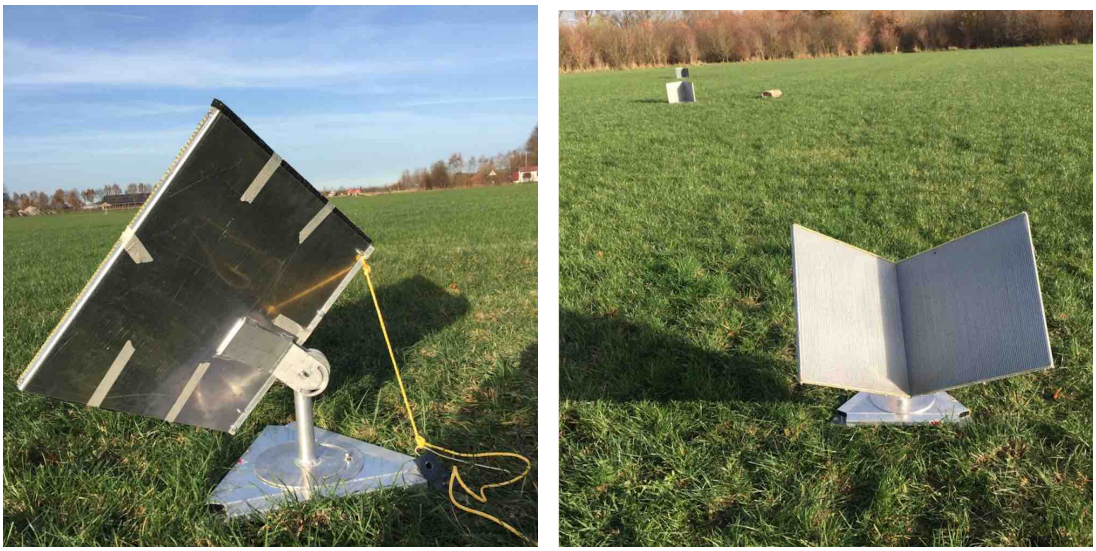

(a) *(b)*

Figure 3.34: *Elevation angle rotation for the gridded dihedral and gridded trihedral corner reflectors. (a) Using a rope to support the reflector, and (b) Front look of the gridded dihedral reflector.*

3.6 Summary

The chapter presented the selection, design, manufacture, and deployment of sixteen trihedral, and dihedral corner reflectors in the field used for the calibration of the XP-SAR airborne. The reflectors were a combination of classic trihedral, and dihedral corner reflectors, as well as gridded trihedral and gridded dihedral corner reflectors, with carefully surveyed and oriented positions for the test flights. In the following chapter, we present the calibration of three different fully polarimetric SAR sensors: L-, X-, and P-band in two parts. The first part is the calibration of an L-band SAR sensor using two square trihedral corner reflectors. The second part is the calibration of X- and P-band SAR sensors, using six corner reflectors (three trihedral, and three dihedral rotated by 45°) for X-band, and two trihedral corner reflectors for P-band.

Table 3.4: *The effect of spacing and grid width on maximum radar cross section with four different gap sizes and three different sizes of grids*

Gap	Grid	Orientation	RCS dBm^2	Discrimination
$\lambda/20$	0.5 mm	Parallel	20.4	40.6 dB
		Perpendicular	-20.2	
	1 mm	Parallel	20.4	32.2 dB
		Perpendicular	-11.8	
	1.5 mm	Parallel	20.4	26.1 dB
		Perpendicular	-5.6	
$\lambda/10$	0.5 mm	Parallel	20.1	40.9 dB
		Perpendicular	-20.8	
	1 mm	Parallel	20.2	35.3 dB
		Perpendicular	-15.1	
	1.5 mm	Parallel	20.3	29.2 dB
		Perpendicular	-8.9	
$\lambda/6$	0.5 mm	Parallel	19.1	39.9 dB
		Perpendicular	-20.8	
	1 mm	Parallel	19.5	36.3 dB
		Perpendicular	-16.8	
	1.5 mm	Parallel	19.6	31.6 dB
		Perpendicular	-12.1	
$\lambda/4$	0.5 mm	Parallel	17.2	34.5 dB
		Perpendicular	-17.7	
	1 mm	Parallel	18	34.5 dB
		Perpendicular	-17.3	
	1.5 mm	Parallel	18.5	32.8 dB
		Perpendicular	-14.3	

Table 3.7: *Angles rotation of the corner reflectors in elevation for all the reflectors in three different fields*

Fields	Triangular Trihedral	Square Trihedral	Dihedral
Near Field	+ 3.03°	+ 13.03°	+ 48.03°
Mid Field	- 15.19°	- 5.19°	+ 29.81°
Far Field	- 25.3°	- 15.3°	+ 19.70°

Chapter 4

Fully Polarimetric Image Calibration

This chapter aims at presenting the calibration of three different fully polarimetric SAR sensors. The first sensor is an L-band SAR sensor which is owned by Metasensing, and they allowed us to acquire the data using their two square trihedral corner reflectors in 2015, which were deployed inside Teuge airport, the Netherlands. The other two SAR sensors are X- and P-band SAR sensors, which are owned by KACST, and manufactured in partnership with droneSAR and Metasensing. Both of them are fully polarimetric and we acquired polarimetric data in 2016 using our corner reflectors, which were detailed in Chapter 3.

In the following, we first introduce the calibration of an L-band SAR sensor in Section 4.2, which includes the system installation on a Cessna 208 Grand Caravan, the deployment of the two square corner reflectors, crosstalk estimation and correction using two crosstalk methods, phase and channel imbalance, and finally the radiometric correction. Secondly, in Section 4.3.2 we present the calibration of X-band SAR sensor using three trihedral corner reflectors and three dihedral corner reflectors rotated by 45° to generate cross-polarisation components. The section includes crosstalk estimation and correction using the Ainsworth method, phase and channel imbalance, and radiometric correction. The section also includes a geometric calibration to relate each pixel in the image to

its geographic coordinates, as well as noise equivalent sigma zero measurements. Finally, we present the calibration of P-band SAR sensor in Section 4.3.5 using two triangular trihedral corner reflectors in the mid- and far-fields. The section includes crosstalk estimation and correction using the Ainsworth method, phase and channel imbalance, and radiometric correction as well as geometric calibration and noise equivalent sigma zero measurements. It is important to note that the pre-processing of the raw data to SLC were done using a software developed by Metasensing Company to generate the SLC images. The processing is not part of the thesis

4.1 Introduction

SAR polarimetric calibration has been the subject of intense investigations for the past several years and it remains one of the major obstacles of having accurate SAR data. Polarimetric calibration is an important pre-processing step for the correction of distortion interference, which is caused by system inaccuracies and atmospheric effects [71] [4]. The effects from atmospheric effects is one of the major topics in the polarimetric calibration field but it will not be focused on in our research because we are collecting our data using airborne SAR systems, not a spaceborne system, to have atmospheric effects. In general, when designing an antenna system, it is difficult, if not possible to have a perfect isolation between the orthogonal channels, and this is what causes the contamination of the measurements.

Synthetic aperture radar measures the complete scattering matrix for each radar resolution element in a scene [76]. The scattering matrix for a target is obtained by using a set of orthogonal polarisations to form a 2×2 scattering matrix in the fully polarimetric mode [109]. The accurate information of the scattering matrix of a target is an important factor towards obtaining biophysical information about the target. A fully polarimetric synthetic aperture radar measures the full scattering matrix for every resolution element in an image. The increase of information with respect to scalar radar comes at a price, not only for the

high cost of building the radar system and processing the data or increasing the complexity of the design, but also for the amount of effort needed to calibrate the data. Furthermore, calibration is particular, and specific to each system since each synthetic aperture radar system has its own calibration needs [110].

4.2 L-band SAR Sensor

The L-band is a fully polarimetric SAR system with a centre frequency of 1.3 GHz and a bandwidth of 200 MHz. The system was developed by Metasensing and we acquired polarimetric data using two square trihedral corner reflectors with 0.5 m inner leg dimensions. Table 4.1 shows the main parameters for the L-band SAR system.

Table 4.1: *L-band radar parameters.*

Parameters	L-band
Frequency	1.3 GHz
Bandwidth	200 MHz
Polarimetry	Quad Polarisation
Interferometry	Single pass
Slant range coverage	4 to 8 Km

4.2.1 System Installation

The L-band SAR sensor was installed on a Cessna 208 Grand Caravan to perform acquisitions. Fig. 4.1 shows the L-band system installation during airborne acquisitions over Teuge Airport on 21 October 2015. Two antennas were mounted on an aluminium frame with the transmitter on top and the receiver on the bottom. Each one of the transmitter and receiver antennas has two ports for horizontal and vertical channels and they are connected as follows:

- *Tx* - vertical and horizontal ports of the antennas, respectively on *Tx* out 1 and out 2 of the RF
- *Rx* - vertical and horizontal ports of the antennas, respectively on *Rx* in 1 and in 2 of the RF

Figure 4.1: *L-band system installation during airborne acquisitions over Teuge Airport on 21 October 2015.*

The values in Table 4.2 had been inserted before the acquisitions for the lever arm between the GPS antenna and IMU reference points.

Table 4.2: *Lever arm between GPS antenna and IMU reference points for L-band SAR system.*

Direction	IMU-GPS antenna
Δ X	0.60 m ± 0.02 m
Δ Y	4.23 m ± 0.02 m
Δ Z	1.10 m ± 0.02 m

The Z measurement had been performed, by considering as the Z-reference point

the top surface of the IMU, instead of the correct point, which is 7 cm lower. Therefore, a more accurate Z-measurement is $\Delta Z = 1.17$ m $\pm$ 0.02 m. Fig. 4.2 shows the distances between the IMU reference points and lower-right corner of each antenna (looking at them from behind).

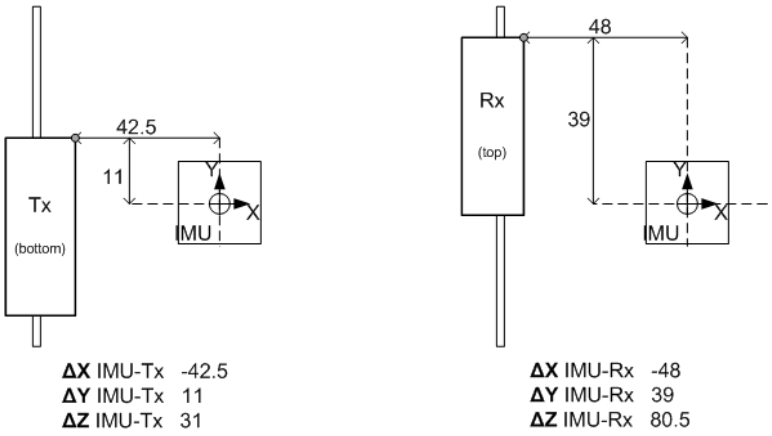

Figure 4.2: *Distances in [cm] in between the IMU reference points and the lower right corner of each antenna. The accuracy of these measurements can be considered to be around 2 cm.*

Table 4.3: *Estimated distances between the IMU reference centre and the antenna centre.*

Direction	*Tx* antenna	*Rx* antenna
Δ X	- 50.5 cm	- 60 cm
Δ Y	- 22.5 cm	5.5 cm
Δ Z	41 cm	94 cm

4.2.2 Corner Reflectors Deployment and SAR Acquisitions

Two square trihedral corner reflectors with 0.5 m inner leg dimensions, as shown in Fig. 4.3, have been paced in an area close to the airport runway, inside the

airport perimeter: Corner 1 (52°14'27.7"N, 6° 2'37.6"E), Corner 2 (52°14'23.9"N, 6° 2'37.3"E). Both of them are aligned to 176°, and tilted in elevation by an angle of 5°. The maximum radar cross section for the square trihedral corner reflector is 16.48 dBm^2.

(a) *(b)*

Figure 4.3: *Corners displacement inside Teuge Airport; they are separated by 130 m in range, and 25 m in azimuth.*

The SAR acquisitions were performed with a Cessna 208 Grand Caravan at 9000 ft (2,7 Km) altitude above the ground level. Main acquisition parameters include: The acquisition area is represented by agricultural lands in the surroundings of Teuge airport. SAR data were acquired on the acquisition track shown in Fig. 4.4, parallel to the airport runway, in which the corners should have been illuminated (track WE), and also on the way back (track EW), along a non-planned track.

Figure 4.4: *Acquisition track (left side looking SAR) parallel to the airport runway.*

4.2.3 Calibration of L-band SAR Sensor

The polarimetric L-band data were processed to level.1 SLC images at 1x1 meter pixel spacing in azimuth and ground range. Fig. 4.5 shows L-band SAR SLC images where; (a) horizontal-horizontal channel, (b) horizontal-vertical channel, (c) vertical-horizontal channel, and (d) vertical-vertical channel.

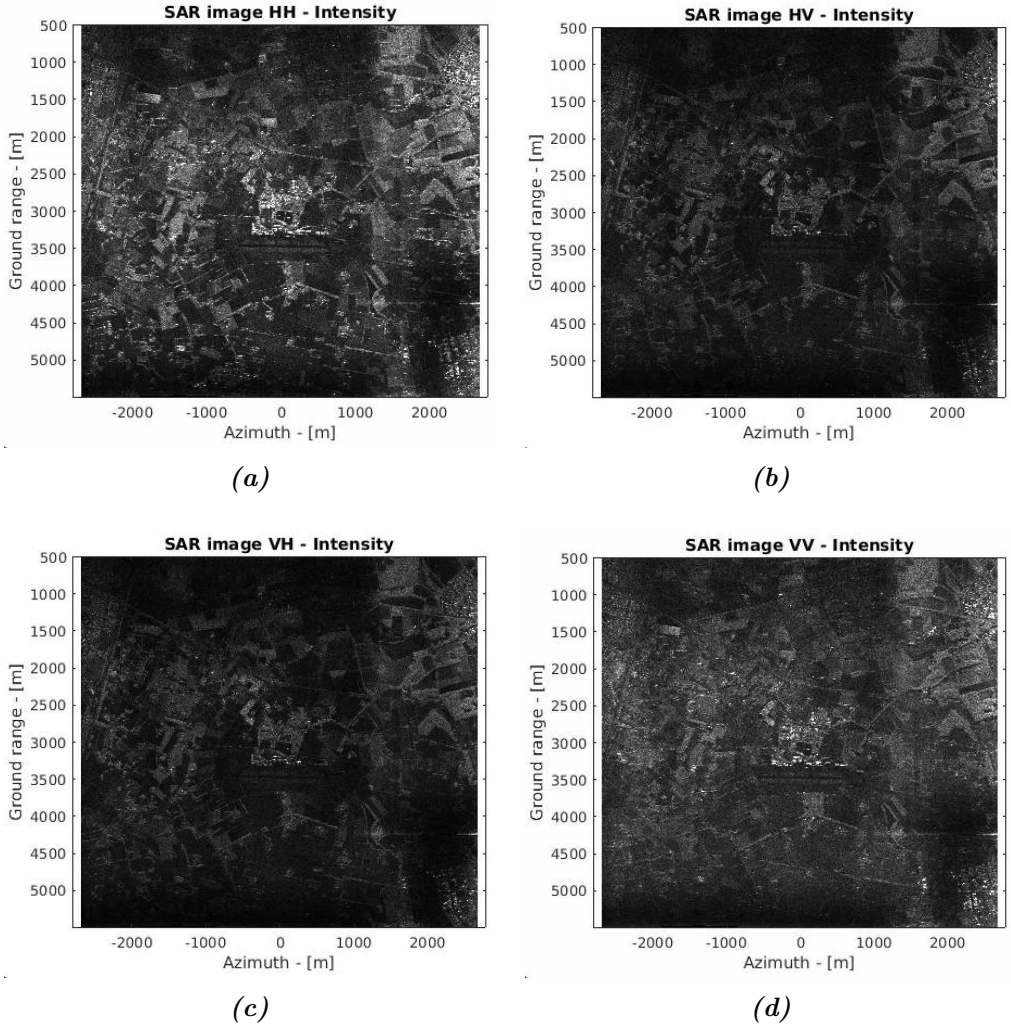

Figure 4.5: *L-band SAR SLC Images where; (a) Horizontal-Horizontal Channel, (b) Horizontal-Vertical Channel, (c) Vertical-Horizontal Channel, and (d) Vertical-Vertical Channel.*

4.2.3.1 Crosstalk Estimation and Correction

The Quegan and Ainsworth methods, introduced in Section 2.2.1, were evaluated in this section. The distortion models of both Quegan (in [60] [61]), and Ainsworth (in [66] [62]) were used for relating (vector O) which is the observed scattering matrix to (vector S) which is the ideal scattering matrix scattering matrix [70].

$$\begin{bmatrix} O_{hh} \\ O_{hv} \\ O_{vh} \\ O_{vv} \end{bmatrix} = Y \begin{bmatrix} 1 & w & v & vw \\ u & 1 & uv & v \\ z & wz & 1 & w \\ uz & z & u & 1 \end{bmatrix} \begin{bmatrix} ak^2 & 0 & 0 & 0 \\ 0 & ak & 0 & 0 \\ 0 & 0 & k & 0 \\ 0 & 0 & 0 & 1 \end{bmatrix} \begin{bmatrix} S_{hh} \\ S_{hv} \\ S_{vh} \\ S_{vv} \end{bmatrix} + \begin{bmatrix} N_{hh} \\ N_{hv} \\ N_{vh} \\ N_{vv} \end{bmatrix} \tag{4.1}$$

Where Y is the absolute gain calibration and it is a complex number, the four crosstalk parameters are (u,v,w,z) and they are assumed to be small compared to 1, the co- and cross-channels imbalance are k and α (assumed on the order of 1), and finally, N is the noise matrix. By assuming the data is calibrated for both radiometric, phase, and co-channel imbalance, we set Y = 1 and k = $1/\sqrt{\alpha}$. Then we rewrite the system model as follows:

$$\begin{bmatrix} O_{hh} \\ O_{hv} \\ O_{vh} \\ O_{vv} \end{bmatrix} = D \begin{bmatrix} S_{hh} \\ S_{hv} \\ S_{vh} \\ S_{vv} \end{bmatrix} + \begin{bmatrix} N_{hh} \\ N_{hv} \\ N_{vh} \\ N_{vv} \end{bmatrix} \tag{4.2}$$

where D is the distortion matrix and is represented as follows:

$$D = \begin{bmatrix} 1 & w/\sqrt{\alpha} & v/\sqrt{\alpha} & vw \\ u & \sqrt{\alpha} & uv/\sqrt{\alpha} & v \\ z & wz/\sqrt{\alpha} & 1/\sqrt{\alpha} & w \\ uz & z/\sqrt{\alpha} & u/\sqrt{\alpha} & 1 \end{bmatrix} \tag{4.3}$$

Finally, the system has the following solution:

$$\begin{bmatrix} S_{hh} \\ S_{hv} \\ S_{vh} \\ S_{vv} \end{bmatrix} = \sum \left[\begin{bmatrix} O_{hh} \\ O_{hv} \\ O_{vh} \\ O_{vv} \end{bmatrix} - \begin{bmatrix} N_{hh} \\ N_{hv} \\ N_{vh} \\ N_{vv} \end{bmatrix} \right] \tag{4.4}$$

where $\sum$ is the calibration matrix and is presented as follows:

$$\sum = \begin{bmatrix} 1 & -w & -v & vw \\ -u/\sqrt{\alpha} & 1/\sqrt{\alpha} & uv/\sqrt{\alpha} & -v/\sqrt{\alpha} \\ -z/\sqrt{\alpha} & wz/\sqrt{\alpha} & \sqrt{\alpha} & -w\sqrt{\alpha} \\ uz & -z & -u & 1 \end{bmatrix} \frac{1}{(uw-1)(vz-1))} \tag{4.5}$$

4.2.3.2 Crosstalk Estimation and Correction using Quegan method

The crosstalk parameters for the Quegan method, which we described in Section 2.2.1.3 and detailed in [61], were estimated as follows:

$$\begin{aligned} u &= (C_{44}C_{21} - C_{41}C_{24})/\Delta & v &= (C_{11}C_{24} - C_{21}C_{14})/\Delta \\ z &= (C_{44}C_{31} - C_{41}C_{34})/\Delta & w &= (C_{11}C_{34} - C_{31}C_{14})/\Delta \end{aligned} \tag{4.6}$$

Where Δ is calculated from the covariance matrix by $C_{11}C_{44} - \mid C_{14} \mid$. Furthermore, the channel imbalance α is estimated as follows:

$$\alpha = \frac{\mid \alpha_1\alpha_2 \mid -1 + \sqrt{(} \mid \alpha_1\alpha_2 \mid -1 + 4 + \mid \alpha_2 \mid^2}{2 \mid \alpha_2 \mid} \frac{\alpha_1}{\mid \alpha_1 \mid} \tag{4.7}$$

$$\begin{aligned} \alpha_1 &= \frac{C_{22} - uC_{12} - vC_{42}}{X} \\ \alpha_2 &= \frac{X^*}{C_{33} - z^*C_{31} - w^*C_{34}} \\ X &= C_{32} - zC_{12} - wC_{42} \end{aligned} \tag{4.8}$$

The estimation of crosstalk parameters are presented in Fig. 4.6, using the Quegan method as a function of ground range and averaged in azimuth for L-band airborne data, which were collected on 21 October 2015 around Teuge Airport, the Netherlands. The initial crosstalk parameters are plotted in red and the residual crosstalk in black after correction. The results showed that the crosstalk parameters are all around -17 dB to -21 dB before calibration, while there is a little improvement in the range of 3 dB after calibration.

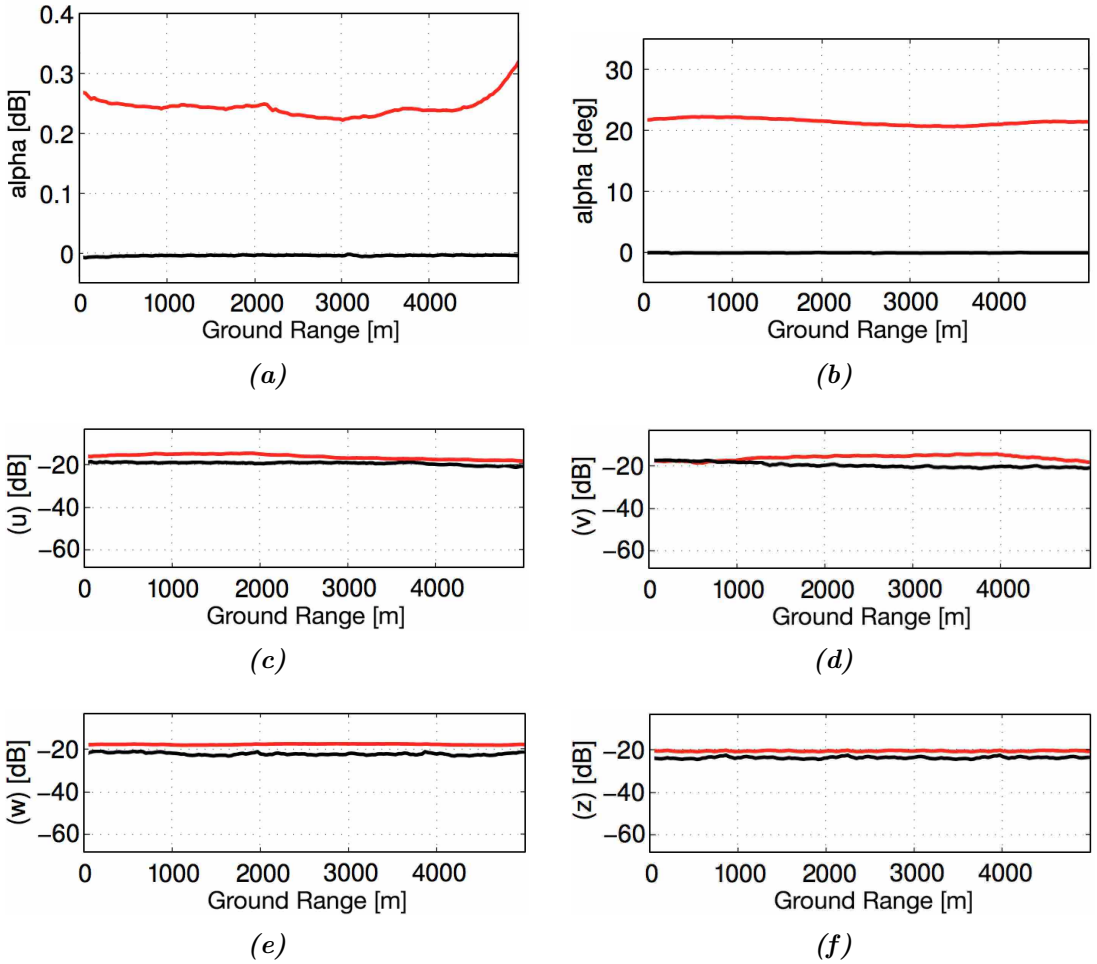

Figure 4.6: *Estimation and correction of crosstalk parameters using the Quegan method for L-band airborne data, which were collected on 21 October 2015 around Teuge Airport, the Netherlands. The initial crosstalk parameters are plotted in red, and the residual crosstalk in black after calibration.*

4.2.3.3 Crosstalk Estimation and Correction using Ainsworth method

The crosstalk parameters for the Ainsworth method, which we described in Section 2.2.1.4 and detailed in [66] [62], were estimated by the solution to the complex linear system of equations:

$$\begin{bmatrix} 0 & C_{hvhv} & C_{vvhh}+C_{hvvh} & C_{hhhh} \\ C_{hhhh} & C_{vvhh}+C_{vhhv} & C_{vhvh} & 0 \\ C_{hvhv} & 0 & C_{vvvv} & C_{hhvv}+C_{hvvh} \\ C_{hhvv}+C_{vhhv} & C_{vvvv} & 0 & C_{vhvh} \end{bmatrix} \begin{bmatrix} u \\ v \\ w \\ z \end{bmatrix} = \begin{bmatrix} C_{hvhh}-A \\ C_{vhhh}-A \\ C_{hvvv}-B \\ C_{vhvv}-B \end{bmatrix} \tag{4.9}$$

Where

$$\begin{aligned} A &= 0.5(C_{hvhh}+C_{vhhh}) \\ B &= 0.5(C_{hvvv}+C_{vhvv}) \\ \alpha &= \frac{C_{vhhv}}{\mid C_{vhhv} \mid}\sqrt{\frac{C_{vhvh}}{\mid C_{hvhv} \mid}} \end{aligned} \tag{4.10}$$

An iterative method used to the crosstalk parameters from the covariance matrix. The estimation of crosstalk parameters are presented in Fig. 4.7 using the Ainsworth method as a function of ground range. The results show that the crosstalk parameters before calibration are around -20 dB, while it is around -40 dB after calibration. By comparing the results from the Ainsworth method to the results of the Quegan method, we can see a much better crosstalk removal in the Ainsworth method. The reason might be that the Quegan method is a direct method while the Ainsworth method is an iterative method.

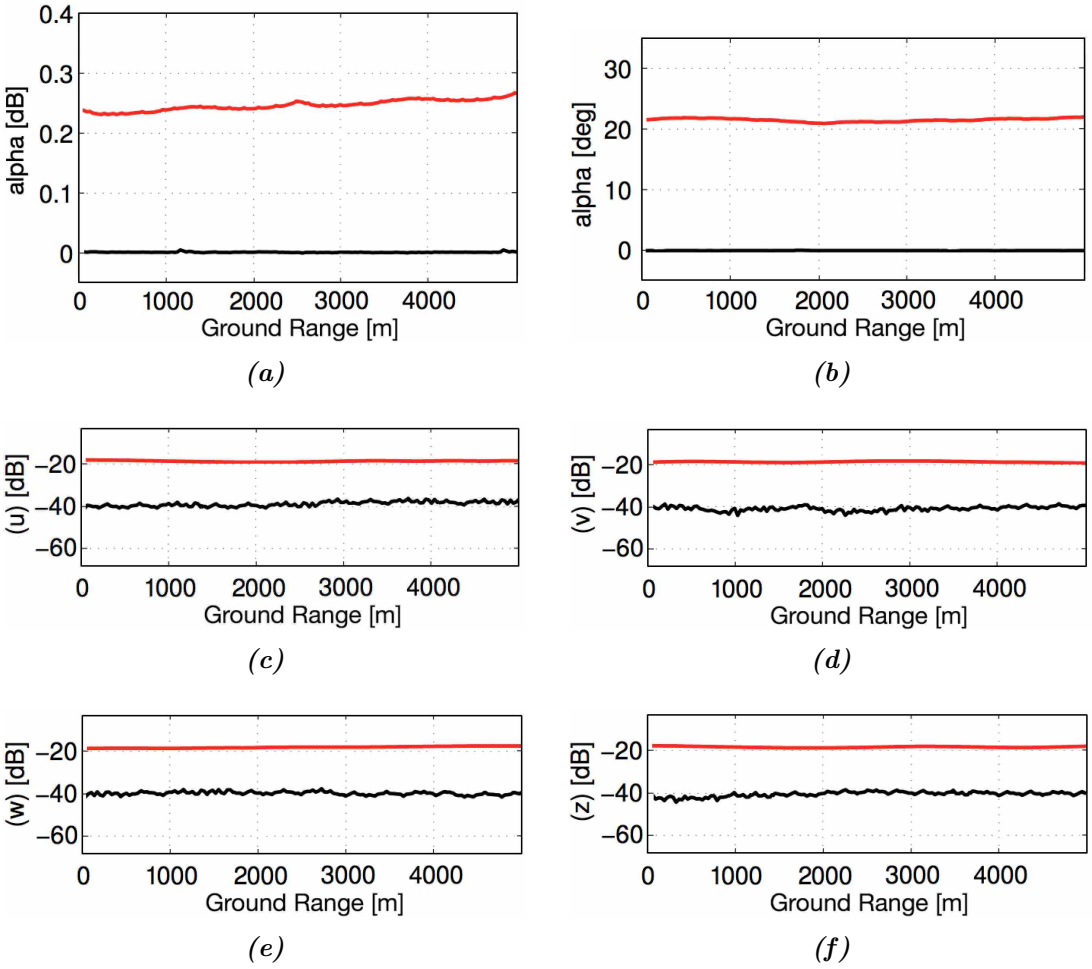

Figure 4.7: *Estimation and correction of crosstalk parameters using the Ainsworth method for L-band airborne data which were collected on 21 October 2015 around Teuge Airport, the Netherlands. The initial crosstalk parameters are plotted in red, and the residual crosstalk in black after calibration.*

4.2.3.4 Polarimetric Phase and Co-Channel Imbalance

The maximum responses from the two square trihedral corner reflectors were used to estimate phase and co-channel imbalance for calibrating the data. We used IDL to read the SLC SAR data and then exported each channel HH, HV, VH, and VV to ENVI for locating and extracting the maximum response from the two square trihedral corner reflectors. Fig. 4.8 shows the use of ENVI to locate

the first corner reflector where; (a) horizontal-horizontal channel, (b) horizontal-vertical channel, (c) vertical-horizontal channel, and (d) vertical-vertical channel. Additionally, Fig. 4.9 shows the use of ENVI to locate the second corner reflector, which is close to the runway for the four polarimetric channels. The horizontal profile represents the ground range in the image while the vertical profile represents the azimuth.

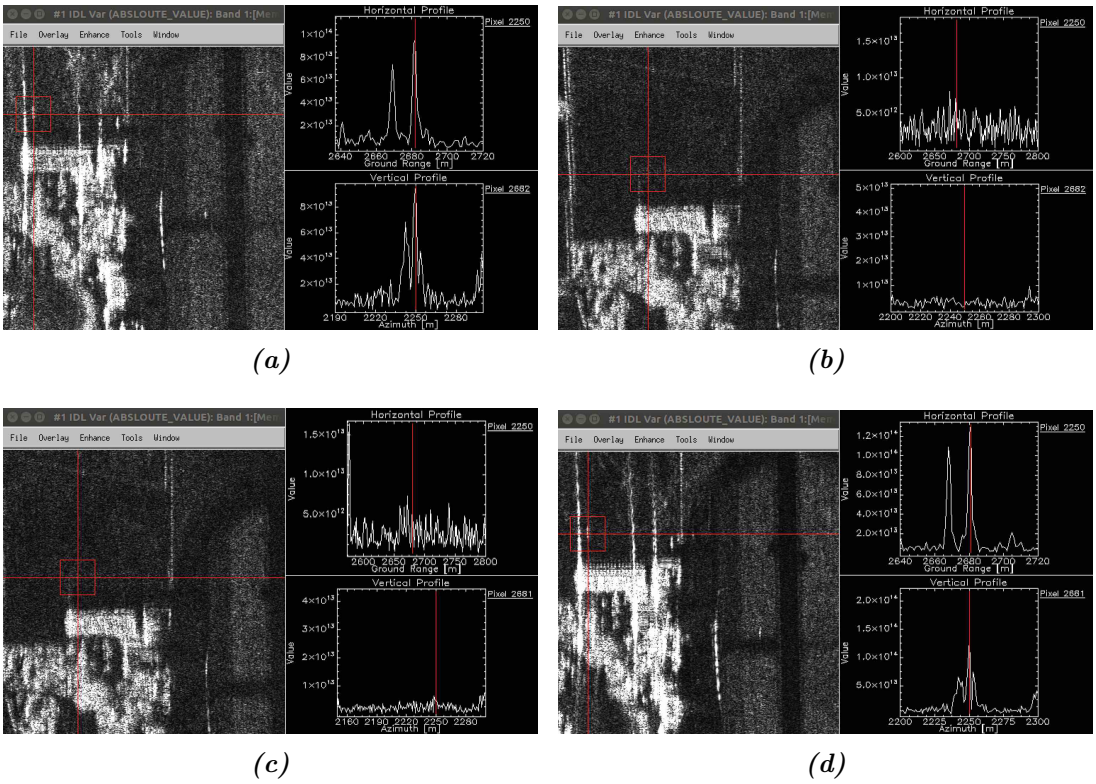

Figure 4.8: *Reading SAR data using IDL and locating first corner reflector where; (a) Horizontal-Horizontal Channel, (b) Horizontal-Vertical Channel, (c) Vertical-Horizontal Channel, and (d) Vertical-Vertical Channel.*

The extracted maximum response on the first corner reflector for HH channel was located at 2250 m in azimuth and 2682 m in ground range, while the extracted maximum response on the first corner reflector for VV channel was located at 2250 m in azimuth and 2681 m in ground range. Moreover, the extracted maximum response on the second corner reflector for HH channel was located at

2264 m in azimuth and 2800 m in ground range, while the extracted maximum response on the first corner reflector for VV channel was located at 2264 m in azimuth and 2799 m in ground range. The registration between the images shows one pixel off in the range.

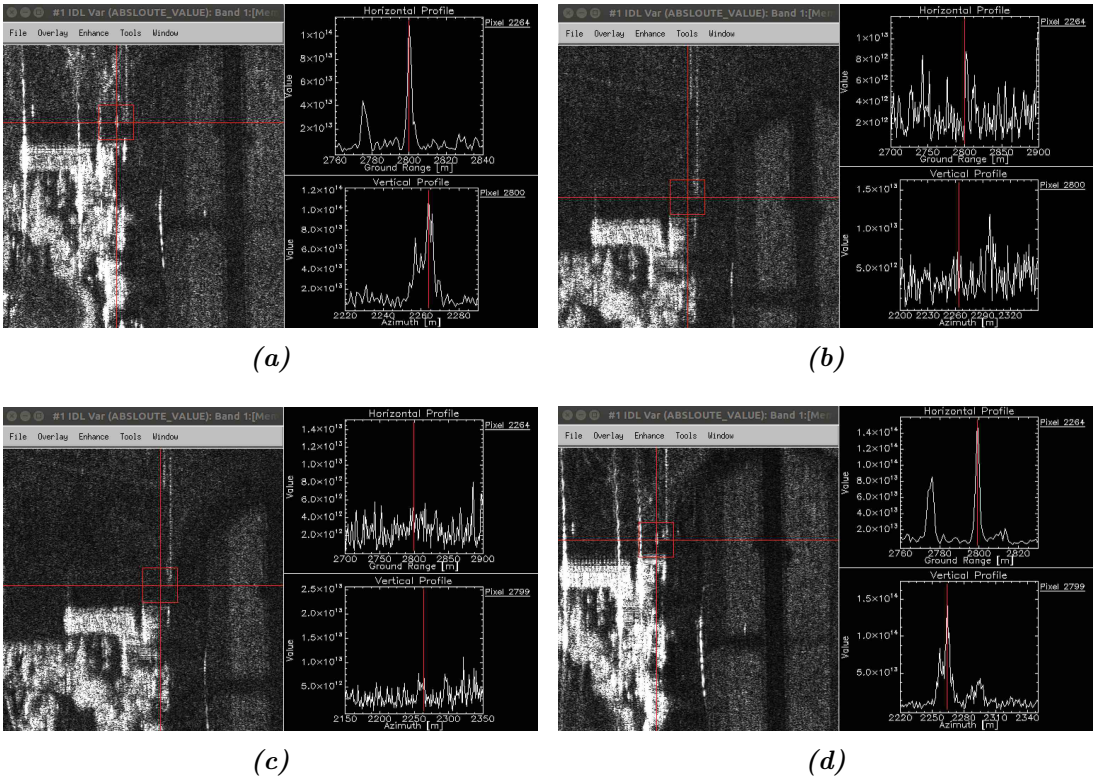

Figure 4.9: *Reading SAR data using IDL, and locating the second corner reflector close to the runway where; (a) Horizontal-Horizontal Channel, (b) Horizontal-Vertical Channel, (c) Vertical-Horizontal Channel, and (d) Vertical-Vertical Channel.*

Co- and cross-polarisation signatures are plotted in Fig. 4.10 and Fig. 4.11 for the two square trihedral corner reflectors before any calibration is applied to the data. The two signatures for the two corner reflectors are not similar and they are distorted by an amount of phase and amplitude which results in a change in the signature.

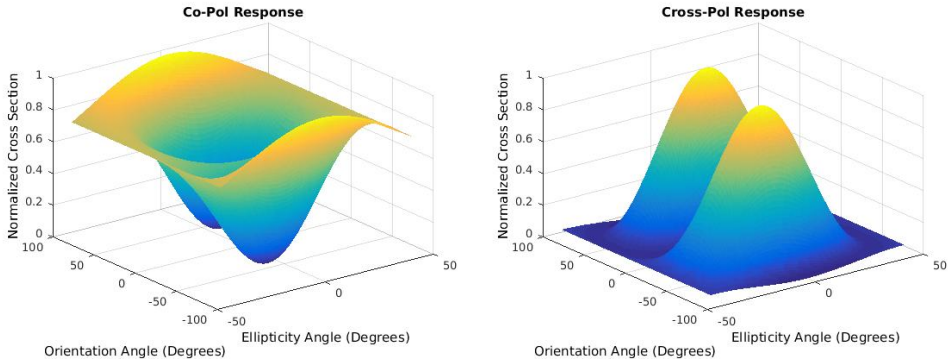

(a) *(b)*

Figure 4.10: *Polarisation signature for L-band dataset, before calibration is applied, for the first corner reflector where; (a) The co-polarisation signature, while (b) The cross-polarisation signature.(See Appendix A.1)*

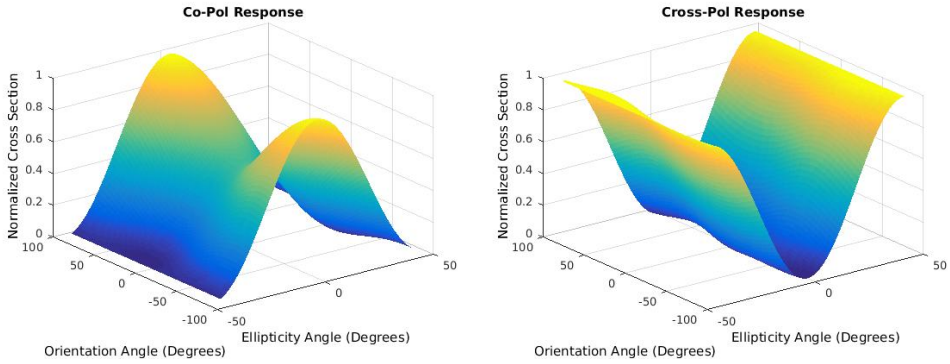

(a) *(b)*

Figure 4.11: *Polarisation signature for L-band data set, before calibration applied, for the second corner reflector close to the runway where; (a) The co-polarisation signature while (b) The cross-polarisation signature.(See Appendix A.2)*

The phase difference between the co-polarisation channels HH - VV for the two square trihedral corner reflectors was corrected using the Zebker method, which we presented in Section 2.2.2.2. The aim of the method is to use the trihedral corner reflectors, where the theoretical phase difference between the co-polarisation channels is zero, to estimate the phase bias between co-polarisation channels HH

- VV by $S'_{vv}S'^{*}_{hh}$. As shown in Fig. 4.12(a), the estimated co-polarisation phase difference HH - VV in red and the corrected phase difference HH - VV in black for the two square trihedral corner reflectors. The first square trihedral corner reflector has a phase bias of 27.9° while the second square trihedral corner reflector, which is close to the run way, has a phase bias of 18.63° before phase rotation. After rotating the phase based on the first corner reflector, the phase difference between the co-polarisation channels HH - VV for the first corner reflector became 6.09°, while it is 0° phase bias for the second corner reflector.

Moreover, the co-channel imbalance (f) was derived using Eq. 4.11 and presented in Fig. 4.12(b). The co-channel imbalance for the two trihedral corner reflectors is 1.17 before correction. The HH channel was used to adjust the channels for the two corner reflectors to be 1 after correction.

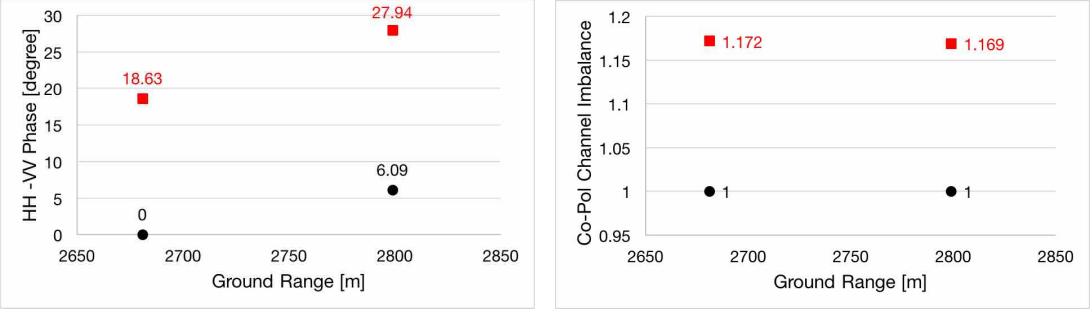

(a) ***(b)***

Figure 4.12: *Co-polarisation phase difference and channel imbalance plotted as a function of ground range before and after calibration. (a) Co-polarisation phase difference correction of two corner reflectors, the red is before calibration, while the black is after calibration, and (b) Co-polarisation channel imbalance before and after calibration.*

$$f_{VV-HH} = \left[S'_{vv}S'^{*}_{vv}/(S'_{hh}S'^{*}_{hh})\right]^{0.25} \tag{4.11}$$

Furthermore, in the cross-polarisation channels, we estimated the cross-polarisation channel imbalance (g) using Eq. 4.12 which computes the average return from the cross-polarisation channels over the image. Also, the phase bias between cross-

polarisation channels HV - VH were estimated using the reciprocity assumption $S_{hv} = S_{vh}$ as $\phi_t - \phi_r = arg(< S'_{hv} S'^{*}_{vh} >)$ and averaged over the image.

$$g = \left[<| S'_{hv} |^2> / <| (S'_{vh} |^2>) \right]^{0.25} \tag{4.12}$$

Finally, the co- and cross-polarisation signatures for the two square trihedral corner reflectors are presented in Fig. 4.13 for the first corner reflector and Fig. 4.14 for the second corner reflector, which is close to the runway. The co- and cross-polarisation signatures for the second corner reflector, which is close to the runway in Fig. 4.13, is exactly the same as the theoretical signature of trihedral corner reflector due to the zero phase bias between co-polarisation channels HH - VV, as well as 1 co-channel imbalance. Moreover, the polarisation signature for the first corner reflector in Fig. 4.14 is distorted by a phase bias of 6° between co-polarisation channels HH - VV but it has a 1 channel imbalance.

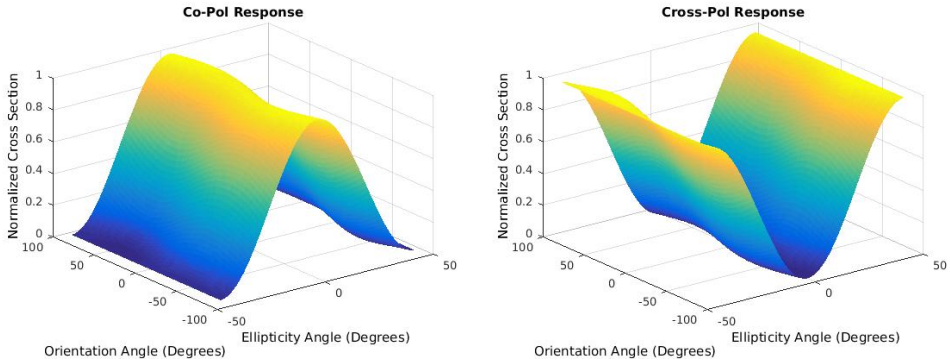

(a) ***(b)***

Figure 4.13: *Polarisation signature for L-band dataset, after calibration is applied, for the first corner reflector where; (a) The co-polarisation signature, while (b) The cross-polarisation signature.(See Appendix A.3)*

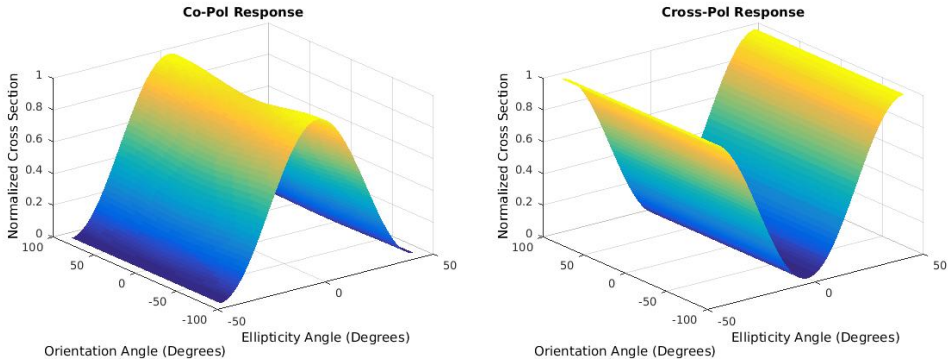

(a) *(b)*

Figure 4.14: *Polarisation signature for L-band dataset, after calibration applied, for the second corner reflector close to the runway where; (a) The co-polarisation signature, while (b) The cross-polarisation signature.(See Appendix A.4)*

4.2.3.5 Radiometric Calibration

The last step in the calibration process is the radiometric calibration of synthetic aperture radar. Since the peak response of the point target strongly depends on the processor focus and resolution, while the integral response from a passive point target is weakly dependent on these parameters. We used the integral method for relating the pixel's values to the backscattering coefficient [87] [88].

As shown in Eq. 4.13, the derivation of the integral method is based on the reflected power from the corner reflector and computed by summing up the power of all the pixels in an area that may include the power from the corner reflector, and then subtracting it from the background clutter by summing all the pixels around the corner reflector and then multiplying the results by the pixel spacing in both range and azimuth [89]. Fig. 4.15(a) is a smaller window in ENVI showing the response from the corner reflector, and (b) is a sketch map of the integral method where the red regions are the response from the corner reflector and the green regions are the background area.

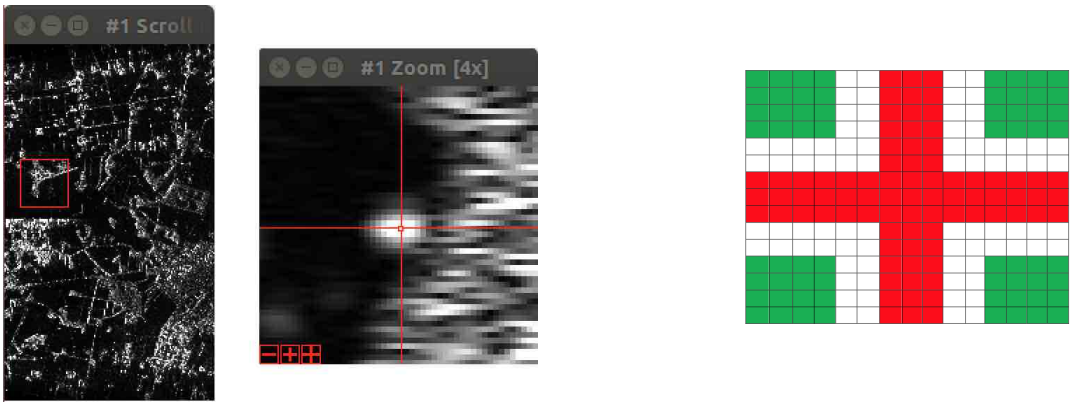

Figure 4.15: *Definition of the integral method. (a) A smaller window in ENVI, showing the response from the corner reflector, and (b) A sketch map of the integral method, where the red regions are the response from the corner reflector, and the green regions are the background area.*

$$\varepsilon_p = (\sum_{i \in A}^{N_A} DN^2 - \frac{N_A}{N_B} \sum_{i \in B}^{N_B} DN^2) \delta_a \delta_b \tag{4.13}$$

Where DN is the digital number representing the power of the pixel, N_A is the number of selected pixels associated with the corner response, N_B is the number of selected pixels associated with the background, and δ_a δ_b are the pixel spacings when we processed the data. Moreover, the calibration constant computed by Eq. 4.14 using the corner reflector energy (ε_p), the incidence angle (θ_i) which we recalculated in Fig. 4.16 based on subtracting the flight altitude of 2750 m with 47 m DEM, and the theoretical RCS of the corner reflector (σ_{ref}) as follows:

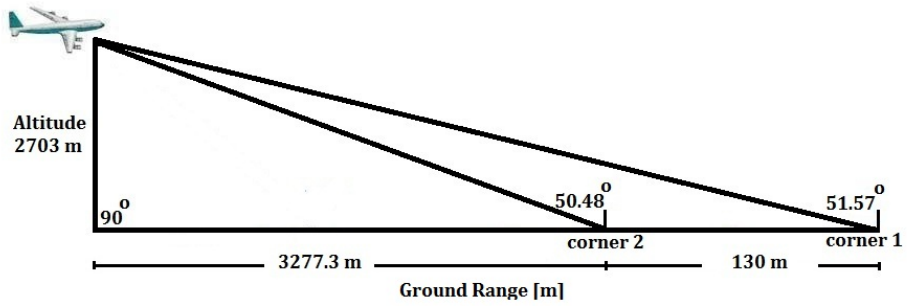

Figure 4.16: *Recalculated two incidence angles for mid- and far-range flying at 703 m altitude perpendicular to the runway.*

$$K = \frac{\varepsilon_p}{\sigma_{ref}\ sin\theta_i} \tag{4.14}$$

Finally, the backscattering coefficient calculation detailed in Table 4.4 and plotted in Fig. 4.17 for the two square trihedral corner reflectors were calculated by using Eq. 4.15, before correction in red and after correction in black. The results show a reduction of about 2.8 dB in the backscattering coefficient of the two square trihedral corner reflectors. We increased the power over the four polarimetric channels by 2.8 dB to relate the energy associated with the point target to it is theoretical RCS.

$$\sigma_o = \frac{DN^2}{K}\ sin\theta_i \tag{4.15}$$

Table 4.4: *Integral method parameters calculation for L-band radiometric calibration.*

CR	CR Energy ε_p	Calibration Constant K	θ_i	σ_o
CR1	2.24103e28	7.01e26	50.48	22.9011
CR2	1.70030e28	5.27e26	51.57	23.370

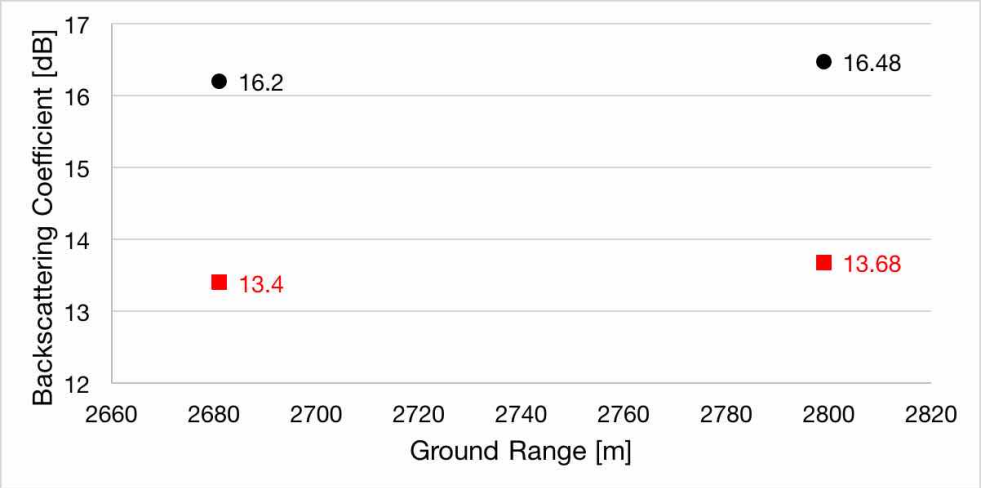

Figure 4.17: *Backscattering coefficient for the two square trihedral corner reflectors before correction in red and after in black.*

4.3 X- and P-band SAR Sensors

Two dual polarimetric microstrip patch antennas were used for the X-band as shown in Fig. 4.18(a), connectors are present in the back side of the antenna, one for each linear polarisation, H and V. A FMCW modulation technique was used at X-band. On the other hand, a pulsed approach is used at P-band, for minimise the encumbrance of the system. Given the larger dimension of the antenna, a Yagi array antenna composed of two elements is used for each polarisation, as shown in Fig. 4.18(b).

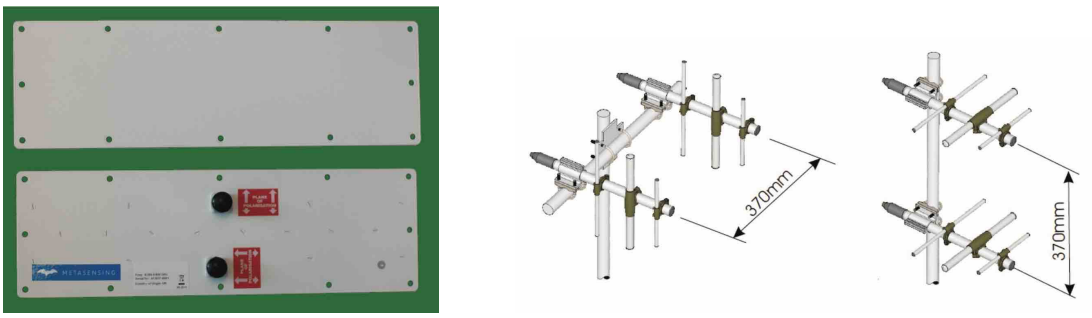

(a) *(b)*

Figure 4.18: *(a) X-band antenna based on microstrip patch technology (Front and back views respectively on the top and on the bottom) and (b) P-band are Yagi array antennas, in which the elements are spaced 370 mm from each other. Vertical and Horizontal polarisations are shown on the left and on the right of the figure, respectively.*

4.3.1 System Installation and SAR Acquisitions

The aircraft platform used for the tests is a Cessna 208. As shown in Fig. 4.19: XP-SAR system installation during airborne acquisitions over Teuge Airport. The wide cargo door on one side of the aircraft allows for SAR operations with the antennas mounted inside the fuselage of the aircraft. A distinct enclosure is used for each of the two frequency bands. On top of each sensor a navigation unit is installed, i.e. an integrated GPS-IMU device. On one side of the enclosure some fan-furnished heat dissipaters are placed to keep the internal circuitry at

the correct temperature. The two sensors X and P were installed inside the fuselage of the Cessna 208 by exploiting the seat rails available on the floor. The antennas were installed on an adjustable aluminium frame, which is fastened to the cabin floor of the aircraft by means of the seat rails.

Figure 4.19: *XP-SAR system installation during airborne acquisitions over Teuge Airport.*

A unique GPS antenna is used for the two navigation systems, the signal being split in two by means of a RF signal divider. The GPS antenna is permanently installed on the roof of the aircraft on the rear part. The lever arm between the reference points of each IMU and GPS antenna is summarised in Table 4.5, for each frequency band. The adopted reference system is shown in Fig. 4.20.

Table 4.5: *Lever arm between the IMU antenna and GPS antenna for XP-SAR system.*

Direction	X-Band	P-Band
Δ X	-0.21 m ± 0.02 m	-0.23 m ± 0.02 m
Δ Y	-1.72 m ± 0.02 m	-1.14 m ± 0.02 m
Δ Z	1.05 m ± 0.02 m	1.05 m ± 0.02 m

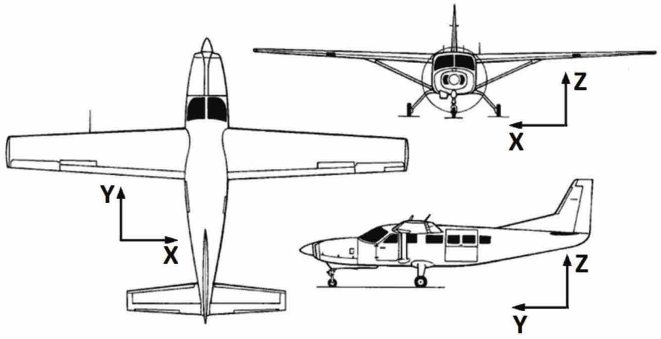

Figure 4.20: *Reference system of the XP-SAR navigation systems during airborne acquisitions over Teuge Airport.*

Starting and stopping way-points were designed so that the acquisition trajectory would be perpendicular to the airport track:

Starting point: $A1 \quad 52°15'57"N \quad 06°01'41"E$
Ending point: $B1 \quad 52°13'01"N \quad 06°02'03"E$

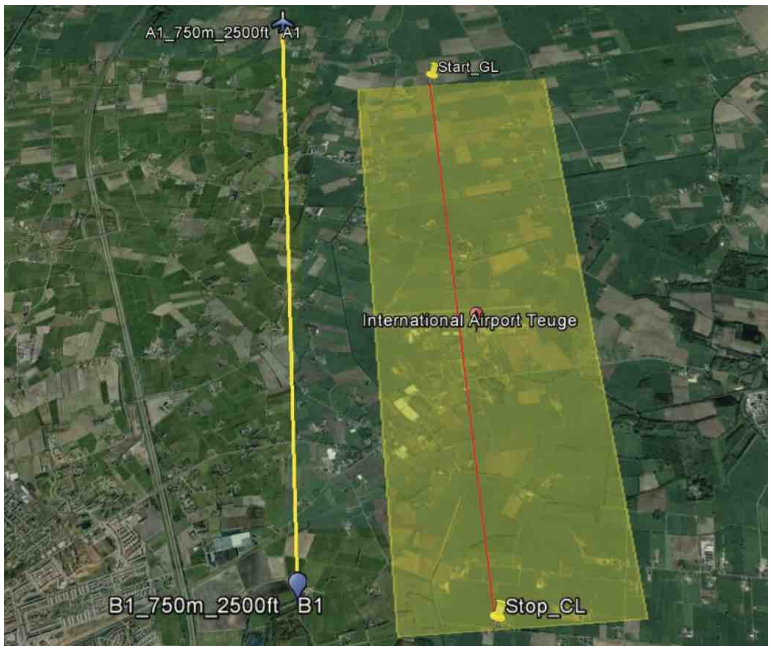

Figure 4.21: *Designed acquisition way-points, and expected ground swath extension (yellow area).*

4.3.2 Calibration of X-band SAR Sensor

The polarimetric X-band raw data were processed to level.1 SLC images generated with a presuming factor of 8 and a Doppler centroid of 1039 Hz. Data were acquired in fully polarimetric mode, flying at 750 m above the ground and transmitting at 500 MHz bandwidth. Fig. 4.22 shows X-band SAR SLC Images where; (a) horizontal-horizontal channel, (b) horizontal-vertical channel, (c) vertical-horizontal channel, and (d) vertical-vertical channel.

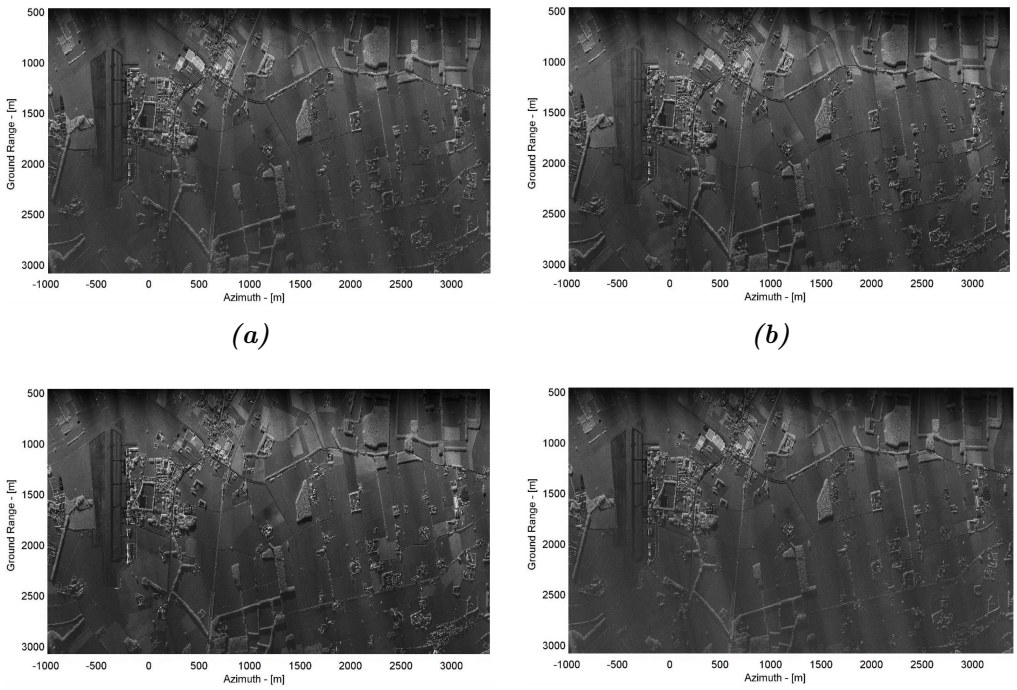

Figure 4.22: *X-band SAR SLC images where; (a) Horizontal-Horizontal Channel, (b) Horizontal-Vertical Channel, (c) Vertical-Horizontal Channel, and (d) Vertical-Vertical Channel.*

4.3.2.1 Crosstalk Estimation and Correction

The crosstalk estimation and corrections were done by using the Ainsworth method, which we detailed in Section 4.2.3.3 and detailed in [66] [62] [70]. Es-

timation and correction of crosstalk parameters are presented in Fig. 4.23 as a function of ground range averaged in azimuth using the Ainsworth method for X-band airborne data which were collected on 30 November 2016 around Teuge Airport, the Netherlands. The initial crosstalk parameters are plotted in red and the residual crosstalk in black after calibration. The crosstalk for all the parameters before calibration are around -23 dB and they are around -43 dB after calibration.

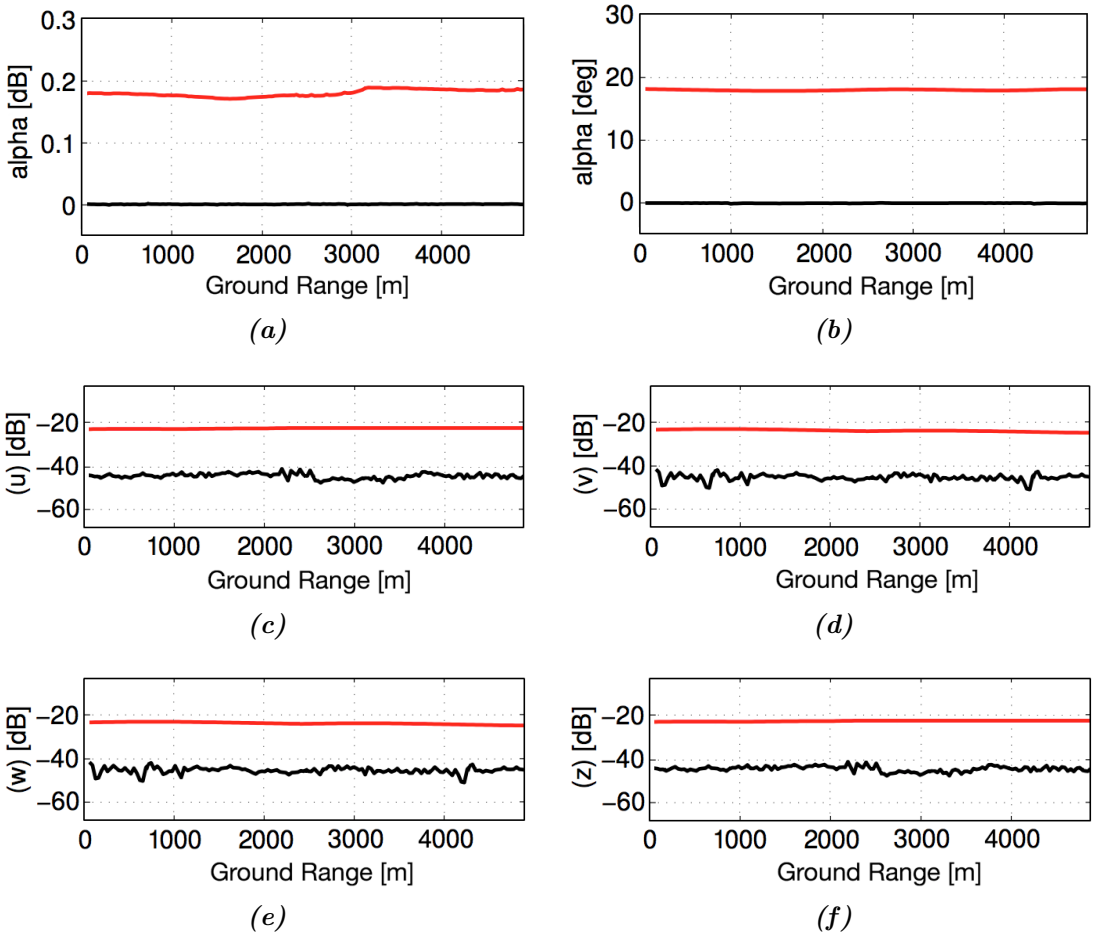

Figure 4.23: *Estimation and correction of crosstalk parameters as a function of ground range averaged in azimuth using the Ainsworth method for X-band airborne data which were collected on 30 November 2016 around Teuge Airport, the Netherlands. The initial crosstalk parameters are plotted in red and the residual crosstalk in black after calibration.*

4.3.2.2 Polarimetric Phase and Channel Imbalance

Six corner reflectors were used for phase and channel imbalance for both co- and cross-channels. The first three square trihedral corner reflectors in the near, mid, and far ranges were used for the calibration of co-phase and co-channel imbalance while the other three dihedral corner reflectors rotated by 45° were used for the calibration of cross-phase and cross-channel imbalance.

4.3.2.2.1 Co-Phase and Co-Channel Imbalance The maximum response from each trihedral corner reflectors in near, mid, and far field was obtained by exporting the SLC images from IDL to ENVI to extract the scattering matrix for each reflector. Figs. 4.24 and 4.25 show the maximum response for each reflector from both HH channel and VV channel.

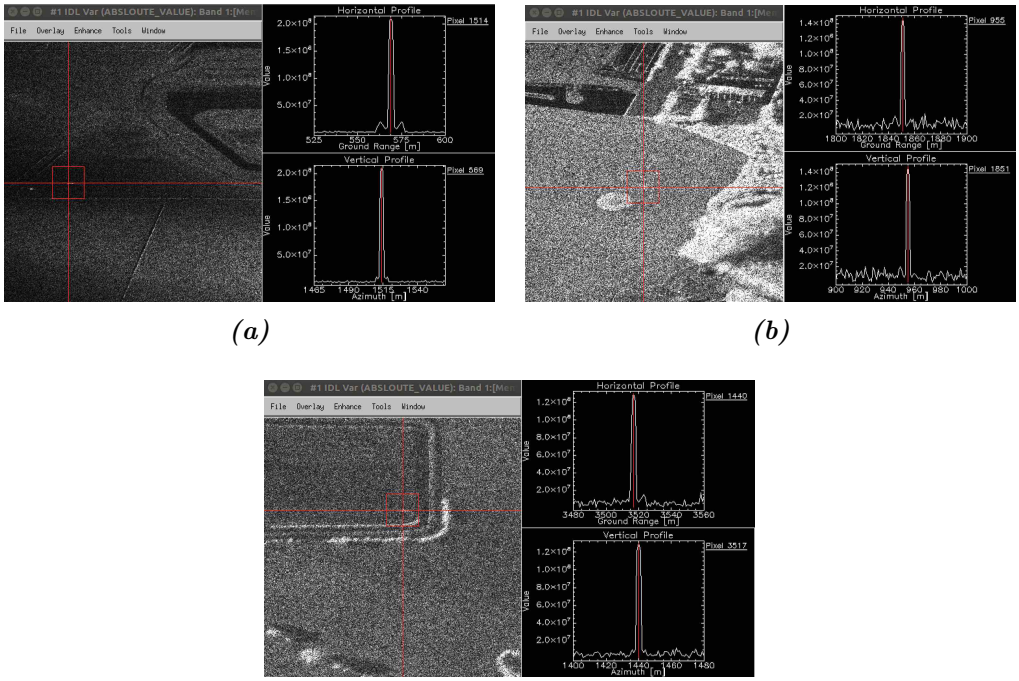

(a) *(b)*

(c)

Figure 4.24: *Extracting the maximum response from HH Channel using ENVI where; (a) Near field reflector, (b) Mid field reflector, and (c) Far field reflector.*

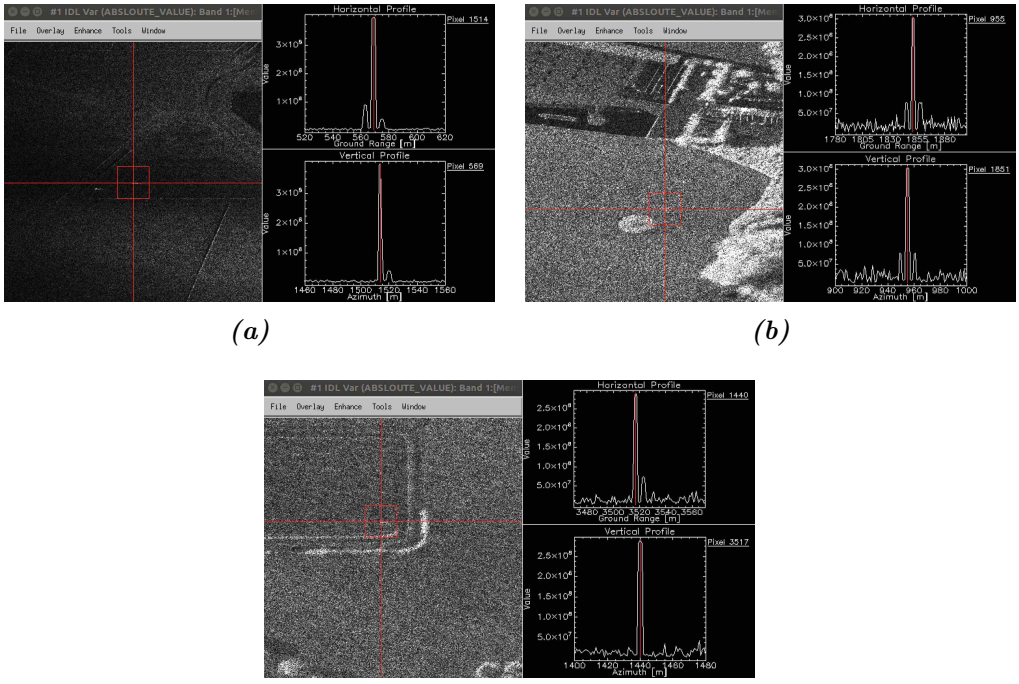

Figure 4.25: *Exacting the maximum response from VV channel using ENVI where; (a) Near field reflector, (b) Mid field reflector, and (c) Far field reflector.*

After extracting the maximum response from both HH and VV channels using ENVI, the images have an excellent registration between them over the three fields. The maximum response for the near reflector was at pixel 1514 in a horizontal profile and pixel 569 in a vertical profile. For the mid field, the maximum response was at pixel 955 in a horizontal profile and pixel 1851 in a vertical profile. Finally, the maximum response for the far reflector was at pixel 1440 in a horizontal profile and pixel 3517 in a vertical profile.

Co- and cross-polarisation signatures are plotted in Fig. 4.26 for the trihedral corner reflector in the near field and Fig. 4.27 for the trihedral corner reflector in the mid field, and finally Fig. 4.28 for the trihedral corner reflector in the far field. The polarisation signatures for the two trihedral corner reflectors in the mid and far fields are similar, while the polarisation signature for the trihedral corner reflector in the near field is different due to more phase bias and channel

imbalance.

It is important to note that When we calibrate the X-band date using the three corner reflectors in each field for both co- and cross-channels, we used the corner reflector in the mid field as the main reflector for rotating the phase and adjusting the channel imbalance and that is why the near and far field reflectors signatures appear to have become distorted after the calibration while the mid reflector showing a perfect signature. But if we see the amount of distortion is very small 1.2° for the near field and 0.5° for the far field after calibration comparing to 63.7° in the near field and 62° in the far field before calibration.

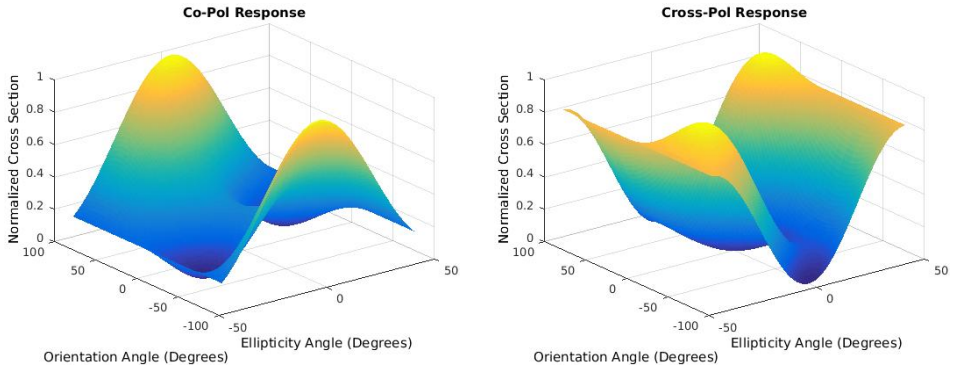

(a) *(b)*

Figure 4.26: *Polarisation signature for co-channels of X-band, before calibration is applied, for the near field corner reflector where; (a) The co-polarisation signature, while (b) The cross-polarisation signature.(See Appendix A.5)*

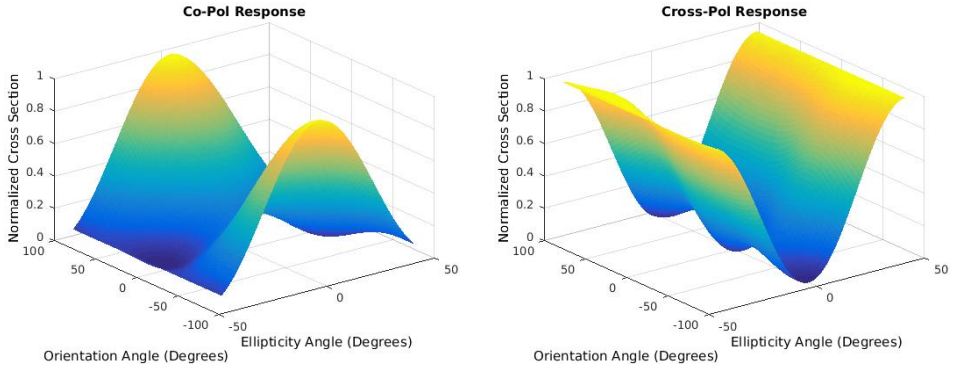

(a) *(b)*

Figure 4.27: *Polarisation signature for co-channels of X-band, before calibration is applied, for the mid field corner reflector where; (a) The co-polarisation signature, while (b) The cross-polarisation signature.(See Appendix A.6)*

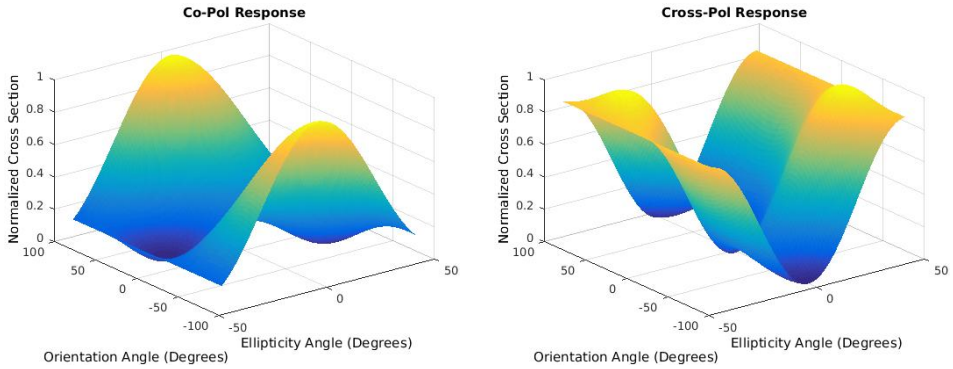

(a) *(b)*

Figure 4.28: *Polarisation signature for co-channels of X-band, before calibration is applied, for the far field corner reflector where; (a) The co-polarisation signature, while (b) The cross-polarisation signature.(See Appendix A.7)*

The phase difference between the co-polarisation channels HH - VV for the three trihedral corner reflectors was corrected using the Zebker et al. method which we presented in Section 2.2.2.2. As shown in Fig. 4.29(a), the co-polarisation phase bias HH - VV is estimated by $S'_{vv}S'^{*}_{hh}$ and shown in red before correction and the corrected phase difference HH - VV in black for the three trihedral corner reflectors as a function of incidence angle. The measured phase bias of

the HH channels signal relative to the VV channels signal for the near field corner reflector is about 1° higher than the other two trihedral corner reflectors in the mid and far fields.

Furthermore, the co-channel imbalance (f) was derived using Eq. 4.11 and presented in Fig. 4.29(b), the co-channel imbalance for the three trihedral corner reflectors are 1.4, 1.44, and 1.49 before correction, meaning an increase of 0.04 from the corner reflector in the near to the far field. We used the trihedral corner reflector in the mid range to be the main reference point while rotating the phase as well as adjusting the channel imbalance.

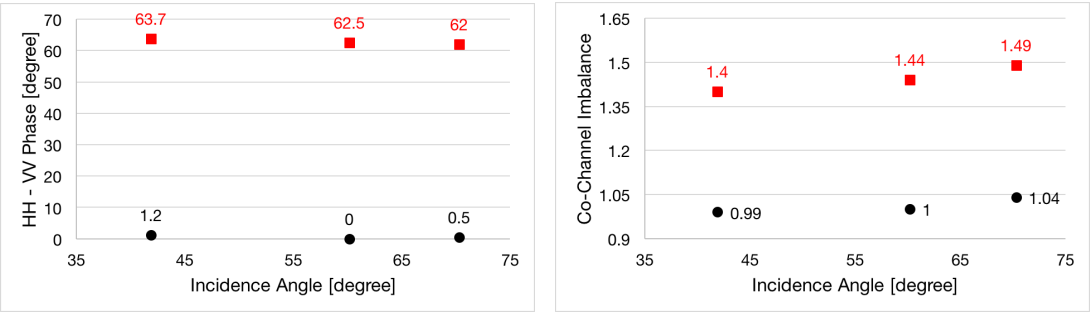

(a) *(b)*

Figure 4.29: *Co-polarisation phase difference and co-channel imbalance plotted as a function of incidence angle for X-band on 30 November 2016 before and after calibration. (a) Co-polarisation phase difference correction of three corner reflectors, the red is before calibration while the black is after calibration, and (b) Co-channel imbalance before calibration in red and after calibration in black.*

The polarisation signatures after phase correction and channel imbalance for the three trihedral corner reflectors in the near, mid, and far fields are presented in Fig. 4.30, 4.31, and 4.32. The polarisation signature for the trihedral corner reflector in the near range is more distorted due to the phase bias of 1.2°, while the polarisation signature in the far field is distorted a little due to the co-channel imbalance of 1.04 after calibration. Moreover, the polarisation signature for the corner reflector in the mid range is a perfect trihedral signature with zero phase difference between HH-VV channels, as well as a co-channel imbalance of 1.

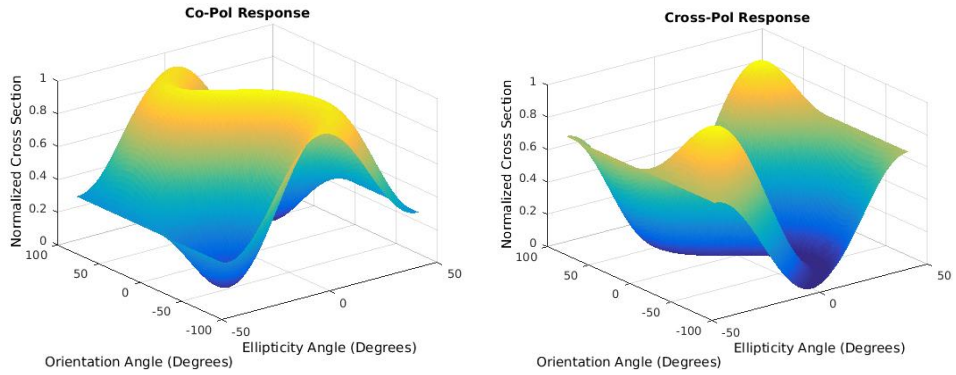

(a) *(b)*

Figure 4.30: *Polarisation signature for co-channels of X-band dataset after calibration is applied for the near field corner reflector where; (a) The co-polarisation signature, while (b) The cross-polarisation signature.(See Appendix A.8)*

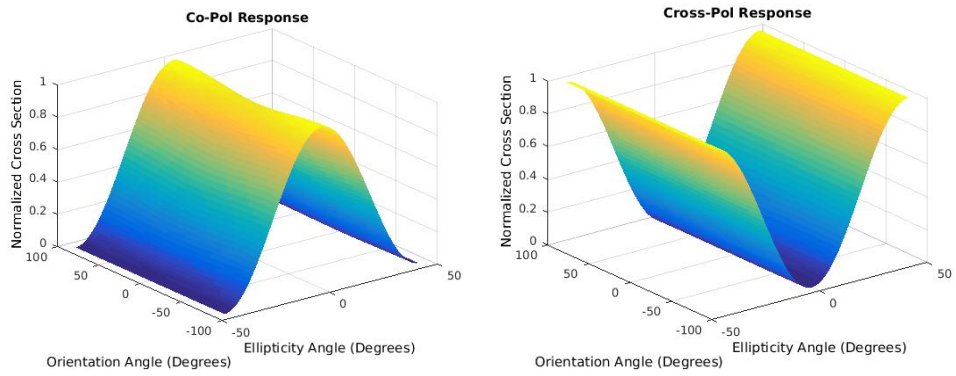

(a) *(b)*

Figure 4.31: *Polarisation signature for co-channels of X-band dataset after calibration is applied for the mid field corner reflector where; (a) The co-polarisation signature, while (b) The cross-polarisation signature.(See Appendix A.9)*

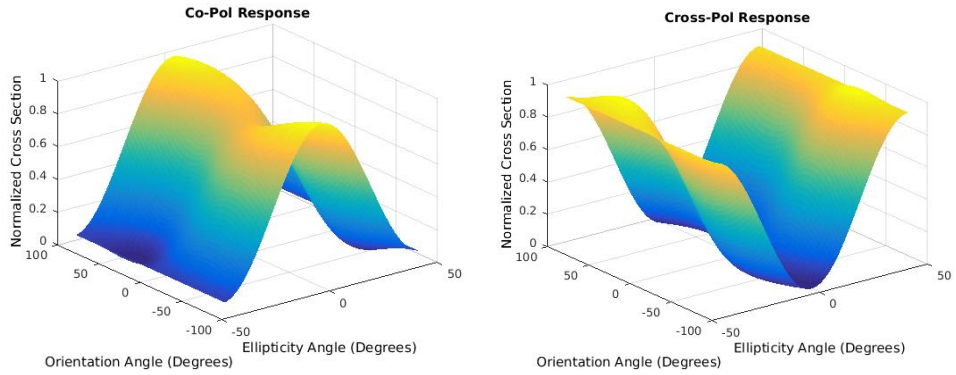

(a) *(b)*

Figure 4.32: *Polarisation signature for co-channels of X-band dataset after calibration is applied for the far field corner reflector where; (a) The co-polarisation signature while, (b) The cross-polarisation signature.(See Appendix A.10)*

4.3.2.2.2 Cross-Phase and Cross-Channel Imbalance Since we have three dihedral corner reflectors rotated by 45° to generate cross polarisation components HV and VH, the cross-channels were corrected for phase and channel imbalance based on the Zebker et al. method which we presented in Section 2.2.2.2, and we used it for the co-polarisation channels. The maximum responses from the three dihedral corner reflectors rotated by 45° were used to estimate phase and co-channel imbalance parameters for calibrating the data. We used IDL to read the SLC SAR data and then exported each channel HV and VH to ENVI for locating and extracting the maximum response from the three dihedral corner reflectors. Figs. 4.33 and 4.34 show the use of ENVI to locate the maximum response from the three dihedral corner reflectors for HV and VH channels, where; (a) near field, (b) mid field, and (c) far field.

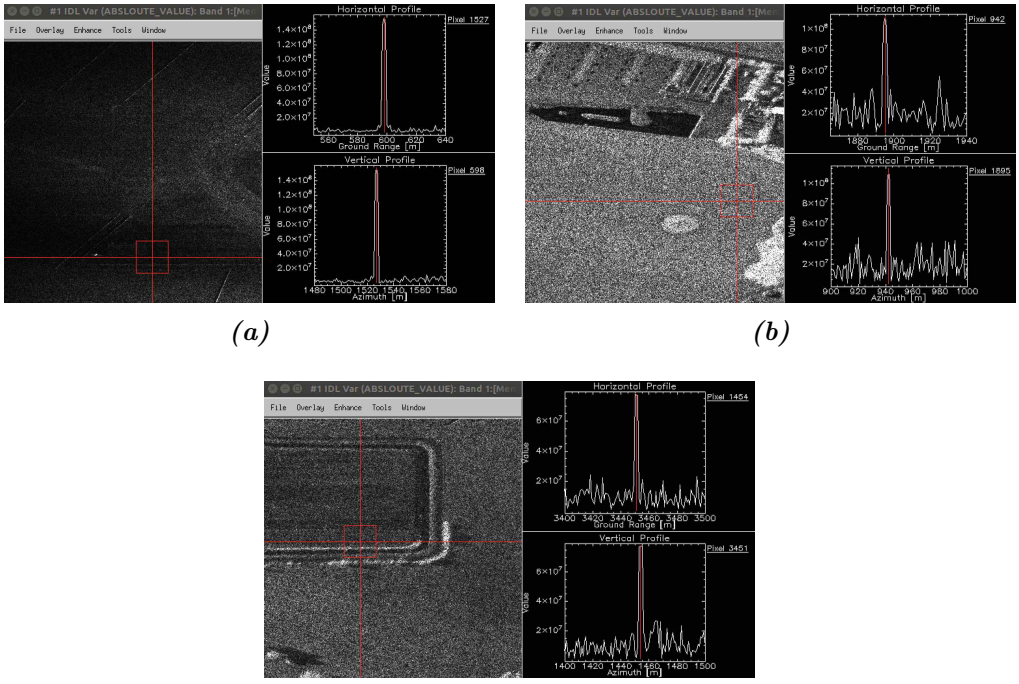

(a) *(b)*

(c)

Figure 4.33: *Reading SAR data using IDL and locating corner reflector for HV channel in all the three fields where; (a) Near field, (b) Mid field, and (c) Far field.*

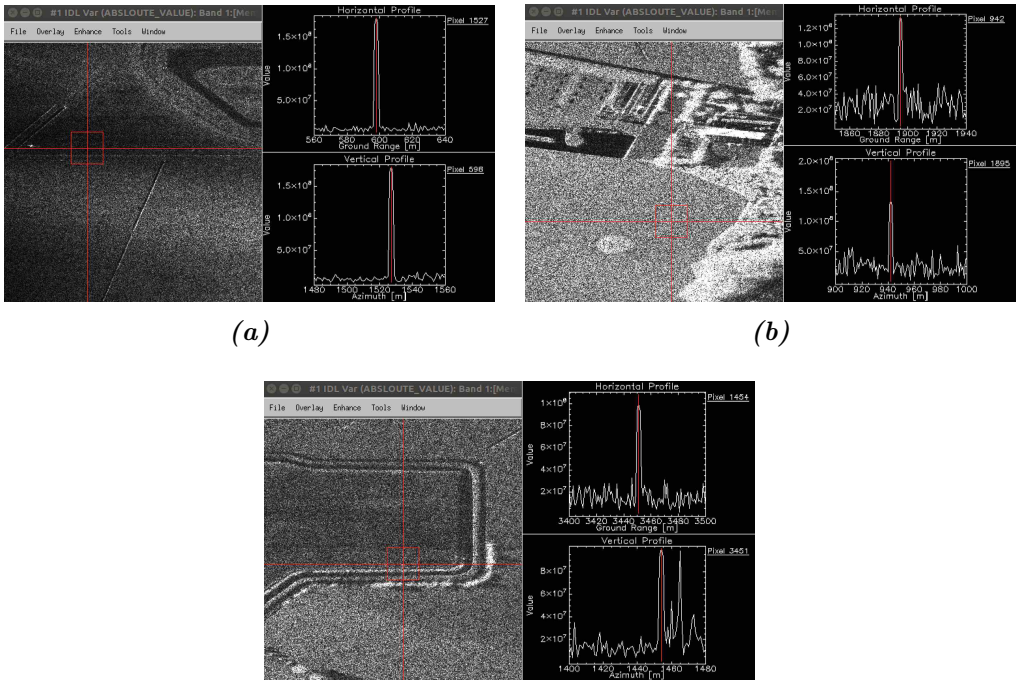

(a) *(b)*

(c)

Figure 4.34: *Reading SAR data using IDL and locating corner reflector for VH channel in all the three fields where; (a) Near field, (b) Mid field, and (c) Far field.*

The theoretical polarisation signature for dihedral corner reflector rotated by 45° is presented in Fig. 4.35, where; (a) is the co-polarisation signature, while (b) is the cross-polarisation signature.

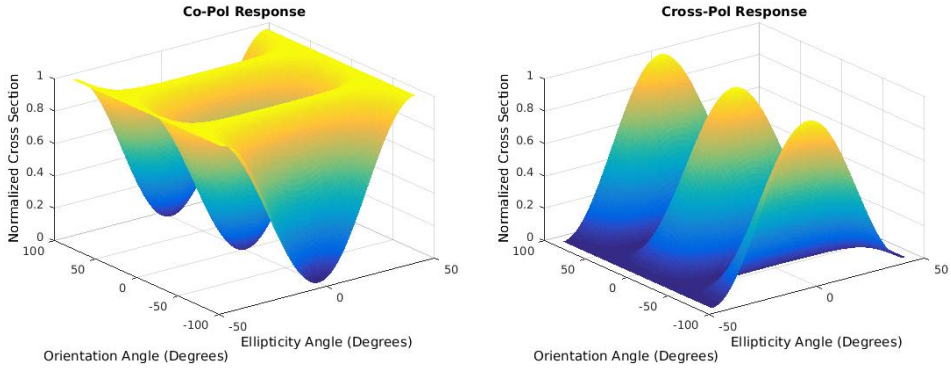

(a) *(b)*

Figure 4.35: *Theoretical polarisation signature for cross-channels with a zero cross-phase channels and 1 channels imbalance where; (a) The co-polarisation signature, while (b) The cross-polarisation signature.(See Appendix A.11)*

After we extract the scattering matrix for each dihedral corner reflector, co- and cross-polarisation signatures are plotted in Figs. 4.36, 4.37, and 4.38 for the near, mid, and far dihedral corner reflectors.

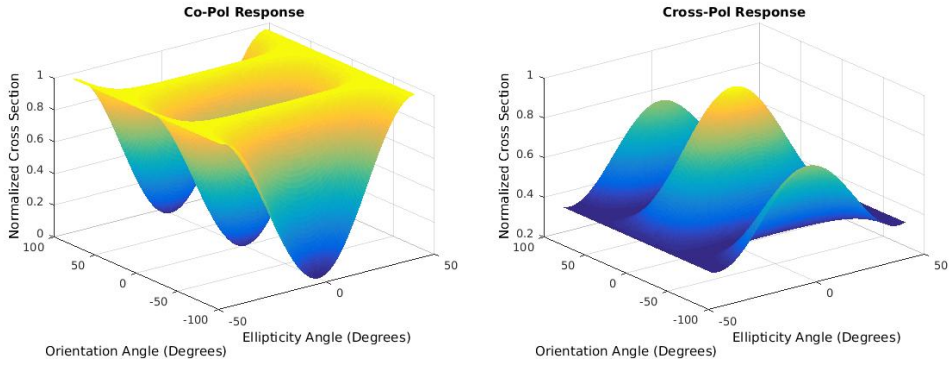

(a) *(b)*

Figure 4.36: *Polarisation signature for cross-channels of X-band, before calibration is applied, for the near field corner reflector where; (a) The co-polarisation signature, while (b) The cross-polarisation signature.(See Appendix A.12)*

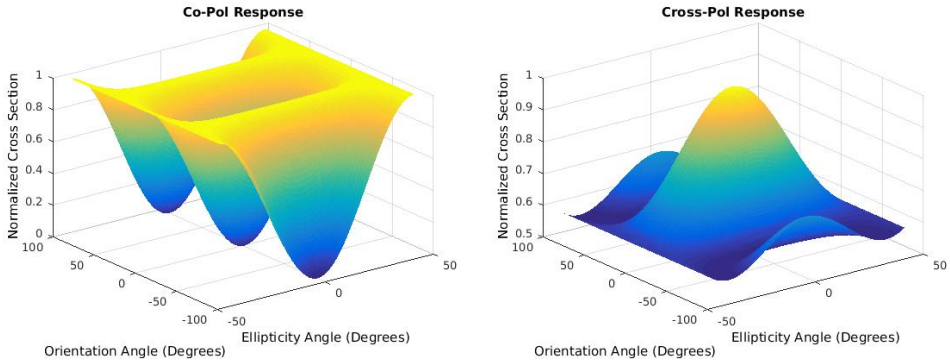

(a) *(b)*

Figure 4.37: *Polarisation signature for cross-channels of X-band, before calibration is applied, for the mid field corner reflector where; (a) The co-polarisation signature, while (b) The cross-polarisation signature.(See Appendix A.13)*

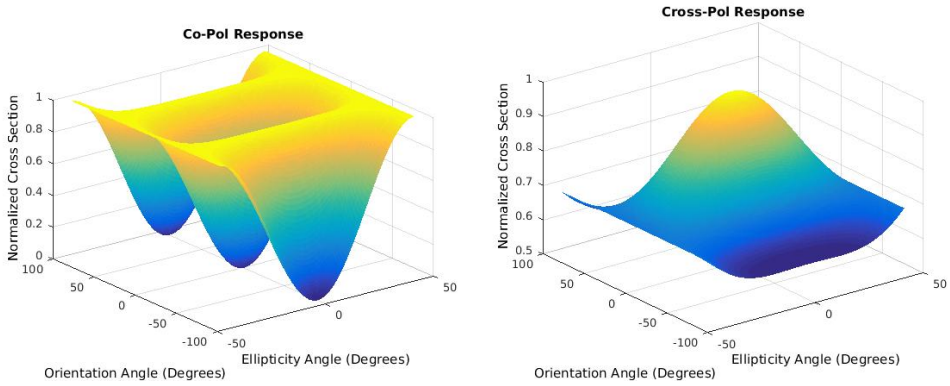

(a) *(b)*

Figure 4.38: *Polarisation signature for cross-channels of X-band, before calibration is applied, for the far field corner reflector where; (a) The co-polarisation signature, while (b) The cross-polarisation signature.(See Appendix A.14)*

Cross-polarisation phase difference HV - VH is plotted as a function of the incidence angle in Fig. 4.39(a), before and after the phase rotation for the three dihedral corner reflectors. The dihedral corner reflectors in the near and mid fields have a phase bias in the order of -108° before phase calibration, while the dihedral corner reflector in the far field has a 2° phase bias higher than the

previous two dihedral reflectors. After rotating the phase, we had a zero phase difference for the near field cross channels HV - VH. Additionally, the dihedral corner reflector in the mid field has a phase bias of 0.5°. Finally, the dihedral corner reflector in the far field has a phase bias of 2.5°.

Moreover, the cross-channel imbalance (f) was derived using Eq. 4.16 and presented in Fig. 4.39(b). The cross-channel imbalance for the three dihedral corner reflectors is 1.06, 1.09, and 1.13 before correction, respectively. The HH channel was used to adjust the channels for the three dihedral corner reflectors and the results showed a cross channel imbalance of 1 for the near field reflector and 1.02 and 1.06 for the mid and far fields dihedral reflectors.

$$f_{VH-HV} = \left[S'_{vh}S'^{*}_{vh}/(S'_{hv}S'^{*}_{hv})\right]^{0.25} \tag{4.16}$$

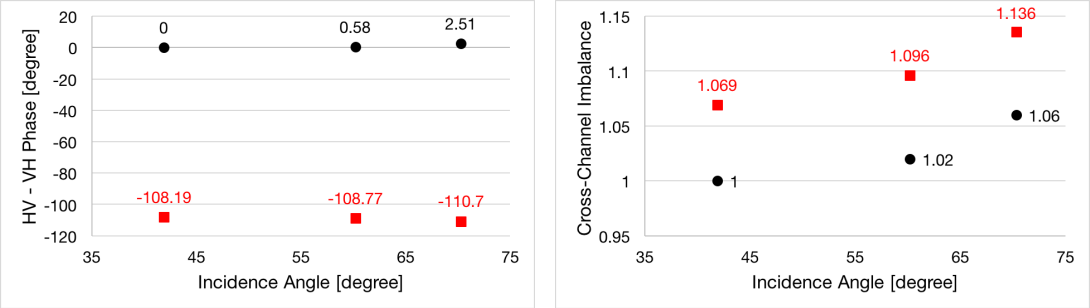

(a) *(b)*

Figure 4.39: *Cross-polarisation phase difference and cross-channel imbalance plotted as a function of the incidence angle for X-band on 30 November 2016 before and after calibration. (a) Cross-polarisation phase difference correction of three corner reflectors, the red is before calibration while the black is after calibration, and (b) Cross-channel imbalance before calibration in red and after calibration in black.*

The polarisation signatures after cross-phase correction and cross-channel imbalance for the three dihedral corner reflectors in the near, mid, and far fields are presented in Figs. 4.40, 4.41, and 4.42. The polarisation signature for the dihedral corner reflector in the near range is perfect and matches the theoretical polarisation signature of the dihedral corner reflector due to the zero phase difference between the cross-polarisation channels, as well as the perfect channel imbalance.

Additionally, the polarisation signature for the dihedral corner reflector in the mid field is a little distorted due to the small phase bias of 0.58°, while the polarisation signature for the dihedral corner reflector in the far field is more distorted due to the high phase bias of 2.5°.

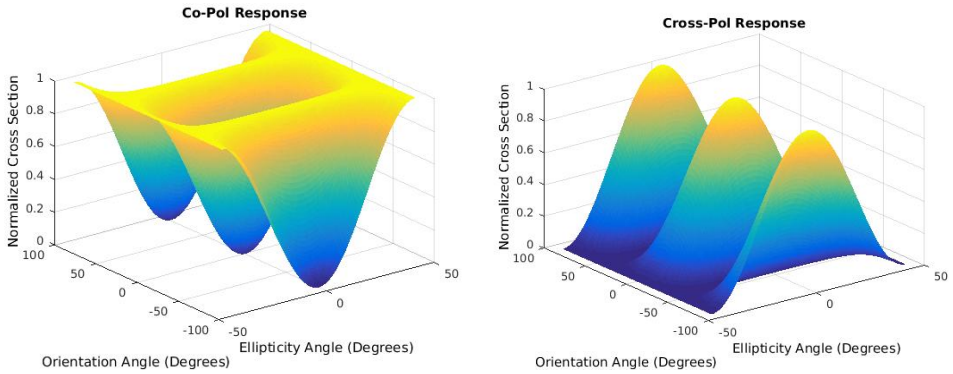

(a) *(b)*

Figure 4.40: *Polarisation signature for cross-channels of X-band, after calibration is applied, for the near field corner reflector where; (a) The co-polarisation signature, while (b) The cross-polarisation signature.(See Appendix A.15)*

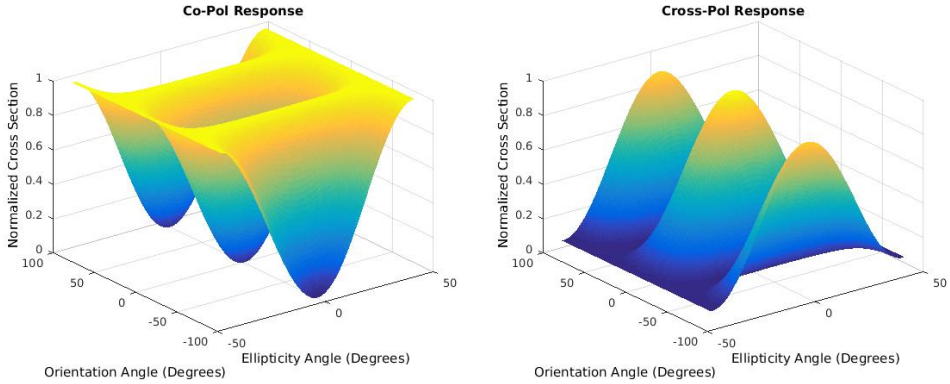

(a) *(b)*

Figure 4.41: *Polarisation signature for cross-channels of X-band, after calibration is applied, for the mid field corner reflector where; (a) The co-polarisation signature, while (b) The cross-polarisation signature.(See Appendix A.16)*

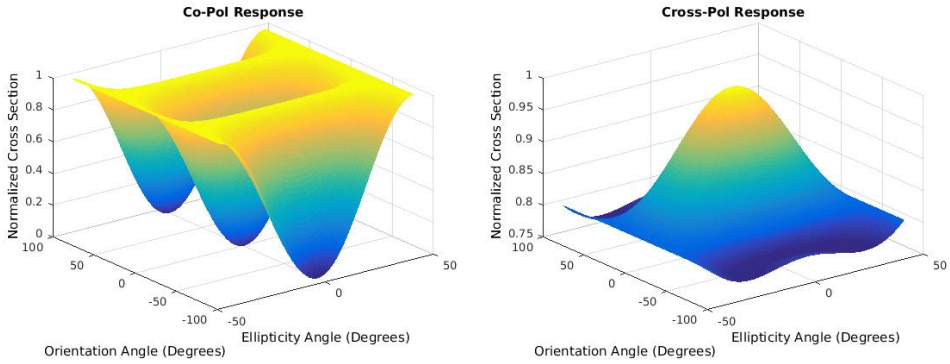

(a) *(b)*

Figure 4.42: *Polarisation signature for cross-channels of X-band, after calibration is applied, for the far field corner reflector where; (a) The co-polarisation signature, while (b) The cross-polarisation signature.(See Appendix A.17)*

4.3.2.3 Radiometric Calibration

The radiometric calibration was done for both co- and cross-channels, based on the three trihedral corner reflectors in the co-channels and the three dihedral corner reflectors in the cross-channels, to relate the pixel's values of the corner reflectors to their backscattering coefficient by using the integral method, which we detailed in Section 2.2.3. The incidence angles (θ_i) for the three fields were recalculated in Fig. 4.43 based on subtracting the flight altitude of 750 m with 47 m DEM as follows:

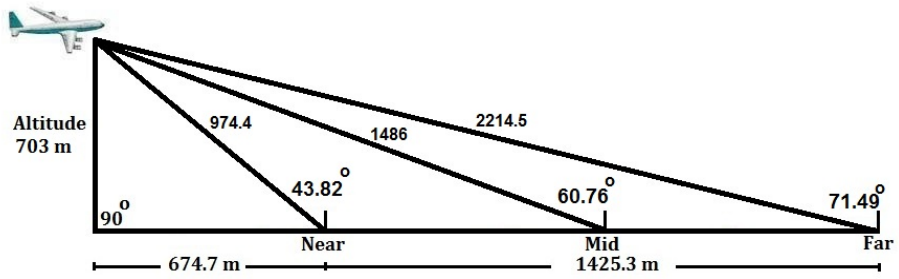

Figure 4.43: *Recalculated incidence angles for the three fields*

The integral method's parameters for the co-channels were computed and presented in Table 4.6, and plotted before correction in red and after correction in black in Fig. 4.44 for the three trihedral corner reflectors in the near, mid, and far fields. The result showed a very small reduction in the overall backscattering coefficient for the three corner reflectors by about 0.5 dB.

Table 4.6: *Integral method parameters calculation for co-channels of X-band radiometric calibration*

CR	CR Energy ε_p	Calibration Constant K	θ_i	σ_o
N	7.48377e16	4.5e13	43.82	2258.641
M	7.04953e16	3.3e13	60.76	2318.599
F	6.60751e16	2.8e13	71.49	2346.825

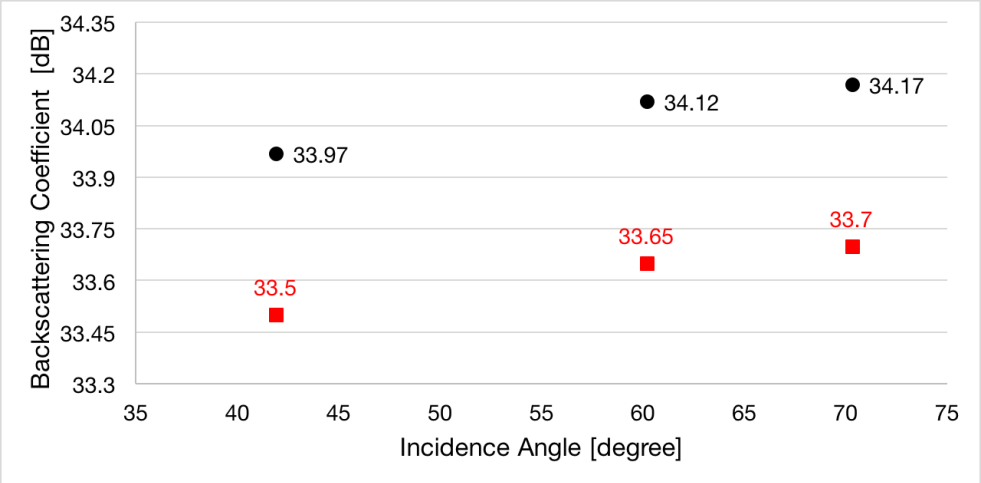

Figure 4.44: *Backscattering coefficient for the three trihedral corner reflectors in co-channels, before correction in red and after correction in black.*

Furthermore, we estimated the parameters of the integral method for the cross-channels and presented in Table 4.7, and plotted before correction in red and after correction in black in Fig. 4.45 for the three dihedral corner reflectors in near, mid, and far fields. The result showed a very small reduction in the overall backscattering coefficient as we got for the co-channels for the three corner reflectors by about 0.5 dB.

Table 4.7: *Integral method parameters calculation for cross-channels of X-band radiometric calibration*

CR	CR Energy ε_p	Calibration Constant K	θ_i	σ_o
N	1.552192e16	1.4e13	43.82	1470.133
M	1.368606e16	9.6e12	60.76	1524.627
F	9.832600e15	6.2e12	71.49	1442.219

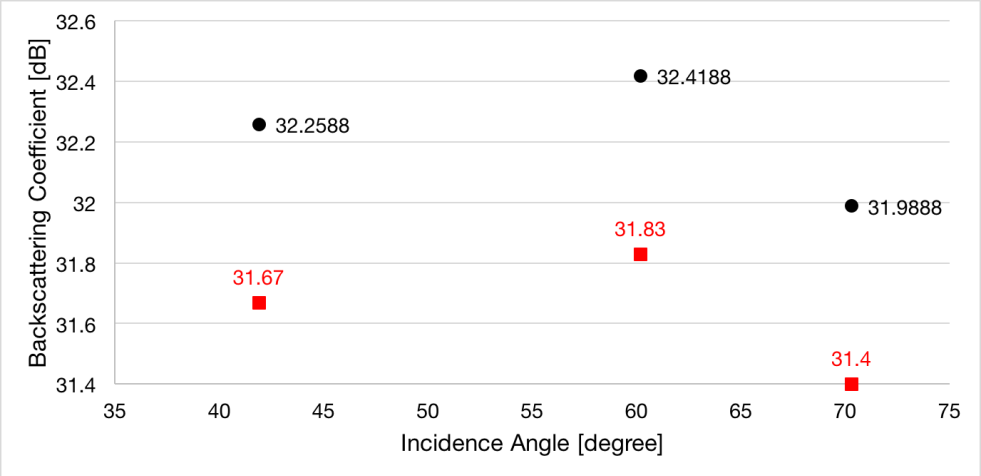

Figure 4.45: *Backscattering coefficient for the three dihedral corner reflectors in cross-channels, before correction in red and after correction in black.*

4.3.3 Geometric Correction

UTM coordinates have been extracted from the focused SAR image. The SAR image was focused by using a flat earth DEM of 47 meter altitude, while the GNSS elevation measured on the corner was around 48.5/49 m, and without considering the slant range offset of 2.85 m of the cable connecting the antennas to the X-band subsystem. Each cable connecting the sensor and the transmitting and receiving antenna are indeed 2 m long, corresponding to a travelling path of 2.83 m, considering a slowing factor of 0.707 in the travelling speed of the radio waves in the cable. Tables 4.8 and 4.9 present the positions of the P-band corner reflectors from the image as well as the difference between the surveyed positions and the positions in the image for the six corner reflectors in the near, mid, and far fields. Moreover, the results plotted in Fig. 4.46 show the difference between surveyed and image positions with an RMS of 1.48 m in northing and an RMS of 4.73 m in easting, before applying any correction.

Table 4.8: *Position of the X-band corner reflectors from the image on 30 November 2016*

Parameters	Trihedral Corner Reflector		Dihedral Corner Reflector	
	Easting [m]	Northing [m]	Easting [m]	Northing [m]
Near Field	297962.67	5791998.46	297978.03	5791986.41
Mid Field	298583.84	5792578.52	298605.47	5792591.66
Far Field	299432.14	5792121.82	299399.13	5792105.84

Table 4.9: *Different between the surveyed positions and the positions in the image*

Parameters	Trihedral Corner Reflector		Dihedral Corner Reflector	
	ΔEasting [m]	ΔNorthing [m]	ΔEasting [m]	ΔNorthing [m]
Near Field	-5.81	0.57	-5.41	0.73
Mid Field	-3.74	2.5	-3.96	1.38
Far Field	-4.95	1.07	-4.14	1.73

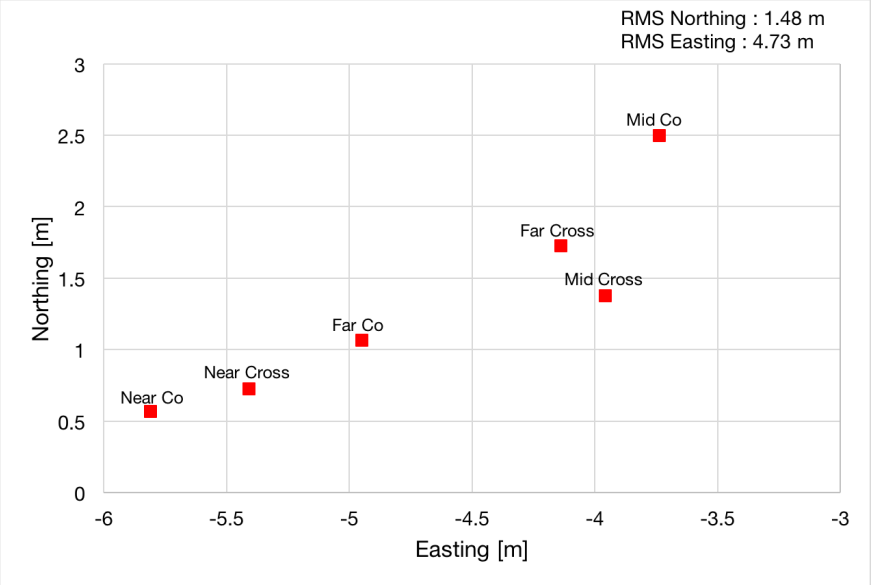

Figure 4.46: *Difference between the surveyed positions and the positions in the image before correction for the six corner reflectors*

Fortunately, the test site is very flat, so it was possible to discover the slant ranges based on aircraft height above ground, and assume the corner reflectors at ground level. Fig. 4.47 illustrates as example of the absolute geometric error introduced by using a DEM with 2 meter error in elevation on a flat earth when flying at 750 m altitude. Furthermore, the hardware offset in the slant range data before SAR focusing can also introduce a similar behaviour. A range offset of range profiles could, for example, be due to the use of cable connecting the radar antennas and the radar instrument. By using the recalculated slant ranges in Fig. 4.43, the DEM elevation error and radar slant range offset were estimated and presented in Fig. 4.48.(b) to be 0.1 for near field, 0.8 m for mid field, and 0.6 m for far field in northing. Additionally, 5.1 m for near field, 4.5 m for mid field, and 3.9 m for far field in easting. The geometric correction showed an RMS of 0.943 m in northing and 0.769 m in easting.

Moreover, Fig. 4.48(a), shows the geometric correction for the six corner reflectors using an averaging approach, where the results are close to the previous correction and showed an RMS of 0.6502 m in northing and 0.7719 m in easting. The averaging approach was done by subtracting the average error in east -4.73 m and north 1.48 m by each position in the image.

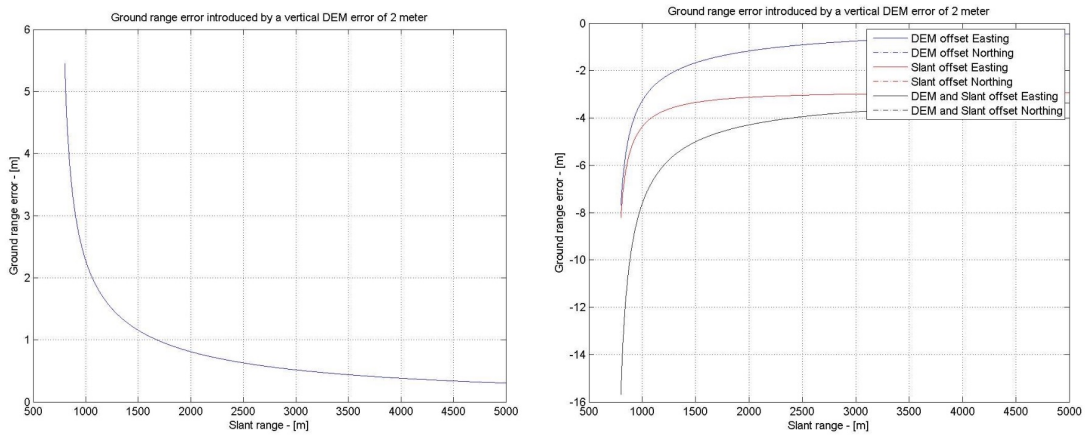

(a) *(b)*

Figure 4.47: *Ground range geometric error. (a)DEM with 2 m error in elevation on a flat earth when flying at 750 m altitude, and (b) DEM elevation error and radar slant range offset. [105]*

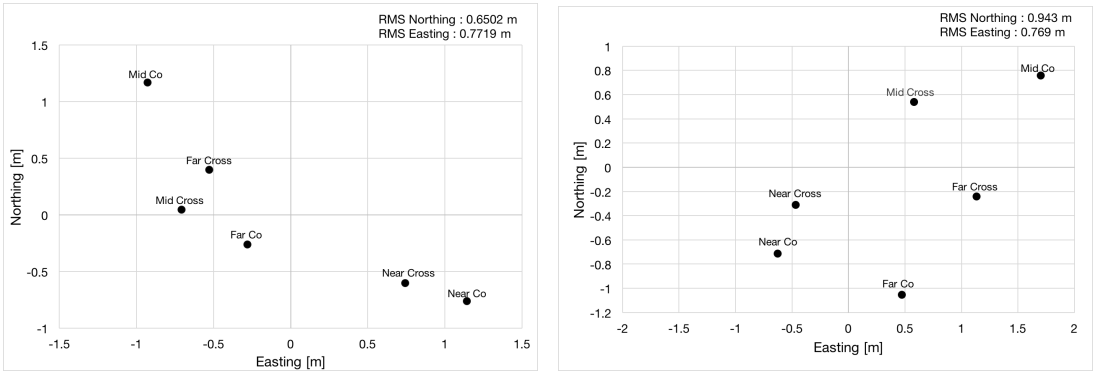

(a) *(b)*

Figure 4.48: *Geometric difference between surveyed positions and positions in the image for six X-band corner reflectors where; (a) After correction using the average approach, and (b) After correction using DEM and slant range offset correction.*

4.3.4 Noise Equivalent Sigma Zero

The noise equivalent sigma zero is known as the measurement of the sensitivity of the SAR system to areas of low radar backscatter. It is given by the value of the backscatter coefficient corresponding to a signal to noise ratio of unity [111]. The estimation of a signal to noise ratio is very important over various polarimetric channels due to different requirements of different applications for the signal to noise ratio so the estimation of a signal noise ratio lets us clearly understand whether or not the dataset is suitable for a given application [112]. The performance of our SAR system was evaluated in terms of the noise equivalent sigma zero (NESZ). As shown in Fig. 4.49, we selected diverse areas in the image where it had a backscatter from grass in the VV channel (Near, mid, and far) and a very low backscatter from the airport runway to measure the sensitivity of the system. The backscatter from the runway is 54.3 dB, while the backscatter from the grass in the mid field is 60.6 dB at a slant range of 1500 m and 60.76° look angle, which means an achieved SNR of more than 6.2 dB over grass areas. From the Handbook of Radar Scattering Statistics for Terrain by Ulaby, Table E5, page 247, the RCS of grass at X band at 60 degrees equal to -14 dB [113].

We can deduce that flying at 750 m above the ground; we have a NESZ of more than -20 dB at 60 degrees.

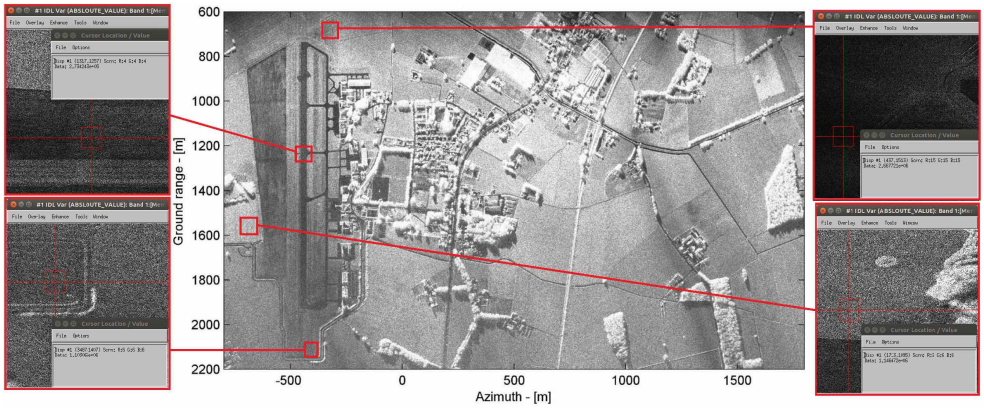

Figure 4.49: *Noise equivalent sigma zero measurements for X-band.*

It is very important to note that this achieved NESZ is at a low flying altitude of 750 m, and the NESZ would be lower when we fly at a higher altitude. For example, taking the backscatter from the far end of the image, the backscatter from the grass is 60.5 dB at a slant range of 3170 m and 76.3° look angle, which means an achieved SNR of more than 6 dB over grass areas. Additionally, from the Handbook of Radar Scattering Statistics for Terrain by Ulaby [113], Table E5, the RCS of grass at X-band at 76.3° is equal to -16.5 dB. We can deduce that flying at 750 m above the ground; we have a NESZ of -22.5 dB at 76.3°. When flying at 1000 m, the slant range at 76.3° degree is 4225 m. When scaling the NESZ for a distance factor only, we need to multiply the ratio of distances to the power of three. In our case, going from a slant range of 3170 m to 4225 m corresponds to a scaling factor of -3.75 dB. An additional scaling of 5.22 dB needs to be taken into account considering that the data were acquired at transmitting 500 MHz, while the requirements are for 150 MHz. Furthermore, another 3 dB needs to be considered because of the full polarisation acquisition mode, consisting in alternating V and H polarisation in transmission. Therefore the total scaling factor is 4.42 dB and the achieved scaled NESZ is -26.92 dB.

4.3.5 Calibration of P-band SAR Sensor

The polarimetric P-band data were processed to level.1 and SLC images generated with a presuming factor of 32, and Doppler centroid of 0 Hz and with data were acquired in fully polarimetric mode, flying at 750 m above the ground. Presuming is a common SAR technique used when processing the raw data to SLC for the purpose of decreasing the processing image size. Fig. 4.50 shows P-band SAR SLC images

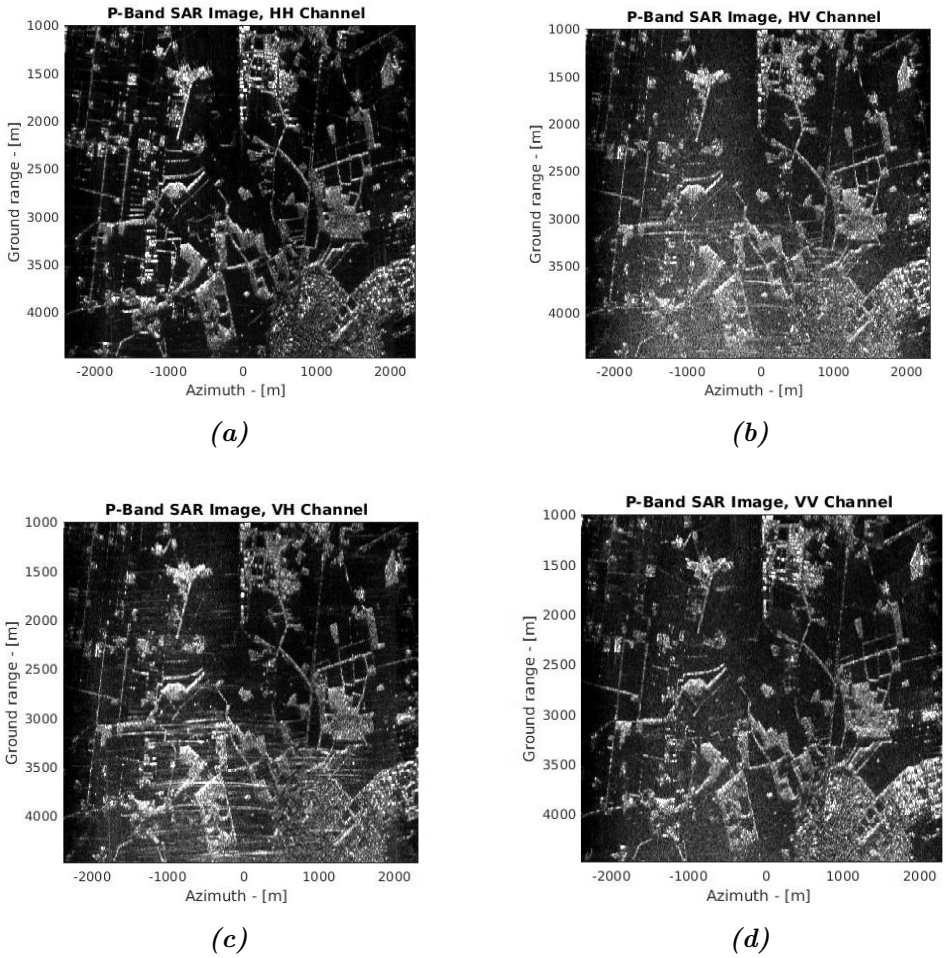

Figure 4.50: *P-band SAR SLC images where; (a) Horizontal-Horizontal Channel, (b) Horizontal-Vertical Channel, (c) Vertical-Horizontal Channel, and (d) Vertical-Vertical Channel.*

4.3.5.1 Crosstalk Estimation and Correction

The Ainsworth method was used for the crosstalk estimation and correction which we detailed in Section 4.2.3.3 and detailed in [66] [62] [70]. The results are presented in Fig. 4.51. The initial crosstalk parameters are plotted in red and the residual crosstalk in black after calibration. The crosstalk for all the parameters before calibration are around -10 dB and they are around -30 dB after calibration.

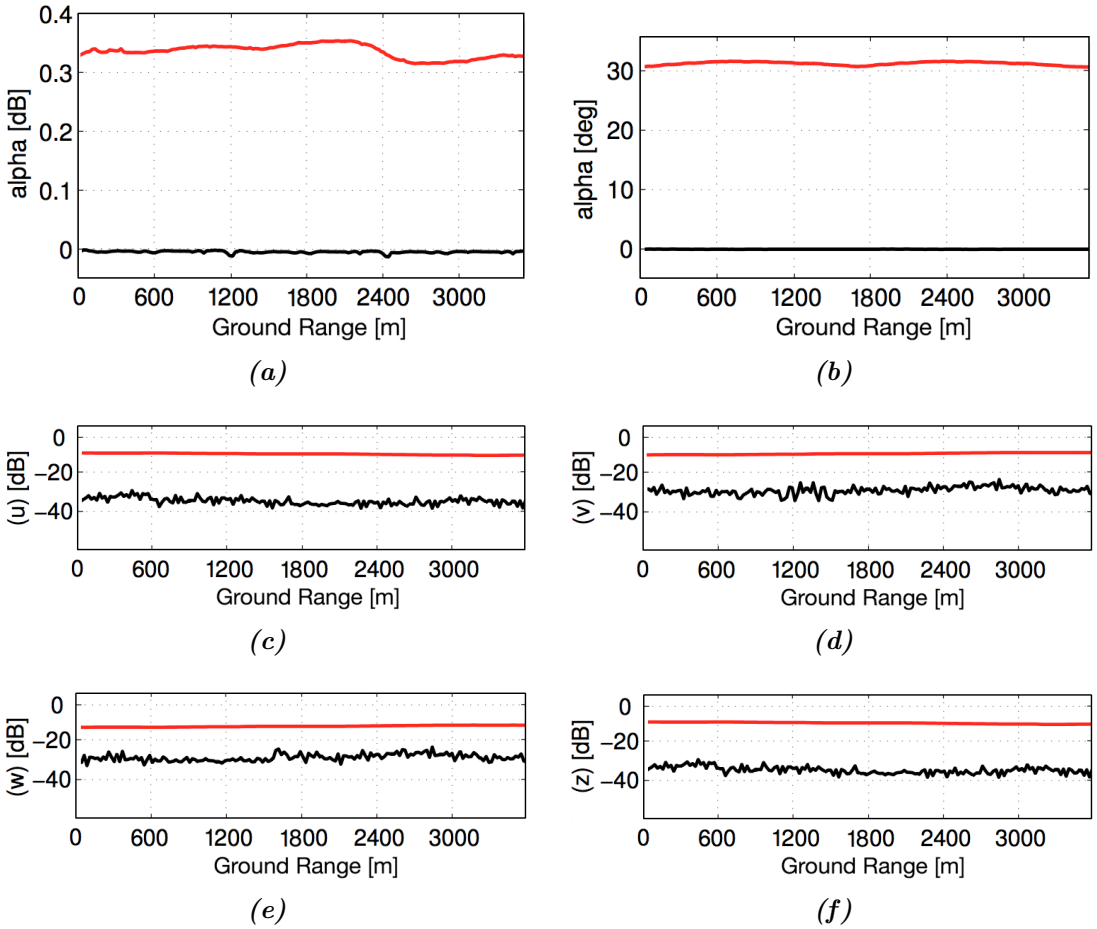

Figure 4.51: *Estimation and correction of crosstalk parameters as a function of ground range averaged in azimuth using the Ainsworth method. The initial crosstalk parameters are plotted in red, and the residual crosstalk in black after calibration.*

4.3.5.2 Polarimetric Phase and Co-Channel Imbalance

Three triangular trihedral corner reflectors were deployed in the three sites (near, mid, far) to correct the phase, channel imbalance, and radiometric calibration. After we processed the data, the corner reflector in the near range was out of the acquired swath by a number of meters. We used the two triangular trihedral corner reflectors in the mid and far field to correct the phase, channel imbalance, and radiometric calibration parameters for the data. We used IDL to read the SLC SAR data and then export each channel HH,HV,VH, and VV to ENVI for locating and extracting the maximum response from the two triangular trihedral corner reflectors to form the scattering matrix for each corner reflector. Figs. 4.52 and 4.53 show the use of ENVI to locate the two corner reflectors.

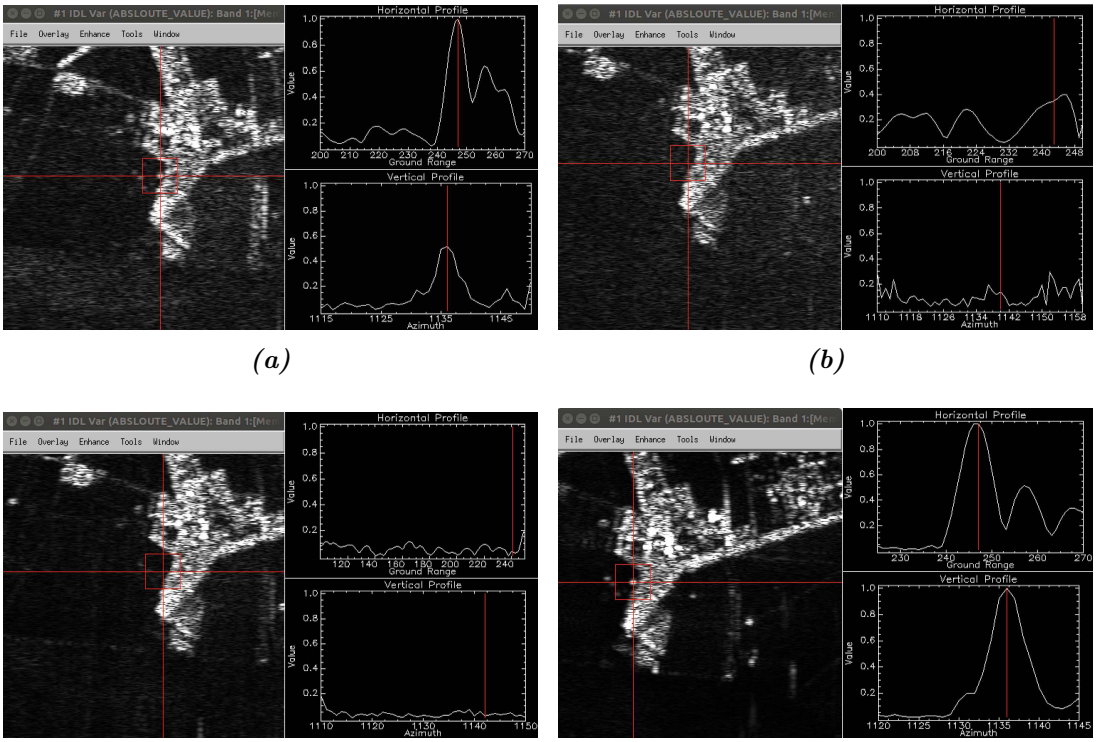

Figure 4.52: *Reading SAR data using IDL and locating the corner reflector in the mid field where; (a) Horizontal-Horizontal Channel, (b) Horizontal-Vertical Channel, (c) Vertical-Horizontal Channel, and (d) Vertical-Vertical Channel.*

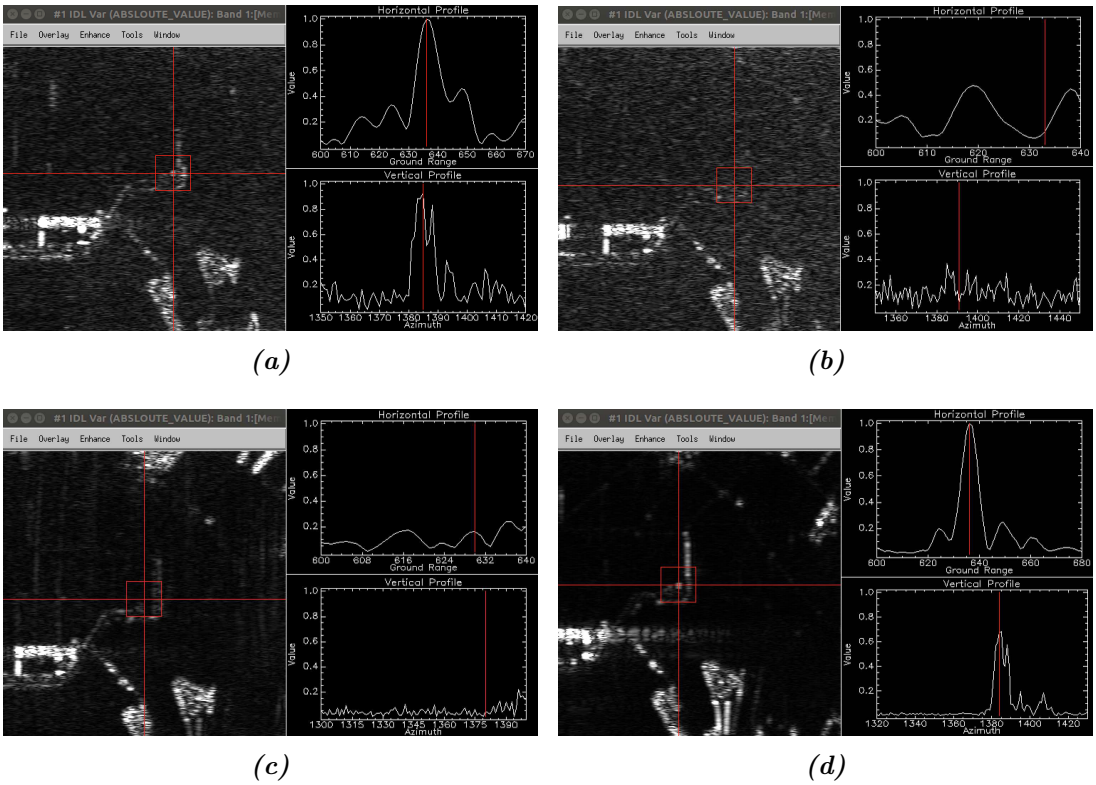

Figure 4.53: *Reading SAR data using IDL and locating the corner reflector in the far field where (a) Horizontal-Horizontal Channel, (b) Horizontal-Vertical Channel, (c) Vertical-Horizontal Channel, and (d) Vertical-Vertical Channel.*

Co- and cross-polarisation signatures are plotted in Fig. 4.54 and Fig. 4.55 for the two triangular trihedral corner reflectors before any phase and channel imbalance corrections are applied to the data. The two signatures for the two corner reflectors are similar.

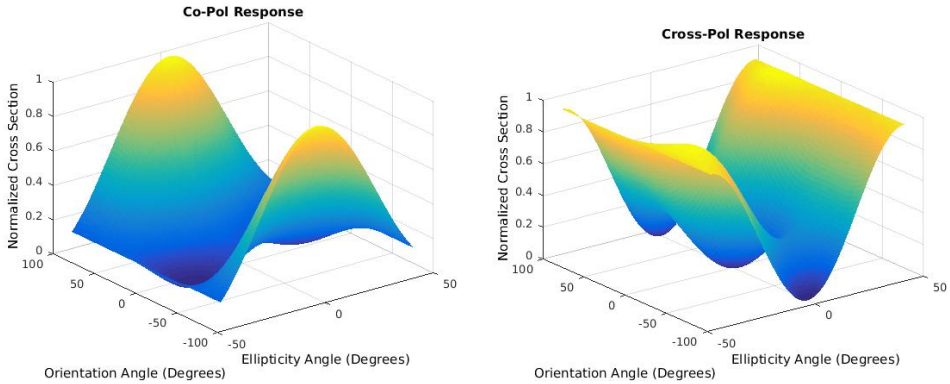

(a) *(b)*

Figure 4.54: *Polarisation signature before calibration is applied for the mid field trihedral corner reflector where; (a) The co-polarisation signature, while (b) The cross-polarisation signature.(See Appendix A.18)*

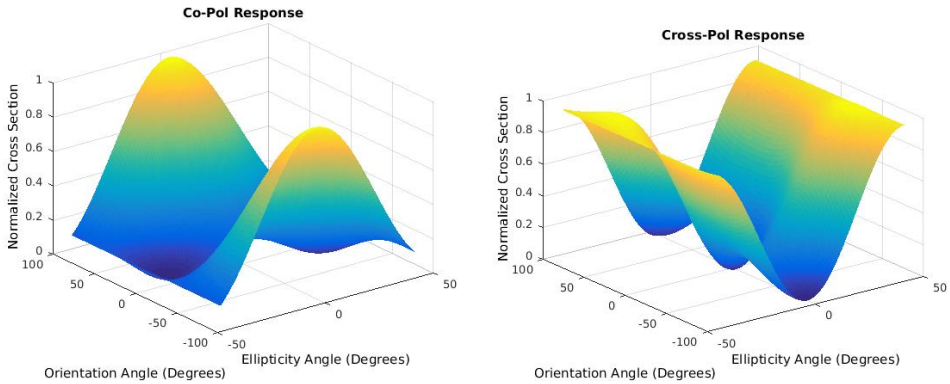

(a) *(b)*

Figure 4.55: *Polarisation signature before calibration is applied for the far field trihedral corner reflector where; (a) The co-polarisation signature, while (b) The cross-polarisation signature.(See Appendix A.19)*

The phase difference between the co-polarisation channels HH - VV for the two triangular trihedral corner reflectors was corrected using the Zebker et al. method which we presented in Section 2.2.2.2 to estimate the phase bias between co-polarisation channels HH - VV by $S'_{vv}S'^{*}_{hh}$. As shown in Fig. 4.56(a), the estimated co-polarisation phase difference HH - VV in red and the corrected phase difference between HH - VV in black for the two triangular trihedral corner reflectors. The

first triangular trihedral corner reflector in the mid field has a phase bias of -158.4°, while the second triangular trihedral corner reflector in the far field has a phase bias of -159.4° before phase rotation. After rotating the phase based on the first corner reflector, the phase difference between the co-polarisation channels HH - VV for the first corner reflector became 1.06°, while it is 0° phase bias for the second corner reflector.

Moreover, the co-channel imbalance (f) was derived using Eq. 4.11 and presented in Fig. 4.56(b). The co-channel imbalance for the first triangular trihedral corner reflector in the mid field is 1.75, while the second triangular trihedral corner reflector in the far field is 1.59 before channel imbalance. The HH channel was used to adjust the channels for the two corner reflectors to be 1 after correction.

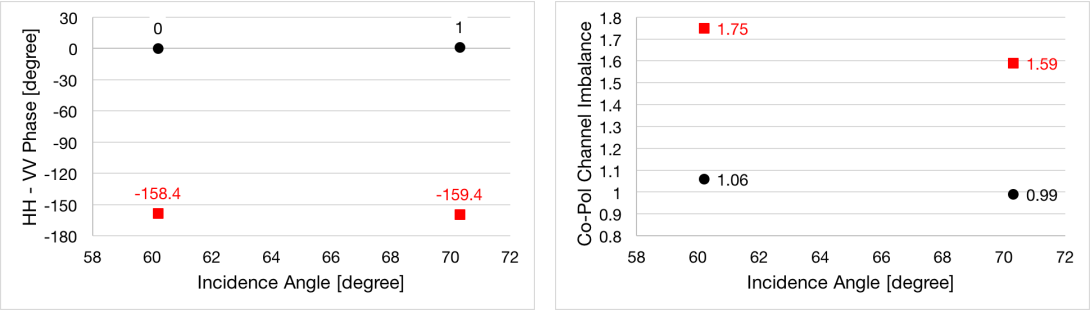

(a) ***(b)***

Figure 4.56: *Co-polarisation phase difference and co-channel imbalance plotted as a function of the incidence angle for P-band on 23 November 2016 before and after calibration. (a) Co-polarisation phase difference correction of three corner reflectors, the red is before calibration while the black is after calibration, and (b) Co-channel imbalance before calibration in red, and after calibration in black.*

Furthermore, in the cross-polarisation channels, we estimated the cross polarisation channel imbalance (g) using Eq. 4.12 which computes the average return from the cross polarisation channels over the image. Additionally, the phase bias between cross-polarisation channels HV - VH were estimated using the reciprocity assumption $S_{hv} = S_{vh}$ as $\phi_t - \phi_r = arg(< S'_{hv} S'^{*}_{vh} >)$ and averaged over the image.

Finally, the co- and cross-polarisation signatures for the two triangular trihedral corner reflectors are presented in Fig. 4.57 for the trihedral corner reflector in the mid field and Fig. 4.58 for the trihedral corner reflector in the far field. The co- and cross-polarisation signatures for the mid field corner reflector has a small distortion due to the phase bias of 1.06°, while the polarisation signature for the far field corner reflector is a perfect trihedral signature with a zero phase difference HH - VV between the co-channels and 1 channel imbalance. It is important to note that when we calibrated the P-band data, we used the mid field reflector as a main point target for rotating the phase and adjusting the channel imbalance. The far field reflector showed one-degree distortion in phase after calibration but it is very small.

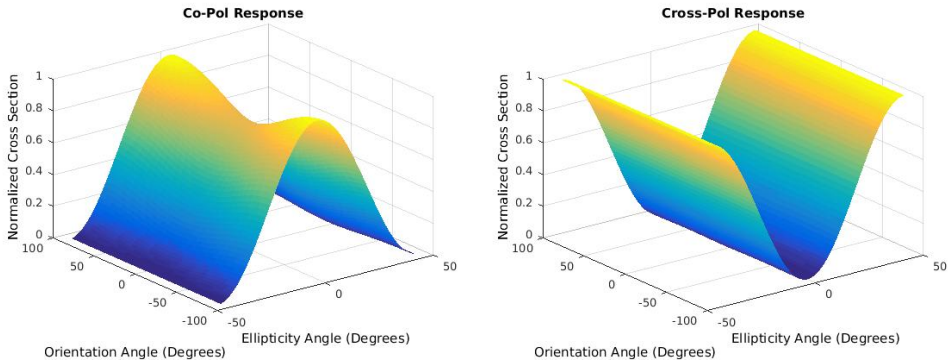

(a) *(b)*

Figure 4.57: *Polarisation signature after calibration is applied for the mid field trihedral corner reflector where; (a) The co-polarisation signature, while (b) The cross-polarisation signature.(See Appendix A.20)*

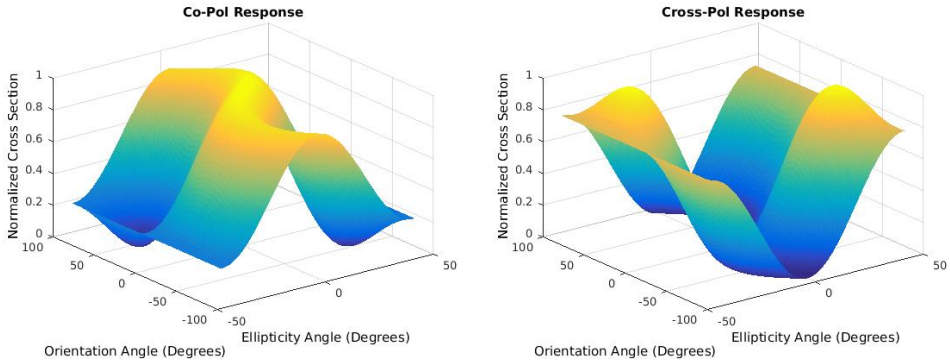

(a) *(b)*

Figure 4.58: *Polarisation signature after calibration applied for the far field trihedral corner reflector where; (a) The co-polarisation signature, while (b) The cross-polarisation signature.(See Appendix A.21)*

4.3.5.3 Radiometric Calibration

The radiometric calibration for P-band was done by using the integral method to relate the pixel's values associated with the two triangular trihedral corner reflectors in the mid and far fields to their backscattering coefficient. The two incidence angles for the mid and far field which we recalculate in Fig. 4.43, was used to compute the parameters of the integral method. The parameters are presented in Table 4.10 and plotted before correction in red and after correction in black in Fig. 4.59 for the two triangular trihedral corner reflectors in the mid and far fields. The results showed a backscattering coefficient for the trihedral corner reflector in the mid field of 14 dB, while it is a little more for the trihedral corner reflector in the far field 14.8 dB before correction. We increased the power by 0.96 dB over the four polarimetric channels to have a backscattering coefficient of 14.96 dB for the trihedral corner reflector in the mid field and 15.76 dB for the trihedral corner reflector in the far field .

Table 4.10: *Integral method parameters calculation for P-band radiometric calibration*

CR	CR Energy ε_p	Calibration Constant K	θ_i	σ_o
N	4.2790e25	1.39e24	60.76	25.12477
F	1.0491e25	3.08e23	71.49	30.64980

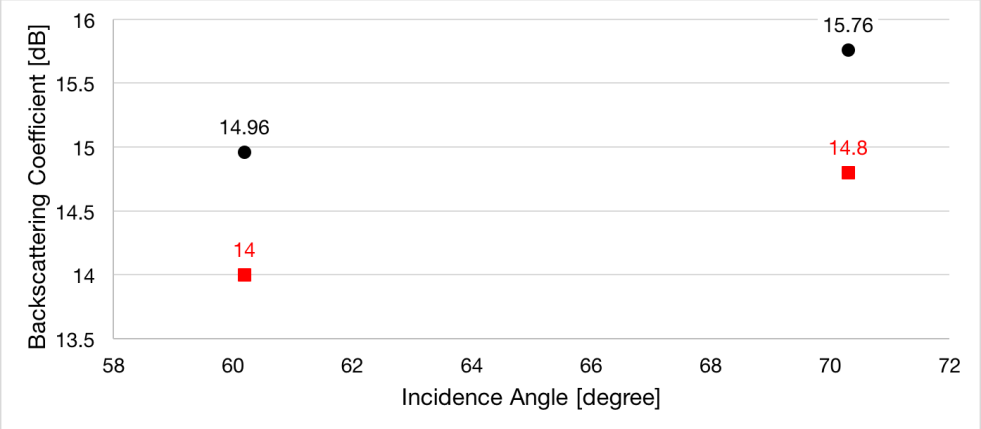

Figure 4.59: *Backscattering coefficient for the two triangular trihedral corner reflectors before correction in red, and after correction in black.*

4.3.6 Geometric Correction

The geographic UTM coordinates from the GNSS for P-band in Table 3.6 were used to relate each pixel in the image to its geographic coordinates. Table 4.11 presents the positions of the P-band corner reflectors from the image as well as the differences between the surveyed positions and the positions in the image for the two corner reflectors in the mid and far field. Moreover, the results plotted in Fig. 4.60 show the difference between the surveyed and image positions, with a 2.536 m RMS in northing and an RMS of 4.019 m in easting, before applying any correction.

Table 4.11: *Position of the P-band corner reflectors from the image on 23 November 2016*

Parameters	Trihedral Corner Reflector		Δ(Image-GNSS)	
	Easting [m]	Northing [m]	ΔEasting [m]	ΔNorthing [m]
Mid Field	298587.67	5792576.17	-3.83	2.35
Far Field	299436.34	5792119.11	-4.2	2.71

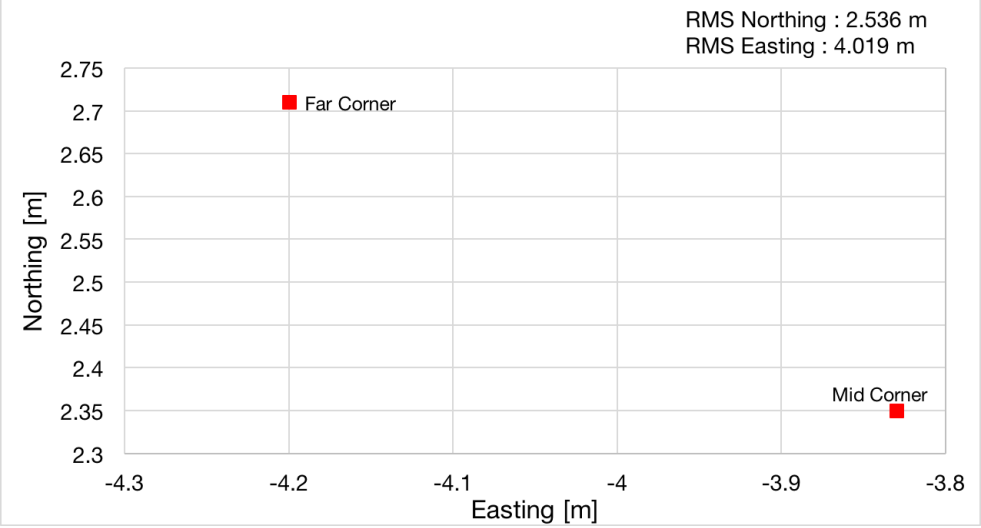

Figure 4.60: *Different between the surveyed positions, and positions in the image before correction*

The geometric corrections were achieved using two approaches which were detailed in Section 4.3.3, and the results are presented in Fig. 4.61. The results after the DEM and slant range offset removal showed an RMS of 1.85 m in northing and an RMS of 0.34 m in easting. Additionally, the averaging approach showed an RMS of 0 m in northing and an RMS of 0.185 m in easting.

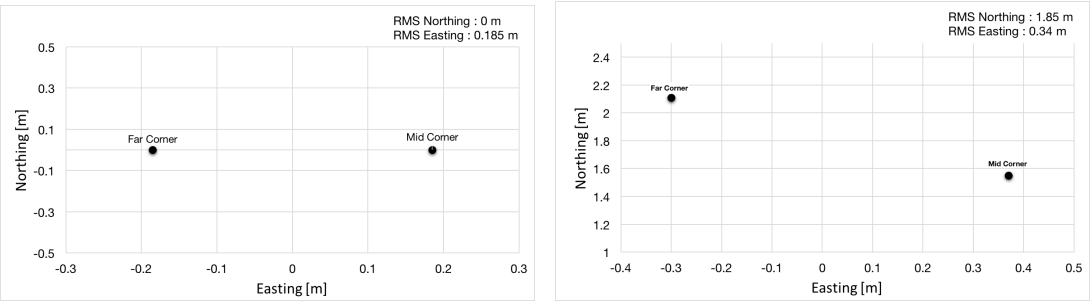

(a) *(b)*

Figure 4.61: *Geometric difference between surveyed positions, and positions in the image for two corner reflectors where; (a) After correction using the average approach, and (b) After correction using the DEM and slant range offset correction.*

4.3.7 Noise Equivalent Sigma Zero

Synthetic aperture radar, with longer wavelength, is susceptible to the influence of the radio frequency interference signals which seriously affecting the SAR image interpretation [114]. At low frequencies, such as P-band, the possibilities of radio frequency interference rise due to television broadcasting signals, particularly in urban areas or populated areas like in the Netherlands.

Moreover, the telecommunications tower at Teuge airport could have caused interference to the P-band SAR signal. The P-band date which we acquired on 24 November 2016 had strong interference as illustrated in Fig. 4.62 where; a)HH channel, b)HV channel, c)VH channel, and d)VV channel. The HH and HV channels show a higher RFI noise compared to the VH and VV channels.

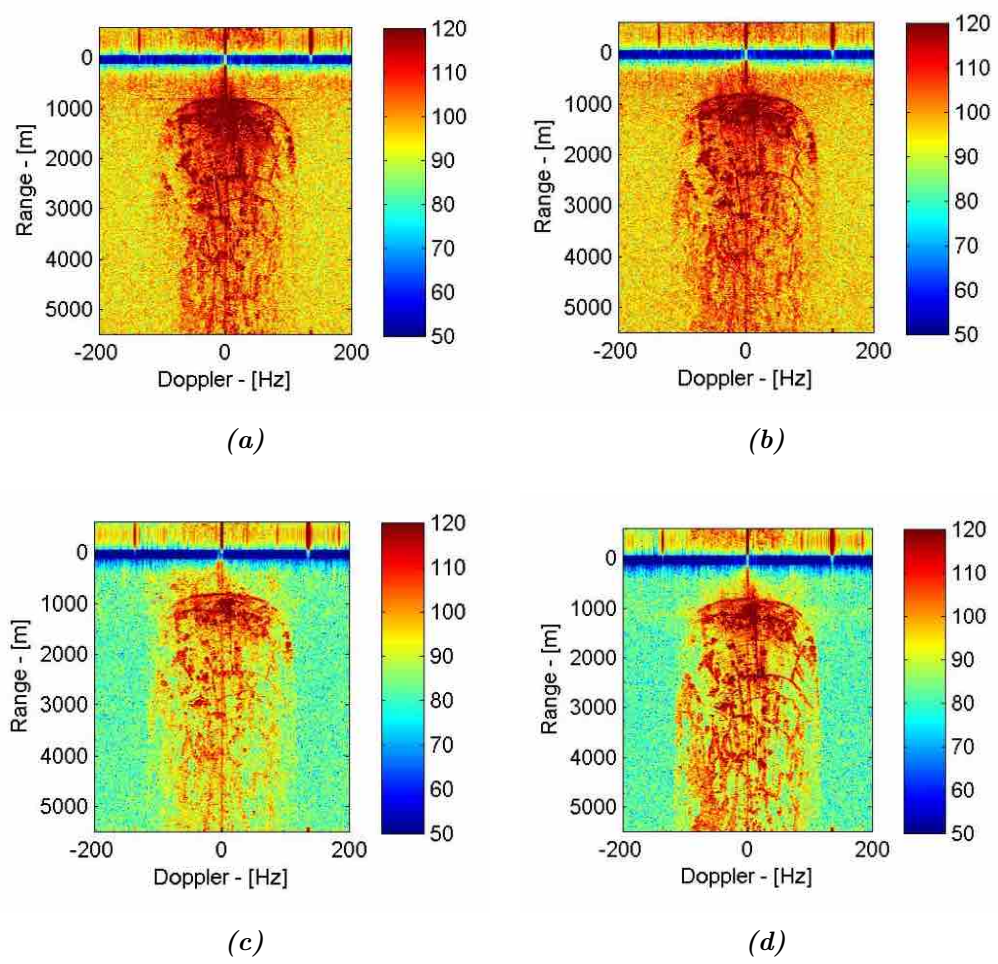

Figure 4.62: *Range Compressed Doppler spectrum where; a)HH Channel, b)HV Channel, c)VH Channel, and d)VV Channel.*

Furthermore, the noise floor is greatly affected by the RFI. In order to quantify the RFI effect on the noise floor, two acquisitions with the same radar and hardware configuration were compared by generating a range frequency Doppler frequency spectrum, processing the same number of raw samples as shown in Fig. 4.63, where; (a) is the range frequency Doppler frequency spectrum of an acquisition performed flying at an altitude of 750 m, VV channel, and, (b) is the range frequency Doppler frequency spectrum of an acquisition performed in the lab with antennas connected, VV channel. Approximately 22 dB difference is

noticeable between the noise floor in the two acquisitions.

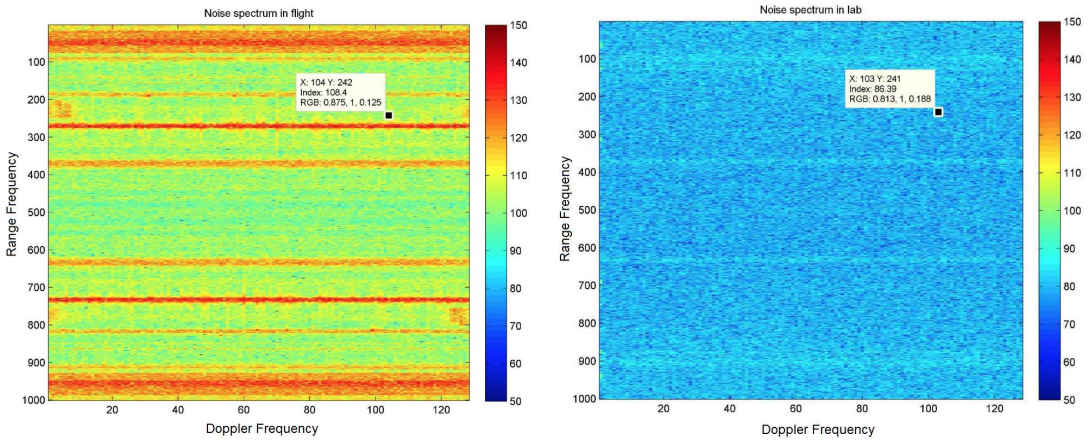

(a) *(b)*

Figure 4.63: *Range Frequency Doppler frequency spectrum of two acquisitions where; (a) Performed flying at an altitude of 750 m, VV channel, and, (b) Performed in the Lab with antennas connected, VV channel.*

We used the runway of the airport as the noise floor due to its lower noise and it was in the middle of the three ranges. Then we selected two areas in the image where it had grass in order to measure the backscatter from the two areas of the grass. As shown in Fig. 4.64, the backscatter from the runway of the airport was 201.4 dB, while the backscatter from the grass in the mid range was 213 dB giving a difference of 11.6 dB. Additionally, the second grass area in the far range gave a backscatter of 211.7 dB showing a difference of 10.3 dB.

(a) *(b)*

Figure 4.64: *Noise floor and grass backscatter where; (a) Backscatter from the runway of the airport, and (b) Backscatter from grass in the mid field.*

Unlike the X-band, the P-band lacks reference for backscatter measurements, and the only backscattering measurements, with the only literature available being written by Freeman et al. in [115] which had an average P-band backscatter value, and estimated scattering mechanism contributions for various land cover types. We selected a farmland, which had a backscatter of -20.3 dB, because there was no grass among the different land cover types. We expected a NESZ of -31.9 dB in the mid range, and -30.6 dB without considering the 22 dB which represents the RFI effect on the noise floor.

4.4 Summary

In this chapter, we presented the installation of three SAR sensors on a Cessna 208 Grand Caravan. Then, we detailed the fully polarimetric calibration of three SAR sensors which were L-, X-, and P-band using multiple passive point targets. The calibration included the crosstalk estimation, phase difference, channel imbalance, radiometric calibration, geometric correction, and noise equivalent sigma zero measurements. The crosstalk parameters were estimated and corrected without using corner reflectors, while the other parameters such as phase, channel imbalance, radiometric, and geometric calibration required the corner reflectors to be estimated and corrected. In the following chapter, we will

present the performance of the gridded trihedral, and gridded dihedral corner reflectors. Furthermore, the chapter includes the compact polarimetric calibration over three compact polarimetric modes using a square trihedral corner reflector.

Chapter 5

Compact Polarimetric Calibration

This chapter presents the performance of gridded trihedral, and gridded dihedral corner reflectors, which were introduced in Section 3.3.4. Additionally, the chapter includes the compact polarimetric calibration over three compact polarimetric modes, using the square trihedral corner reflector in the mid field for X-band dataset, which we fully calibrated in Section 4.3.2. In the following, we first investigate the performance of the two gridded trihedral corner reflectors deployed on 30 November 2016 in the mid field next to the regular trihedral corner reflector to compare the results. The first gridded trihedral corner reflector has horizontal wires, to have a reflection on the horizontal channel, while the second gridded trihedral corner reflector has vertical wires, to have a reflection on the vertical channel.

Secondly, we investigate the performance of the two gridded dihedral corner reflectors deployed 10 m away from the previous gridded trihedral corner reflectors. The first gridded dihedral corner reflector has horizontal wires, to have a reflection on the horizontal channel, while the second gridded dihedral corner reflector has vertical wires, to have a reflection on the vertical channel. Finally, in Section 5.3 we present the calibration of three compact polarimetric modes on X-band dataset which we acquired on 30 November 2016 using the trihedral

corner reflector in the mid field, as well as the gridded trihedral, and gridded dihedral corner reflectors. In the calibration of the three compact polarimetric modes $\pi/4$, DCP, and CTLR, we were interested in the phase and amplitude correction using the corner reflector, as well as measuring the performance of the gridded corner reflectors.

5.1 Introduction

Compact polarimetric SAR is an appropriate concept for the generation of compact polarimetry from a horizontal-vertical polarised antenna. The generation of the compact channels is accomplished by adding the horizontal-vertical channels in quadrature of phase, in order to have a compact polarimetric wave, that is transmitted by the antenna. In practice, however, it is very difficult, if not impossible, to generate a perfect compact polarimetric wave using the actual technology, and an error in phase occurs as a result of the quadrature phase combination of the horizontal-vertical channels [101]. Compact Polarimetry (CP) has the ability of reducing complexity, cost, mass, and data rate of a (SAR) system, while attempting to obtain many capabilities of quad polarisations systems [12].

The compact polarimetric SAR system provides several advantages compared to a full polarimetric SAR system [13] [14] [116]. One of the most important advantages is the doubling of the swath width, and lower energy consumption, as a result of a half pulse repetition frequency of a fully polarimetric system. Moreover, with only one channel in transmission, and two channels in receiving, the data rate can be significantly reduced, and this would be a superior advantage for compact polarimetric systems, especially for a spaceborne SAR system where the data rate is a critical problem [117]. These advantages led to the simpler designs of compact polarimetric SAR systems, with lower costs and lower mass.

To date, the studies from the Indian's first spaceborne SAR system, which can acquire data on compact polarimetric mode (Hybrid mode), are confined to a simulated hybrid polarisation using existing fully polarimetric data without acquiring actual compact polarimetric SAR data [118].

5.2 Performance of Gridded Corner Reflectors

The idea behind designing, and using the gridded trihedral and gridded dihedral corner reflectors, was to have a passive point target reflecting from only one of the four polarisation channels in the fully polarimetric mode. The reflection would happen if the incident wave was parallel to the wires while it would be absorbed if the incident wave was perpendicular to the wires.

The scattering matrix for the gridded corner reflector is presented in Eq. 5.1 for the return from the horizontal channel, when the the grid is horizontal, while Eq. 5.2 is for the return from the vertical channel when the grid is vertical. For example, if we deploy a dihedral corner reflector with a horizontal wires, and transmitting horizontal and vertical polarisations, the horizontal polarisation will be reflected from the dihedral corner reflector, while the vertical polarisation will not.

$$S_{HG} = \begin{bmatrix} 1 & 0 \\ 0 & 0 \end{bmatrix} \tag{5.1}$$

$$S_{VG} = \begin{bmatrix} 0 & 0 \\ 0 & 1 \end{bmatrix} \tag{5.2}$$

Figs. 5.1 and 5.2 illustrate the theoretical polarisation signatures for the gridded corner reflector when the reflection is only from the horizontal channel, while the remaining three channels HV, VH, and VV are zeros, as well as, when the reflection is only from the vertical channel, while the remaining three channels HH, HV, and VH are zeros. These signatures will be used to compare the polarisation signatures from the gridded trihedral and dihedral corner reflectors when we extract their scattering matrix.

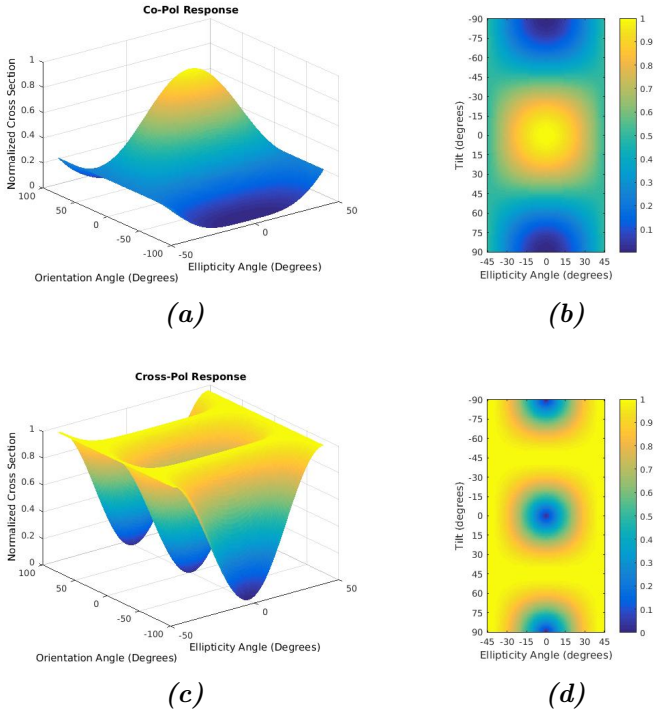

Figure 5.1: *Theoretical polarisation signatures for the gridded corner reflector when the reflection is only from the horizontal channel where; (a) and (b) are the co-polarisation signature, while (c) and (d) are the cross-polarisation signature.*

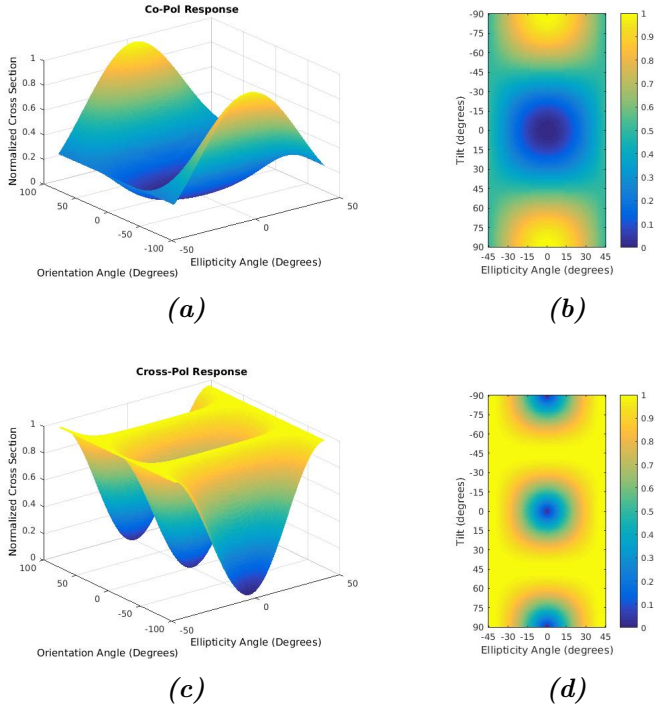

Figure 5.2: *Theoretical polarisation signatures for the gridded corner reflector when the reflection is only from the vertical channel where; (a) and (b) are the co-polarisation signature, while (c) and (d) are the cross-polarisation signature.*

5.2.1 Gridded Trihedral Corner Reflectors

After reading the four polarimetric channels of X-band data on IDL, we exported them to ENVI in order to locate the gridded trihedral corner reflectors, and extract the scattering matrix for both gridded with horizontal wires, and gridded with vertical wires. Figs. 5.3 and 5.4 illustrate the extraction of the gridded trihedral corner reflectors from both the horizontal-horizontal channel, and vertical-vertical channel. These figures from ENVI were taken before any phase and amplitude correction, which we described in Section 4.3.2.2.1. The two gridded trihedral corner reflectors showed a 1.44 channel imbalance (between the two gridded trihedral corner reflectors, and from the channels in which they have the reflection) before correction, and a channel imbalance of 1, after correction,

which is similar to the square trihedral corner reflector in the mid field.

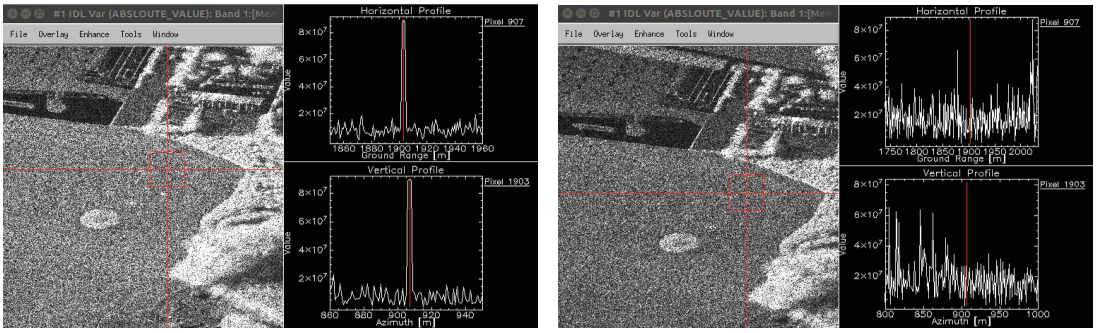

(a) *(b)*

Figure 5.3: *Reading SAR data using IDL, and locating the gridded trihedral corner reflector with horizontal wires on ENVI where; (a) Horizontal-Horizontal Channel, and (b) Vertical-Vertical Channel.*

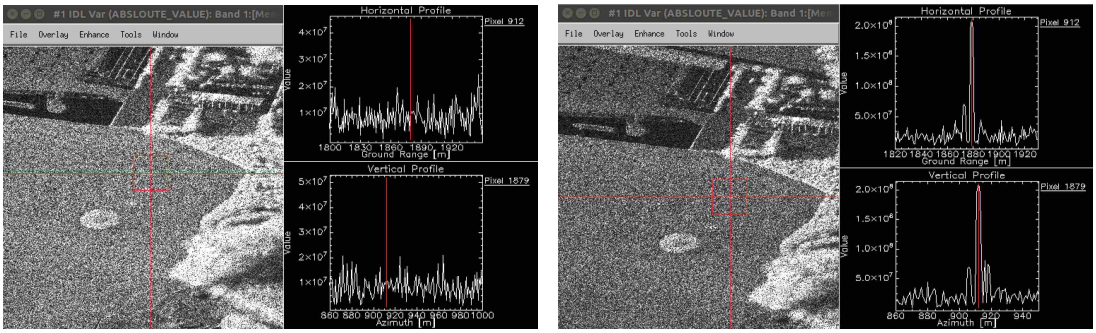

(a) *(b)*

Figure 5.4: *Reading SAR data using IDL, and locating the gridded trihedral corner reflector with vertical wires on ENVI where; (a) Horizontal-Horizontal Channel, and (b) Vertical-Vertical Channel.*

Furthermore, the response from the two gridded trihedral corner reflectors is perfect and shows a return on the horizontal channel if the incidence wave is horizontal, showing a return on the vertical channel if the incidence wave is vertical, while the remaining channels show no return. Additionally, it is not possible to use the gridded trihedral corner reflectors as a calibration target to correct the phase, we need a return from two channels to have a zero phase

difference between the polarisation channels H - V. The polarisation signatures for the two gridded trihedral corner reflectors are presented in Figs. 5.5 and 5.6. The polarisation signatures for the two gridded trihedral corner reflectors match the theoretical polarisation signature in Figs. 5.1 and 5.2.

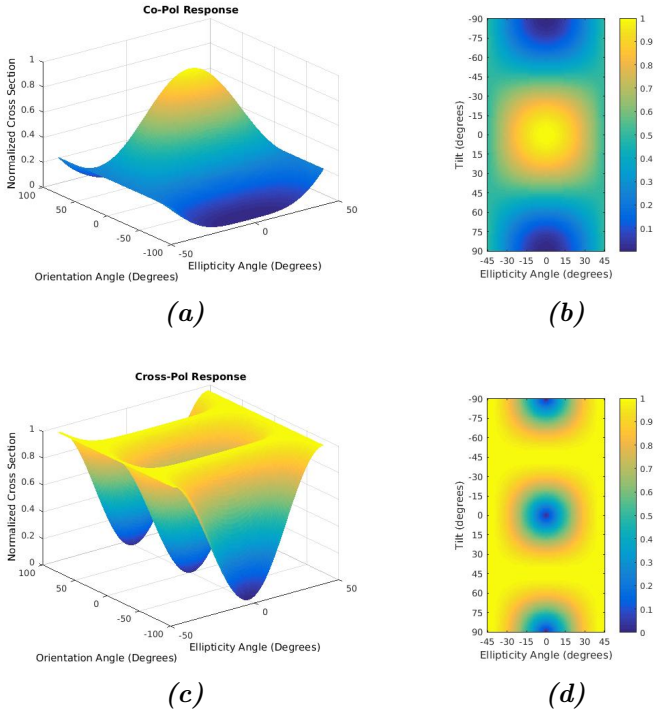

Figure 5.5: *Polarisation signature for the gridded trihedral corner reflector with horizontal wires where; (a) and (b) are the co-polarisation signature, while (c) and (d) are the cross-polarisation signature.*

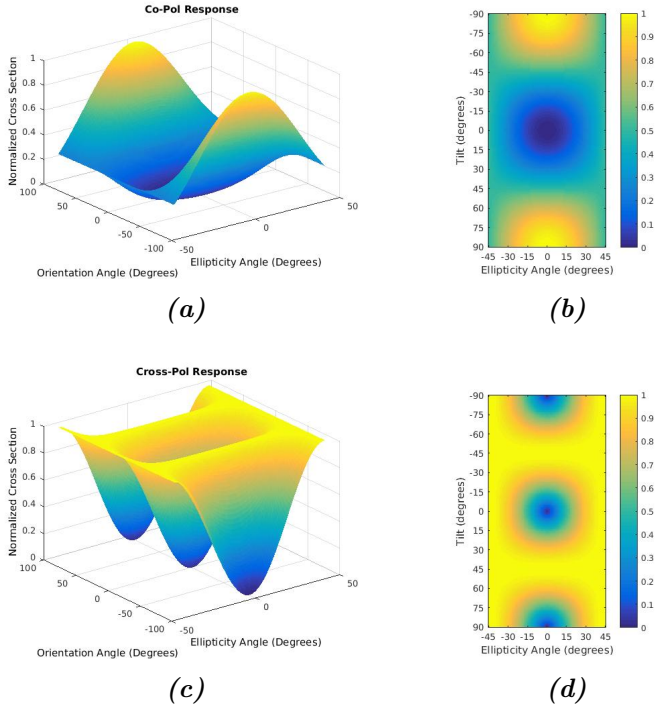

Figure 5.6: *Polarisation signature for the gridded trihedral corner reflector with vertical wires where; (a) and (b) are the co-polarisation signature, while (c) and (d) are the cross-polarisation signature.*

Moreover, we used the integral method for relating the pixel's values of the gridded trihedral corner reflector, which has the return to the backscattering coefficient. Table 5.1 illustrates the integral method parameters calculation for the gridded trihedral corner reflector, and the backscattering coefficient of the gridded trihedral corner reflector. The results showed a reduction of more than 2 dB from the gridded trihedral corner reflector compared to the regular trihedral corner reflector in the mid field. The backscattering coefficient for the two gridded trihedral corner reflectors where we have the reflection is 32 dB. By comparing this to the simulation in Section 3.3.4.3, we can see that the reduction in RCS of 5 dB in simulation, and 2 dB in measurements. The reason is because, when we construct the gridded trihedral corner reflectors, we increased the size of the plates by about 7 cm while cutting the plates, which results in an increase in the total RCS

Table 5.1: *Integral method parameters calculation for gridded trihedral corner reflectors for radiometric calibration*

CR	CR Energy ε_p	Calibration Constant K	θ_i	σ_o
HG	3.9940e16	1.870e13	60.76	1745.40
VG	3.9844e16	1.865e13	60.76	1750.00

5.2.2 Gridded Dihedral Corner Reflectors

The two gridded dihedral corner reflectors, where one with a horizontal reflection, and the other vertical reflection, were deployed in the mid field about 10 m away from both gridded trihedral corner reflectors, as well as, the regular square trihedral corner reflector during the acquisition on 30 November 2016.

Figs. 5.7 and 5.8 show the extraction of the two gridded dihedral corner reflectors from both the horizontal-horizontal channel, and the vertical-vertical channel before any phase and amplitude correction. The two gridded dihedral corner reflectors showed a 1.44 channel imbalance (between the two gridded dihedral corner reflectors and from the channels which have the reflection), before correction, and a channel imbalance of 1 after correction.

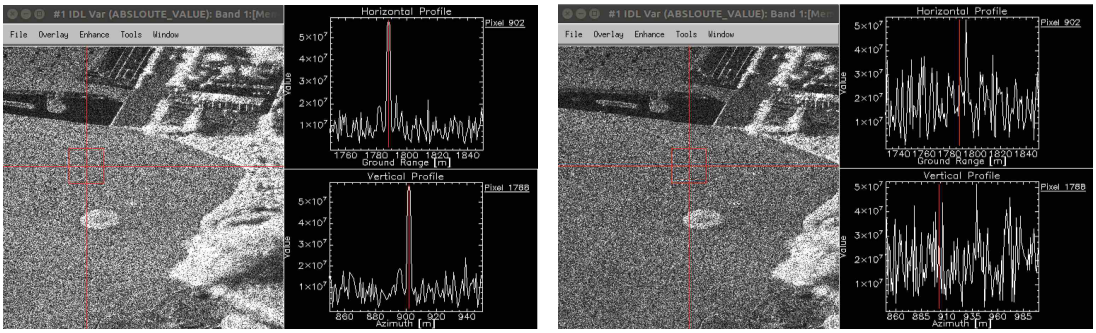

(a) ***(b)***

Figure 5.7: *Reading SAR data using IDL, and locating the gridded dihedral corner reflector with horizontal wires on ENVI where; (a) Horizontal-Horizontal Channel, and (b) Vertical-Vertical Channel.*

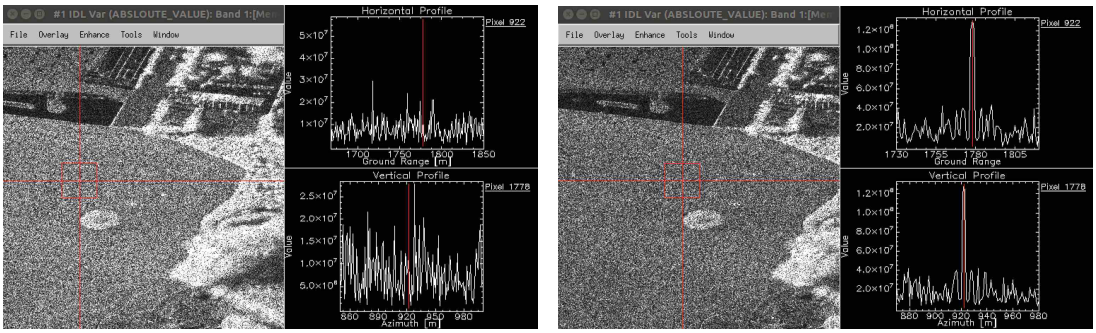

(a) ***(b)***

Figure 5.8: *Reading SAR data using IDL, and locating the gridded dihedral corner reflector with vertical wires on ENVI where; (a) Horizontal-Horizontal Channel, and (b) Vertical-Vertical Channel.*

Moreover, the polarisation signatures for the two gridded dihedral corner reflectors are plotted in Figs. 5.9 and 5.10, showing a perfect response for the two gridded corner reflectors compared to the theoretical response. Additionally, it is not possible to use the gridded dihedral corner reflectors as a calibration target to correct the phase, as we need a return from two channels to have a zero phase difference between the polarisation channels H - V.

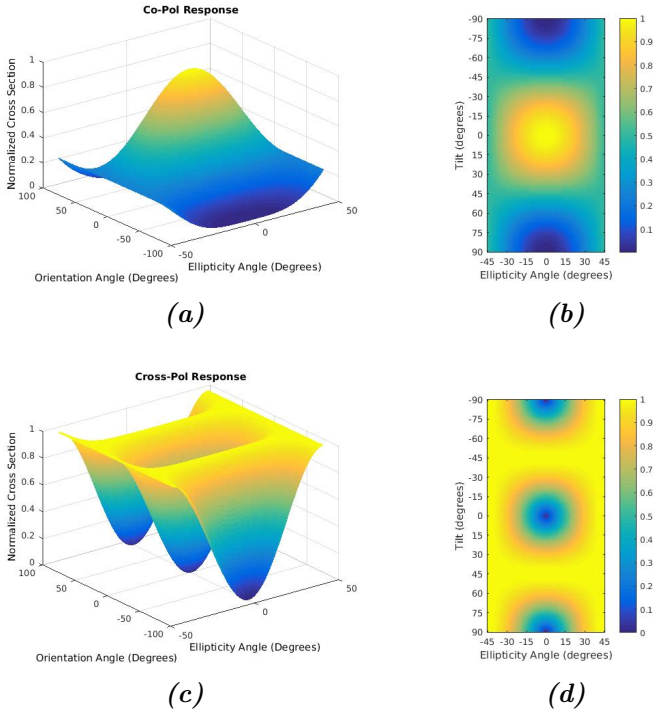

Figure 5.9: *Polarisation signature for the gridded dihedral corner reflector with horizontal wires where; (a) and (b) are the co-polarization signature, while (c) and (d) are the cross-polarisation signature.*

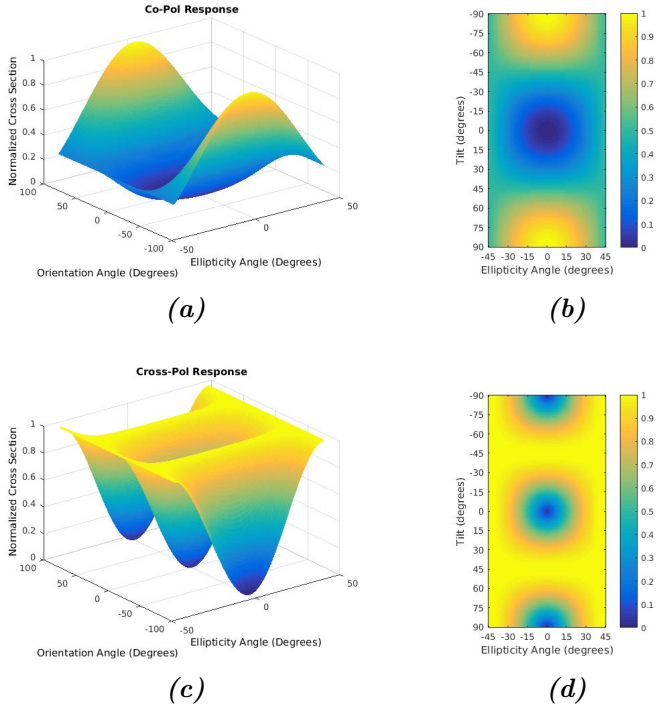

Figure 5.10: *Polarisation signature for the gridded dihedral corner reflector with vertical wires where; (a) and (b) are the co-polarisation signature, while (c) and (d) are the cross-polarisation signature.*

Finally, we used the integral method to relate the pixel's values of the gridded dihedral corner reflector which has the return to the backscattering coefficient. Table 5.2 shows the integral method parameters calculation for the gridded dihedral corner reflector, and the backscattering coefficient of the gridded dihedral corner reflector. The results showed a reduction of 0.6 dB. The backscattering coefficient for the two gridded dihedral corner reflectors, where we have the reflection is 31.8 dB. By comparing this to the simulation in Section 3.3.4.2, we can see that the reduction in RCS of 2 dB in simulation and 0.6 dB in measurements. The difference between the simulation and construction is due to the 7 cm increase while cutting the aluminium plates, which results in an increase in the total RCS.

Table 5.2: *Integral method parameters calculation for gridded dihedral corner reflector for radiometric calibration*

CR	CR Energy ε_p	Calibration Constant K	θ_i	σ_o
HG	1.2817e16	9e12	60.76	1532.22
VG	1.2784e16	8.98e12	60.76	1535.63

The performance of the gridded trihedral and gridded dihedral corner reflectors is perfect for amplitude correction but they cannot be used for correcting the phase in compact polarimetric modes, because we only have the reflection from one polarization channel. In the following, we will use the square trihedral corner reflector, which we deployed in the mid field, to calibrate the three compact polarimetric modes, and we are not using the gridded corner reflectors for amplitude correction, because the results are similar to the regular trihedral corner reflector in the mid field.

5.3 Calibration of Compact Polarimetry

Three compact polarimetric modes were evaluated for phase and channel imbalance correction, using a square trihedral corner reflector, deployed in the mid field on X-band dataset, which we collected on 30 November 2016. Our main focus was on the parameters which we estimated using corner reflectors, such as phase and amplitude correction, as well as radiometric calibration if possible. The data which we used is a fully polarimetric X-band dataset, and it is calibrated as per details mentioned in Section 4.3.2, and we used the scattering vectors in Table 1.1 to generate the three compact polarimetric datasets.

5.3.1 Calibration of $\pi/4$ mode

The first compact polarimetric mode is the $\pi/4$ mode, where we transmit a 45°, and receive both linear horizontal, and vertical polarisations. From the scattering

vectors for the $\pi/4$ mode in Table 1.1, we can see that the two compact channels are derived by adding the HV channel to both HH, and VV to generate the scattering vector. The results of the phase difference and the channel imbalance for the square trihedral corner reflector in the mid field between the two compact polarimetric channels, are presented in Fig. 5.11. The results showed no change in phase between the two compact polarimetric channels, as well as no change in the channel imbalance, due to a zero amount of HV channel from the corner reflector.

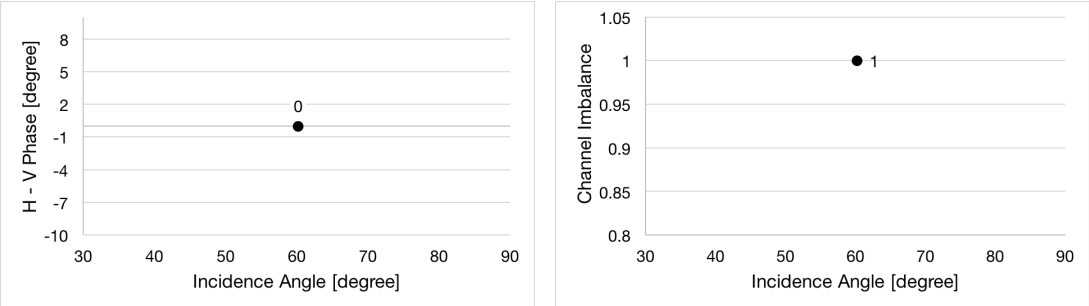

(a) *(b)*

Figure 5.11: *Phase difference and channel imbalance for the $\pi/4$ mode plotted as a function of incidence angle for the mid field corner reflector. (a) Polarisation phase difference for the mid field corner reflector, and (b) Channel imbalance for the mid field corner reflector.*

5.3.2 Calibration of Circular Receive and Linear Transmit (CRLT) Mode

The second compact polarimetric mode is the circular receive and linear transmit (CRLT) mode, where we transmit a left or right circular polarisation, and receive both linear horizontal, and vertical polarisations. From the scattering vectors for the CRLT mode in Table 1.1, we can see that the two compact channels are derived by subtracting the HV channel from the first channel, and adding the HV channel to the second channel, but there was a multiplication by j which caused a shift in the phase. The results are presented in Fig. 5.12 for both phase difference, and channel imbalance between the two compact polarimetric

channels. The results showed a very small change in the channel imbalance of 0.004, due to the small amount of HV channel of the trihedral corner reflector, which is close to zero. Additionally, the phase difference between the two compact polarimetric channels showed a difference in phase of 90°, and we corrected the phase by rotating the H channel until we had a zero phase difference between the two compact polarimetric channels.

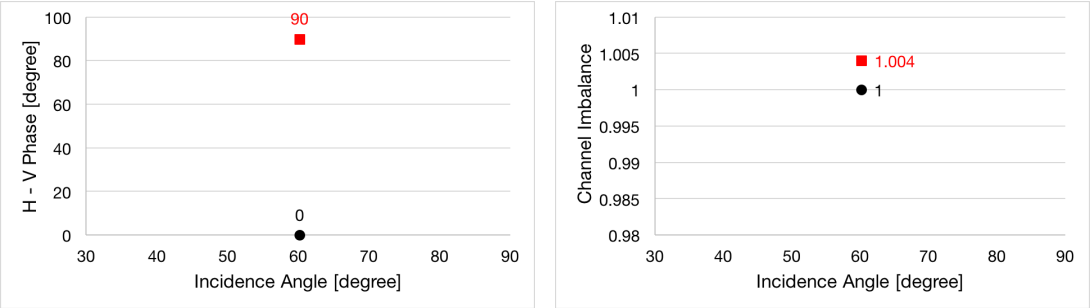

(a) *(b)*

Figure 5.12: *Phase difference and channel imbalance for the CRLT mode plotted as a function of incidence angle for the mid field corner reflector before and after calibration. (a) Polarisation phase difference correction, the red is before calibration while black is after calibration, and (b) Channel imbalance before calibration in red and after calibration in black.*

5.3.3 Calibration of Dual-Circular Polarimetric (DCP) Mode

The third compact polarimetric mode is the dual-circular polarimetric (DCP) mode, where we transmit a left or right circular polarisation, and receive both circular left and right polarisations. From the scattering vectors for the DCP mode in Table 1.1, we can see that the two compact channels are derived by subtracting the VV channel from the HH, and then adding the HV, multiplied by 2j for the first compact channel, while the second compact channel is derived by adding the HH channel to the VV channel, multiplied by j. The results are presented in Fig. 5.13 for both phase difference and channel imbalance between the two compact polarimetric channels. The results for the phase difference be-

tween the two compact polarimetric channels showed a 64.43 ° phase difference, and it was corrected by rotating the H channel until we had a zero phase difference between the two compact polarimetric channels. Furthermore, the channel imbalance was very high, at 45.92, between the two compact polarimetric channels, as a result of adding subtracting the VV channel from the HH for the first channel, as well as, the result of adding the HH channel to the VV channel for the second compact polarimetric channel. The two compact polarimetric channels were adjusted to have a channel imbalance if 1.

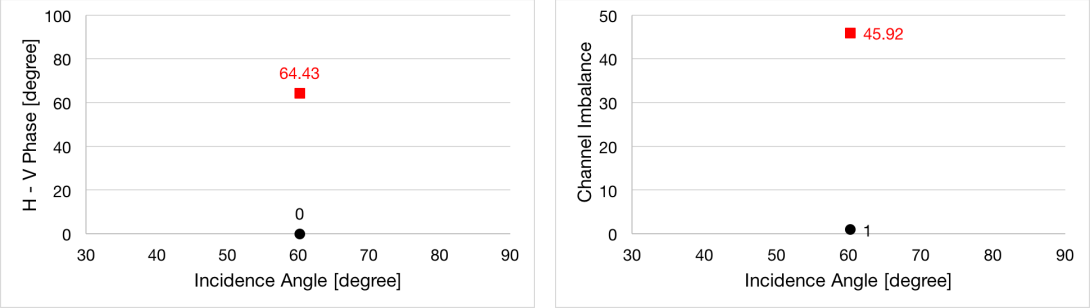

(a) *(b)*

Figure 5.13: *Phase difference and channel imbalance for the DCP mode plotted as a function of incidence angle for the mid field corner reflector before and after calibration. (a) Polarisation phase difference correction of three corner reflectors, the red is before calibration while black is after calibration, and (b) Channel imbalance before calibration in red and after calibration in black.*

In conclusion, by comparing the full polarimetric SAR system to the compact SAR system in terms of crosstalk, the crosstalk for the fully polarimetric SAR system could be estimated and corrected, without relying on corner reflectors based on the Ainsworth method, because it showed much better results compared to the Quegan method. On the other hand, all the existing compact calibration methods are built on the assumption that the compact system transmits a perfect circular polarisation. Unfortunately, the actual technology does not permit the generation of a perfect compact polarisation wave.

Moreover, when comparing the fully polarimetric SAR system to a compact SAR system, in terms of phase, channel imbalance, and radiometric calibration, a fully

polarimetric SAR system has four receiving channels (HH, HV, VH, VV), and by using the trihedral and dihedral corner reflectors rotated by 45°, we have the return from the four polarimetric channels to correct the phase and channel imbalance. Additionally, by using the reciprocity assumption, which assumed the backscatter from the cross-polarisation channels is equal, the trihedral corner reflector is enough for the correction of the phase, and channel imbalance, because we only need the return from the two channels (HH and VV).

On the other hand, the compact polarimetric SAR system has only two receiving channels (H and V), which reduces the number of unknowns, and results, in less corner reflectors to be used for phase and channel correction. Furthermore, the reciprocity assumption is not able to be used in compact modes as there are no cross-polarisation channels. Moreover, one corner reflector is enough for the phase, and channel imbalance, for both fully, and compact SAR systems, while the radiometric calibration required more than one corner reflector along the swath, in order to have a precise radiometric calibration over the entire swath.

5.4 Summary

The chapter illustrated the performance of two gridded trihedral, and two gridded dihedral corner reflectors, and then compared to a classical trihedral corner reflector. Following that, we elaborated the calibration of the three compact polarimetric modes using a square trihedral corner reflector. The $\pi/4$ mode showed no change in phase and channel imbalance, while the CRLT mode showed a small amount of channel imbalance, and a phase difference of 90° before calibration. Finally, the DCP mode showed a 64.43 ° phase difference and when corrected to be zero, and the channel imbalance was very high at 45.92, and was adjusted to be 1. In the following chapter, we performed an experiment to measure the penetration of P-band signal, using two corner reflectors. Also, we measured the polarimetric degradation of trihedral corner reflector immersed in vegetation.

Chapter 6

Penetration of P-band Quad and Compact Polarimetric Signal Into Vegetation

This chapter presents a measurement of signal penetration of low radar frequency on trees, using two triangular trihedral corner reflectors for quad and compact polarimetry. The chapter details the reduction of signal from a triangular trihedral corner reflector, which was immersed in vegetation (trees) compared to another triangular trihedral corner reflector a distance from clutter. In the following, we first introduce a list of previous studies which previously exposed the penetration of low frequency on vegetation and other different applications.

Secondly, we present the deployment of the two triangular trihedral corner reflectors around Teuge airport, the Netherlands, as well as the SAR acquisitions on the 24 November 2016. In Section 6.4 we present an analysis of signal penetration of a fully polarimetric P-band SAR system on trees, using two triangular trihedral corner reflectors. The analysis measures the reduction of amplitude on HH and VV channels, as well as showing the polarimetric degradation of a triangular trihedral corner reflector immersed in trees, after calibration based on the reflector in the clear. Finally, in Section 6.5 we present an analysis of signal

penetration of a P-band SAR system on trees over three compact polarimetric modes.

6.1 Introduction

Synthetic aperture radars (SAR) with longer wavelength enable new opportunities in different SAR applications, such as forested areas and vegetation, due to the penetration capabilities of lower frequencies. For example, L-band and P-band (24 cm wavelength, and 75 cm wavelength) have demonstrated the ability to penetrate to the ground in several forest cover situations [119], while other radar frequencies such as X-band (3 cm wavelength), will penetrate to a lesser extent, and the return is from the top of the canopy. Fig. 6.1 shows the proportional relation between; increasing the radar wavelength, and the rate of penetration to the canopy for three radar frequencies (X-, C-, and L-band).

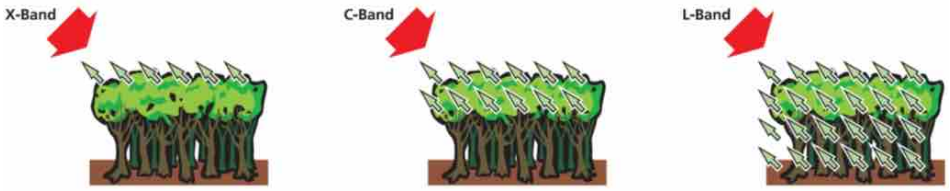

Figure 6.1: *Comparison of the penetration depth in three different radar frequencies; X-band, C-band, and L-band for vegetation [120].*

The potential of using different (SAR) polarisation was brought up by different researchers [121]. For example, the results in [122] [123] [124] [125] showed that the return from the cross-polarisation channels (HV, VH), are more sensitive to forest canopies than co-polarisation channels (HH, VV). Additionally, these observations were supported in [126], who presented a model for P-band backscatter. It showed that the co-polarisation is less correlated to forest biomass than cross-polarisation. The model was able to prove that the backscatter from the HV is faintly sensitive to terrain conditions, and the HH channel is mainly returned as multiple trunkground interactions. Furthermore, a high direct surface scattering in, from either HH or VV polarisation channels, was confirmed

by others in [127] [128] [129] particularly under wet weather conditions. Finally, the comparison between the HH and VV showed differences between the channels. The results showed that the VV channel presented less backscatter than the HH channel. These differences were related to several phenomena such as dihedral [123] [130], or canopy absorption [131] [132].

6.2 Background

The early work in radar vegetation penetration started in the 1970's and came from the military sector. The historical development of foliage penetration was introduced by Surgent, by using a radar operating at frequencies near 140 MHz, and mounted on a helicopter, tower, or hand-held [133]. The author was able to achieve some success in delineating point targets, at fairly high incidence angles, with foliage depths of up to 100 m. Moreover, a similar result was reported by Currie et al. for both one-way, and two-way measurements of foliage attenuation of radar [134]. Both measurements of vegetation used 35 GHz and 95 GHz, and the attenuation increased with the incidence angle because of the subsequent larger path length through the foliage.

During the 1980's Imhoff et al., published results of forest canopy characterisation and vegetation penetration with Spaceborne Radar [135]. They used three L-band SAR data sets with different incidence angles of; 26°, 46°, and 58° which were acquired over the mangrove jungles of Southern Bangladesh. The results showed that the change of incident angle on the canopy from 26° to 58° did not have any effect. The authors think it might have been due to the canopy mass presented in this situation exerting no significant differences in attenuation of the L-band data, which were used over the three incident angles.

In 1994 Wang and Filoso from the centre for remote sensing at the University of California, published a canopy penetration studies of the Amazon floodplain forests using; C-, L-, and P-band [136]. The results showed that the scattering at HH and VV from the C-band, and the VV from L-band, are not able to penetrate the canopies in the stands. The microwave energy penetrated the

canopies, when trunk-ground and canopy-ground terms contributed significantly to the total backscatter. Additionally, the scattering at HH and VV channels for the P-band, as well as the HH channel for L-band, were able to penetrate the canopies, and detect boundaries between flooded and non-flooded forests [137].

In 2007 Redadaa et al. presented a study of P-band penetration capabilities [138]. The paper was addressing the problem of attenuation due to the sub-surface propagation phenomenon using P-band (435 MHz). The Paper presented a different theoretical study about the predictions of attenuation by soil propagation, which depends on incidence angle, polarisation, and moist content. The study concludes with a penetration depth up to 17 m for dry soil before a 3 dB attenuation of the incident wave.

In 2008 Marino et al. published a paper detailing the effect of foliage penetration on polarimetric SAR [139]. They concluded that in a forest environment, it is complicated to predict the interaction of electromagnetic waves, because of the penetration of the target. The results showed that the penetration in a canopy for high frequencies such as C- and X-band were slightly better than expectations, due to the fact that, incoherent scattering of the forest particles is related to their electrical dimensions. The Authors suggested that a better measurement would be by using a bright target such as corner reflector under the canopy.

In 2009 Freeman et al. published a paper on a compact polarimetry mode at low frequency for vegetation applications [140]. The paper detailed the concept of compact polarimetry between the three configurations, as well as the evaluation of which structure is the best for vegetation applications. The choice of transmit polarisation showed that at lower frequency, the circular polarised wave is the optimum choice.

In 2002 Pastore et al. published an evaluation of P-band foliage penetration through polarimetric high resolution SAR imaging with the RAMSES radar [141]. The evaluation was carried out around a cultivated pine forest in south west France using P-band (435 MHz), which has a high resolution (2 m), with full polarimetric capability. The dihedral and trihedral corner reflectors were deployed, the vehicles were also included. The results showed that the returns

from the cover reflector attenuation in horizontal polarisation, depends on the angle of view which is more in vertical polarisation. Moreover, the antenna patterns are wide (+30°) and results in images up to aircraft nadir, which indicate, a confirmation of important penetration through foliage on vertical polarisation.

6.3 Deployment of Corner Reflectors and SAR Acquisitions

Not only the test site was around Teuge airport, the Netherlands used to acquire the data. The airport was also used for the system installation, and making of the corner reflectors prior to deployment. The selected area is only 500 m from the runway as shown in Fig. 6.2. The two yellow place-markers are the two selected areas, where one is immersed in the trees, and the other is outside the trees with about a 100 m distance between them. The outside area is a grass covered field, which is used for parachuting activities, as well as being a distance from clutter. Additionally, the flight path is perpendicular to the runway with a left side looking SAR system.

Figure 6.2: *Test site for collecting the data around Teuge airport, the Netherlands. The flight path is parallel to the airport runway, and the yellow reference point below the runway is for azimuth angle adjustment.*

Furthermore, Fig. 6.3 shows a clear look of the two deployment sites (Between, and outside the trees where the red circle indicate the site of deploying the corner reflector between the trees.

Figure 6.3: *A photo from the airplane over the two sites before collection the data on 24 November 2016*

Two triangular trihedral corner reflectors of 1.5 m inner leg dimension were used for the measurements of P-band signal reduction between and outside the trees. The maximum radar cross section for P-band is 17 dB from both triangular trihedral corner reflectors. Fig. 6.4 shows two different views for the first triangular trihedral corner reflector; mounted on a tripod, and deployed in the open field with a distance from clutter. The corner reflector is about 10 m away from the trees, and deployed on a flat surface.

After levelling the corner reflector, by using the digital angle level levelling, we used the gun-sight to point the reflector toward the reference point, which is the edge of the Gray building in Fig. 3.30(b), and then we rotate the reflector 55°, to have the bottom front edge of the triangular trihedral corner reflector parallel with the flight path, using the digital degree wheel device. Moreover, the incidence angle is calculated to be 60.19° based on the 750 m flight altitude, and a distance of 1309 m from the corner reflector to the flight path.

(a) *(b)*

Figure 6.4: *Two different views of corner reflector on the clear. (a) and (b) Triangular trihedral reflector outside the trees and mounted on a tripod.*

The second triangular trihedral corner reflector, as shown in Fig. 6.5, was immersed in the trees without using the tripod because it was very difficult to move between the trees. The triangular trihedral corner reflector was mounted on the ground, and we used wood to support the reflector from the back, to adjust the angle of the corner reflector in elevation. After levelling the corner reflector on the ground, and pointing it toward the reference point, we rotated the corner reflector by 52° from the reference point, to be parallel to the flight path.

(a) *(b)*

Figure 6.5: *Deployment of triangular trihedral corner reflector immersed in the trees; (a) Back view of the corner reflector, and (b) Front view of the corner reflector.*

The raw data were processed to level.1 SLC images with a presumming factor of 32. Fig. 6.6 shows the SLC Images from 24 November 2016 where; (a) horizontal-horizontal channel, and (b) vertical-vertical channel. The red squares in both images are the two sites were we deployed the triangular trihedral corner reflectors between, and outside the trees.

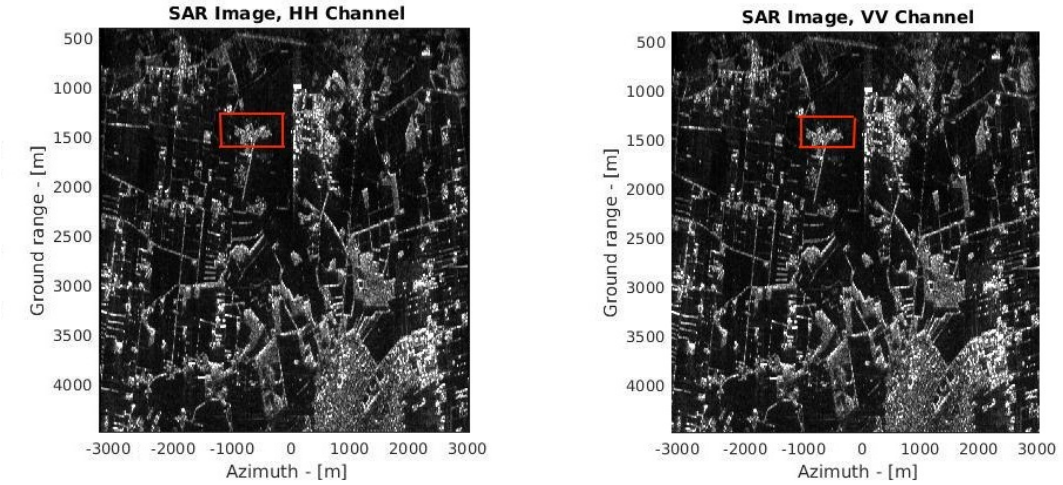

(a) *(b)*

Figure 6.6: *P-band SAR SLC Images from 24 November 2016 where; (a) Horizontal-Horizontal Channel, and, (b) Vertical-Vertical Channel.*

6.4 Penetration of P-Band for Quad Polarimetry

The analysis for the penetration of P-band signal was based on the maximum return from the two channels, HH and VV, for the two triangular trihedral corner reflectors between, and outside the trees. The reason is because the triangular trihedral corner reflector will not generate cross-polarisation components (HV = VH = 0). Also, the horizontal and vertical backscattering cross sections are identical (HH = VV).

Fig. 6.7 shows the extraction of the two corner reflectors location where; (a)

horizontal-horizontal channel outside the trees, and (b) horizontal-horizontal channel immersed in the trees. We used IDL to read the SLC data for each channel (HV = VH), and then imported it to ENVI to locate the maximum response, and exact pixel, where the reflectors are located. Further, Fig. 6.8 shows the two triangular trihedral corner reflectors between and outside the trees for the VV channel where; (a) vertical-vertical channel outside the trees, and (b) vertical-vertical channel immersed in the trees.

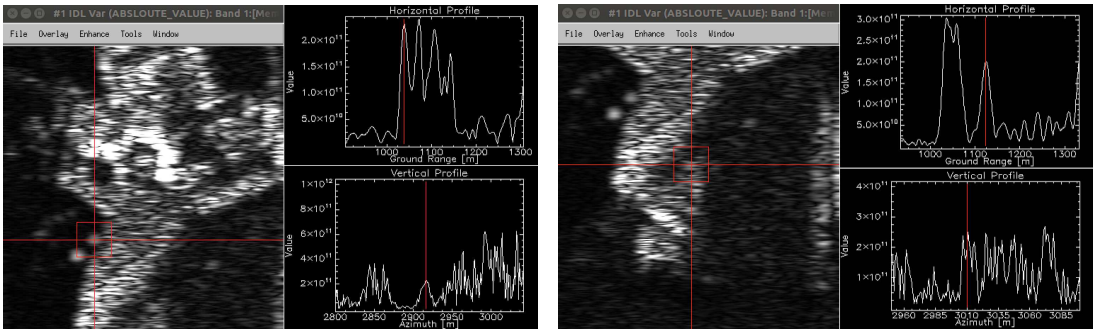

(a) *(b)*

Figure 6.7: *Reading SAR data using IDL, and locating the corner reflector between, and outside the trees using ENVI. (a) Horizontal-Horizontal channel outside the trees, and (b) Horizontal-Horizontal channel immersed in the trees.*

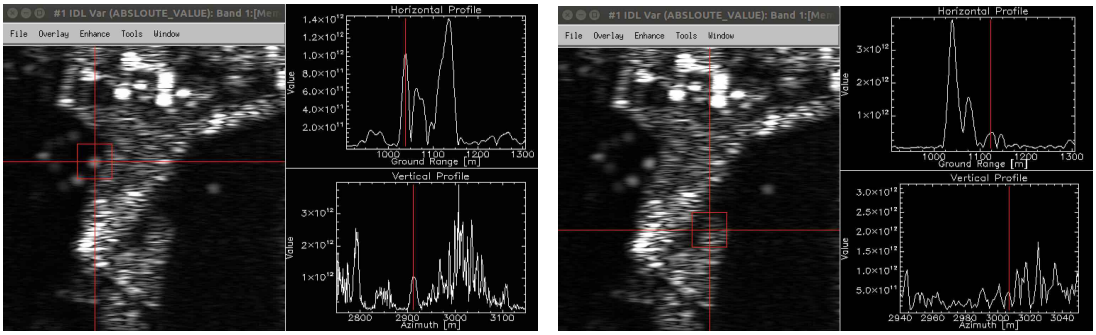

(a) *(b)*

Figure 6.8: *Reading SAR data using IDL, and locating the corner reflector between, and outside the trees using ENVI. (a) Vertical-Vertical channel outside the trees, and (b) Vertical-Vertical channel between the trees.*

The co-polarisation signature for the triangular trihedral corner reflector outside the trees before any phase calibration, and channel imbalance is shown in Fig. 6.9. Additionally, Fig. 6.10 shows the polarisation signature before any phase calibration and channel imbalance.

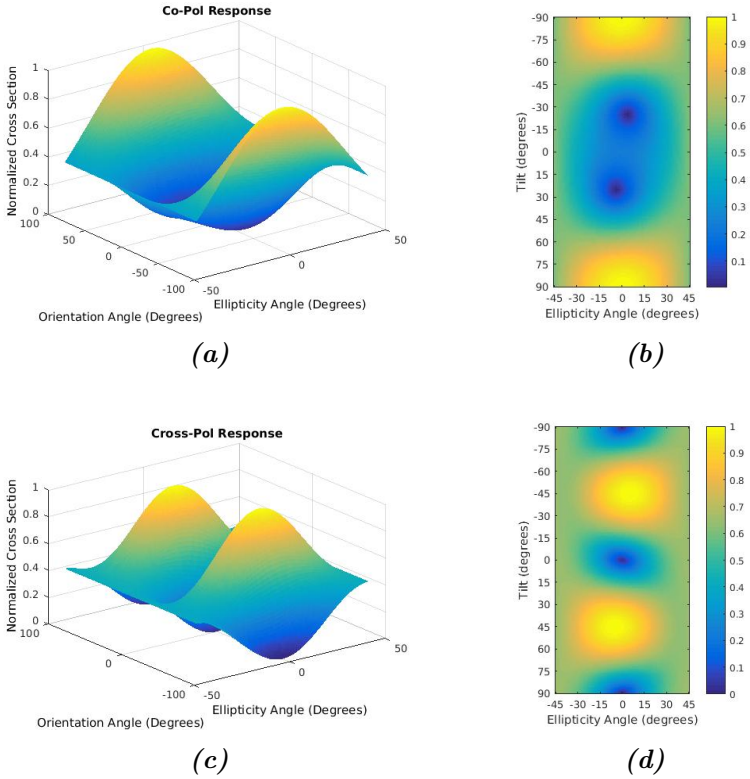

Figure 6.9: *Polarisation signature for the triangular trihedral corner reflector outside the trees before calibration where; (a) and (b) are the co-polarisation signature, while (c) and (d) are the cross-polarisation signature.*

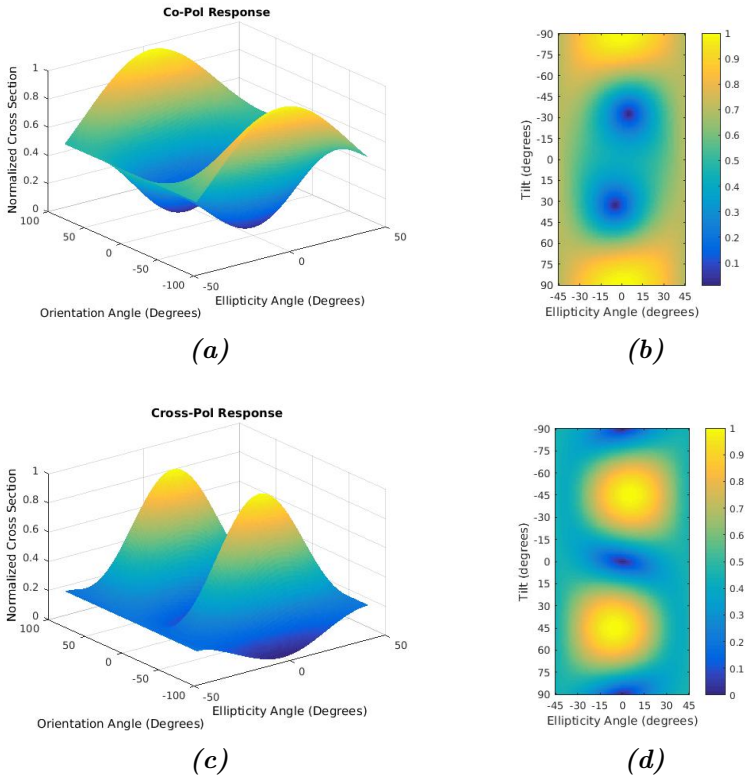

Figure 6.10: *Polarisation signature for the triangular trihedral corner reflectors between the trees before calibration where; (a) and (b) are the co-polarisation signature, while (c) and (d) are the cross-polarisation signature.*

The triangular trihedral corner reflector, which was deployed on the clear (grass covered field), was used as a point target for the calibration of phase and co-channel imbalance. Then, we compared to the results with the other triangular trihedral corner, immersed in the trees, to measure the signal reduction, and also measured the polarimetric degradation of the triangular trihedral corner reflector immersed in vegetation (trees). The phase for the HH channel, before and after calibration, is shown in Fig. 6.11. The phase before calibration of the corner reflector outside the trees is 1.29°, while it is -39° for the triangular trihedral corner reflector, which was immersed in the trees. After the phase calibration, the phase is 157.83° for the triangular trihedral reflector outside the trees, and 154.35° for the triangular trihedral corner reflector immersed in the trees.

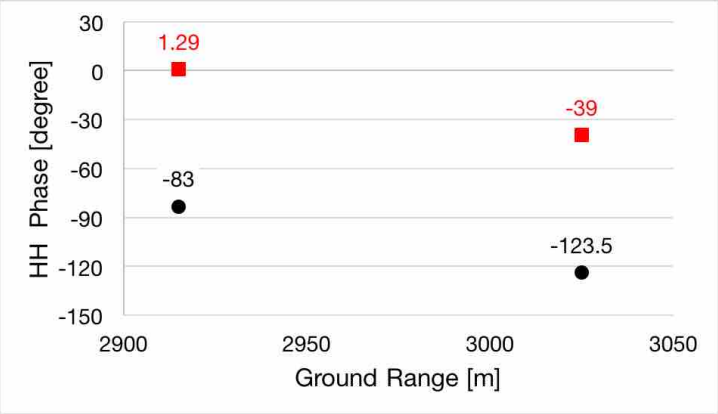

Figure 6.11: *Horizontal-Horizontal channel phase for the two corner reflectors before calibration in red, and after calibration in black.*

Fig. 6.12 shows the co-polarisation phase difference (HH - VV) for the two corner reflectors. The co-polarisation phase difference for the triangular corner reflector, which was outside the trees, is -84.47° before phase calibration, while it is -21.6° for the triangular corner reflector which was immersed in the trees. We used the Zebker method by relying on external passive point targets such as a trihedral corner reflector for the phase calibration which was presented in Section 2.2.2.2. Furthermore, the results for the co-polarisation phase difference are zero degrees for the triangular corner reflector which was outside the trees, and 62.85° for the corner reflector immersed in the trees.

The co-channel imbalance is 2.1 for the triangular trihedral corner reflector outside the trees, as shown in Fig. 6.13, while it is 1.55 for the triangular trihedral corner reflector, which was immersed in the trees before any phase and channel imbalance calibration. After the co-channel imbalance calibration, it is exactly 1 for the triangular trihedral corner reflector outside the trees, and 0.73 for the triangular trihedral corner reflector immersed in the trees.

The co-channel imbalance for the triangular trihedral corner reflector between the trees is less than 1, showing the reduction in the VV channel is more than the HH channel. The reduction of signal is measured by taking the ratio of the HH channel, as well as the ratio of the VV channel. The results showed a reduction of 0.6 dB in the HH channel, while it is 2.28 dB in the VV channel. The larger

attenuation at VV is attributable to the vertical structure of the trees.

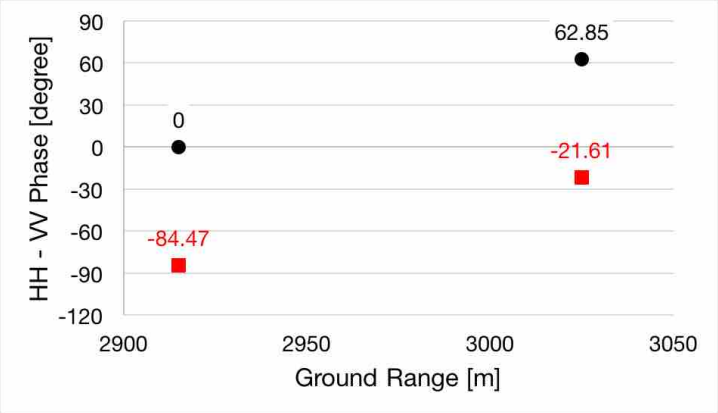

Figure 6.12: *Co-polarisation phase difference correction of the two corner reflectors between, and outside the trees plotted as a function of ground range, the red is before calibration, while the black is after calibration*

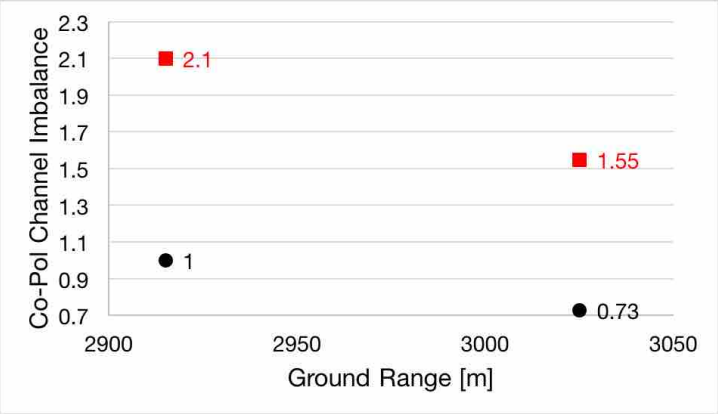

Figure 6.13: *Channel imbalance plotted as a function of ground range before and after calibration. Before calibration in red, and after calibration in black.*

Finally, the polarisation signature is plotted again after calibration for both triangular trihedral corner reflectors between, and outside the trees. Fig. 6.14 shows the polarisation signature after phase calibration, and channel imbalance. The signature matches with the theoretical polarisation signature for a perfect trihedral corner reflector, with a zero phase difference between the co-polarisation channels, as well as a co-channel imbalance at exactly 1. Moreover, the polar-

isation signature for the second triangular trihedral corner reflector, which was immersed in the trees, is shown in Fig. 6.15. The signature is distorted as a result of 62.85° difference in phase between HH and VV channels, as well as a 0.73 for the co-channel imbalance.

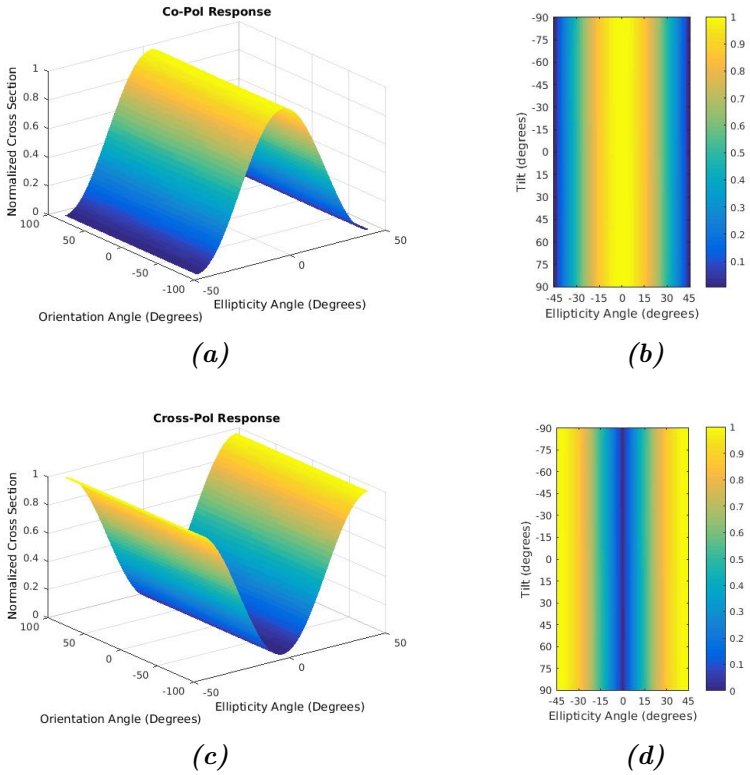

Figure 6.14: *Polarisation signature for the triangular trihedral corner reflectors outside the trees after calibration where; (a) and (b) are the co-polarisation signature, while (c) and (d) are the cross-polarisation signature.*

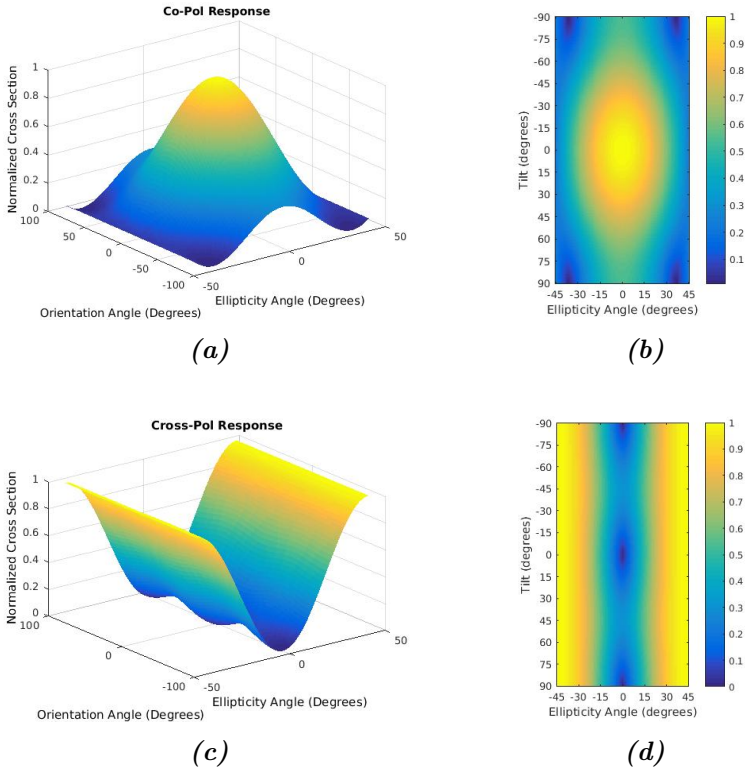

Figure 6.15: *Polarisation signature for the triangular trihedral corner reflectors between the trees after calibration where; (a) and (b) are the co-polarisation signature, while (c) and (d) are the cross-polarisation signature.*

6.5 Penetration of P-Band for Compact Polarimetry

The three compact polarimetric modes were derived from the calibrated fully polarimetric data using the scattering vectors in Table 1.1 for the three different compact polarimetric modes; $\pi/4$, DCP, and CTLR. After deriving these modes, the triangular trihedral corner reflector, outside the trees, was used as a reference target to calibrate the phase different between the H - V channels to be zero for each mode, and then the channel imbalance to be 1 for the three compact polarimetric modes. Finally, the reduction in signal, as well as the polarimetric

degradation of the triangular trihedral corner reflector immersed in trees were measured by comparing the triangular trihedral corner reflector outside the trees, with the triangular trihedral corner reflector immersed in the trees.

6.5.1 Penetration of $\pi/4$ mode

The first compact polarimetric mode is $\pi/4$ mode where we transmit a 45°, and receive both linear horizontal and vertical polarisation. As shown in 6.16 the phase difference H - V, and channel imbalance for the $\pi/4$ mode are plotted as a function of ground range. The phase difference between both linear horizontal, and vertical channels for the triangular trihedral corner reflector outside the trees, is zero and 62.85° for the corner reflector between the trees. Moreover, the channel imbalance is 1 for the corner reflector outside the trees, while it is 0.73 for the corner reflector between the trees. The reduction of signal in both channels is 0.6 dB in the HH channel, while it is 2.28 dB in the VV channel which is similar to the fully polarimetric signal reduction measurements. The only change is a 1.5 dB reduction in amplitude for both linear horizontal, and vertical channels from fully polarimetric data, due to the division of both channels by square root of 2.

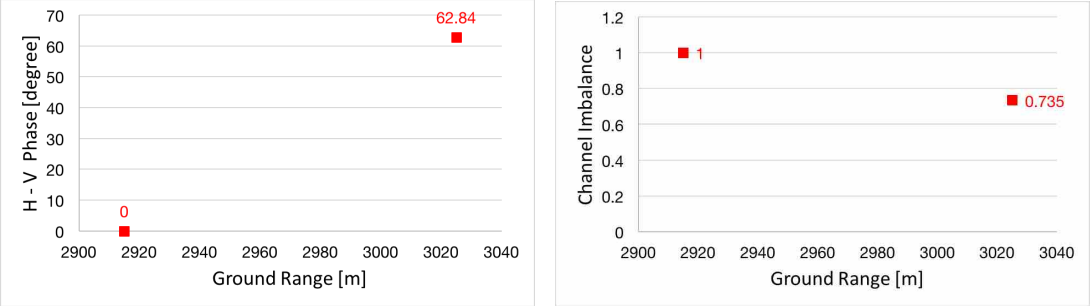

(a) *(b)*

Figure 6.16: *H - V phase difference and channel imbalance for the $\pi/4$ mode plotted as a function of ground range before calibration. Where; (a) H - V phase difference of the two corner reflectors between and outside the trees, and (b) H - V polarisation channel imbalance.*

6.5.2 Penetration of Dual-Circular Polarimetry (DCP) Mode

The second compact polarimetric mode is the DCP mode where we transmit a left or right circular polarisation, and receive both circular left and right polarisation. The results for both phase difference, and channel imbalance for the DCP mode is presented in Fig. 6.17 for the two corner reflectors between, and outside the trees. The triangular trihedral corner reflectors outside the trees showed a calibration phase difference of 78.99°, and a very high channel imbalance of 53.46, as well as a phase different of 143.63°, and a 1.22 channel imbalance for the corner reflector immersed in the trees. The measurement for the signal reduction was done after calibrating both phase, and channel imbalance using the corner reflector outside the trees. The results after calibration showed a zero phase difference for the corner reflector outside the trees, while it showed a 64.66° phase difference for the corner reflector immersed in the trees. Additionally, the channel imbalance was 1 for the corner reflector outside the trees, while it was 0.023 channel imbalance for the corner reflector immersed in the trees. The reduction of signal is -30.4 dB in the horizontal channel, and it is 2.36 dB in the vertical channel.

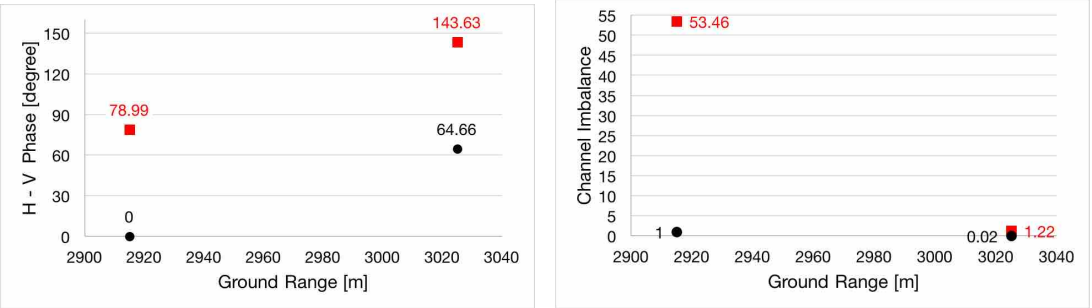

(a) *(b)*

Figure 6.17: *H - V phase difference and channel imbalance for the DCP mode plotted as a function of ground range before and after calibration. Where; (a) H - V phase difference correction of the two corner reflectors between and outside the trees, the red is before calibration while the black is after calibration, and (b) H - V polarisation channel imbalance before calibration in red, and after calibration in black.*

6.5.3 Penetration of Circular Receive and Linear Transmit (CRLT) Mode

The third compact polarimetric mode is the CRLT mode where we transmit a left or right circular polarisation and receive both linear horizontal and vertical polarisation. Fig. 6.18 shows the results for both H - V phase difference and channel imbalance for the two triangular corner reflectors between and outside the trees. The phase difference between the two channels is -90° for the triangular trihedral corner reflector outside the tress while it is -27.15° for the corner reflector immersed in the trees. Additionally, the results from the channel imbalance is the same as the fully polarimetric data, meaning the same reduction in both horizontal and vertical channels, where it is 0.6 dB in the horizontal channel while it is 2.28 dB in the vertical channel. A reduction of 1.5 dB in amplitude for both linear horizontal and vertical channels from the fully polarimetric data occurs due to the division of both channels by square root of 2.

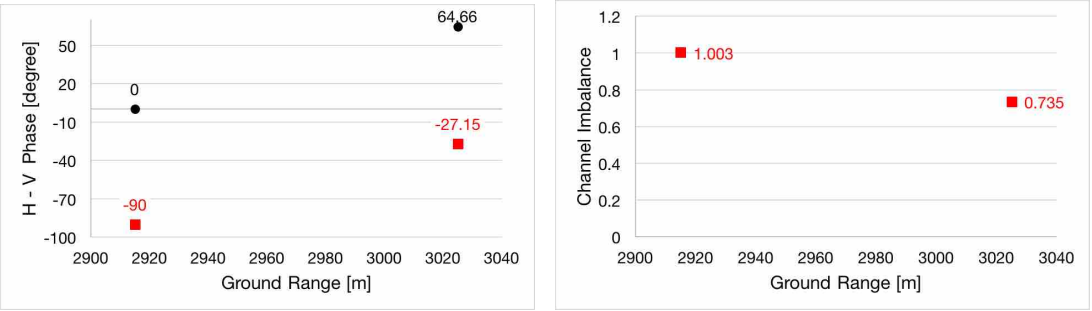

(a) *(b)*

Figure 6.18: *H - V phase difference and channel imbalance for the CRLT mode plotted as a function of ground range before and after calibration. Where; (a) H - V phase difference correction of the two corner reflectors between and outside the trees, the red is before calibration while the black is after calibration, and (b) Channel imbalance before calibration in red, and after calibration in black.*

6.6 Summary

In this chapter, we presented a limited review of the literature of foliage penetration with imaging radar. Then, we illustrated the deployment of two triangular trihedral corner reflectors; where one in a deciduous grove of trees, while the other one was deployed a 10 m distance away in a grass covered field. In time, we presented experimental results for measuring the signal penetration of P-band, fully and compact, SAR systems through the trees using two triangular trihedral corner reflectors around Teuge airport in the Netherlands. Furthermore, we measured the polarimetric degradation of a triangular trihedral corner reflector immersed in vegetation (trees). In the following chapter, we conclude the thesis and suggest a list of topics for future research, related to the field of synthetic aperture radar polarimetry.

Chapter 7

Conclusions

In this dissertation, we used a combination of classic trihedral and dihedral corner reflectors, as well as gridded trihedral and gridded dihedral corner reflectors for the calibration of L-, X-, and P-band synthetic aperture radar. In addition, penetration measurements were performed for a low frequency using two triangular trihedral corner reflectors, as well as a measurement of polarimetric degradation of a triangular trihedral corner reflector immersed in vegetation.

The characteristics of the corner reflectors showed a design of twelve classic trihedral and dihedral corner reflectors (0.5 m inner leg dimension for X-band, and, 1.5 m inner leg dimensions for P-band) using a very thick 1.2 mm aluminium plate and supported by plastic gussets to assure the orthogonality of the plates. Moreover, the results of perforating the corner reflectors showed that the best choice is one-sixth of the wavelength of X-band, and the centre spacing hole is 12 mm. The reason behind the choice is because the reduction will be 1 dBm^2, and we will have a more open area to allow for: quick drainage from heavy rain, cleansing from dust and reduction of the effects of wind, as well as reduction in the total weight of the corner reflectors. Furthermore, the design of the gridded corner reflectors showed that a 3 mm gap and a 0.5 mm wire has the best discrimination, but the construction is difficult because 0.5 mm is very thin and the gap is small.

The calibration of L-band showed an evaluation of the two crosstalk methods, which are the Quegan and Ainsworth methods, and the results for Quegan showed the crosstalk parameters are all around -17 dB to -21 dB before calibration, while there is a small improvement in the range of 3 dB after calibration, while the Ainsworth method showed the cross talk parameters before calibration to be around -20 dB, while it is around -40 dB after calibration. The two square corner reflectors were used for the co-phase and co-channel imbalance estimation and corrections. The radiometric calibration showed a reduction of about 2.8 dB in the backscattering coefficient of the two square trihedral corner reflectors.

Moreover, the calibration of X-band showed the crosstalk for all the parameters before calibration to be around -23 dB, and they are around -43 dB after calibration, by using the Ainsworth method. Six corner reflectors were used for the co- and cross-phase, and co- and cross-channel imbalance, as well as radiometric calibration. The results showed a very small reduction in overall backscattering coefficient for the three corner reflectors of about 0.5 dB. In addition, the results from the geometric correction showed an RMS of 1.48 m in northing and an RMS of 4.73 m in easting before correction, and an RMS of 0.943 m in northing, and an RMS of 0.769 m in easting after correction.

Furthermore, the calibration of P-band showed the crosstalk for all the parameters before calibration to be around -10 dB, and around -30 dB after calibration, by using the Ainsworth method. The two triangular trihedral corner reflectors in the mid and far fields were used for the co-phase and co-channel imbalance estimation and correction, as well as radiometric calibration. The results showed a backscattering coefficient for the reflector in the mid field of 14 dB, while it is a little more for the reflector in far field 14.8 dB. Additionally, the geometric correction results showed an RMS of 2.536 m in northing, and an RMS of 4.019 m in easting before correction, and an RMS of 1.85 m in northing, and an RMS of 0.34 m in easting after correction.

The performance of both gridded trihedral, and gridded dihedral corner reflectors are perfect targets for correcting the amplitude, and the results are similar to the regular square trihedral corner reflector in the mid field in terms of amplitude.

However, it is not possible to use the gridded corner reflectors as a calibration target because in order to correct the phase, we need a return from the two channels to have a zero phase difference between the polarisation channels H - V. The gridded trihedral and gridded dihedral corner reflectors showed a 1.44 channel imbalance (between the two gridded trihedral corner reflectors and from the channels which they obtain the reflection) before correction, and a channel imbalance of 1 after correction. Furthermore, the reduction in RCS for the gridded trihedral corner reflector was 5 dB in simulation, and 2 dB in measurements. Additionally, the backscattering coefficient for the two gridded dihedral corner reflectors where we have the reflection is 31.8 dB giving a reduction in RCS of 0.6 dB in measurements, while it was 2 dB in simulation.

The difference between the simulation and construction for both gridded reflectors is due to the increase in the size of the plates of about 7 cm during the cutting the plates during the construction phase, which results in an increase in the total RCS. Furthermore, the compact polarimetric calibration, using the square trihedral corner reflector in the mid field, showed no changes in the phase between the two compact polarimetric channels, as well as no change in the channel imbalance due to the zero amount of HV channel from the corner reflector for the $\pi/4$ mode. The CRLT mode showed a very small change in the channel imbalance of 0.004, and the phase difference between the two compact polarimetric channels showed a difference in phase of 90°, so we corrected the phase between the two compact polarimetric channels to have a zero phase difference. Finally, the results for the DCP mode showed a 64.43° phase difference, and it was corrected to have a zero phase difference between the two compact polarimetric channels. Additionally, the channel imbalance was a very high 45.92 between the two channels, so the two compact polarimetric channels were adjusted to have a channel imbalance of 1.

The signal penetration measurements of a P-band SAR system in vegetation (trees), using two triangular trihedral corner reflectors for fully polarimetry, showed a reduction of 0.6 dB in the HH channel, while it is 2.28 dB in the VV channel. The larger reduction in the VV channel is due to the vertical construction of the trees. Furthermore, the co-polarisation phase difference is zero

degrees for the triangular corner reflector, which was outside the trees, and the polarimetric degradation of the triangular trihedral corner reflector immersed in trees was 62.85°.

Moreover, the reduction of P-band signal over the three compact polarimetric modes $\pi/4$, DCP, and CTLR, showed the $\pi/4$ mode has a 1.5 dB reduction in amplitude for both horizontal and vertical channels from fully polarimetric data. The CRLT mode showed similar results to the $\pi/4$ mode, except the phase difference between the horizontal and vertical polarisation was -90° for the corner reflector outside the trees before calibration. After calibrating the data, using the corner reflector outside the trees as a reference point target, the reduction in signal, as well as the phase difference, became similar to the $\pi/4$ mode. Finally, the results from the DCP mode after calibration showed a zero phase difference for the corner reflector outside the trees, while a 64.66° phase difference for the corner reflector immersed in the trees. Additionally, the channel imbalance of 1 for the corner reflector outside the trees, while a 0.023 channel imbalance for the corner reflector immersed in the trees. The reduction of signal is -30.4 dB in the horizontal channel, and it is 2.36 dB in the vertical channel.

7.0.1 Future Work

A list of suggested topics for future research in the field of synthetic aperture radar polarimetry are presented hereafter.

- The research focused on the calibration of a multistatic SAR system and all the corner reflectors which we used, are related to the calibration of a fully polarimetric multistatic SAR system. An opportunity of research would be to investigate the calibration of fully polarimetric bistatic SAR systems, as well as developing a passive point targets for the calibration of bistatic SAR systems.
- Our P-band data were collected from an Airborne SAR system. If the data was from a spaceborne SAR system, the calibration would need more effort for Faraday rotation corrections and ionospheric effects removal.

- A very challenging future project is the development of an active radar calibrator, for the calibration of both fully and compact polarimetric SAR systems.
- Unlike the X-band, the P-band lack of reference for backscatter measurements and the only backscattering measurements available in literature is by Freeman et al. It would be a better chance to investigate the backscatter from different land covers, such as grass and sand, at a different incidence angle for a P-band SAR system, as well as the attenuation of a P-band SAR system by sand.
- Looking at different forest types and how the penetration varies, and comparing the results to our P-band data.
- Investigate other parameters in fully polarimetric calibration such as 3 dB resolution in range and azimuth, PSLR, ISLR.
- Comparing the results between un-calibrated and calibrated full-pol data for different compact polarimetric modes and then calibrate

Bibliography

[1] R. Guran, A. Mittra and P. Moser, *Electromagnetic Wave Interactions*. World Scientific Pub Co Inc, 1997. 1

[2] J. Lee and E. Pottier, *Polarimetric Radar Imaging From Basics to Applications*. Taylor & Francis, 2009. 1, 2

[3] R. Huynen, *Phenomenological Theory of Radar Targets*. PhD thesis, University of Technology,Delft,The Netherlands, Dec 1970. 1

[4] A. Villa, L. Iannini, D. Guarnieri, A. Mont-Guarnieri, and S. Tebaldini, "Calibration of SAR polarimetric images by means of a covariance matching approach," *Geoscience and Remote Sensing, IEEE Transactions on*, vol. 53, no. 2, pp. 674–686, 2014. 2, 93

[5] W. Yang, C. Xi, G. Jialong, and J. Kai, "Internal and external calibration of POLINSAR," in *Radar, 2011. CIE '11. International Conference*, vol. 1, pp. 879–882, Oct 2006. 2

[6] A. Freeman, "SAR calibration: An overview," *Geoscience and Remote Sensing, IEEE Transactions on*, vol. 30, no. 6, pp. 1107–1121, 1992. 2, 37, 47

[7] A. Freeman, "Radiometric calibration of SAR image data," *XVII Congress for Photogrammetry and Remote Sensing(ISPRS)*, pp. 212–222, 1993. 2

[8] A. Hein, *Processing of SAR Data*. Springer, 2004. 3

[9] B. Wolfgang, *Polarimetry in radar remote sensing. Basic and applied concepts, In manual of remote sensing: Principle and Applications of Imaging Radar*. Wiley, 1998. 3

[10] A. Kumar and R. Panigrahi, "Classification of hybrid-pol data based on euclidean distance between stokes vectors," in *Radar Conference, 2015. Proceedings of the IEEE*, pp. 422–425, 2015. 3

[11] M. Lavalle, *Full and Compact Polarimetric Radar Interferometry for Vegetation Remote Sensing*. PhD thesis, University of Rennes,France, May 2010. 4, 36, 66

[12] M. Nord, T. Ainsworth, J. Lee, and N. Stacy, "Comparison of compact polarimetric synthetic aperture radar modes," *Geoscience and Remote Sensing, IEEE Transactions on*, vol. 44, no. 1, pp. 174–188, 2009. 4, 5, 155

[13] J. Souyris, P. Imbo, R. Fjortoft, S. Mingot, and J. Lee, "Compact polarimetry based on symmetry properties of geophysical media: The $\pi/4$ mode," *Geoscience and Remote Sensing, IEEE Transactions on*, vol. 43, no. 3, pp. 634–646, 2005. 4, 51, 155

[14] R. Raney, "Hybrid-polarity SAR architecture," *Geoscience and Remote Sensing, IEEE Transactions on*, vol. 45, no. 11, pp. 3397–3404, 2007. 4, 155

[15] N. Stacy and M. Preiss, "Compact polarimetric analysis of X-band SAR data," in *Radar Conference. EUSAR 2006. European.* 5

[16] B. Souissi, M. Ouarzeddine, and A. Belhadj-Aissa, "Yamagushi decomposition based on the compact polarimetry mode using RADARSAT-2 data," in *Signal Image Technology and Internet Based Systems, 2012. SITIS. 18th International Conference on*, pp. 209–213, 2012. 5

[17] B. Souissi, M. Ouarzeddine, and A. Belhadj-Aissa, "Investigation of the capability of the compact polarimetry mode to reconstruct full polarimetry mode using RADARSAT2 data," *Advanced Electromagnetics*, vol. 1, no. 1, pp. 19–28, 2012. 5

[18] V. Nandan, *Retrieval of volume scatterer information using three-component decompostion model, based on compact polarimetry*. PhD thesis, University of Twente,The Netherlands, March 2012. 6

[19] K. Sarabandi, L. Pierce, M. Dobson, F. Ulaby, A. Freeman, P. Dubois, J. Stiles, T. Chiu, R. De Roo, R. Hartikka, and A. Zambetti, "Polarimetric calibration of SIR-C using point and distributed targets," *Geoscience and Remote Sensing, IEEE Transactions on*, vol. 33, no. 4, pp. 858–866, 1995. 7, 29

[20] B. Doring, P. Looser, M. Jirousek, and M. Schwerdt, "Reference target correction based on point-target SAR simulation," *Geoscience and Remote Sensing, IEEE Transactions on*, vol. 50, no. 3, pp. 951–959, 2012. 7, 9

[21] D. Brunfeldt and F. Ulaby, "Active reflector for radar calibration," *Geoscience and Remote Sensing, IEEE Transactions on*, vol. GE-22, no. 2, pp. 165–169, 1984. 7, 28

[22] J. Richards, *Remote Sensing with Imaging Radar*. Springer, 2009. 7, 8, 9

[23] H. Hanado, H. Kumagai, T. Iguchi, T. Kozu, K. Nakamura, and H. Horie, "Calibration of an airborne multiparameter precipitation radar with an active radar calibrator," in *Geoscience and Remote Sensing Symposium (IGARSS), 1996 IEEE International*, pp. 512–514, May 1996. 7

[24] S. Yueh, J. Kong, and R. Shin, "Calibration of polarimetric radars using in-scene reflectors," *Electromagnetic Waves and Applications*, vol. 4, no. 1, pp. 27–48, 1990. 8

[25] M. Satake, T. Kobayshi, T. Manabe, and H. Masuko, "Polarimetric calibration of X-band airborne synthetic aperture radar using corner reflectors and an active radar calibrator," in *Geoscience and Remote Sensing Symposium (IGARSS), 1994 IEEE International*, pp. 2209–2211, Aug 1994. 8

[26] K. Sarabandi and T. Chiu, "Optimum corner reflectors for calibration of imaging radars," in *Geoscience and Remote Sensing Symposium (IGARSS), 1995 IEEE International*, pp. 2241–2243, July 1995. 8, 30, 56

[27] P. Ferrer, C. Lopez-Martinez, A. Aguasca, L. Pipia, J. Gonzalez-Arbesu, X. Fabregas, and J. Romeu, "Transpolarizing trihedral corner reflector characterization using a GB-SAR system," *Geoscience and Remote Sensing, IEEE Transactions on*, vol. 8, no. 4, pp. 774–778, 2011. 8

[28] T. Osman and A. Alzubaidi, "Analysis of radar cross sectional area of corner reflectors," *Proceedings of the IOSR*, vol. 4, pp. 47–51, December 2014. 8

[29] N. Vyjayanthi, *Synthetic Aperture Radar Data Analysis for Vegetation Classification and Biomass Estimation of Tropical Forest Area*. PhD thesis, Jawaharlal Nehru Technological University, April 2012. 10

[30] J. Van Zyl and K. Yunjin, *Synthetic Aperture Radar Polarimetry*. Wiley, 2011. 10, 44, 45, 47, 56

[31] A. Algafsh, M. Inggs, and A. Mishra, "Investigation of calibration aspects of fully and compact polarimetric SAR systems," in *Microwave Conference (APMC), 2016 Asia-Pacific, IEEE Conference on*, pp. 1–5, Dec 2016. 14

[32] A. Algafsh, M. Inggs, and A. Mishra, "The effect of perforating the corner reflector on maximum radar cross section," in *Microwave Symposium (MMS), 2016 16th Mediterranean, IEEE Conference on*, pp. 1–4, Nov 2016. 14

[33] H. Hirosawa and Y. Matsuzaka, "Calibration of a cross-polarized SAR image using dihedral corner reflectors," *Geoscience and Remote Sensing, IEEE Transactions on*, vol. 26, no. 5, pp. 697–700, 1988. 28

[34] D. Kahny and J. Van Zyl, "How does corner reflector construction affect polarimetric SAR calibration?," in *Geoscience and Remote Sensing Symposium (IGARSS), 1990 IEEE International*, pp. 1093–1097, May 1990. 28

[35] C. Unal, R. Niemeijer, J. Van Sinttruyen, and L. Ligthart, "Calibration of a polarimetric radar using a rotatable dihedral corner reflector," *Geoscience and Remote Sensing, IEEE Transactions on*, vol. 32, no. 4, pp. 837–845, 1994. 29

[36] K. Sarabandi, L. Pierce, Y. O., M. Dobson, F. Ulaby, A. Freeman, and P. Dubois, "Cross calibration experiment of JPL AIRSAR and truck mounted polarimetric scatterometer," *Geoscience and Remote Sensing, IEEE Transactions on*, vol. 32, no. 5, pp. 975–985, 1994. 29

[37] D. Ugsang, K. Honda, and S. Genya, "Assessment of small passive corner reflectors for geometric correction of RADARSfine mode SAR data," in *Asian Conference on Remote Sensing*, November 2001. 30

[38] M. Satake, T. Umehara, A. Nadai, H. Maeno, S. Uratsuka, T. Matsuoka, and H. Honma, "Development of polarization selective corner reflectors and its experiment for calibration of airborne polarimetric synthetic aperture radar," in *Geoscience and Remote Sensing Symposium (IGARSS), 2001 IEEE International*, pp. 417–419, July 2001. 30

[39] H. Wakabayashi, T. Tadono, M. Matsuoka, T. Matsuoka, M. Shimada, and S. Uratsuka, "Cross-calibration experiment of airborne L-band polarimetric SAR," in *Geoscience and Remote Sensing Symposium (IGARSS), 2001 IEEE International*, pp. 423–425, July 2001. 31

[40] D. J., M. Schwerdt, and R. Bauer, "TerraSAR-X calibration ground equipment," in *Wave Propagation in Communication, Microwave Systems and Navigation, 2007. WFMN07. Conference on*, July 2007. 31

[41] Y. Lihai, G. Jialong, J. Kai, and Y. Yanmei, "Research on synthetic aperture radar imaging characteristics of point targets," in *Synthetic Aperture Radar, 2009 APSAR 2nd Asian-Pacific Conference on*, pp. 282–285, 2009. 31

[42] C. Li, J. Zhao, Y. Jingyuan, G. Zhang, and X. Shan, "Analysis of RCS characteristic of dihedral corner and triangular trihedral corner reflectors,"

in *Computer Science and Education, 2010 ICCSE 5th International Conference on*, pp. 40–43, 2010. 32

[43] E. Chapin, A. Chau, J. Chen, B. Heavey, S. Hensley, Y. Lou, R. Machuzak, and M. Moghaddam, "Airmoss: An airborne p-band SAR to measure root-zone soil moisture," in *Radar Conference, 2012. Proceedings of the IEEE*, pp. 693–698, 2012. 32, 57

[44] M. Garthwaite, M. Thankappan, M. Williams, S. Nancarrow, A. Hislop, and J. Dawson, "Corner reflectors for the australian geophysical observing system and support for calibration of satellite-borne synthetic aperture radars," in *Geoscience and Remote Sensing Symposium (IGARSS), 2013 IEEE International*, pp. 266–269, July 2013. 32, 75

[45] Y. Qin, D. Perissin, and L. Lei, "The design and experiments on corner reflectors for urban ground deformation," *International Journal of Antennas and Propagation*, vol. 2013, 2013. 33

[46] Y. Zhou, C. Li, L. Ma, M. Yang, and Q. Liu, "Improved trihedral corner reflector for high-precision SAR calibration and validation," in *Geoscience and Remote Sensing Symposium (IGARSS), 2014 IEEE International*, pp. 454–457, July 2014. 33

[47] S. D. Robertson, "Targets for microwave radar navigation," in *Bell System Technical Journal, 1947. Proceedings of the IEEE*, vol. 26, pp. 852–869, 1947. 34

[48] M. Zink and H. Kietzmann, "Next generation SAR - external calibration," in *German Aerospace Center (DLR)*, 1995. 34

[49] S. Zhang and B. Sun, "Imaging characteristics of corner reflector under multi-azimuth angles," in *Electromagnetic Research Symposium (PIERS), 2016 Progress in*, pp. 2898–2909, 2016. 34

[50] D. Sheen, E. Johansen, L. Elenbogen, and E. Kasischke, "The gridded trihedral: a new polarimetric SAR calibration reflector," *Geoscience and*

Remote Sensing, IEEE Transactions on, vol. 30, no. 6, pp. 1149–1153, 1992. 34

[51] J. Van Zyl, H. Zebker, and C. Elachi, "Imaging radar polarization signatures: Theory and observation," *Radio Science*, vol. 24, pp. 529–543, July 1987. 35

[52] D. Sheen, E. Johansen, and L. Elenbogen, "Evaluation of gridded trihedrals for polarimetric calibration of SAR images," in *Geoscience and Remote Sensing Symposium (IGARSS), 1991 IEEE International*, pp. 1393–1396, Jun 1991. 35

[53] M. Lavalle, E. Pottier, T. Ainsworth, D. Solimini, and B. Rosich, "Calibration of dual polarimetric C-band SAR data: a possible approach for sentinel-1," in *Science and Applications of SAR Polarimetry and Polarimetric Interferometry, PolInSAR 2009 Workshop on*, 2009. 35, 66

[54] J. Chen and S. Quegan, "Calibration of spaceborne CTLR compact polarimetric low-frequency SAR using mixed radar calibrators," *Geoscience and Remote Sensing, IEEE Transactions on*, vol. 49, no. 7, pp. 2712–2723, 2011. 37, 52, 66

[55] H. Zhang, C. Wang, P. Ma, W. Lu, Z. Shan, and J. Chen, "Improvement of pol SAR calibration based on the ainsworth algorithm," in *Synthetic Aperture Radar, 2012. EUSAR. 9th European Conference on*, pp. 531–534, April. 37, 38, 41, 43

[56] J. Van Zyl, "Calibration of polarimetric radar images using only image parameters and trihedral corner reflector responses," *Geoscience and Remote Sensing, IEEE Transactions on*, vol. 28, no. 3, pp. 337–348, 1990. 37, 38

[57] R. Touzi and M. Chimada, "Calibration and validation of polarimetric ALOS2," in *Geoscience and Remote Sensing Symposium (IGARSS), 2015 IEEE International*, pp. 4113–4116, July 2015. 37

[58] X. Chen, T. Wu, and X. Zhong, "Airborne polarimetric SAR experiments with different crosstalk calibration techniques," in *Radar, 2011. CIE. International Conference on*, pp. 1393–1401, Oct 2011. 38, 40, 42, 43

[59] J. Klein and A. Freeman, "Quadpolarisation SAR calibration using target reciprocity," *Electromagnetic Waves and Applications*, vol. 5, pp. 735–751, 1991. 38, 40

[60] H. kriver, J. Dall, and S. Madsen, "External polarimetric calibration of the danish polarimetric C-band SAR," in *Geoscience and Remote Sensing Symposium (IGARSS), 1994 IEEE International*, pp. 1105–1107, Aug 1994. 38, 40, 41, 42, 99

[61] S. Quegan, "A unified algorithm for phase and cross-talk calibration of polarimetric data-theory and observations," *Geoscience and Remote Sensing, IEEE Transactions on*, vol. 32, no. 1, pp. 89–99, 1994. 38, 40, 99, 100

[62] T. Ainsworth, L. Ferro-Famil, and J.-S. L., "Orientation angle preserving a posteriori polarimetric SAR calibration," *Geoscience and Remote Sensing, IEEE Transactions on*, vol. 44, no. 4, pp. 994–1003, 2006. 38, 41, 99, 102, 116, 140

[63] H. Zhang, C. Wang, P. Ma, W. Lu, Z. Shan, and J. Chen, "Improvement of polarimetric SAR calibration based on the ainsworth algorithm for chinese airborne polSAR data," *Geoscience and Remote Sensing, IEEE Transactions on*, vol. 10, no. 4, pp. 898–902, 2013. 38, 41, 43

[64] J. Klein, "Calibration of complex polarimetric SAR imagery using backscatter correlations," *Aerospace and Electronic Systems, IEEE Transactions on*, vol. 28, no. 1, pp. 183–194, 1992. 40

[65] H. Kimura, T. Mizuno, K. Papathanassiou, and I. Hajnsek, "Improvement of polarimetric SAR calibration based on the quegan algorithm," in *Geoscience and Remote Sensing Symposium (IGARSS), 2004 IEEE International*, pp. 184–187, Sept 2004. 41

[66] T. Ainsworth and J. Lee, "A new method for a posteriori polarimetric SAR calibration," in *Geoscience and Remote Sensing Symposium (IGARSS), 2001 IEEE International*, pp. 420–422, July 2001. 41, 99, 102, 116, 140

[67] H. Skriver, P. Mortensen, and P. Gudmandsen, "Calibration and modelling of MAESTRO-1 polarimetric SAR data of a forest area in les landes, france," *International Journal of Remote Sensing*, vol. 15, no. 14, pp. 2737–2754, 1994. 42

[68] L. Wuping, W. Chao, Z. Hong, J. Kai, and C. Xi, "Comparison of polarimetric calibration techniques and their applications," in *Geoscience and Remote Sensing Symposium (IGARSS), 2010 IEEE International*, pp. 2888–2891, July 2010. 42

[69] H. Zhang, C. Wang, P. Ma, W. Lu, Z. Shan, and J. Chen, "An improved crosstalk estimation algorithm o polarimetric and interferometric SAR calibration," in *Science and Applications of SAR Polarimetry and Polarimetric Interferometry, PolInSAR 2011 Workshop on*, 2011. 43

[70] A. Fore, B. Chapman, B. Hawkins, C. Jones, T. Michel, and R. Muellerschoen, "UAVSAR polarimetric calibration," *Geoscience and Remote Sensing, IEEE Transactions on*, vol. 53, no. 6, pp. 3481–3491, 2015. 43, 99, 116, 140

[71] H. Zebker, J. van Zyl, S. Durden, and L. Norikane, "Calibrated imaging radar polarimetry: technique, examples, and applications," *Geoscience and Remote Sensing, IEEE Transactions on*, vol. 29, no. 6, pp. 942–961, 1991. 44, 46, 93

[72] D. Sheen, A. Freeman, and E. Kasischke, "Phase calibration of polarimetric radar images," *Geoscience and Remote Sensing, IEEE Transactions on*, vol. 27, no. 6, pp. 719–731, 1989. 44

[73] J. Van Zyl, H. Zebker, and D. Held, "Imaging radar polarimetry from wave synthesis," *Journal of Geophysical Research*, vol. 92, no. B1, pp. 683–701, 1987. 44

[74] Y. Lou and J. Van Zyl, "Relative phase calibration of the NASAD/C-8 three frequency polarimetric SAR system," in *Geoscience and Remote Sensing Symposium (IGARSS), 2004 IEEE International*, pp. 104–105, May 1992. 44, 45

[75] H. Zebker and Y. Lou, "Phase calibration of imaging radar polarimeter stokes matrices," in *Geoscience and Remote Sensing Symposium (IGARSS), 1989 IEEE International*, pp. 2881–2884, July 1989. 46

[76] H. Zebker and Y. Lou, "Phase calibration of imaging radar polarimeter stokes matrices," *Geoscience and Remote Sensing, IEEE Transactions on*, vol. 28, no. 2, pp. 246–252, 1990. 46, 93

[77] Y. Lihai, G. Jialong, and J. Kai, "Research on efficient calibration techniques for airborne SAR systems," in *Synthetic Aperture Radar, 2009 APSAR 2nd Asian-Pacific Conference on*, pp. 266–269, 2009. 47

[78] M. Schwerdt, B. Brautigam, and M. Bachmann, "Final terraSAR-X calibration results based on novel efficient methods," *Geoscience and Remote Sensing, IEEE Transactions on*, vol. 48, no. 2, pp. 677–689, 2009. 47

[79] A. Shimada, T. Tadono, and M. Matsuoka, "Calibration and validation of PALSAR," in *Geoscience and Remote Sensing Symposium (IGARSS), 2002 IEEE International*, pp. 384–386, June 2002. 47

[80] M. Dobson, F. Ulaby, and D. Brunfeldt, "External calibration of SIR-B imagery with area- extendedand and point targets," *Geoscience and Remote Sensing, IEEE Transactions on*, vol. GE-24, no. 4, pp. 453–461, 1986. 47

[81] A. Luscombe, "Image quality and calibration of RADARSAT-2," in *Geoscience and Remote Sensing Symposium (IGARSS), 2009 IEEE International*, pp. 757–760, June 2009. 47

[82] E. S. Kasischke, "Practical SAR radiometric calibration measurements and experiments," in *Geoscience and Remote Sensing Symposium (IGARSS), 1989 IEEE International*, pp. 234–237, July 1989. 47

[83] L. Frulla, J. Milovich, and H. Karszenbaum, "Radiometric corrections and calibration of SAR images," in *Geoscience and Remote Sensing Symposium (IGARSS), 1998 IEEE International*, pp. 1147–1149, July 1998. 47

[84] H. Jun, Z. Bing-Rong, and W. Hong-Qi, "The progress of the airborne SAR calibration techniques in China," in *Geoscience and Remote Sensing Symposium (IGARSS), 1999 IEEE International*, pp. 422–424, Jun 1999. 47

[85] B. Doring, P. Looser, and M. Jirousek, "Point target correction coefficients for absolute SAR calibration," in *Instrumentation and Measurement Technology Conference, 2011. Proceedings of the IEEE*, 2011. 48

[86] Y. Desnos, F. Seifert, and M. Loiselet, "A workstation for Ers-1 / J-ers-1 / multifrequency polarimetric SAR calibration and validation," in *Geoscience and Remote Sensing Symposium (IGARSS), 1992 IEEE International*, pp. 659–662, May 1992. 48

[87] A. Gray, P. Vachon, and C. Livingstone, "Synthetic aperture radar calibration using reference reflectors," *Geoscience and Remote Sensing, IEEE Transactions on*, vol. 28, no. 3, pp. 374–383, 1990. 48, 109

[88] Q. Wang, Q. Zeng, and J. Jiao, "Determination of vertical antenna pattern of high-resolution airborne SAR and radiometric calibration," in *Geoscience and Remote Sensing Symposium (IGARSS), 2012 IEEE International*, pp. 4022–4025, July 2012. 48, 49, 109

[89] M. Satake, T. Umehara, and T. Kobayashi, "Corner reflectors' responses observed by X-band polarimetric airborne synthetic aperture radar," in *Geoscience and Remote Sensing Symposium (IGARSS), 1999 IEEE International*, pp. 2667–2669, July 1999. 48, 109

[90] A. Woode, Y. Desnos, and H. Jackson, "The development and first results from the ESTEC ERS-1 active radar calibration unit," *Geoscience and Remote Sensing, IEEE Transactions on*, vol. 30, no. 6, pp. 1122–1130, 1992. 48

[91] Y. Desnos and M. Loiselet, "ERS-1 ans multifrequency polarimetric SAR calibration-validation results," *Advanced Electromagnetics*, vol. 2, no. 2, pp. 22–31, 1993. 48

[92] I. Ulander, "Accuracy of using point targets for SAR calibration," *Aerospace and Electronic Systems, IEEE Transactions on*, vol. 27, no. 1, pp. 139–148, 1991. 48

[93] F. Holecz, E. Meier, and J. Piesbergen, "Radiometric calibration of airborne SAR imagery," in *Geoscience and Remote Sensing Symposium (IGARSS), 1994 IEEE International*, pp. 1096–1098, Aug 1994. 49

[94] E. Kasischke, D. Sheen, and G. Fowler, "Radiometric calibration of airborne SAR data," in *Geoscience and Remote Sensing Symposium (IGARSS), 1988 IEEE International*, pp. 711–714, Sep 1988. 49

[95] M. Dostovalov, A. Kadantsev, and V. Shaposhnikov, "Improvement of radiometric calibration accuracy using super resolution methods," in *Synthetic Aperture Radar, 2008. EUSAR. 7th European Conference on*, pp. 1–4, 2008. 49

[96] F. Zongmin, H. Lei, T. Zhihua, L. Jiuli, and Z. Liangbo, "Airborne SAR radiometric calibration using point targets," in *Symposium on Remote Sensing of Environment (ISRE35), 2014 International*, pp. 1–6, June 2014. 50

[97] K. El-Darymli, P. McGuire, and E. Gill, "Understanding the significance of radiometric calibration for synthetic aperture radar imagery," in *Electrical and Computer Engineering, 2014. (CCECE). 27th Canadian Conference on*, pp. 1–6, May 2014. 50

[98] S. Upadhayay, B. Rani, and S. Pandey, "Radiometric correction of RISAT-1 data," in *Communication and Signal Processing (ICCSP), 2016 IEEE International Conference on*, pp. 86–90, Nov 2016. 50

[99] M. Mishra, P. Patel, H. Srivastava, and A. Shukla, "Absolute radiometric calibration of FRS-1 and MRS mode of RISAT-1 synthetic aperture radar

SAR data using corner reflectors," *International Journal of Advanced Engineering Research and Science (IJAERS)*, vol. 1, no. 6, pp. 78–89, 2014. 50

[100] M. Mishra, P. Patel, H. Srivastava, and A. Shukla, "Approach for absolute radiometric calibration of RISAT-1 SAR data using standard target," *International Journal of Remote Sensing and Geoscince*, vol. 4, no. 1, pp. 28–32, 2015. 50

[101] R. Touzi and F. Charbonneau, "Requirements on the calibration of hybrid-compact SAR," in *Geoscience and Remote Sensing Symposium (IGARSS), 2014 IEEE International*, pp. 1109 – 1112, July 2014. 51, 53, 155

[102] A. Freeman, P. Dubois-Fernandez, and M. Truong-Loi, "Compact polarimetry at longer wavelengths calibration," in *Synthetic Aperture Radar, 2008. EUSAR. 7th European Conference on*, pp. 1–4, 2008. 52

[103] M. Truong-Loi, P. Dubois-Fernandez, E. Pottier, A. Freeman, and J. Souyris, "Potentials of a compact polarimetric SAR system," in *Geoscience and Remote Sensing Symposium (IGARSS), 2010 IEEE International*, pp. 742–745, July 2010. 52

[104] J. Hong and H. Tan, "Correction of transmit crosstalk in reconstruction of quad-pol data from compact polarimetry data," *Geoscience and Remote Sensing, IEEE Transactions on*, vol. 12, no. 5, pp. 1051–1055, 2015. 53

[105] M. BV, "Waseda xp-SAR system technical specifications," tech. rep., Sep 2015. 56, 60, 136

[106] P. J. Ferrer, C. Lopez-Martinez, A. Aguasca, L. Pipia, J. M. Gonzalez-Arbesu, X. Fabregas, and J. Romeu, "Transpolarizing trihedral corner reflector characterization using a GB-SAR system," *Geoscience and Remote Sensing, IEEE Transactions on*, vol. 8, no. 4, pp. 774–778, 2011. 66, 67

[107] J. Pere, J. Gonzalez-Arbesu, C. Craeye, and J. Romeu, "Transpolarizing surfaces and potential applications," in *Microwave, 2008. EuMC. 38th European Conference on*, pp. 281–284, 2008. 67

[108] P. J. Ferrer, C. Lopez-Martinez, A. Aguasca, L. Pipia, J. M. Gonzalez-Arbesu, X. Fabregas, and J. Romeu, "Transpolarizing surfaces for polarimetric SAR systems calibration," *Geoscience and Remote Sensing Symposium, IEEE Transactions on*, pp. 1585–1588, 2007. 67

[109] K. Sarabandi, E. Pierce, and F. Ulaby, "Calibration of a polarimetric imaging SAR," *Geoscience and Remote Sensing, IEEE Transactions*, vol. 30, no. 3, pp. 540–549, 1992. 93

[110] V. Alberga, *Comparison of polarimetric methods in image classification and SAR interferometry applications*. PhD thesis, Institut of Hochfrequenztechnik and Radar systeme,Germany, January 2004. 94

[111] M. Younis, S. Huber, A. Patyuchenko, F. Bordoni, and G. Krieger, "Performance comparison of reflector- and planar-antenna based digital beam-forming SAR," *International Journal of Antennas and Propagation*, vol. 2009, 2008. 137

[112] M. Villano, "SNR and noise variance estimation in polarimetric SAR data," *Geoscience and Remote Sensing Letters, IEEE Transactions*, vol. 11, no. 1, pp. 278–282, 2014. 137

[113] F. Ulaby and C. Dobson, *Handbook of Radar Scattering Statistics for Terrain*. Artech House, 1989. 137, 138

[114] P. Wu, L. Yang, Y. Zhang, Z. Dong, M. Wang, and S. Du, "A modified notch filter for suppressing radio-frequency-interference in P-band SAR data," in *Geoscience and Remote Sensing Symposium (IGARSS), 2016 IEEE International*, July 2016. 149

[115] A. Freeman and S. L. Durden, "A three-component scattering model for polarimetric SAR data," *Geoscience and Remote Sensing, IEEE Transactions*, vol. 36, no. 3, pp. 963–973, 1998. 152

[116] A. Freeman, "On the design of spaceborne polarimetric SARs," in *Radar Conference (RADAR), 2009 IEEE*, May 2009. 155

[117] J. Hong and H. Tan, "Calibration of compact polarimetric SAR images using distributed targets and one corner reflector," *Geoscience and Remote Sensing, IEEE Transactions*, vol. 54, no. 8, pp. 4433–4444, 2016. 155

[118] V. Turkar, S. De, and Y. Rao, "Comparative analysis of classification accuracy for RISAT-1 compact polarimetric data for various land-covers," in *Geoscience and Remote Sensing Symposium (IGARSS), 2013 IEEE International*, July 2013. 155

[119] B. Mercer, J. Maduck, and E. Kahr, "Validation of dtms beneath forest canopy derived from p-band polarimetric insar." http://http://www.isprs.org/proceedings/XXXVI/part1/Papers/T03-10.pdf. Accessed: 1-Nov-2016. 172

[120] Microwaves and R. InstituteDLR, "Penetration depth in X-band, C-band and L-band." http://http://www.dlr.de/hr/en/desktopdefault.aspx/tabid-8113/14171_read-35852/. Accessed: 1-January-2017. 172

[121] N. Ackermann, *Growing Stock Volume Estimation in Temperate Forested Areas Using a Fusion Approach with SAR Satellites Imagery*. Springer, 2015. 172

[122] T. Toan, A. Beaudoin, and J. Riom, "Relating forest biomass to SAR data," *Geoscience and Remote Sensing, IEEE Transactions on*, vol. 30, no. 2, pp. 403–411, 1992. 172

[123] F. Ulaby, M. Dobson, and T. Toan, "Dependence of radar backscatter on coniferous forest biomass," *Geoscience and Remote Sensing, IEEE Transactions on*, vol. 30, no. 2, pp. 412–415, 1992. 172, 173

[124] W. Shih-tseng and A. Steven, "Multipolarization SAR data for surface feature delineation and forest vegetation characterization," *Geoscience and Remote Sensing, IEEE Transactions on*, vol. GE-25, no. 1, pp. 67–76, 1987. 172

[125] Y. Hussin, R. Reich, and R. Hoffer, "Estimating splash pine biomass using radar backscatter," *Geoscience and Remote Sensing, IEEE Transactions on*, vol. 29, no. 3, pp. 427–431, 1991. 172

[126] A. Beaudoin, T. Toan, S. Goze, E. Nezry, E. Lopes, A. Mougin, C. Hsu, H. Han, J. Kong, and R. Shin, "Retrieval of forest biomass from SAR data," *International Journal of Remote Sensing*, vol. 15, no. 14, pp. 2777–2796, 1994. 172

[127] K. Ranson and G. Sun, "Effects of environmental conditions on boreal forest classification and biomass estimates with SAR," *Geoscience and Remote Sensing, IEEE Transactions on*, vol. 38, no. 3, pp. 1242–1252, 2000. 173

[128] H. Balzter, J. Baker, M. Hallikainen, and E. Tomppo, "Retrieval of timber volume and snow water equivalent over a finnish boreal forest from airborne polarimetric synthetic aperture radar," *International Journal of Remote Sensing*, vol. 23, no. 16, pp. 3185–3208, 2002. 173

[129] M. Santoro, L. Eriksson, J. Askne, and C. Schmullius, "Assessment of standwise stem volume retrieval in boreal forest from JERS1 Lband SAR backscatter," *International Journal of Remote Sensing*, vol. 27, no. 16, pp. 3425–3454, 2006. 173

[130] M. Watanabe, M. Shimada, A. Rosenqvist, T. Tadono, M. Matsuoka, S. Romshoo, K. Ohta, R. Furuta, K. Nakamura, and T. Moriyama, "Forest structure dependency of the relation between L-band sigma and biophysical parameters," *Geoscience and Remote Sensing, IEEE Transactions on*, vol. 44, no. 11, pp. 3154–3165, 2006. 173

[131] J. Van Zyl, "The effect of topography on radar scattering from vegetated areas," *Geoscience and Remote Sensing, IEEE Transactions on*, vol. 31, no. 1, pp. 153–160, 1993. 173

[132] M. Santoro, J. Fransson, L. Eriksson, M. Magnusson, L. Ulander, and H. Olsson, "Signatures of ALOS PALSAR L-band backscatter in swedish

forest," *Geoscience and Remote Sensing, IEEE Transactions on*, vol. 47, no. 12, pp. 4001–4019, 2009. 173

[133] J. Surgent and V. Louis, "Foliage penetration radar: History and developed technology," tech. rep., Georgia Institute of Technology, 12 1975. 173

[134] C. Currie, E. Martin, and B. Dyer, "Radar foliage penetration measurements at millimeter wavelengths," tech. rep., Army Land Warfare Laboratory, 05 1974. 173

[135] M. Imhoff, M. Story, C. Vermillion, F. Khan, and F. Polcyn, "Forest canopy characterization and vegetation penetration assessment with space-borne radar," *Geoscience and Remote Sensing, IEEE Transactions on*, vol. GE-24, pp. 535–542, 1986. 173

[136] Y. Wang, L. Hess, and S. Filoso, "Canopy penetration studies: modeled radar backscatter from amazon floodplain forests at C-, L-, and P-band," in *Geoscience and Remote Sensing Symposium (IGARSS), 1994 IEEE International*, pp. 1060–1062, Aug 1994. 173

[137] G. Sun, *Radar Backscattering Modeling of Coniferous Forest Canopies*. PhD thesis, University of California,Santa Barbara,USA, Dec 1990. 174

[138] S. Redadaa, A. Boualleg, N. Merabtine, and M. Benslama, "A study of P-band penetration capabilities: Application in sub-surface remote sensing." 2007. 174

[139] A. Marino, R. Horn, and K. Viergever, "Foliage penetration effect on polarimetric SAR interferometry observation of forest," in *Radar Conference, 2008. EUSAR 2008. 7th European*, 2006. 174

[140] A. Freeman, P. Dubois-Fernandez, and M. Truong-Loi, "Compact polarimetry mode at low frequency for vegetation applications," in *Radar Conference, 2009. Proceedings of the International*, pp. 309–314, 2009. 174

[141] L. Pastore and H. Cantalloube, "Evaluation of P-band foliage penetration through polarimetric high resolution SAR imaging with the RAMSES

radar," in *Radar Conference, 2002. Proceedings of the International*, pp. 1–4, 2002. 174

Appendix A

Polarisation Signature

A.1 L-Band Polarisation Signature

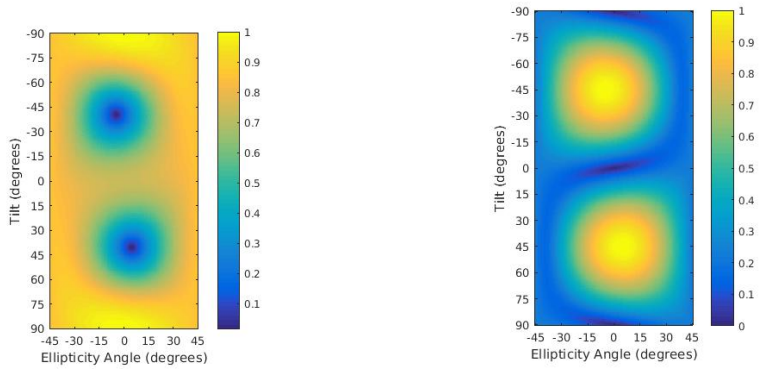

(a) *(b)*

Figure A.1: *Polarisation signature for L-band dataset, before calibration is applied, for the first corner reflector where; (a) The co-polarisation signature, while (b) The cross-polarisation signature.*

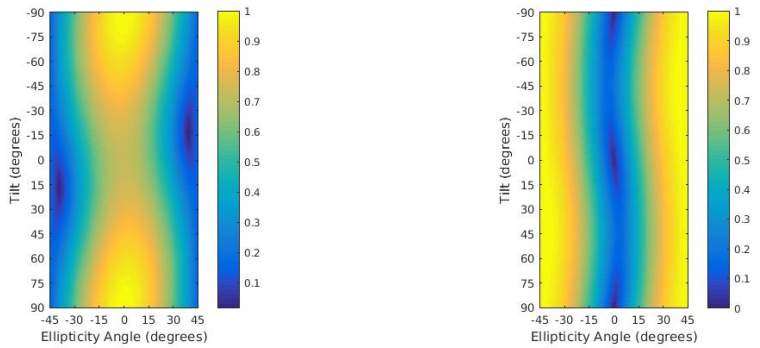

(a) ***(b)***

Figure A.2: *Polarisation signature for L-band dataset, before calibration is applied, for the second corner reflector close to the runway where; (a) The co-polarisation signature, while (b) The cross-polarisation signature.*

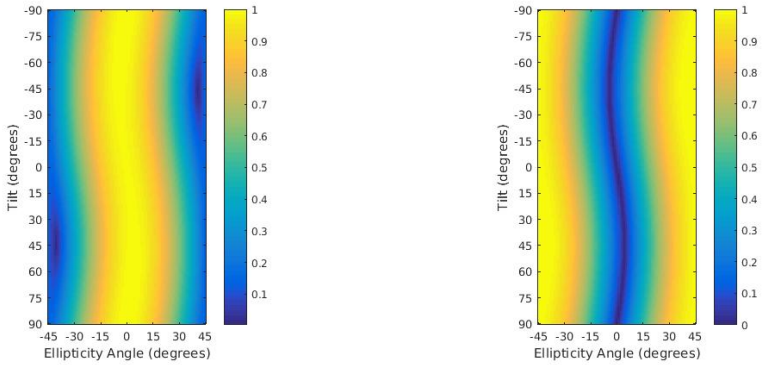

(a) ***(b)***

Figure A.3: *Polarisation signature for L-band dataset, after calibration is applied, for the first corner reflector where; (a) The co-polarisation signature, while (b) The cross-polarisation signature.*

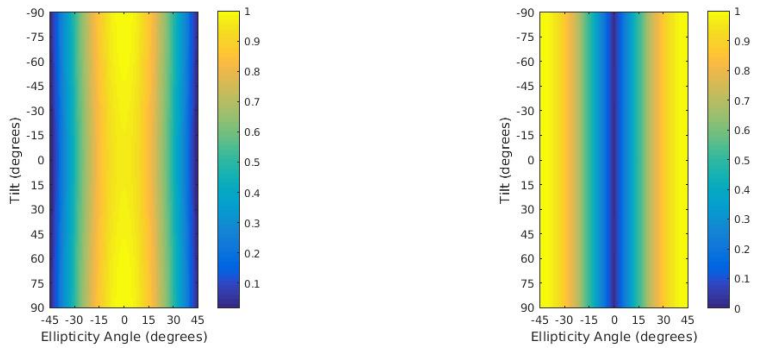

(a) ***(b)***

Figure A.4: *Polarisation signature for L-band dataset, after calibration is applied, for the second corner reflector close to the runway where; (a) The co-polarisation signature, while (b) The cross-polarisation signature.*

A.2 X-Band Polarisation Signature for Co-Channels

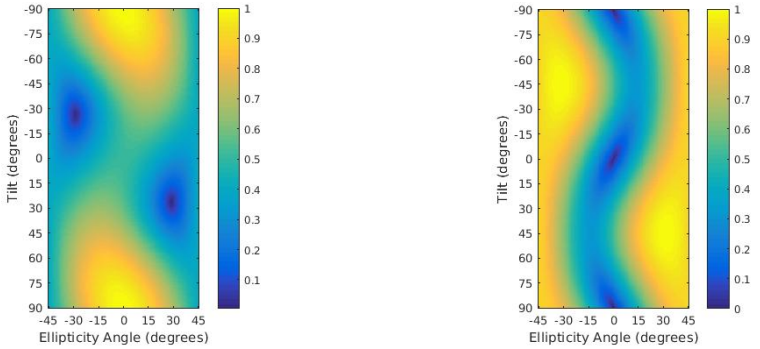

(a) ***(b)***

Figure A.5: *Polarisation signature for co-channels of X-band, before calibration applied, for the near field corner reflector where; (a) The co-polarisation signature, while (b) The cross-polarisation signature.*

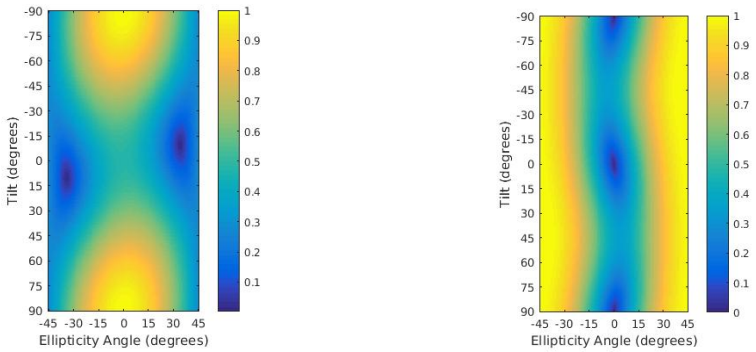

(a) ***(b)***

Figure A.6: *Polarisation signature for co-channels of X-band, before calibration applied, for the mid field corner reflector where; (a) The co-polarisation signature while, (b) The cross-polarisation signature.*

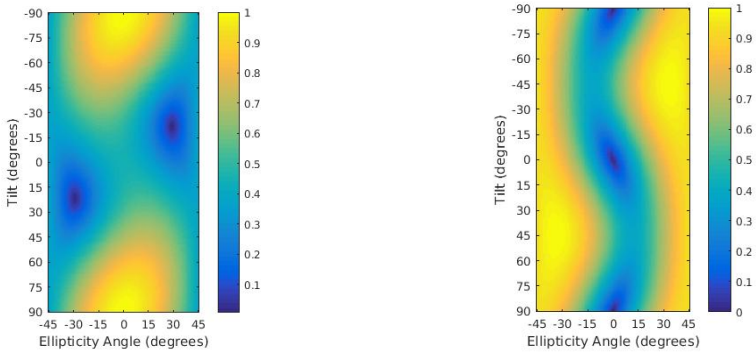

(a) ***(b)***

Figure A.7: *Polarisation signature for co-channels of X-band, before calibration applied, for the far field corner reflector where; (a) The co-polarisation signature while, (b) The cross-polarisation signature.*

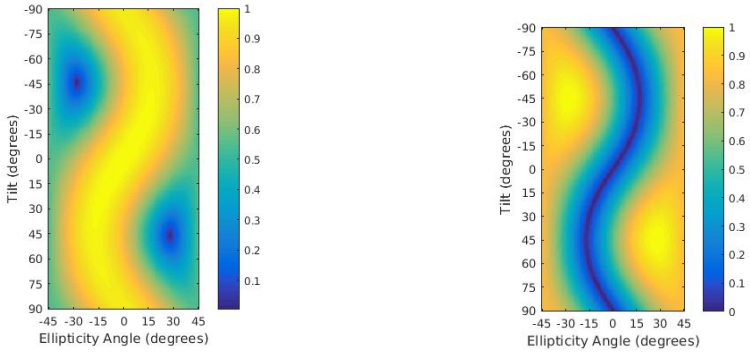

(a) *(b)*

Figure A.8: *Polarisation signature for co-channels of X-band dataset, after calibration is applied, for the near field corner reflector where; (a) The co-polarisation signature, while (b) The cross-polarisation signature.*

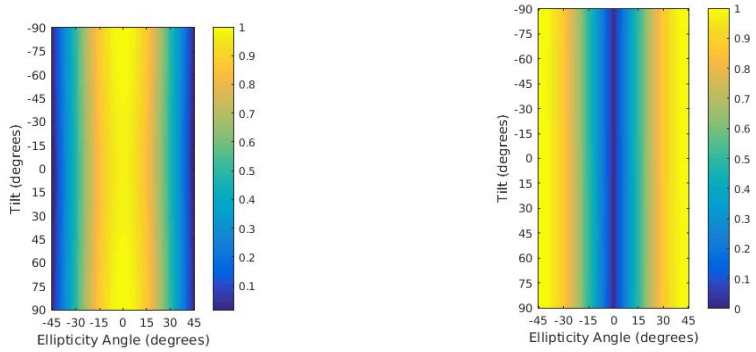

(a) *(b)*

Figure A.9: *Polarisation signature for co-channels of X-band dataset, after calibration applied, for the mid field corner reflector where; (a) The co-polarisation signature, while (b) The cross-polarisation signature.*

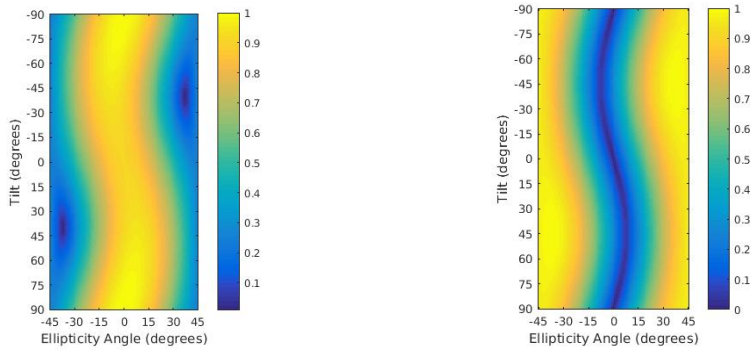

(a) ***(b)***

Figure A.10: *Polarisation signature for co-channels of X-band dataset, after calibration is applied, for the far field corner reflector where; (a) The co-polarisation signature, while (b) The cross-polarisation signature.*

A.3 X-Band Polarisation Signature for Cross-Channels

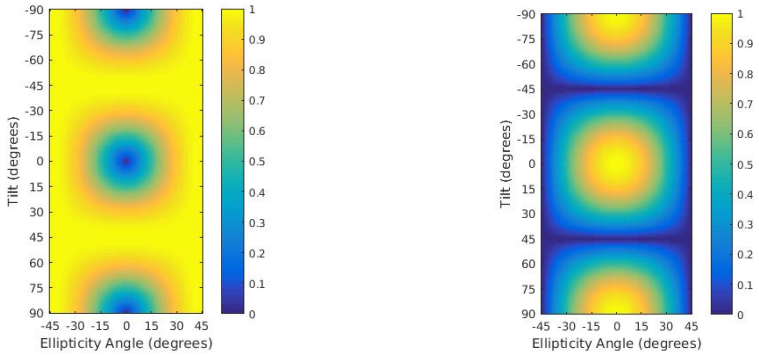

(a) ***(b)***

Figure A.11: *Theoretical polarisation signature for cross-channels with a zero cross-phase channels and 1 channels imbalance where; (a) The co-polarisation signature, while (b) The cross-polarisation signature.*

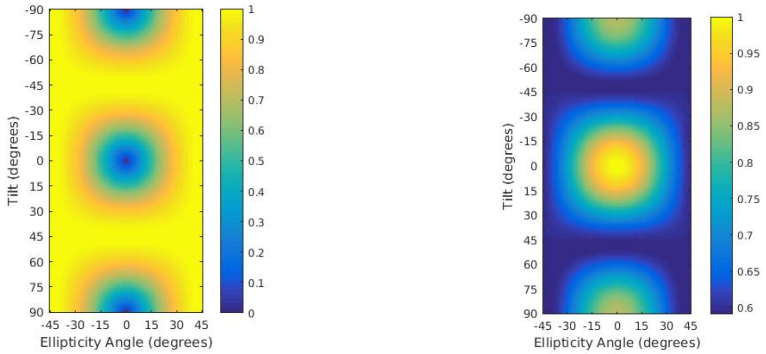

(a) ***(b)***

Figure A.12: *Polarisation signature for cross-channels of X-band, before calibration is applied, for the near field corner reflector where; (a) The co-polarisation signature, while (b) The cross-polarisation signature.*

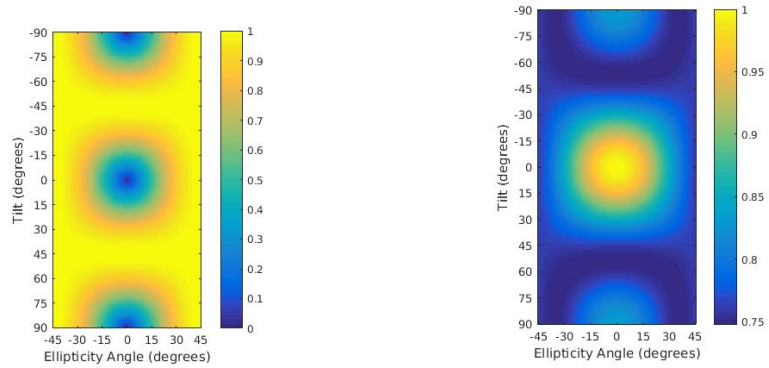

(a) ***(b)***

Figure A.13: *Polarisation signature for cross-channels of X-band, before calibration is applied, for the mid field corner reflector where; (a) The co-polarisation signature, while (b) The cross-polarisation signature.*

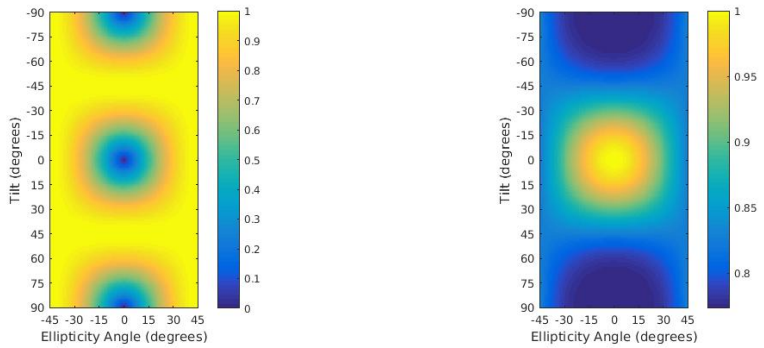

(a) ***(b)***

Figure A.14: *Polarisation signature for cross-channels of X-band, before calibration is applied, for the far field corner reflector where; (a) The co-polarisation signature, while (b) The cross-polarisation signature.*

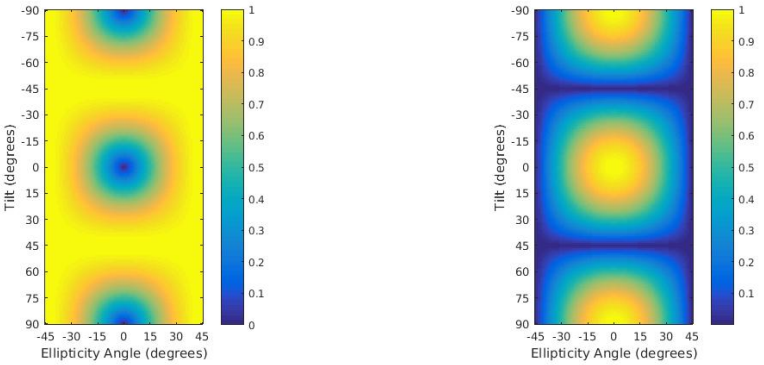

(a) ***(b)***

Figure A.15: *Polarisation signature for cross-channels of X-band, after calibration applied, for the near field corner reflector where; (a) The co-polarisation signature, while (b) The cross-polarisation signature.*

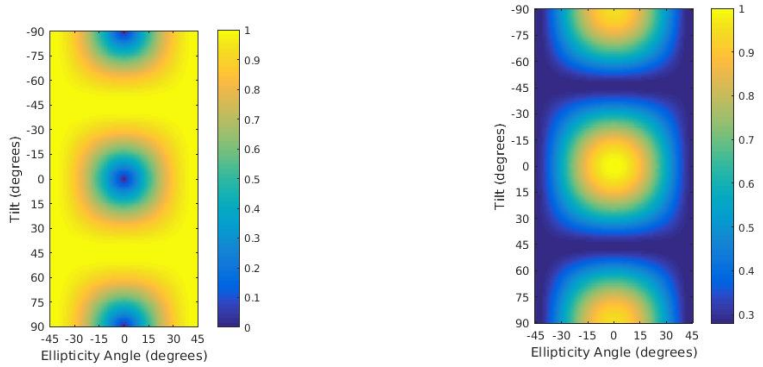

(a) ***(b)***

Figure A.16: *Polarisation signature for cross-channels of X-band, after calibration applied, for the mid field corner reflector where; (a) The co-polarisation signature, while (b) The cross-polarisation signature.*

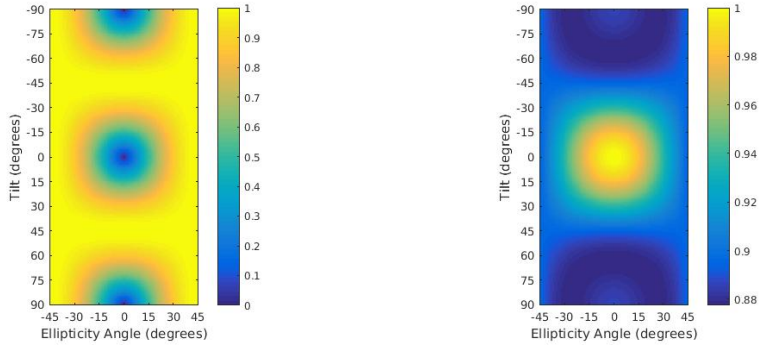

(a) ***(b)***

Figure A.17: *Polarisation signature for cross-channels of X-band, after calibration applied, for the far field corner reflector where; (a) The co-polarisation signature, while (b) The cross-polarisation signature.*

A.4 P-Band Polarisation Signature

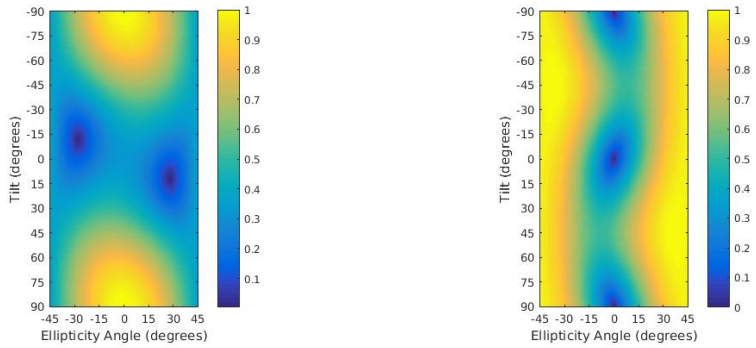

(a) ***(b)***

Figure A.18: *Polarisation signature, before calibration is applied, for the mid field trihedral corner reflector where; (a) The co-polarisation signature, while (b) The cross-polarisation signature.*

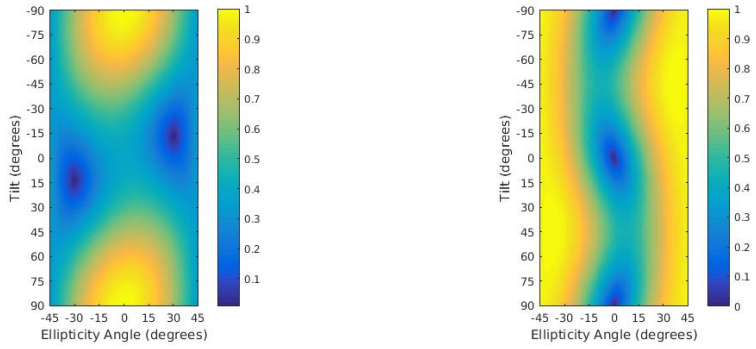

(a) ***(b)***

Figure A.19: *Polarisation signature, before calibration is applied, for the far field trihedral corner reflector where; (a) The co-polarisation signature, while (b) The cross-polarisation signature.*

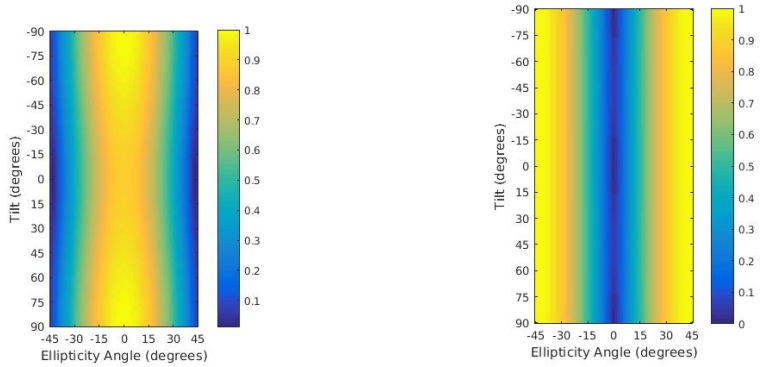

(a) ***(b)***

Figure A.20: *Polarisation signature, after calibration is applied, for the mid field trihedral corner reflector where; (a) The co-polarisation signature, while (b) The cross-polarisation signature.*

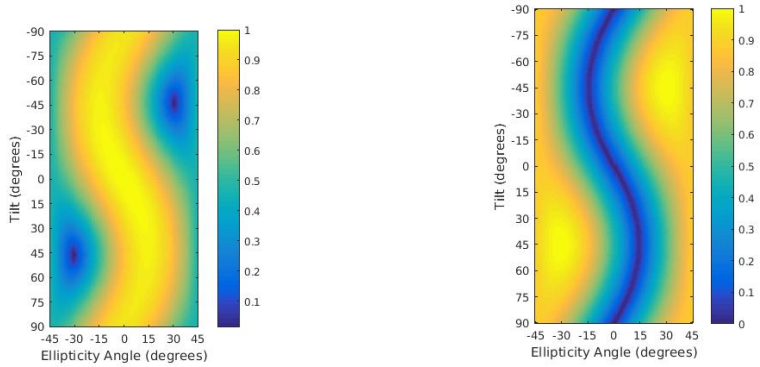

(a) ***(b)***

Figure A.21: *Polarisation signature, after calibration is applied, for the far field trihedral corner reflector where; (a) The co-polarisation signature, while (b) The cross-polarisation signature.*

Appendix B

Reading and Plotting Focused Data on IDL

```
pro readCUDAGBP, rootin, filename, fdc, presumming

FileNameImageSAR = rootin + 'SAR_CPLX_' + filename + '_pres_' + strtrim(string↩
    (presumming),2) + '_fdc_' + strtrim(string(fdc), 2) + '.sar'
;FileNameImageWeight = rootin + 'WEIGHT_IMAGE_' + filename + '_pres_' + ↩
    strtrim(string(presumming),2) + '_fdc_' + strtrim(string(fdc), 2) +'.wgt'
;FileNameImageNorm = rootin + 'NORM_IMAGE_' + filename + '_pres_' + strtrim(↩
    string(presumming),2) + '_fdc_' + strtrim(string(fdc), 2) +'.nrm'
FileNameImageOrbit = rootin + 'ORBIT_IMAGE_'+ filename+ '_pres_'+ strtrim(↩
    string(presumming),2)+ '_fdc_' + strtrim(string(fdc), 2) +'.orb'
FileNameXAxis = rootin + 'SAR_X_AXIS_' + filename +  '_pres_' + strtrim(string↩
    (presumming),2) + '_fdc_' + strtrim(string(fdc), 2) +'.axi'
FileNameYAxis = rootin + 'SAR_Y_AXIS_' + filename +  '_pres_' + strtrim(string↩
    (presumming),2) + '_fdc_' + strtrim(string(fdc), 2) +'.axi'

dim  = lonarr(2)
type = 0l
openr, rr, FileNameXAxis, /get_lun
readu, rr, dim
readu, rr, type
aux = 0d
readu, rr, aux
XAxis = aux
while (~EOF(rr)) do begin
    readu, rr, aux
    XAxis = [XAxis, aux]
```

```
endwhile
free_lun, rr

openr, rr, FileNameYAxis, /get_lun
readu, rr, dim
readu, rr, type
aux = 0d
readu, rr, aux
YAxis = aux
while (~EOF(rr)) do begin
    readu, rr, aux
    YAxis = [YAxis, aux]
endwhile
free_lun, rr

openr, rr, FileNameImageOrbit, /get_lun
readu, rr, dim
readu, rr, type
aux = fltarr(dim[0])
readu, rr, aux
OrbitImage = aux
while (~EOF(rr)) do begin
    readu, rr, aux
    OrbitImage = [[temporary(OrbitImage)], [aux]]
endwhile
free_lun, rr

openr, rr, FileNameImageSAR, /get_lun
readu, rr, dim
readu, rr, type
aux = dblarr(2*dim[0])
readu, rr, aux
SARImage = aux
while (~EOF(rr)) do begin
    readu, rr, aux
    SARImage = [[temporary(SARImage)], [aux]]
endwhile
indxre   = 2*dindgen(dim[0])
indxim   = 2*dindgen(dim[0]) + 1
SARImage = complex(SARImage[indxre,*], SARImage[indxim,*])
free_lun, rr

sz = size(SARImage)
Nr = sz[0];
Na = sz[1];

if (Na gt n_elements(XAxis)) then begin
    SARImage = SARImage(*, 0:n_elements(XAxis)-1);
    print, 'Lenght of SAR image reduced'
endif
```

```
if (n_elements(XAxis) gt Na) then begin
    XAxis = XAxis(0:Na-1);
    print, 'Lenght of X axis reduced'
endif

SARImage_sm     = smooth(abs(SARImage)^2., [2, 2], /edge_truncate);
SARImage_sm_lin = SARImage_sm^(0.7/2);
SARImage_sm_dB  = 10*alog10(SARImage_sm);

index = where(SARImage_sm_lin(*) gt 0);
len   = float(n_elements(index))
hist_val = float(histogram(SARImage_sm_lin[index], nbins=1000., locations = ↩
    hist_pos))
hist_val = hist_val/len;
hist_val_cum_sum = total(hist_val, /cum);

pos05  = (where(hist_val_cum_sum gt 0.05))[0];
pos98  = (where(hist_val_cum_sum gt 0.98))[0];
val05  = hist_pos[pos05];
val98  = hist_pos[pos98];

hist_valdB = float(histogram(SARImage_sm_dB[index], nbins=1000., locations = ↩
    hist_posdB))
hist_valdB = hist_valdB/len;
hist_valdB_cum_sum = total(hist_valdB, /cum);

pos05dB  = (where(hist_valdB_cum_sum gt 0.05))[0];
pos98dB  = (where(hist_valdB_cum_sum gt 0.98))[0];
val05dB  = hist_posdB[pos05dB];
val98dB  = hist_posdB[pos98dB];

window,/f, xsize=512, ysize=512, title = 'SAR image, linear scale'
tv, bytscl(congrid(SARImage_sm_lin, 512, 512, /interp), val05,val98)
var=tvrd(true=1)

if ~keyword_set(tiff) then begin
    filename_png = rootin + 'SARImage_sm_lin_' + filename + '_fdc_' + strtrim(↩
        string(fdc), 2) + '_pres_' + strtrim(string(presumming),2)
    write_png, filename_png+'.png',var
endif else begin
    filename_tif = rootin + 'SARImage_sm_lin_' + filename + '_fdc_' + strtrim(↩
        string(fdc), 2) + '_pres_' + strtrim(string(presumming),2)
    write_tiff, filename_tif +'.tiff',var,orientation=0
endelse

sz = size(SARImage_sm_lin)
window,/f, xsize=sz[1], ysize=sz[2], title = 'SAR image, linear scale' ,/↩
    pixmap
tv, bytscl(SARImage_sm_lin, val05,val98)
var=tvrd(true=1)
```

```
if ~keyword_set(tiff) then begin
    filename_png = rootin + 'SARImage_sm_lin_' + filename + '_fdc_' + strtrim(↩
        string(fdc), 2) + '_pres_' + strtrim(string(presumming),2) + '_full'
    write_png, filename_png+'.png',var
endif else begin
    filename_tif = rootin + 'SARImage_sm_lin_' + filename + '_fdc_' + strtrim(↩
        string(fdc), 2) + '_pres_' + strtrim(string(presumming),2) + '_full'
    write_tiff, filename_tif +'.tiff',var,orientation=0
endelse
wdelete

window,/f, xsize=512, ysize=512, title = 'SAR image, dB scale'
tv, bytscl(congrid(SARImage_sm_dB, 512, 512, /interp), val05dB,val98dB)
var=tvrd(true=1)

if ~keyword_set(tiff) then begin
    filename_png = rootin + 'SARImage_sm_dB_' + filename + '_fdc_' + strtrim(↩
        string(fdc), 2) + '_pres_' + strtrim(string(presumming),2)
    write_png, filename_png+'.png',var
endif else begin
    filename_tif = rootin + 'SARImage_sm_dB_' + filename + '_fdc_' + strtrim(↩
        string(fdc), 2) + '_pres_' + strtrim(string(presumming),2)
    write_tiff, filename_tif +'.tiff',var,orientation=0
endelse

sz = size(SARImage_sm_dB)
window,/f, xsize=sz[1], ysize=sz[2], title = 'SAR image, dB scale', /pixmap
tv, bytscl(SARImage_sm_dB, val05dB,val98dB)
var=tvrd(true=1)

if ~keyword_set(tiff) then begin
    filename_png = rootin + 'SARImage_sm_dB_' + filename + '_fdc_' + strtrim(↩
        string(fdc), 2) + '_pres_' + strtrim(string(presumming),2) + '_full'
    write_png, filename_png+'.png',var
endif else begin
    filename_tif = rootin + 'SARImage_sm_dB_' + filename + '_fdc_' + strtrim(↩
        string(fdc), 2) + '_pres_' + strtrim(string(presumming),2) + '_full'
    write_tiff, filename_tif +'.tiff',var,orientation=0
endelse
wdelete

stop
end
```

Appendix C

Reading Geolocation UTM on Matlab

```
clear all;
close all;

figure_number_nom = 200;
rootin = '/home/waseda/Desktop/P-Band-23rd/GeoLocation/';
namefile1 = '20161123150940_11';
namefile2 = '20161123150940_22';
fdc = 0;
presum = 32;

FileNameImageSAR = [rootin, 'SAR_CPLX_', namefile1, '_pres_', num2str(presum),↩
    '_fdc_', num2str(fdc),'.sar'];
FileNameImageWeight = [rootin, 'WEIGHT_IMAGE_', namefile1, '_pres_', num2str(↩
    presum), '_fdc_', num2str(fdc),'.wgt'];
FileNameImageNorm = [rootin, 'NORM_IMAGE_', namefile1, '_pres_', num2str(↩
    presum), '_fdc_', num2str(fdc),'.nrm'];
FileNameImageOrbit = [rootin, 'ORBIT_IMAGE_', namefile1, '_pres_', num2str(↩
    presum), '_fdc_', num2str(fdc),'.orb'];
FileNameXAxis = [rootin, 'SAR_X_AXIS_', namefile1,  '_pres_', num2str(presum),↩
    '_fdc_', num2str(fdc),'.axi'];
FileNameYAxis = [rootin, 'SAR_Y_AXIS_', namefile1,  '_pres_', num2str(presum),↩
    '_fdc_', num2str(fdc),'.axi'];
FileNameNav = [rootin, 'NAvigation\NavAnt_', namefile1,  '_pres_', num2str(↩
    presum),'.nav'];
```

```
FileNameImageSAR2 = [rootin, 'SAR_CPLX_', namefile2, '_pres_', num2str(presum)↩
    , '_fdc_', num2str(fdc),'.sar'];
FileNameImageWeight2 = [rootin, 'WEIGHT_IMAGE_', namefile2, '_pres_', num2str(↩
    presum), '_fdc_', num2str(fdc),'.wgt'];
FileNameImageNorm2 = [rootin, 'NORM_IMAGE_', namefile2, '_pres_', num2str(↩
    presum), '_fdc_', num2str(fdc),'.nrm'];
FileNameImageOrbit2 = [rootin, 'ORBIT_IMAGE_', namefile2, '_pres_', num2str(↩
    presum), '_fdc_', num2str(fdc),'.orb'];
FileNameXAxis2 = [rootin, 'SAR_X_AXIS_', namefile2,  '_pres_', num2str(presum)↩
    , '_fdc_', num2str(fdc),'.axi'];
FileNameYAxis2 = [rootin, 'SAR_Y_AXIS_', namefile2,  '_pres_', num2str(presum)↩
    , '_fdc_', num2str(fdc),'.axi'];
FileNameNav2 = [rootin, 'NAvigation\NavAnt_', namefile2,  '_pres_', num2str(↩
    presum),'.nav'];

fid = fopen(FileNameXAxis, 'rb');
    n = fread(fid, 1, 'int32');
    m = fread(fid, 1, 'int32');
    t = fread(fid, 1, 'int32');
XAxis = fread(fid, 'double');
fclose(fid);

fid = fopen(FileNameYAxis, 'rb');
    n = fread(fid, 1, 'int32');
    m = fread(fid, 1, 'int32');
    t = fread(fid, 1, 'int32');
YAxis = fread(fid, 'double');
fclose(fid);

Nr = length(YAxis);

fid = fopen(FileNameImageOrbit, 'rb');
    Nr = fread(fid, 1, 'int32');
    m = fread(fid, 1, 'int32');
    t = fread(fid, 1, 'int32');
OrbitImage = fread(fid, [Nr inf], 'single');
fclose(fid);

fid = fopen(FileNameImageSAR, 'rb');
    Nr = fread(fid, 1, 'int32');
    m = fread(fid, 1, 'int32');
    t = fread(fid, 1, 'int32');
SARImage = fread(fid, [Nr*2 inf], 'double');
fclose(fid);
SARImage = SARImage(1:2:end, :) + j*SARImage(2:2:end, :);
[Nr Na] = size(SARImage);

fid = fopen(FileNameImageSAR2, 'rb');
    Nr2 = fread(fid, 1, 'int32');
    m = fread(fid, 1, 'int32');
```

```
    t = fread(fid, 1, 'int32');
SARImage2 = fread(fid, [Nr2*2 inf], 'double');
fclose(fid);
SARImage2 = SARImage2(1:2:end, :) + j*SARImage2(2:2:end, :);
[Nr2 Na2] = size(SARImage2);

fid = fopen(FileNameXAxis2, 'rb');
    n = fread(fid, 1, 'int32');
    m = fread(fid, 1, 'int32');
    t = fread(fid, 1, 'int32');
XAxis2 = fread(fid, 'double');
fclose(fid);

fid = fopen(FileNameYAxis2, 'rb');
    n = fread(fid, 1, 'int32');
    m = fread(fid, 1, 'int32');
    t = fread(fid, 1, 'int32');
YAxis2 = fread(fid, 'double');
fclose(fid);

if (Na > length(XAxis))
            SARImage = SARImage(:, 1:Na);
            disp('Lenght of SAR image reduced');
        end
        if (length(XAxis) > Na)
            XAxis = XAxis(1:Na);
            disp('Lenght of X axis reduced');
        end

        if (Na2 > length(XAxis2))
            SARImage2 = SARImage2(:, 1:Na2);
            disp('Lenght of SAR image reduced');
        end
        if (length(XAxis2) > Na2)
            XAxis2 = XAxis2(1:Na2);
            disp('Lenght of X axis reduced');
        end

        SARImage = SARImage(:, 1:length(XAxis));
        SARImage2 = SARImage2(:, 1:length(XAxis2));

        X1 = XAxis(1);
        da = XAxis(2)-XAxis(1);

        shiftXn = round( (XAxis2(1) - X1)/da);
        if (shiftXn >= 0)
            az1_co = 1 + shiftXn;
            az2_co = min(Na, Na2 + shiftXn);
            az1 = 1;
            az2 = min(Na - shiftXn, Na2);
```

```
        else
            az1_co = 1;
            az2_co = min(Na, Na2+shiftXn);
            az1 = 1 - shiftXn;
            az2 = min(Na-shiftXn, Na2);
        end

        SARImageCo2 = zeros(Nr, Na);
        SARImageCo2(:, az1_co:az2_co) = SARImage2(1:Nr, az1:az2);

FileNameMaster = ['/home/waseda/Desktop/P-Band-23rd/GeoLocation/Settings↩
    /20161123150940.mst'];
        fidMst = fopen(FileNameMaster, 'rb');

        utmX0 = fread(fidMst, 1, 'double');
        utmY0 = fread(fidMst, 1, 'double');
        utmZ0 = fread(fidMst, 1, 'double');
        utmZone = fread(fidMst, 1, 'double');
        utmEmisphere = fread(fidMst, 1, 'double');
        utmXdir = fread(fidMst, 1, 'double');
        utmYdir = fread(fidMst, 1, 'double');
        utmZdir = fread(fidMst, 1, 'double');

        fclose(fidMst);

        heading = atan2(utmXdir, utmYdir);
        UTMXImage = zeros(Nr, Na);
        UTMYImage = zeros(Nr, Na);
        LeftLooking = 1;

        if (LeftLooking)
            MatrixTrans = [ sin(heading), -cos(heading);
                cos(heading),  sin(heading)];
        else
            MatrixTrans = [ sin(heading),  cos(heading);
                cos(heading),  -sin(heading)];
        end

        XY0 = [utmX0; utmY0];

        for indy = 1:Nr
            for indx = 1: Na
                utmxy = MatrixTrans * [XAxis(indx); YAxis(indy)] + XY0;

                UTMXImage(indy, indx) = utmxy(1);
                UTMYImage(indy, indx) = utmxy(2);
            end
        end
```